UNIVERSITY OF ROCHESTER
LABORATORY FOR LASER ENERGETICS

Volume 104
July–September 2005
DOE/SF/19460-643

LLE Review

Quarterly Report

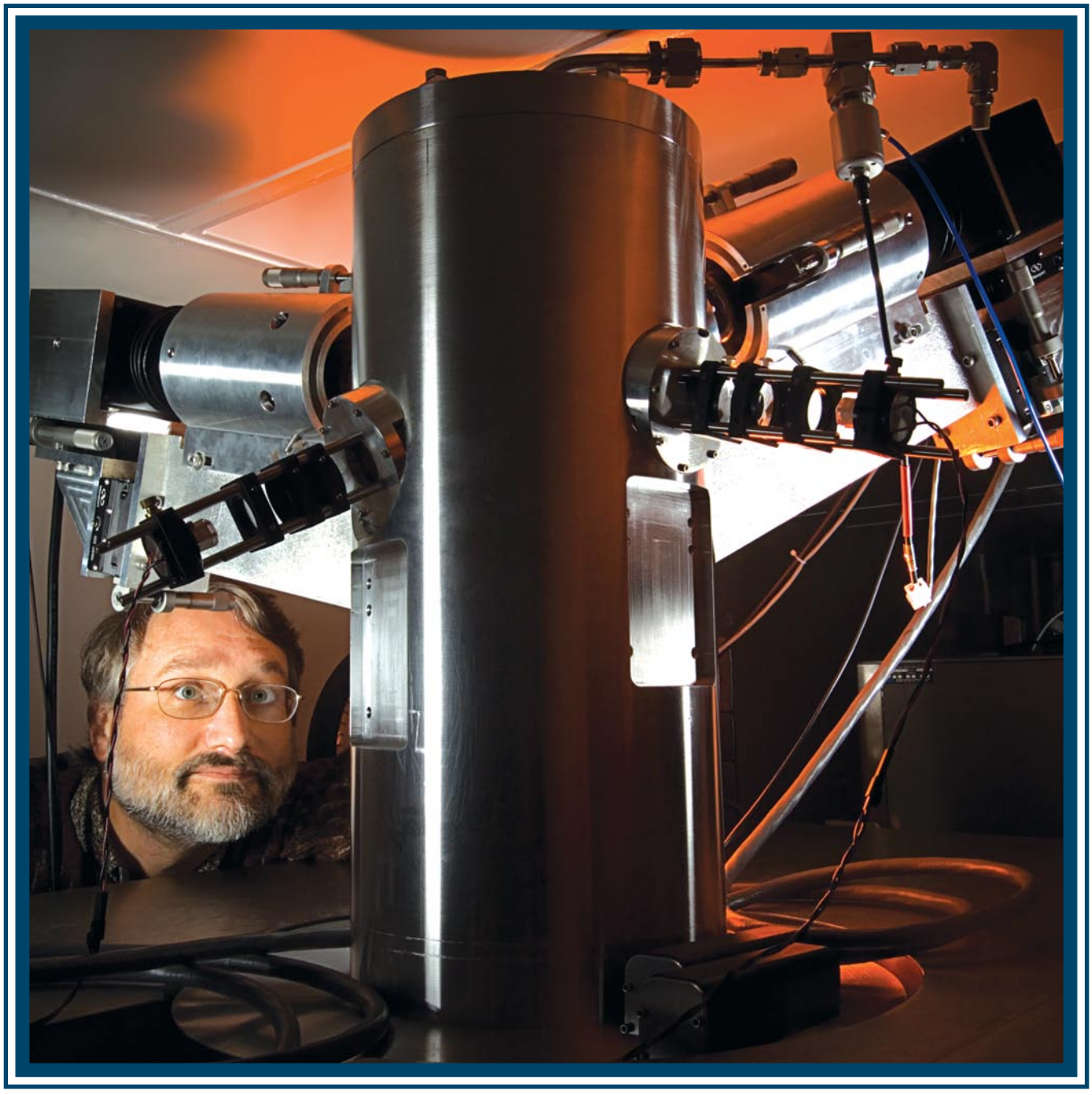

About the Cover:

Scientist Dana Edgell examines target Characterization Station #2. Cryogenic targets are inserted into the column (center) from a Moving Cryostat Transport Cart (MCTC) docked underneath the station. Two sets of cameras and collection optics, shown extending back off either side of the column, provide nearly orthogonal simultaneous views of a cryogenic target. High-luminescence LED's, backlighting the targets, are shown coming off the central column opposite each camera. The reflection of this light off the inner surface of the cryogenic target's hydrogenic ice layer produces a characteristic ring in the camera shadowgraph images. The smoothness of the ice surface is measured by analysis of this "bright ring."

The photo on the left shows the cryogenic target MCTC and layering team (from left to right: Senior Laboratory Engineer Luke Elasky, Senior Technician Al Weaver, Senior Technician Steve Verbridge, and high school summer student Lauren Weiss) layering and characterizing a target in preparation for an OMEGA cryogenic target shot. Characterization Station #2's target viewing cameras and optics, shown on the cover, can be seen above the platform while the MCTC is docked below it.

The work described in this volume includes current research at the Laboratory for Laser Energetics, which is supported by New York State Energy Research and Development Authority, the University of Rochester, the U.S. Department of Energy Office of Inertial Confinement Fusion under Cooperative Agreement No. DE-FC03-92SF19460, and other agencies.

Printed in the United States of America
Available from
National Technical Information Services
U.S. Department of Commerce
5285 Port Royal Road
Springfield, VA 22161
Price codes: Printed Copy A04
Microfiche A01

For questions or comments, contact Jason Myatt, Editor, Laboratory for Laser Energetics, 250 East River Road, Rochester, NY 14623-1299, (585) 275-5772.

Worldwide-Web Home Page: http://www.lle.rochester.edu/

UNIVERSITY OF ROCHESTER
LABORATORY FOR LASER ENERGETICS

Volume 104
July–September 2005
DOE/SF/19460-643

LLE Review

Quarterly Report

UR LLE

Contents

In Brief

This volume of the LLE Review, covering July–September 2005, features "Three-Dimensional Characterization of Cryogenic Target Ice Layers Using Multiple Shadowgraph Views," by D. H. Edgell, R. S. Craxton, L. M. Elasky, D. R. Harding, L. S. Iwan, R. L. Keck, L. D. Lund, S. J. Verbridge, M. D. Wittman, W. Seka (LLE), A. Warrick (LLNL), and T. Brown (UR Institute of Optics). In this article (p. 169), the authors report on backlit optical shadowgraphy, the primary diagnostic for D_2 ice layer characterization of cryogenic targets for the OMEGA Laser System. Measurement of the position of the most prominent rings, caused by the reflection and refraction of light in the ice layer, in conjunction with ray-trace model predictions allows construction of a 3-D ice layer representation, an estimation of the global surface roughness, and a determination of a Legendre-mode spectrum suitable for implosion modeling.

In the second article (p. 178) T. R. Boehly, E. Vianello, J. E. Miller, R. S. Craxton, T. J. B. Collins, V. N. Goncharov, I. V. Igumenshchev, and D. D. Meyerhofer (LLE) with D. G. Hicks, P. M. Celliers, and G. W. Collins of LLNL describe velocity interferometry and optical self-emission measurements from shock waves in polystyrene targets driven by two 90-ps pulses separated by 1.5 to 2 ns. The velocity histories, coalescence times, and transit times are unambiguously observed and are in good agreement with one-dimensional code predictions. The timing of multiple shock waves is crucial to the performance of inertial confinement fusion ignition targets.

Additional highlights of research presented in this issue include the following:

- S. Skupsky, R. S. Craxton, F. J. Marshall, R. Betti, T. J. B. Collins, R. Epstein, V. N. Goncharov, I. V. Igumenshchev, J. A. Marozas, P. W. McKenty, P. B. Radha, D. D. Meyerhofer, T. C. Sangster, and R. L. McCrory with J. D. Kilkenny of General Atomics examine designs set to achieve direct-drive ignition on the NIF at 1 MJ using the x-ray-drive beam configuration (p. 186). This approach, known as polar direct drive (PDD), achieves the required irradiation uniformity by repointing some of the beams toward the target equator and by increasing the laser intensity at the equator to compensate for the reduced laser coupling from oblique irradiation.

- J. A. Delettrez, J. Myatt, P. B. Radha, C. Stoeckl, S. Skupsky, and D. D. Meyerhofer present simulations of integrated fast-ignition experiments on the combined OMEGA/OMEGA EP laser systems with the multidimensional hydrodynamic code *DRACO* (p. 189). An OMEGA cryogenic DT target, designed to reach a 1-D fuel ρR of 0.5 g/cm^2, has been simulated in 2-D with and without nonuniformities. The neutron yield is predicted to be in excess of 10^{15} (compared to ~10^{14} without an ignitor beam) over a synchronization range of ~80 ps.

- J. L. DeCiantis, F. H. Séguin, J. A. Frenje, V. Berube, M. J. Canavan, C. D. Chen, S. Kurebayashi, C. K. Li, J. R. Rygg, B. E. Schwartz, and R. D. Petrasso, (Plasma Science and Fusion Center, MIT) along with J. A. Delettrez, S. P. Regan, V. A. Smalyuk, J. P. Knauer, F. J. Marshall, D. D. Meyerhofer, S. Roberts, T. C. Sangster, C. Stoeckl (LLE), K. Mikaelian, H. S. Park, and H. F. Robey (LLNL) describe the development of a proton emission imaging system that has been used to measure the nuclear burn

regions in the cores of inertial confinement fusion implosions (p. 196). The imaging technique relies on the penumbral imaging of 14.7-MeV D^3He fusion protons. Experimental data, analysis, and error analysis are presented for a representative symmetric implosion of a fuel capsule with 20-μm-thick plastic shell and 18 atm of D^3He gas fill.

- W. Theobald, J. A. Delettrez, C. Mileham, J. Myatt, S. P. Regan, H. Sawada, C. Stoeckl, M. Storm, T. C. Sangster (LLE), S. Glenzer, G. Gregori, N. Izumi, J. A. Koch, J. Kuba, A. J. MacKinnon, M. Key, H. S. Park, P. Patel, R. Shepherd, R. Snavely (LLNL), K. Akli, J. A. King, B. Zhang (Department of Applied Sciences, University of CA, Davis), J. Pasely, R. B. Stephens (GA), R. R. Freeman (College of Mathematical and Physical Sciences, OH State University), R. Clarke, J. Green, R. Heathcote, K. Lancaster, D. Neely, and P. A. Norreys (Rutherford Appleton Laboratory) present observations of a hot, T_e ~ 2- to 3-keV surface plasma in the interaction of a 0.7-ps petawatt laser beam with solid copper-foil targets at intensities $>10^{20}$ W/cm^2 (p. 208). These temperatures were inferred from Cu, He_α, and Ly_α emission lines, which have not previously been observed with ultrafast laser pulses.
- This volume concludes with a summary of LLE's Summer High School Research Program (p. 221), the FY05 Laser Facility Report (p. 223), and the National Laser Users' Facility and External Users' Programs (p. 225).

Jason Myatt
Editor

Three-Dimensional Characterization of Cryogenic Target Ice Layers Using Multiple Shadowgraph Views

Introduction

The 60-beam, 30-kJ OMEGA Laser System[1] studies the laser-driven direct-drive ignition approach to inertial confinement fusion (ICF) in which many individual high-power laser beams directly illuminate a spherical target to create a spherically symmetric implosion. Current designs for high-gain ICF targets include a layer of condensed hydrogen fuel that adheres to the inner surface of a thin spherical shell ablator. Laser energy delivered to the target ablates its outer surface and the ablation pressure drives the fuel layer inward, compressing both it and the gaseous fuel at the target's center. The drive pressure is varied in time such that the fuel density is compressed by a factor of as much as 4000 while remaining relatively cold. However, shock waves resulting from the drive-pressure variations, along with compressive work, heat the gaseous core "hot spot" to the high temperatures needed to initiate burning the fuel.

"Hot-spot" ignition is a common feature of all standard ignition experiments. This requires spherically symmetric implosions to limit the effects of hydrodynamic instabilities that can reduce fusion yield or prevent ignition by causing cold fuel to mix into the hot spot or target breakup. Asymmetry-induced hydrodynamics reduce the performance of most ICF targets well below that predicted by 1-D modeling.[2] The symmetry requirement imposes strong constraints on the uniformity of the laser illumination and on the sphericity of the target.[3] LLE has made great strides in reducing illumination asymmetries[2] due to drive imbalance between different beams and laser imprint. Efforts are also under way at LLE to reduce the asymmetries inherent in the target ice layer.[4]

The quality of a fuel–ice layer depends on the method used to form it. Extremely slow cooling (~1 mK/min) is required to avoid the formation of multiple crystals of different orientations.[5] Volumetric heating, in the form of infrared heating,[6] improves the sphericity of ice layers by driving ice mass from thicker sections of the layer to thinner areas via vapor pressure and sublimation. Ice surfaces in OMEGA cryogenic targets are beginning to approach the 1-μm root-mean-square (rms) deviation requirement[3] for successful ignition on the NIF.[7]

The degrading effect of surface roughness on implosion performance depends on the perturbation's mode number, which is the ratio of the capsule's circumference to the wavelength of the perturbation. The surface roughness is characterized in terms of a mode spectrum analogous to Fourier analysis. Since the target geometry is spherical, however, spherical harmonics

$$Y_{\ell m}(\theta,\phi) \equiv \left[\frac{(2\ell+1)}{4\pi}\frac{(\ell-m)!}{(\ell+m)!}\right]^{1/2} P_{\ell m}(\cos\theta)e^{im\phi}$$

$$-\ell \le m \le \ell, \tag{1}$$

where $P_{\ell m}$ are the associated Legendre functions, form the base functions used for the mode spectrum. Accurate surface characterization of ice layers requires reliable measurement of the layer's surface with submicron resolution at many points distributed over the surface of a target. Hydrodynamic codes then calculate capsule implosion performance using the measured surface mode power spectrum. The benchmarking of calculated target performance with experimental results is essential for designing ignition-scale targets and specifying their allowable surface roughness with confidence.

This article describes the optical backlit shadowgraphic characterization of cryogenic target ice layers with submicron resolution at LLE. A novel feature of this work is the ability to image the target from many different views. The analyses of multiple images of the target from different views are combined to construct a 3-D representation of the ice layer and an ice-roughness power spectrum in terms of spherical harmonics. There are many advantages to using a full 3-D representation over a single view or even over a few orthogonal views.

- The probability of missing significant local defects in the ice layer is greatly reduced.
- A 2-D surface-roughness spectrum suitable for input into a hydrodynamic code can be directly calculated. A single view provides only a 1-D Fourier roughness spectrum.

- Future detailed comparison of experimental implosions and 3-D simulations will require full surface ice characterization.

- Discrimination is possible between bumps/divots and ridges/troughs that could appear similar in a single view.

- Discrimination is possible between some outer-surface perturbation effects on the bright ring and actual ice layer defects.

Shadowgraphic Characterization of Ice Layers (p. 170) briefly describes the principles and equipment used to record a cryogenic target shadowgraph at LLE and is followed by details of the analysis of an individual shadowgraph in **Analysis of Individual Shadowgraphs** (p. 171). The 3-D ice layer reconstruction and determination of the global surface roughness power spectrum from multiple target views are reported in **Three-Dimensional Ice Layer Reconstruction Using Multiple Shadowgraph Views** (p. 175).

Shadowgraphic Characterization of Ice Layers

Optical backlit shadowgraphy is a primary diagnostic for ICF target ice layer roughness measurements.[6,8–12] A shadowgraph records the image of light rays passing through a backlit target. The rays are reflected and refracted at the shell wall and ice layer surfaces; some rays are focused into characteristic rings. Ray-trace modeling has identified specific reflections/refractions responsible for the brightest rings (see Fig. 104.1). The most prominent or "bright" ring is the result of total internal reflection off the inner solid–vapor interface of the ice layer. The position of the bright ring in the shadowgraph is directly correlated with the position of the inner surface of the ice layer and thus allows characterization of the nonuniformity of the inner surface.

A high-magnification, high-fidelity backlit optical shadowgraphy system (Fig. 104.2) is used to diagnose the ice layer quality while a target is in one of two characterization stations. A 612-nm red LED provides backlighting, and a 0.1- to 30-ms pulse drives the LED that is coupled to a 450-μm multimode fiber used to illuminate (~*f*/23) the target. An *f*/6 imaging optic magnifies the target on a Dalsa CCD camera (12 bit, 1024 × 1024) (Ref. 13) such that the camera typically images about 1.2 μm per pixel. The camera is triggered by and integrates over the same pulse that drives the LED.

A sample shadowgraph of a LLE cryogenic target suspended from a beryllium "c mount" by four threads of spider silk (a polymerized scleroprotein)[14] is shown in Fig. 104.3. The strong, unbroken bright ring and mostly featureless central spot are indicative of the high quality of this ice layer. Two inner rings are also clearly visible.

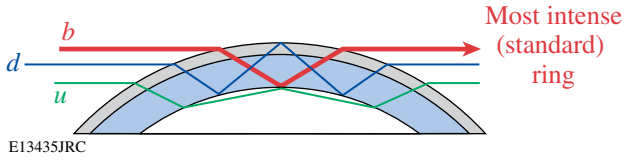

Figure 104.1
Ray-trace modeling of a cryogenic target has identified the sources of the most intense rings. The bright ring *b* is by far the most intense.

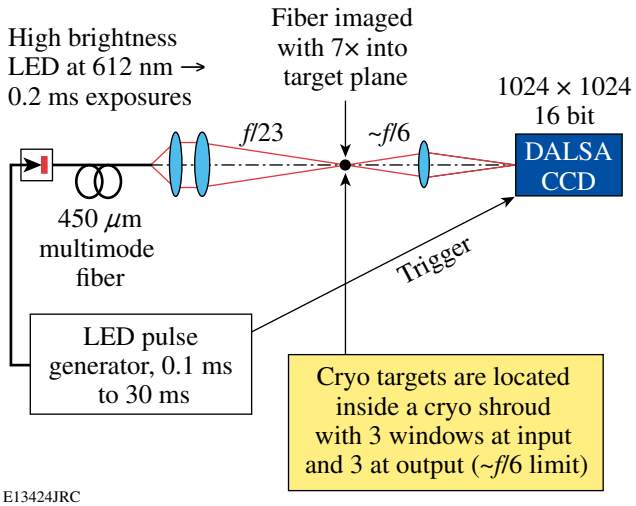

Figure 104.2
The LLE cryogenic target characterization stations are based on a diffuse *f*/23 source and *f*/6 imaging optics.

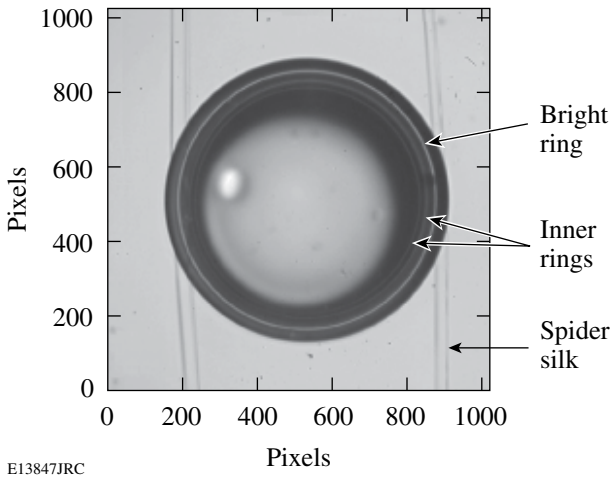

Figure 104.3
Shadowgraph of a cryogenic target in a logarithmic scale. The fainter inner rings are clearly visible in the image.

Analysis of Individual Shadowgraphs

The shadowgraph analysis is performed by a MATLAB[15] routine, *viewcryo*, that uses several automated steps that include:

1. Rough estimation of the target radius and center
2. Unwrapping the image in polar coordinates
3. Identification of spider webs
4. Refinement of the target edge and center estimate
5. Repetition of steps 2–4 until the target center coordinates change by less than ~0.005 μm
6. Identification of the bright ring using Gaussian fitting routines
7. Determination of the ice layer thickness
8. Fourier analysis of the ice layer

Details regarding each step are given below.

1. Rough Estimation of the Target Radius and Center

The target image is roughly centered in the CCD image by design and alignment. A first rough estimate of the target center location is obtained from horizontal and vertical lineouts (e.g., Fig. 104.4) averaged over several (~10) pixels. Taking the midpoints between the clearly visible target edges yields target center coordinates that are typically within one pixel of the more accurate center-finding routines discussed below.

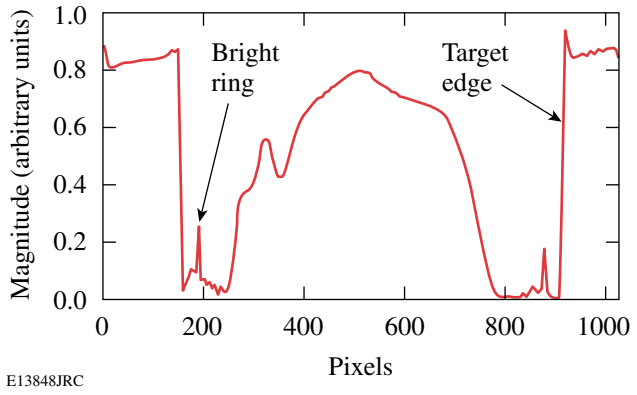

Figure 104.4
Horizontal lineout through the center of the image shown in Fig. 104.3 and averaged over ~10 pixels.

2. Unwrapping the Image in Polar Coordinates

With an estimate of the target center, the image can be mapped to (θ,r) polar coordinates by determining the image intensity along radial lines at fixed angular intervals. A super-Gaussian interpolation function unwraps the target image to an evenly spaced grid in (θ,r), and the interpolation function has separate Gaussian widths optimized for the angular and radial dimensions.[16] The separation of interpolation parameters allows subpixel resolution in the radial direction necessary to determine the roughness of the rather smooth outer-target surface and inner-ice layer. Pixel smoothing in the angular dimension is possible while allowing resolution of high mode numbers in the Fourier analysis of the target surfaces. Figure 104.5 shows the unwrapped image of the target edge using the initial rough estimate of the target center for the shadowgraph shown in Fig. 104.3. The unwrapped target edge shows a large $n = 1$ Fourier component, indicating an offset in the actual target center from the initial estimate. This $n = 1$ component is used below to correct the target center coordinates and, after several iterations, the center coordinates converge to a ≤0.005-μm variation from iteration to iteration.

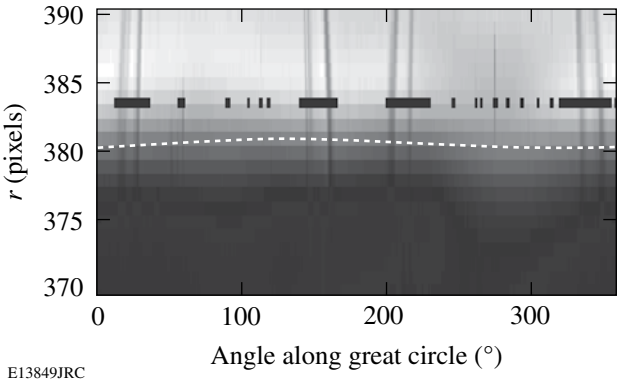

Figure 104.5
Close-up of the step in intensity at the target edge for the initial unwrapping of the shadowgraph shown in Fig. 104.3. The black bars indicate gaps where the edge data is *not* used to determine the target center due to the influence of spider webs and other image features outside the target. The white dotted line shows the position of the target edge (midpoint of the intensity step). The $n = 1$ component in the target edge results from an offset in the estimated target center that has not yet been removed.

3. Identification of Spider Webs

The four spider webs used to support the cryogenic targets appear in every shadowgraphic image of the target. Absorption/reflection/diffraction of light by the webs distorts the CCD image of the target's outer surface where the web images cross. These corrupted portions of the outer edge images are not used in the target-edge and center-finding routines discussed below.

The *viewcryo* code identifies where the web traces intersect the target edge by examining the region of the unwrapped image just outside the edge and isolating sections where pixel values differ significantly from a local median value. The local median is calculated for a section broad enough that it is not

located on a web. The results of the spider web identification for an initial image unwrapping are shown in Fig. 104.5.

4. Refinement of the Target Edge and Center Estimates

The target center position in the image is accurately determined by removing the $n = 1$ Fourier component of the target edge measurements in the unwrapped image. This component corresponds to a linear offset in the determination of the target center. The target edge is determined by examining the radial variation in intensity at each angular position in the unwrapped image (e.g., the data points in Fig. 104.6). While the edge corresponds to a step in intensity, no single smooth-step function (e.g., an error function) would be a good match to the data mainly because of the "overshoot" at the top of the step. A least-squares fit of the data to a set of many smooth step functions produces a good fit to the features of the measured step along with essentially flat regions on either side of the step as shown by the solid line in Fig. 104.6. The step function set consists of many (~35) error-function traces of varying widths and centers covering a range appropriate for the target edge. Negative fitting coefficients enable the fit to replicate the "overshoot" and other nonmonotonic features. Least-squares fitting via a matrix inversion results in a very fast fit. The target-edge position is defined as the radial point where the fit height is halfway between the heights of the flat regions on either side of the edge step. The radial location of this halfway point can be resolved to 0.1 pixel as is shown in **Shadowgraph Resolution** (p. 174). The data points in Fig. 104.7 show the angular variation in target's outer-edge position along a great circle.

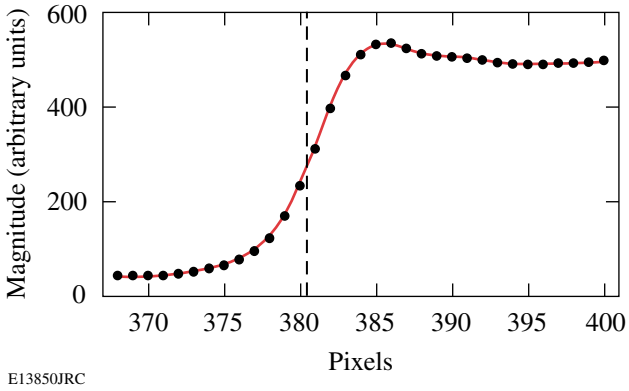

Figure 104.6
Radial variation of intensity at a specific angular position in an unwrapped image (circles) and the result of a least-squares fit to a set of error functions (solid line). The edge location (dashed line) is taken to be the radial point where the fit height is half way between the heights of the flat regions on either side of the edge step.

The variation in target-edge position with angular position is decomposed into its low-mode number (up to $n = 6$) Fourier components to remove the $n = 1$ component. These modes are sufficient to determine the large amplitude variations in the target-edge position as shown by the reconstruction (solid line) in Fig. 104.7. As mentioned previously, angular regions previously identified by the spider web finding routine are excluded from the Fourier decomposition. The routine also automatically excludes outliers from the target center finding Fourier decomposition. Outliers are identified by their deviation from the Fourier reconstruction as compared to the standard deviation and determined in terms of deviation in fitted step height, width, and radial position. The Fourier decomposition is performed iteratively with outliers excluded to ensure a self-consistent result is found. Outliers automatically identified in this way typically result from additional corruption of the edge image by spider webs, dust, and other image defects.

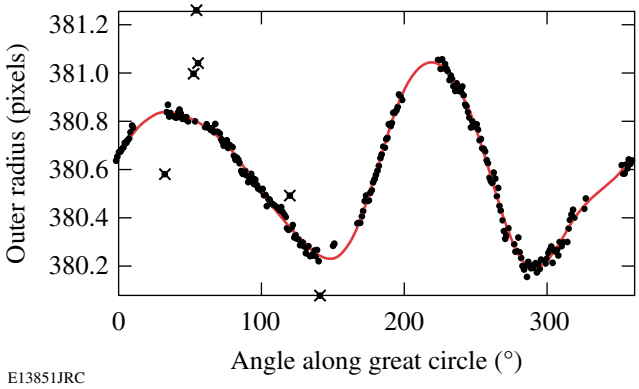

Figure 104.7
Angular variation in target edge radius as determined by the analysis of the image in Fig. 104.3 (dots) along with the fit to low mode number (up to $n = 6$) Fourier components (line). The x's indicate data points automatically excluded from the Fourier decomposition as outliers. The large angular gaps in the data indicate regions excluded from the decomposition by the spider web finding routine.

The estimated target center position is now adjusted to eliminate the $n = 1$ Fourier component of the target's outer edge found by the decomposition that corresponds to a linear target offset. The unwrapping, spider web finding, and target edge determination are repeated iteratively until the $n = 1$ target offset is reduced to some arbitrarily small number, typically $\leq 0.005\ \mu$m.

5. Identification of the Bright Ring and Determination of the Ice Surface Radius

The bright ring location is identified by fitting a Gaussian peak to the radial intensity profile in the vicinity of the ring at each angular position of the unwrapped image (Fig. 104.8). The data points in Fig. 104.9 show the angular variation in bright position around the target. The bright ring intensity is well fit by a Gaussian peak, provided the image is focused on that ring. Ray-trace modeling of a typical cryogenic target using the *PEGASUS* code[17] has not only identified the sources of the prominent shadowgraph rings, but also how the ring positions vary with the target parameters such as shell outer radius, shell thickness, D_2 ice thickness, shell index of refraction, and the D_2 index of refraction. The *PEGASUS* code is 2-D and assumes spherical symmetry in the target. A linearized formula derived from this modeling is used to determine the inner-ice-surface radius from the position of the bright ring for given target parameters. Efforts are currently under way to extend the ray-trace modeling to 3-D and to explore the effects of ice-surface roughness on the bright ring in detail.

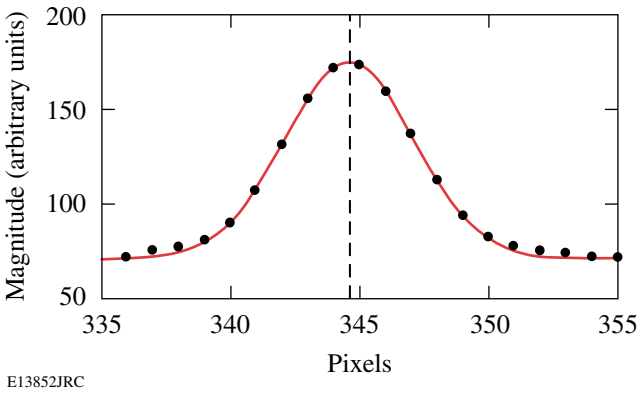

Figure 104.8
The radial location of the bright ring (dashed line) is determined by the center of a Gaussian fit (solid line) to the radial variation in intensity across the ring (dots).

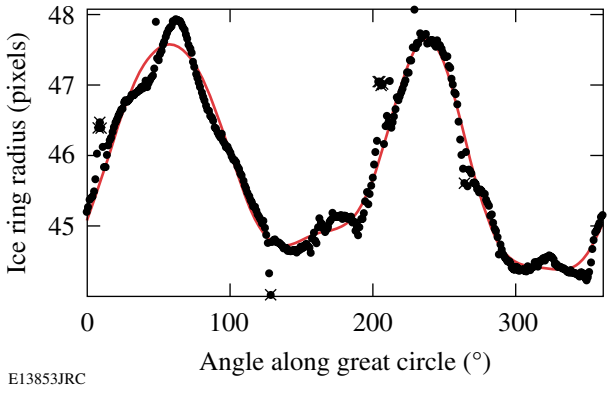

Figure 104.9
Typical angular variation in bright ring radius as determined by the analysis (dots) along with the fit to low-mode number (up to $n = 9$) Fourier components (line). The x's indicate data points automatically excluded from the Fourier decomposition as outliers.

6. Fourier Analysis of the Ice Layer

The roughness and asymmetry of the inner-ice surface can degrade the performance of a cryogenic target on implosion. The Fourier power spectrum of the ice layer roughness around a great circle of the target is calculated directly from the variation in ice layer thickness or inner-ice-surface position $R(\theta)$ as determined from the bright ring analysis. We use the convenient series

$$R(\theta) = a_0 + \sqrt{2}\sum_{n=1}^{\infty}\left[a_n\cos(n\theta) + b_n\sin(n\theta)\right](\mu\text{m}) \qquad (2)$$

for Fourier decomposition. The $\sqrt{2}$ factor results in a total variance and a 1-D Fourier power spectrum of

$$\sigma^2_{\text{rms}} = \frac{1}{2\pi}\int_{-\pi}^{\pi}\left[R(\theta) - \overline{R}\right] = \sum_{n=1}^{\infty} P_n \ (\mu\text{m}) \qquad (3)$$

and

$$P_n = a_n^2 + b_n^2 \ (\mu\text{m}^2), \qquad (4)$$

respectively. The 1-D power spectrum of the cryogenic ice layer from the shadowgraph of Fig. 104.3 is shown in Fig. 104.10. The total 1-D rms of this layer is 1.36 μm. The majority of this roughness is due to the large $n = 2$ component. The total 1-D rms of all modes except $n = 2$ is less than 0.2 μm.

The 1-D Fourier power spectrum derived from a great circle ice layer measurement is a useful gauge of target quality. However, a computer simulation of implosions including instability growth and implosion performance requires a true spherical harmonic surface representation of the ice layer roughness. In **Three-Dimensional Ice Layer Reconstruction Using Multiple Shadowgraph Views** (p. 175), we will discuss using multiple shadowgraphs of different views to determine the surface asymmetry and ice roughness in terms of spherical harmonics.

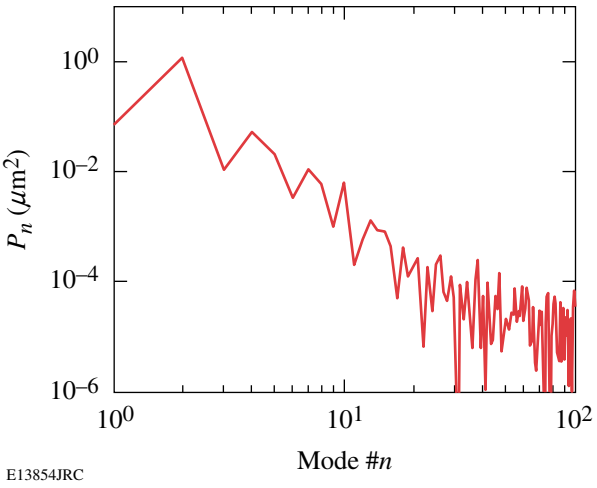

Figure 104.10
Fourier power spectrum of the ice layer from analysis of the shadowgraph shown in Fig. 104.3.

The modal analysis can be complicated by gaps in the bright ring due to ice or other defects. Direct Fourier decomposition of only the good points between the gaps is limited to relatively low mode numbers whose exact limit depends on the size of the gaps. This method prevents estimation of the high-mode ice roughness and aliases the high-mode information into errors in the low-mode determinations. Interpolation is used to bridge the gaps before the Fourier analysis. As the interpolation over small gaps preserves low-mode structure, the error due to the interpolation tends to be concentrated in higher modes, typically increasing the estimate of the higher-mode ice roughness along with an accurate determination of the low-mode ice asymmetries despite the gaps. Ice surface defects that cause gaps should ideally be included in the surface roughness analysis; however, determining the true nature of the defects is difficult. Efforts are under way to identify ice defects using nonbright ring rays from multiple views.[18]

7. Shadowgraph Resolution

The resolution of the shadowgraphic analysis has been examined using a sapphire sphere surrogate target for the outer-edge determination and a cryogenic target with a melted layer for the bright ring measurements. Figure 104.11 shows the scatter in outer-edge analysis from several images of a sapphire sphere at the same rotated position scaled to the nominal outer radius of 395 μm. Small vibrations varied the target's position by a few microns between the various images ensuring that the edge crossed the CCD pixel array pattern (~1 pixel/μm) at different locations in each image. Both large- and small-scale features in the edge analysis are highly repeatable. The standard deviation between the analyses is of the order 0.01 μm at all angles. The peak-to-peak variation in edge radius is comparable to that measured for the sphere by an atomic force microscope[19] along different great circles.

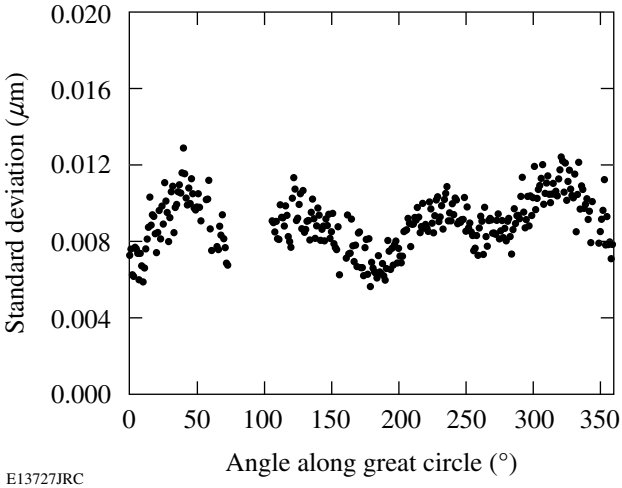

Figure 104.11
Standard deviation between outer-edge measurements of 17 different shadowgraphs viewing a sapphire sphere at slightly different positions due to vibrations of the order of a pixel. The target-mounting stalk is at 90° and causes the gap in the data at that angle.

The resolution of the bright ring measurements has been studied by analyzing the bright ring from targets whose ice layer has partially or fully melted (for an example see Fig. 104.12). In both cases, the bright ring from the very smooth liquid hydrogen surface shows an rms roughness of about 0.1 pixel (~0.12 μm).

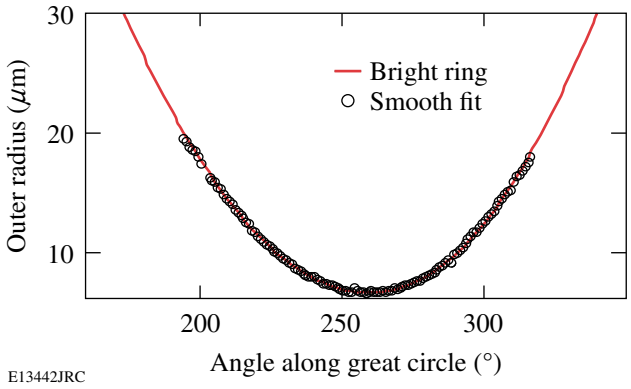

Figure 104.12
Bright ring measurements for the liquid portion of a partially melted target show a 0.1-pixel (~12-μm) rms roughness versus a smooth fit using Fourier modes 0, 1, and 2.

An error analysis of the shadowgraphic target characterization using a fully atomic-force-microscope–characterized sapphire sphere surrogate target and precision planar pattern targets is under way and will be reported in a future publication.

Three-Dimensional Ice Layer Reconstruction Using Multiple Shadowgraph Views

An important feature of LLE's cryogenic target shadowgraph system is the use of multiple views of the target to fully characterize the ice layer. Multiple views allow a far more complete layer characterization than is possible from a single view. In fact, even with three mutually orthogonal views, it can be shown that there is only a small chance of detecting many local ice defects.[19] The targets are rotated in the cryogenic target characterization stations, providing a large number of different views for a single camera. The maximum number of views is limited only by the rotation stepper motor step size of a few tenths of a degree.

Shadowgraphs are typically recorded at 15° intervals, producing a total of 48 independent views between two cameras in each station. It takes less than a minute to rotate the target to each image view. After an image is taken, the target is rotated back to its "home" position for a short rest. This procedure prevents significant changes in the ice layer due to the changing target position with respect to the geometry of the isotherms in the layering sphere. The time constant for an ice layer to change because of target rotation is of the order of 15 to 25 min, much longer than the typical time required to obtain an image at any view using this procedure. Figure 104.13 shows a target inner-ice surface reconstructed from 48 separate views. Very different low-mode asymmetries are observed for any given great circle. For this data set, the ice surface 1-D rms roughness of the individual great circle observations varies from 0.72 to 2.9 μm with an average value of 1.7 μm.

The two cameras in each characterization station have approximately orthogonal views. One camera views the target center from an angle of 26.56° above the equator. The second camera is located 109.96° azimuthally from the first and views from 12.72° above the equator. These view angles are determined by the locations of the layering sphere windows that are aligned with the OMEGA target chamber viewing ports used to center the target at shot time. Unfortunately, these views are not optimum for target characterization. An off-the-equator viewing angle always results in regions surrounding the rotation poles that cannot be observed. These unviewable "polar caps" are apparent in Fig. 104.13.

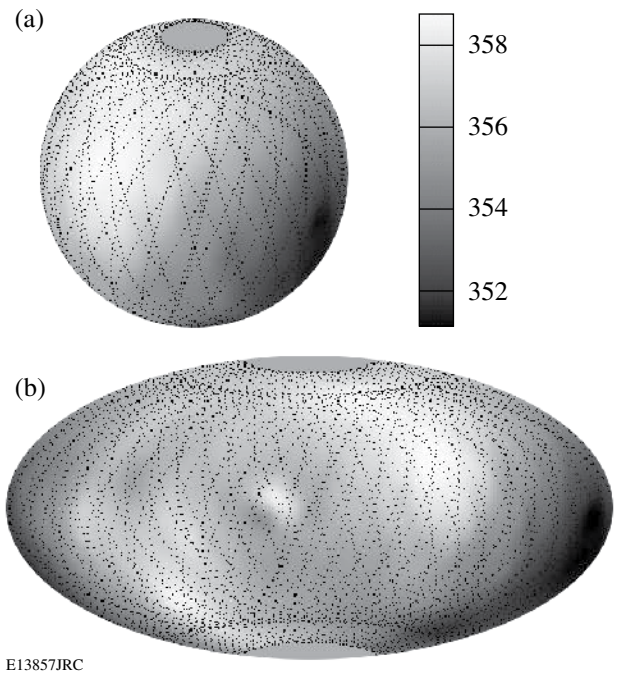

Figure 104.13
Three-dimensional representation of a cryogenic inner-ice surface (μm) displayed (a) on a spherical surface and (b) using the Aitoff projection. These displays are constructed by interpolating all the individual data from the many great circle observations to an evenly spaced (θ,ϕ) surface grid. The dotted lines show the location of the actual great circles observed in the individual shadowgraphs. The polar caps not crossed by the great circle observations are clearly visible. Typical surface structures are much more apparent in false color than in the gray scale representation required for publication.

As mentioned earlier, computer modeling of a spherical implosion including instability growth requires an ice roughness spectrum described in terms of spherical harmonics basis functions $Y_{\ell m}(\theta,\phi)$ on the ice surface.

$$R(\theta,\phi) = \sum_{\ell=0}^{\infty} \sum_{m=-\ell}^{\ell} A_{\ell m} Y_{\ell m}(\theta,\phi) \ (\mu m). \tag{5}$$

This description gives a power spectrum and total surface variance of

$$P_\ell = \frac{1}{4\pi} \sum_{m=-\ell}^{\ell} \left| A_{\ell m} \right|^2 \ \left(\mu \mathrm{m}^2\right) \tag{6}$$

and

$$\sigma_{\mathrm{rms}}^2 = \sum_{\ell=1}^{\infty} P_\ell \left(\mu \mathrm{m}^2\right), \tag{7}$$

respectively. The Legendre mode spectrum P_ℓ represents a sum over all azimuthal modes m. Multiple views allow the inner-ice surface to be directly fit to the $Y_{\ell m}(\theta,\phi)$'s. This fit has an upper limit on the mode number ℓ_{max} determined by the largest space between sampled points on the surface. For typical LLE targets, the largest gap in the surface data occurs at the unviewable polar cap of the target. The many smaller surface gaps between great circle measurements, noise in the data, and uneven surface weighting (sections crossed by several great circles are more heavily weighted) also reduce the maximum mode number that can be reliably fit. These effects typically limit the direct surface fit to mode numbers to about $\ell_{max} = 8$ to 10. The exact limit varies with each data set.

The results of a direct $Y_{\ell m}(\theta,\phi)$ fit are shown in Figs. 104.14 and 104.15. The surface reconstruction in Fig. 104.14 based on the low-mode number fit is a very good match to the data shown in Fig. 104.13. The Legendre power spectrum P_ℓ corresponding to this fit is displayed in Fig. 104.15.

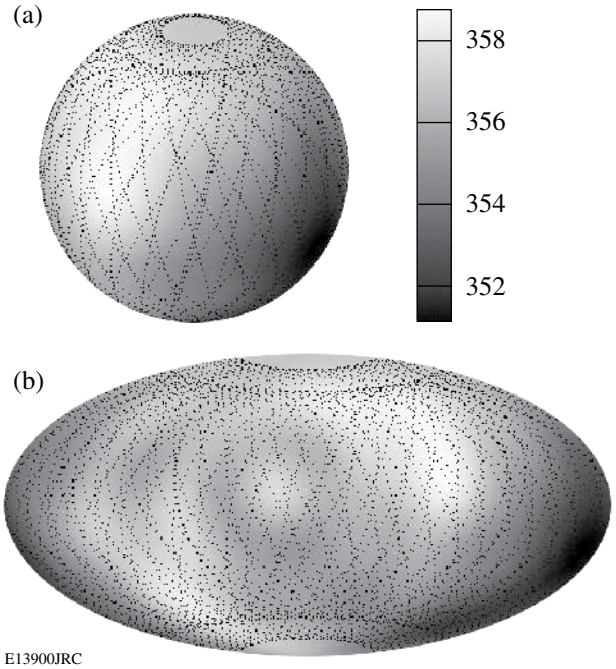

Figure 104.14
Three-dimensional reconstruction of a cryogenic inner-ice surface (μm) based on a direct $Y_{\ell m}(\theta,\phi)$ fit to the measured data. A comparison with Fig. 104.13 shows that the low-mode features are well matched by the fit. Although the actual great circle data are used in the fitting, the results are mapped to an evenly spaced (θ,ϕ) surface grid using the $Y_{\ell m}$ coefficients for better display.

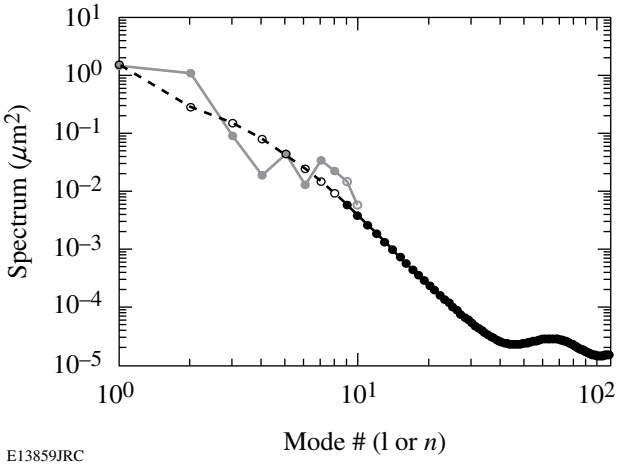

Figure 104.15
Legendre-mode power spectrum P_ℓ of the ice surface. The gray data correspond to the low-mode-number direct fit. The black data are the result from mapping the average Fourier mode spectrum (see Fig. 104.16) of the many great circles.

Mode numbers higher than ℓ_{max} cannot be directly fit, but can be inferred from the Fourier power spectra of the many great circles observed. If one assumes that the surface perturbations are randomly distributed, the great circle 1-D Fourier-mode power spectrum averaged over many great circles can be mapped[20] to an equivalent Legendre-mode power spectrum. The assumption of randomly distributed perturbations limits the applicability of the mapping to higher mode numbers. Mode numbers up to about $\ell_{max} = 8$ to 10 are directly fit to spherical harmonics, while higher mode numbers are determined by this mapping of the average Fourier power spectrum. Figure 104.16 shows the Fourier-mode spectrum $\langle P_n \rangle$ averaged over the many great circle views. $\langle P_n \rangle$ is first smoothed, then mapped to the equivalent high-mode-number Legendre-mode power spectrum P_ℓ shown in Fig. 104.15. The smoothing improves the behavior of the mapping.

The recently updated[21] NIF indirect-drive specification for ice surface roughness is also plotted in Fig. 104.16. For this target, the ice layer roughness is well below the NIF specification for most mode numbers. Only modes $n = 1$ and 2 significantly exceed the specification. The bulk of the surface-roughness rms of 1.7 μm is in these two modes. Efforts are currently under way at LLE to understand and correct the sources of the low-mode asymmetries in the layering-sphere isotherms.[4]

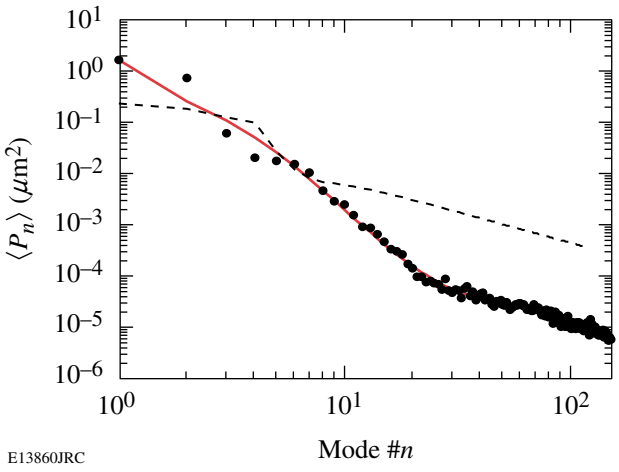

Figure 104.16
Average Fourier-mode spectrum $\langle P_n \rangle$ for the many great circle measurements of the ice surface used in the 3-D layer characterization. The dots are the actual average power for each mode number. The solid line is a smooth fit to the data used for the mapping to a Legendre-mode spectrum. The dashed line shows the recently updated NIF specification for indirect-drive ice layer roughness.

Summary

Analysis of the bright ring in backlit optical shadowgraphs of cryogenic targets is the primary diagnostic for ice layer quality at LLE. The bright ring radius is typically measured with a resolution of about 0.12 μm and is directly correlated to the position of the inner-ice surface. Two approximately orthogonal cameras and *in-situ* rotation of the target produce multiple shadowgraphs and, after analysis, the inner-ice surface radius for many different great circles on the target surface. A 3-D reconstruction of the inner-ice surface from these many views allows a direct fit of the surface roughness in terms of spherical harmonics for mode numbers up to ℓ_{max} = 8 to 10. The surface-roughness Legendre-mode spectrum for higher mode numbers is determined by mapping the 1-D Fourier-mode spectrum averaged over all of the great circles. The final Legendre-mode spectrum for the surface roughness is suitable for input to implosion modeling codes.

ACKNOWLEDGMENTS

This work was supported by the U.S. Department of Energy Office of Inertial Confinement Fusion under Cooperative Agreement No. DE-FC52-92SF19460, the University of Rochester, and the New York State Energy Research and Development Authority. The support of DOE does not constitute an endorsement by DOE of the views expressed in this article.

REFERENCES

1. T. R. Boehly, D. L. Brown, R. S. Craxton, R. L. Keck, J. P. Knauer, J. H. Kelly, T. J. Kessler, S. A. Kumpan, S. J. Loucks, S. A. Letzring, F. J. Marshall, R. L. McCrory, S. F. B. Morse, W. Seka, J. M. Soures, and C. P. Verdon, Opt. Commun. **133**, 495 (1997).
2. D. D. Meyerhofer, J. A. Delettrez, R. Epstein, V. Yu. Glebov, V. N. Goncharov, R. L. Keck, R. L. McCrory, P. W. McKenty, F. J. Marshall, P. B. Radha, S. P. Regan, S. Roberts, W. Seka, S. Skupsky, V. A. Smalyuk, C. Sorce, C. Stoeckl, J. M. Soures, R. P. J. Town, B. Yaakobi, J. D. Zuegel, J. Frenje, C. K. Li, R. D. Petrasso, D. G. Hicks, F. H. Séguin, K. Fletcher, S. Padalino, M. R. Freeman, N. Izumi, R. Lerche, T. W. Phillips, and T. C. Sangster, Phys. Plasmas **8**, 2251 (2001).
3. P. W. McKenty, V. N. Goncharov, R. P. J. Town, S. Skupsky, R. Betti, and R. L. McCrory, Phys. Plasmas **8**, 2315 (2001).
4. *LLE Review Quarterly Report* **99**, 160, Laboratory for Laser Energetics, University of Rochester, Rochester, NY, LLE Document No. DOE/SF/19460-555 (2004).
5. J. Sater *et al*., Fusion Technol. **35**, 229 (1999).
6. D. N. Bittner *et al*., Fusion Technol. **35**, 244 (1999).
7. W. J. Hogan, E. I. Moses, B. E. Warner, M. S. Sorem, and J. M. Soures, Nucl. Fusion **41**, 567 (2001).
8. J. K. Hoffer *et al*., Fusion Technol. **30**, 529 (1996).
9. J. D. Sheliak *et al*., Fusion Technol. **30**, 83 (1996).
10. B. J. Kozioziemski *et al*., in *Inertial Fusion Sciences and Applications 2003*, edited by B. A. Hammel *et al*. (American Nuclear Society, La Grange Park, IL, 2004), pp. 762–765.
11. J. A. Koch *et al*., Fusion Technol. **38**, 123 (2000).
12. J. A. Koch *et al*., Fusion Sci. Technol. **43**, 55 (2003).
13. DALSA, Waterloo, Ontario, Canada, N2V 2E9 (see http://www.dalsa.com).
14. M. J. Bonino, "Material Properties of Spider Silk," M.S. Thesis, University of Rochester, 2003.
15. G. J. Borse, *Numerical Methods with MATLAB:® A Resource for Scientists and Engineers* (PWS Publishing, Boston, 1997).
16. This algorithm was developed by one of the authors, A. Warrick, while on leave of absence at LLE.
17. S. Jin, *2002 Summer Research Program for High School Juniors at the University of Rochester's Laboratory for Laser Energetics*, Rochester, NY, LLE Report No. 329, LLE Document No. DOE/SF/19460-479 (2003).
18. R. B. Stephens *et al*., Fusion Sci. Technol. **45**, 210 (2004).
19. S. Pollaine and S. Hatchett, Nucl. Fusion **44**, 117 (2004).
20. J. D. Moody, Lawrence Livermore National Laboratory, private communication (2005).

Shock-Timing Experiments Using Double-Pulse Laser Irradiation

Introduction

Direct-drive inertial confinement fusion (ICF) targets use temporally shaped drive pulses to optimize the target performance while controlling the Rayleigh–Taylor instability.[1–3] The portion of the pulse preceding the main compression drive is used to create shocks that modify the target adiabat and thereby determine the compressibility and stability of the imploding shell. After the passage of the first shock, the compressed material at the ablation front relaxes to densities below solid, thereby increasing the ablation velocity produced by the main drive providing ablative stabilization.[4–6] Adiabat shaping[7] is a refinement that uses a short pulse (~100 ps) preceding the main pulse to produce an initial shock that is not supported and therefore decays as it propagates through the target shell. Ideally, this decaying shock produces a larger adiabat in the outer portion of the shell (where the shock is stronger) than the inner portion, simultaneously improving target stability and maintaining high compressibility of the main fuel.

An optimized direct-drive ICF implosion requires that the main compression wave overtake the first shock just as that shock reaches the inner surface of the cryogenic fuel layer.[8] (Ideally, the main drive should compress and implode the capsule isentropically. In ICF, this compression is so rapid and steep that it is sometimes referred to as a shock wave.) If the compression wave is too late, the first shock enters the fuel, prematurely compressing and heating it. If it is too early, the inner portion of the target is placed on too high an adiabat, reducing its compressibility. For direct-drive ignition target designs, the compression wave must overtake the first shock to within ±150 ps of the design specification.[9]

Indirect-drive ICF implosions are less susceptible to Rayleigh–Taylor instabilities and are therefore designed to implode along lower adiabats. Ignition designs for indirect drive use three shocks to moderately compress the target shell with a minimal increase to the adiabat before arrival of the compression wave (sometimes referred to as the fourth shock). Indirect-drive ignition target designs specify that the timing of the first three shocks be controlled to ±50 ps and the fourth shock be timed to ±100 ps.

In both of these cases, the target compression requires multiple shock waves to achieve optimal performance. The timing of those shocks is critical to that performance. It is therefore important that the simulation codes used to design ignition targets be validated with experiments that provide information on how multiple shocks propagate in laser-driven targets and provide the timing of those shocks. Experiments at the OMEGA[10] laser are conducted to develop the experimental techniques to do this and to validate direct-drive designs. Eventually, those techniques will be used on the National Ignition Facility (NIF)[11] to evaluate whether a given pulse shape meets the shock-timing specification.

We report on a series of experiments at the OMEGA Laser Facility that study the propagation and timing of multiple shocks in planar targets. In a direct-drive implosion, shock coalescence occurs before significant target motion, making the planar approximation valid. Planar targets are ideally suited to shock-wave experiments because they afford diagnostic access and because shocks can readily be produced at conditions that are relevant to ICF. These experiments demonstrate our ability to observe shock-velocity profiles and discern shock coalescence (timing) with the precision required for ignition targets. Hydrodynamic simulations of these experiments model the time history of the shock velocities and the observed coalescence times to the accuracies required for direct-drive ignition targets.

Experiments

The experiments were performed using planar 125-μm-thick polystyrene (ρ = 1.05 g/cc) targets that were directly irradiated with two 90-ps pulses separated by 1 to 2 ns with 12 OMEGA laser beams.[10] The shocks created by these pulses were observed using a velocity interferometer system for any reflector (VISAR)[12,13] that records the shock velocity as a function of time. The time-resolved optical emission from the shocks was simultaneously recorded. The experimental configuration shown in Fig. 104.17 where two rings of beams (six in each) are shown at their angles of incidence (23° and 48°). Each beam has a phase plate (DPP)[14] that produces a super-Gaussian intensity profile in space described by

$I(r) = I_0 \exp\left[-(r/412\ \mu m)^{4.7}\right]$, with I_0 being $1\text{–}5 \times 10^{14}$ W/cm^2. Obliquity causes the 48° beams to produce a spot on the target that is elongated 40% more than the 23° beams. The rear side of the target is observed with an optical system that also conveys to the target a 532-nm probe beam for the VISAR. In the reverse direction, the reflected probe beam and the self-emission from the target are imaged onto streak cameras.

The experiments were performed with 90-ps pulses, approximately Gaussian in time, in two groups of six beams.

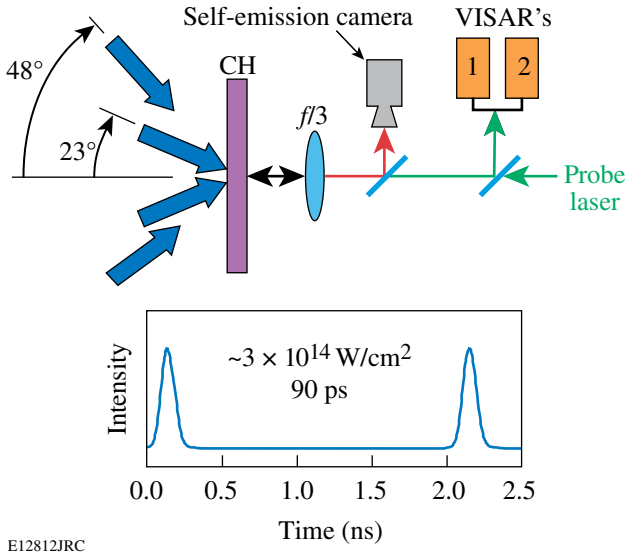

Figure 104.17
Experimental configuration with two short pulses, typically 1 to 2 ns apart. Beams arranged in two rings (having up to six beams each) at 23° and 48° irradiate solid polystyrene targets. A probe laser is image relayed by a *f*/3 telescope to the rear side of the target and reflected off a shock within the target into two VISAR diagnostics. The same telescope images the optical emission from the shock onto a streak camera.

Each group had the same angle of incidence (either 23° or 48°) and was timed so that one group arrived 1 to 2 ns later than the other. These produced two shock waves in the target that are initially separated by the beam delay. The strength and timing of the second drive pulse was arranged so the second shock overtook the first in the target, providing an observable shock-coalescence event. Experiments were performed with either the 23° beams or the 48° beams arriving first, and the relative energies of the two groups were varied. This article presents detailed results from six shots representative of many shock-timing experiments. The laser conditions for these shots are detailed in Table 104.I, which defines the energy and angle of incidence for the two groups of beams (six in each) for each shot number. The first group arrives at $t = 0$, and the arrival time of the second group is shown in the table. Each group comprises six beams oriented in hexagonal symmetry, so that for oblique angles of incidence, there is no directional bias. It should be noted that the laser spots (at normal incidence) were the same size for both sets of beams. As a result of obliquity, the 48° beams produce spots that are more elongated and therefore have, for similar energies, intensities that are 73% of the 23° beams. To accommodate this, the shots with the 48° beams first have the second group delayed an extra 0.5 ns to ensure that the coalescence signal could be observed after the blank out by the second pulse.

These drive intensities produce ~10-Mb shocks that are hot (5,000–50,000 K), dense (2–4 times solid), and have steep gradients. At optical frequencies they are bright and reflective (30%–80%). VISAR has been demonstrated to be a very precise method for measuring shock velocities. It uses interferometry to measure the Doppler shift of a probe beam reflected off the shock front as it traverses the target.[12] A few percent precision in velocity with a time resolution of ~25 ps is routinely obtained.[13]

Table 104.I: Summary of beam-configuration information for shock-timing shots.

Shot #	1st group energy (J)	1st group angle (°)	2nd group delay (ns)	2nd group energy (J)	2nd group angle (°)
32208	120	23	1.5	258	48
32213	252	48	2.0	111	23
32214	111	48	2.0	240	23
32215	73	23	1.5	250	48
32216	119	23	1.5	258	48
32217	236	48	2.0	229	23

VISAR Experiments

VISAR is extensively used in laser-driven equation of state experiments[15–17] where aluminum "pushers" convey the shock into the sample. These pushers act as a standard reference and shield the samples from x rays from the coronal plasma that drives the shock. In contrast, ICF capsules usually contain only low-Z materials, so x rays from the corona readily propagate through the shell and fuel. The optical diagnostics used in shock-timing experiments performed with low-Z materials can be compromised by x rays that photoionize the target material ahead of the shock. This causes the material to become opaque to the VISAR probe laser, thus "blinding" the VISAR diagnostic during the laser pulse. After the drive ends, the ionized electrons recombine, the target transparency is restored, and the shock can again be observed. With short pulses, the diagnostic record is interrupted for only a few hundred picoseconds during each laser pulse and a nearly complete shock-velocity record is obtained.

Figure 104.18 shows the VISAR record for shot 32213 having 240 J in the first group of beams incident at 48° and 111 J in the second (at 23°) that arrived 2 ns later. This figure is a streak-camera record of the VISAR fringes as a function of time with the vertical dimension corresponding to the spatial direction transverse to the drive laser (and shock) propagation direction. The fringes are deliberately superposed on the image of the target and serve as a phase reference, i.e., zero velocity. (In this case, the early signal results from reflection off the front surface of the transparent target; the rear surface has an antireflection coating). For $t < 0$, the fringes are horizontal (constant phase) because the target is not moving. At $t = 0$, the first pulse irradiates the target, forming a coronal plasma on the front side of the target and producing a shock that propagates into the target. The data record shows, that during the laser pulse, x-ray photoionization causes absorption attenuation of the VISAR laser light to below the detection threshold. After the pulse, by $t \sim 0.5$ ns, the target transmissivity rises and the VISAR signal (fringes) are again detected. During this time, a rapidly changing fringe pattern is observed. The fringe position is proportional to the velocity of the reflecting surface (the shock), so the curvature of the fringes represents the decay of the shock velocity as it propagates through the target.

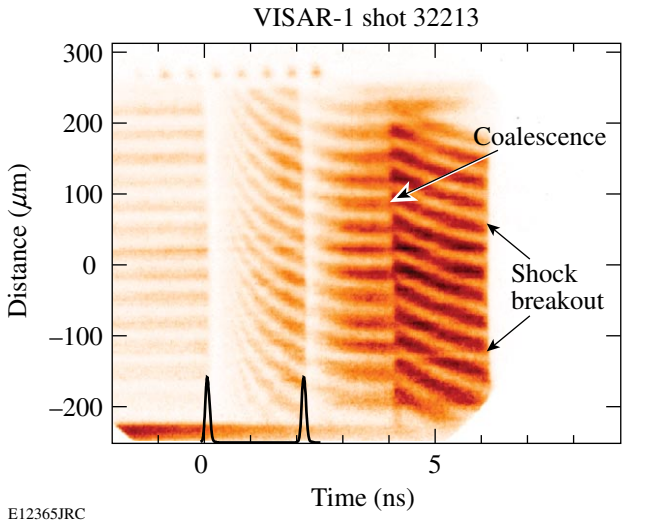

Figure 104.18
Temporally resolved VISAR record from shot 32213 (see text). The fringes are initially horizontal (zero velocity) until they disappear at $t = 0$ because of x-ray ionization in the target bulk. Upon reappearance, they have a curvature that results from the decreasing velocity of an unsupported first shock wave that decays as it propagates through the target. At 2 ns, the second laser pulse produces another burst of ionization, blanking the signal again. At ~4 ns, the second shock overtakes the first and the VISAR fringes have a discontinuous jump in position, brightness, and curvature. This coalesced shock also decays and finally reaches the rear surface (breakout) at ~6.2 ns, at which time the VISAR signal ceases.

At 2 ns, the second pulse irradiates the target. X rays produced by that pulse blind the diagnostic again and the fringes disappear. When the target recovers from the second pulse (at ~3 ns) the fringe record is still due to reflection off the first shock because the first shock is still ahead of the second shock and nearer to the VISAR. (Note the continuity in the slope of the fringes before and after arrival of the second pulse at 2 ns.) The first shock ionizes the CH above the critical density of the probe beam, ensuring that the probe is reflected and preventing the second shock from being "seen" through the first.

The record from ~0.5 ns to 4.0 ns shows the expected monotonic decay[18] of an unsupported shock traversing the target. At 4 ns, the second shock catches up to the first shock, forming a single coalesced shock that is stronger, and therefore faster, than the first shock. This event is recorded as a discontinuous jump in the fringe position (an increase in velocity) and an increase in the VISAR signal that is due to a concomitant jump in reflectivity for the stronger shock. The coalesced shock is also unsupported; it decays as shown by the curvature in the fringe pattern after 4 ns. The fringes from the coalesced shock persist until that shock reaches the rear surface of the target. At this point the shock "breaks out" and the rear surface releases into vacuum. These shocks produce temperatures and pressures sufficient to melt the CH, so as it releases, the material vaporizes, forming a density profile that quickly absorbs the probe laser and the VISAR signal disappears.

In this experiment, the second shock overtook the first shock despite being driven by half the energy of the first. This is the result of the increased sound speed and the particle velocity in the shock material. In the laboratory frame, one must add the particle velocity to the second shock velocity. Shock waves are supersonic relative to the unshocked material but subsonic relative to the shocked material. This is why rarefaction waves, which travel at the sound speed in the shocked material, can overtake shock waves.

Another interesting feature is the temporal rise of the signal intensity, as seen, for example, in Fig. 104.18 from 0.5 ns to 2 ns. The intensity of the VISAR fringes depends on the amount of reflection from the shock; typically, stronger shocks produce more free electrons and therefore have higher reflectivity. The gradual rise noted in Fig. 104.18 results not from increased reflectivity at the shock front because its reflectivity diminishes with decreasing velocity. Instead, the increase results from a decreased path length of the probe beam through the attenuating material as the shock moves toward the rear of the target.

Figure 104.19 shows the velocity profiles derived from the VISAR data recorded during two similar experiments. The solid line is the velocity profile from a two-pulse experiment (#32216) having 119 J in the first pulse (from beams at 23°) and, 1.5 ns later, 258 J (from beams at 48°). The initial shock is observed starting at ~0.3 ns and can be seen to decay continuously until 3.5 ns, when the velocity jumps because the second shock has overtaken it. That coalesced shock then decays and eventually reaches the end of the target at 5 ns. The dashed curve in Fig. 104.19 is the velocity profile for an identical experiment (shot 32215) except that the first pulse has only 75 J. The initial shock (0.3 to ~3 ns) has a lower velocity and, as a result, the second shock overtakes it earlier (at 2.9 ns). Note also that the coalesced shock is stronger (higher velocity) than the coalesced shock in shot 32216 because the second shock overtakes the first shock sooner (earlier in the decay of the shock).

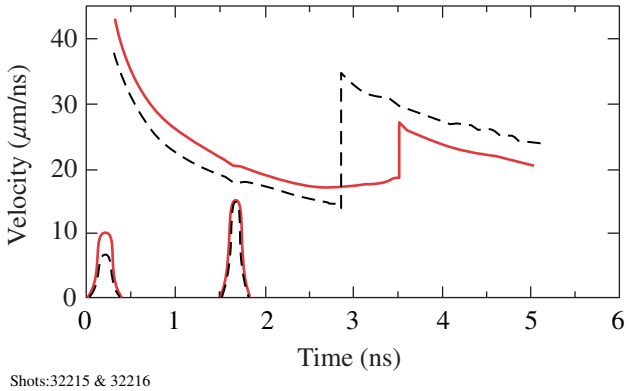

Figure 104.19
The shock-velocity history derived from the VISAR data for shots 32216 (solid) and 32215 (dashed). In both cases the target was irradiated by six beams at 23° and 1.5 ns later, by six beams at 48°. For shot 32166, the first group contained 119 J and the second 258 J. Shot 32215 had 73 J and 250 J, respectively. For shot 32216, the VISAR records the velocity of only the first shock until ~3.5 ns when the second shock overtakes the first. After the shocks coalesce, the velocity recorded by VISAR jumps. In the dashed curve, the catch-up occurs earlier because the initial shock is slower (lower first-pulse energy) and the jump is higher because the second shock has had less time to decay.

When the driving pressure behind a shock relaxes, the shock wave will begin to decay. This occurs because the material behind the shock (that is both heated and compressed) begins to rarefy. In a laser-driven shock that rarefaction begins at the coronal and propagates toward the shock at the local sound speed that is higher than the shock speed. When the rarefaction wave reaches the shock it causes the shock strength to decay at a rate that is proportional to the rarefaction rate. Note that in both experiments shown in Fig. 104.19, the first shock decays more rapidly than the coalesced shock. This is because the first shock traversed less material and hence the rarefaction rate is faster than for the second and coalesced shocks that encountered more material.

In another experiment, the timing of the pulses was reversed (i.e., 48° beams first). Figure 104.20 shows a comparison of the velocity profiles for the two cases. The solid curve is shot 32216 that has the 23° beams first (see solid curve in Fig. 104.19 and its description), and the dashed curve is shot 32214 with 111 J in the 48° beams first and 240 J in the 23° beams second. For the latter, the interbeam timing was lengthened to 2 ns so that the coalescence occurs after the blank out caused by the second pulse. It can be seen that the 48° beams produce a first shock that has 70% of the velocity of that produced by the 23° beams. This is because the 48° beams produce lower intensity and couple less efficiently to the target. In the dashed curve, the slower first-shock velocity reduces the coalescence time despite having the second pulse delayed by 0.5 ns with respect to the other case. The second shock (here produced by the 23° beams) creates a larger jump in velocity for the coalesced shock. This occurs because the 23° beams have a higher intensity and couple more efficiently, thus producing a stronger (and faster) shock.

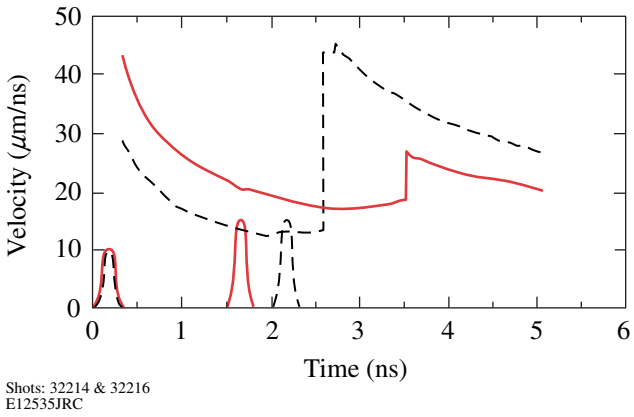

Figure 104.20
Velocity profiles from shot 32216 with 23° then 48° beams (solid) and 32214 (dashed) where the beam timing is reversed (48° beams first). Note that for similar drive energies, the first shock velocity is lower in the latter case. This is because the 48° beams couple less efficiently than the 23° beams. The velocity jump at coalescence is higher because the 23° beams produce a stronger shock.

To obtain the velocity records, the fringe position (phase) as a function of time must be determined. The sensitivity of fringe displacement to velocity is set by the length of the delay etalon in the VISAR interferometer and by the refractive index of the target material (polystyrene n = 1.59). VISAR can produce velocity measurements with accuracies of ~1% based on the ability to detect shifts of about 1/20 of a fringe and because the actual shifts are 3 to 5 fringes. We found that ionization has negligible effect on VISAR sensitivity. We estimated the ionized (or free) electron density using the loss of the VISAR signal as a measure of the absorption coefficient model to infer changes to the refractive index. Ionization fractions of ~0.02 would cause 100 times attenuation of the signal yet result in only a few percent change in the refractive index. Recent experiments have confirmed that severe ionization blanking occurred in polystyrene with only negligible changes in the index of refraction.[20] Preliminary studies of x-ray–induced ionization blanking indicate that, in addition to absorption by free electrons, valance-band vacancies play a role in the absorption of the probe beam. In Figs. 104.19 and 104.20, the experimental velocity profiles for the first shock show negligible change in the slope across the interruption caused by second pulse. Thus, despite large changes in signal level, the inferred velocity profile is negligibly changed.

Self-Emission Measurements

Simultaneous with the VISAR measurements, temporal records of the self-emission (600–1000 nm) from the shocks were acquired using an imaging streak camera with an S20 photocathode.[21] Figure 104.21(a) shows the VISAR record for shot 32208 with the corresponding record of the spatially and temporally resolved self-emission intensity shown in Fig. 104.21(b). This shot has 120 J in first pulse at 23° and 260 J 1.5 ns later at 48°. The spatial resolution of VISAR and the self-emission monitor are along the same direction (vertical on target). The distinct shock coalescence and breakout features discussed above are readily evident in both images. In Fig. 104.21(b), the onset of emission from the shock occurs at ~0.7 ns as an intense planar feature whose intensity decays nearly to the background level at ~3 ns. At about 3.2 ns, the emission suddenly reappears when the second shock overtakes the first and the coalesced shock produces a stronger emission. The abrupt temporal

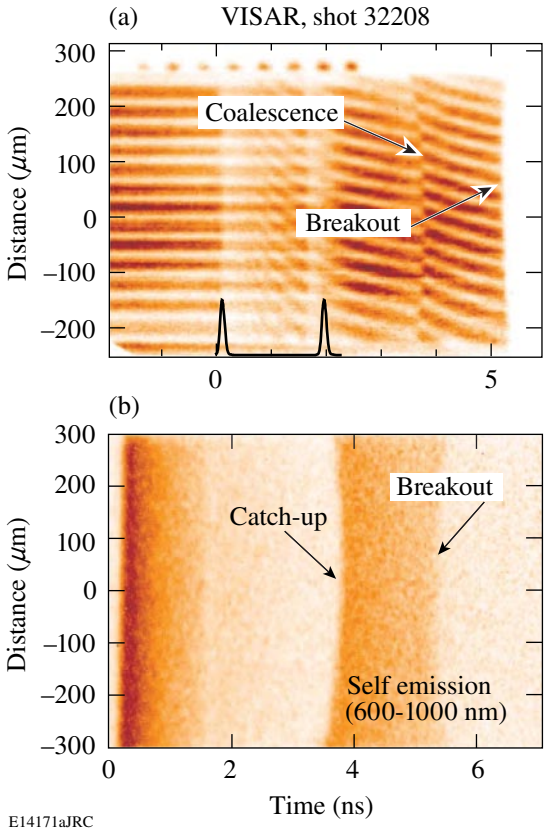

Figure 104.21
(a) The VISAR record and (b) the time-resolved optical self-emission profile for shot 32208. The velocity, catch-up, and breakout features that are seen in the VISAR record are also seen in the self-emission. At about 0.3 ns, the emission from the first shock is visible first, then it decays as the shock velocity decays. At catch-up (~4 ns) the coalesced shocks produce an emission that is again bright. This decays until breakout where emission ceases. The curvature of the catch-up and breakout features is related to the spatial shapes of the shock fronts.

onset of the emission from the coalesced shock indicates that the second (brighter) shock cannot be "seen" through the first shock. Again, this is because the first shock produces material that is overdense for these wavelengths.

For shock velocities of 15 to 40 μm/ns in polystyrene, the shock temperature ranges from 1 to 8 eV and depends quadradically on shock velocity. This dependence causes the self-emission intensity to drop rapidly. It falls below the detection threshold of the device for a portion of the record. These self-emission profiles corroborate the features seen in the velocity profiles. The shock catch-up and breakout times measured by each of the diagnostics agree, and the velocity profiles can be confirmed using the intensity profile as a reference.

In Figs. 104.21(a) and 104.21(b) (and Fig. 104.18 as well), the catch-up and breakout are curved; this curvature provides insight into the two-dimensional behavior of these experiments. The shock-breakout feature in these experiments is curved; the center breaks out before the edges. The curvature is a result of edge effects and velocity dispersion as the shock propagates to the rear of the target. At its edges, the shock has lower pressure because the laser is less intense, and lateral rarefaction waves move into the shock front. As a result, the shock front becomes curved as it propagates. The slower edges take longer to reach the rear surface of the target with respect to the more intense center. The result is the curved breakout signal.

In contrast, note that the coalescence signal in Fig. 104.21 has a curvature opposite of that at breakout. This is a result of the relative planarity of the two shocks. For shot 32208, the first shock was produced by the 23° beams that have a slightly smaller spot and therefore produce a shock with more curvature than that created by the larger spot because of the 48° beams. At coalescence, the flatter second shock overtakes the curved first shock, first at the edges and last at the center. The result is a catch-up signature that is curved opposite of the breakout, as in Figs. 104.21(a) and 104.21(b). In the cases where the 48° beams were first, the catch-up signal was observed to be flat or curved the other way.

Figure 104.22(a) shows the correlation of coalescence and breakout features as measured from the VISAR and self-emission records for shot 32217. The solid lines are the space-time locations of the coalescence and breakout features measured with VISAR, and the dotted lines are those determined from the self-emission record. Figure 104.22(b) is a comparison of the coalescence and breakout times derived from VISAR and self-emission for several shots over a range of detection times.

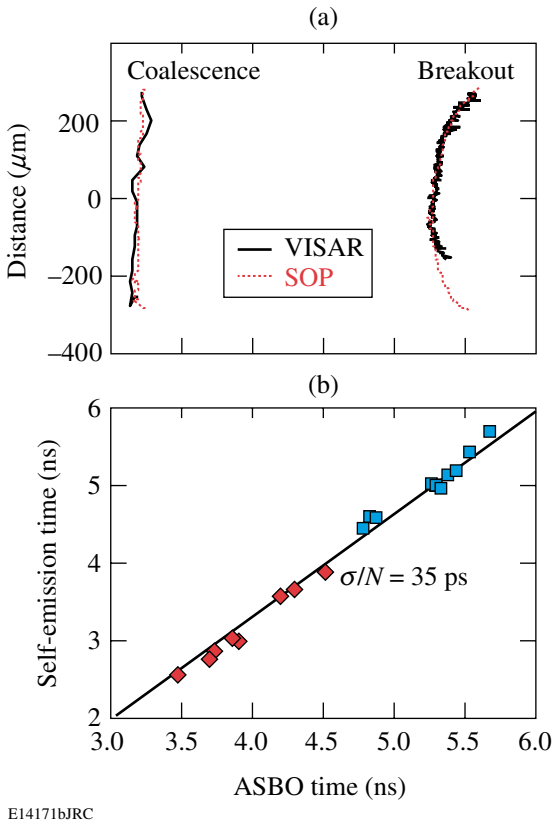

Figure 104.22
(a) Correlation of coalescence and breakout features in VISAR and self-emission data. (b) Correlation of the coalescence and breakout times as measured by VISAR and self-emission. These times agree to about the precision of the shock measurement.

Note that the correlation (±35 ps) is of the order of the accuracy of the VISAR measurements (±25 ps).

Simulations

Simulations of these experiments were performed using the one-dimensional hydrodynamics code *LILAC*.[22] Experimental conditions for the laser and target were inputs and the *SESAME*[23] equation of state was used for the polystyrene. The shock trajectories were found by tracking the shock position defined as the steepest gradient in the pressure. Figure 104.23 shows the velocity profiles from the simulations compared to the velocity profiles measured with VISAR. Figure 104.23(a) shows shot 32215 and Fig. 104.23(b) shows shot 32216. Note that the overall profiles are well modeled, as are the catch-up and breakout times. The simulations used a flux limiter of $f = 0.06$.[24] The effect of the different incident angles uses an algorithm that analytically treats ray tracing in density gradients to provide path length and absorption information to the one-dimensional code.[25] For six such shots, the simulations

were able to predict the shock coalescence and breakout times to better than ±150 ps, the required precision needed for the timing of the shock in direct-drive ignition targets.

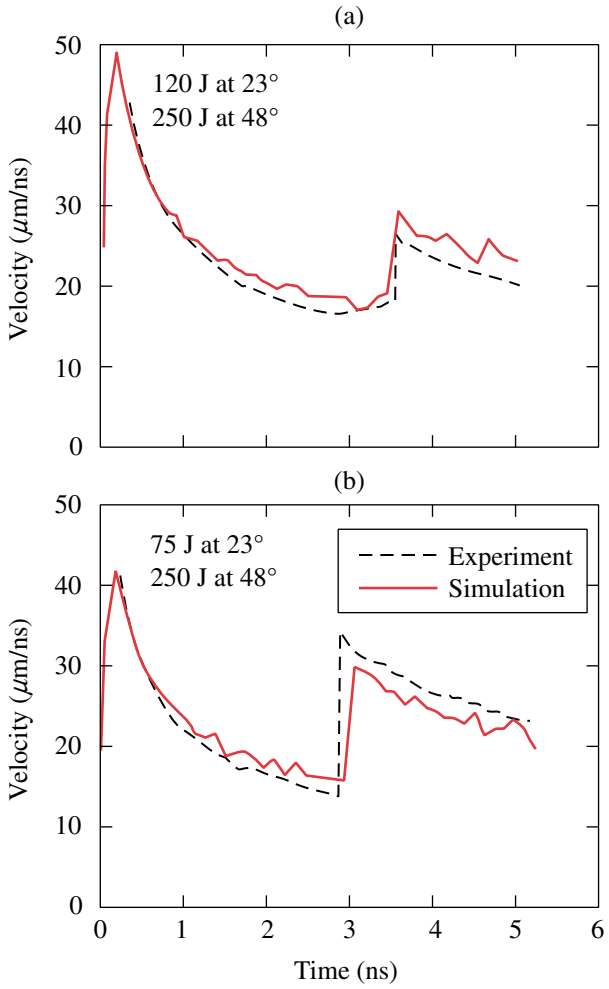

Figure 104.23
Comparison of measured (solid) and simulated (dashed) velocity profiles for (a) shot 32215 and (b) shot 32216. The measured velocities are well modeled, including the catch-up times where the shocks coalesce and the breakout times where the shocks reach the rear surface of the target.

Angle of Incidence

In a similar series of experiments, the effect of the incident angle was studied by inferring the peak shock pressure produced by beams at various angles. The velocity profiles of decaying shocks produced by beams at 23°, 48°, and 62° were compared. The velocity profiles of the decaying shocks were fit to models for unsupported shock waves,[7,18] and the results were used to infer the peak pressure produced by these pulses. The single-drive pulses were 90 ps in duration and the energy or numbers of beams were changed to vary the incident intensity.

Figure 104.24 shows a plot of the inferred peak pressure versus the incident laser intensity. The experimental results for the three angles are shown as solid figures and the simulations of those experiments as open figures. The experiments for 23° produce a larger range of pressures because they have smaller spots and couple more efficiently. The solid line is a power-law fit to the pressure where $P \propto I^{0.65}$, in agreement with established intensity scaling of $P \propto I^{2/3}$ (Ref. 26). Note that the simulations predict the effect of the incident angle quite well.

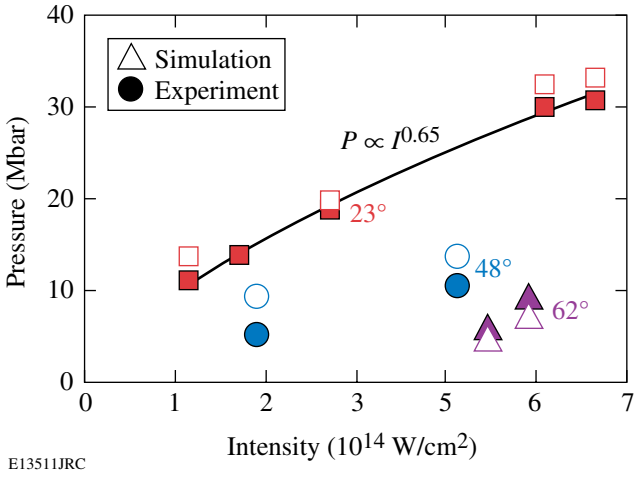

Figure 104.24
Peak shock pressure versus incident laser intensity for beams at incident angles of 23°, 48°, and 62°. The experimental peak pressure (solid points) was inferred from the measured velocity profile using a model for the decay of an unsupported shock wave. The simulated peak pressures are shown as open points. The solid line is a simple power-law scaling for the intensity dependence of pressure.

Conclusions

The velocity profiles of multiple shocks in planar targets irradiated by two short pulses have been measured using VISAR and self-emission data. The deduced velocity profiles show the shocks propagating through the targets and exhibit clear evidence of the time that the second shock overtakes the first. The coalescence times and the arrival of the coalesced shocks at the rear side of the targets are clearly observed and corroborated by the self-emission data. Shock timing and breakout were measured with accuracies of better than ±50 ps. The spatial shape of the catch-up and breakout signals exhibit features that are attributed to two-dimensional effects caused largely by the finite size of the drive pulses.

The velocity profiles and shock timing are well modeled by one-dimensional hydrodynamics codes that include ray tracing to account for oblique incidence. The simulations predict shock

timing and breakout to better than ±150 ps, the required precision for direct-drive ignition targets. These results demonstrate our ability to measure and model the behavior of multiple laser-driven shocks propagating in planar targets irradiated by double laser pulses and provide confidence in the hydrodynamic codes used for to design inertial confinement fusion targets.

These double-pulse experiments will be extended to cryogenic deuterium targets and continuous laser pulses. Similarly, experiments will also be performed with indirect-drive ICF to study the behavior and timing of three shocks driven by hohlraums. These experiments on OMEGA will be used to develop techniques that ultimately will be used to fine-tune targets and pulse shapes for ignition experiments on the NIF.

ACKNOWLEDGMENTS

This work was supported by the U.S. Department of Energy Office of Inertial Confinement Fusion under Cooperative Agreement No. DE-FC03-92SF19460, the University of Rochester, and the New York State Energy Research and Development Authority. The support of DOE does not constitute an endorsement by DOE of the views expressed in this article.

REFERENCES

1. J. D. Lindl, Phys. Plasmas **2**, 3933 (1995).
2. S. E. Bodner, D. G. Colombant, J. H. Gardner, R. H. Lehmberg, S. P. Obenschain, L. Phillips, A. J. Schmitt, J. D. Sethian, R. L. McCrory, W. Seka, C. P. Verdon, J. P. Knauer, B. B. Afeyan, and H. T. Powell, Phys. Plasmas **5**, 1901 (1998).
3. J. D. Kilkenny, S. G. Glendinning, S. W. Haan, B. A. Hammel, J. D. Lindl, D. Munro, B. A. Remington, S. V. Weber, J. P. Knauer, and C. P. Verdon, Phys. Plasmas **1**, 1379 (1994).
4. H. Takabe, L. Montierth, and R. L. Morse, Phys. Fluids **26**, 2299 (1983).
5. R. Betti, V. N. Goncharov, R. L. McCrory, P. Sorotokin, and C. P. Verdon, Phys. Plasmas **3**, 2122 (1996).
6. S. E. Bodner, Phys. Rev. Lett. **33**, 761 (1974).
7. K. Anderson and R. Betti, Phys. Plasmas **10**, 4448 (2003).
8. P. W. McKenty, V. N. Goncharov, R. P. J. Town, S. Skupsky, R. Betti, and R. L. McCrory, Phys. Plasmas **8**, 2315 (2001).
9. *Proposal for Renewal Award for Cooperative Agreement DE-FC03-92SF-19460*, Between the U.S. Department of Energy and the Laboratory for Laser Energetics of the University of Rochester, Addendum: Response to Reviewers' Questions (Rochester, NY, 2001).
10. T. R. Boehly, D. L. Brown, R. S. Craxton, R. L. Keck, J. P. Knauer, J. H. Kelly, T. J. Kessler, S. A. Kumpan, S. J. Loucks, S. A. Letzring, F. J. Marshall, R. L. McCrory, S. F. B. Morse, W. Seka, J. M. Soures, and C. P. Verdon, Opt. Commun. **133**, 495 (1997).
11. J. D. Lindl *et al*., Phys. Plasmas **11**, 339 (2004).
12. L. M. Barker and R. E. Hollenbach, J. Appl. Phys. **43**, 4669 (1972).
13. P. M. Celliers, D. K. Bradley, G. W. Collins, D. G. Hicks, T. R. Boehly, and W. J. Armstrong, Rev. Sci. Instrum. **75**, 4916 (2004).
14. Y. Lin, T. J. Kessler, and G. N. Lawrence, Opt. Lett. **20**, 764 (1995).
15. G. W. Collins *et al*., Science **281**, 1178 (1998).
16. M. Koenig, E. Henry, G. Huser, A. Benuzzi-Mounaix, B. Faral, E. Martinolli, S. Lepape, T. Vinci, D. Batani, M. Tomasini, B. Telaro, P. Loubeyre, T. Hall, P. Celliers, G. Collins, L. DaSilva, R. Cauble, D. Hicks, D. Bradley, A. MacKinnon, P. Patel, J. Eggert, J. Pasley, O. Willi, D. Neely, M. Notley, C. Danson, M. Borghesi, L. Romagnani, T. Boehly, and K. Lee, Nucl. Fusion **44**, S208 (2004).
17. T. R. Boehly, D. G. Hicks, P. M. Celliers, T. J. B. Collins, R. Earley, J. H. Eggert, D. Jacobs-Perkins, S. J. Moon, E. Vianello, D. D. Meyerhofer, and G. W. Collins, Phys. Plasmas **11**, L49 (2004).
18. R. J. Trainor and Y. T. Lee, Phys. Fluids **25**, 1898 (1982).
19. P. Drude, Ann. Phys. **1**, 566 (1900); N. W. Ashcroft and N. D. Mermin, *Solid State Physics*, College ed. (W.B. Saunders, Philadelphia, 1976).
20. W. Theobald, J. E. Miller, T. R. Boehly, E. Vianello, I. V. Igumenshchev, V. N. Goncharov, A. V. Maximov, and T. C. Sangster, Bull. Am. Phys. Soc. **50**, 347 (2005).
21. J. A. Oertel *et al*., Rev. Sci. Instrum. **70**, 803 (1999).
22. J. Delettrez, R. Epstein, M. C. Richardson, P. A. Jaanimagi, and B. L. Henke, Phys. Rev. A **36**, 3926 (1987).
23. G. I. Kerley, J. Chem. Phys. **73**, 469 (1980).
24. R. C. Malone, R. L. McCrory, and R. L. Morse, Phys. Rev. Lett. **34**, 721 (1975).
25. M. Born and E. Wolf, *Principles of Optics: Electromagnetic Theory of Propagation, Interference and Diffraction of Light*, 5th ed. (Pergamon Press, Oxford, 1975).
26. J. D. Lindl, *Inertial Confinement Fusion: The Quest for Ignition and Energy Gain Using Indirect Drive* (Springer-Verlag, New York, 1998), Chap. 5, p. 54.

Polar Direct Drive—Ignition at 1 MJ

Polar direct drive (PDD) is a new and viable option for achieving ignition on the NIF using direct drive while the beams are in the x-ray drive configuration. This allows both x-ray-drive and direct-drive ignition experiments to be performed using the same beam configuration, saving the time and expense that would be incurred from switching beams to different ports. Although PDD target drive will not be as uniform as standard direct drive, computer simulations indicated that moderate to high target gains in the range of 10 to 30 can be achieved (compared to gains of 40 or higher in the symmetric illumination configuration) at the 1-MJ level.

PDD intentionally increases the irradiation intensity at the target equator relative to the pole to compensate for the reduced laser coupling and reduced hydrodynamic efficiency characteristic of oblique irradiation. This is done by a combination of beam pointing, beam focal-spot shaping, and increased laser power of the "equatorial" beams. The beam pointing strategy currently employed is illustrated in Fig. 104.25(a) and the pulse shapes are in Fig. 104.25(b). The beam focal-spot shapes for the polar and midlatitude beams are all circular, with the intensity varying as $\exp[-3(R/R_{\text{target}})^4]$. The equatorial beams use the same circular beam, but with a 5:1 ellipse superposed on them to concentrate a little additional laser intensity at the equator (as discussed in Ref. 1). Also, a wetted-foam target similar to that described in Ref. 1 was used, but scaled down to 1 MJ.

The optimal irradiation pattern is found by varying the pointing, spot shapes, and pulse shapes of the beams. Multidimensional hydrodynamic simulations of the implosion are required to evaluate time-dependent variations in the irradiation pattern caused by the beam axes not pointing toward the target center. A parameter search for the optimal irradiation configuration was done using LLE's 2-D hydrocode *DRACO*. The *DRACO* simulations included a 3-D ray trace to model the laser irradiation and Monte Carlo alpha-particle transport to model the thermonuclear burn.

The pulse shapes were the same for the polar and midlatitude beams. The equatorial beams used a two-parameter

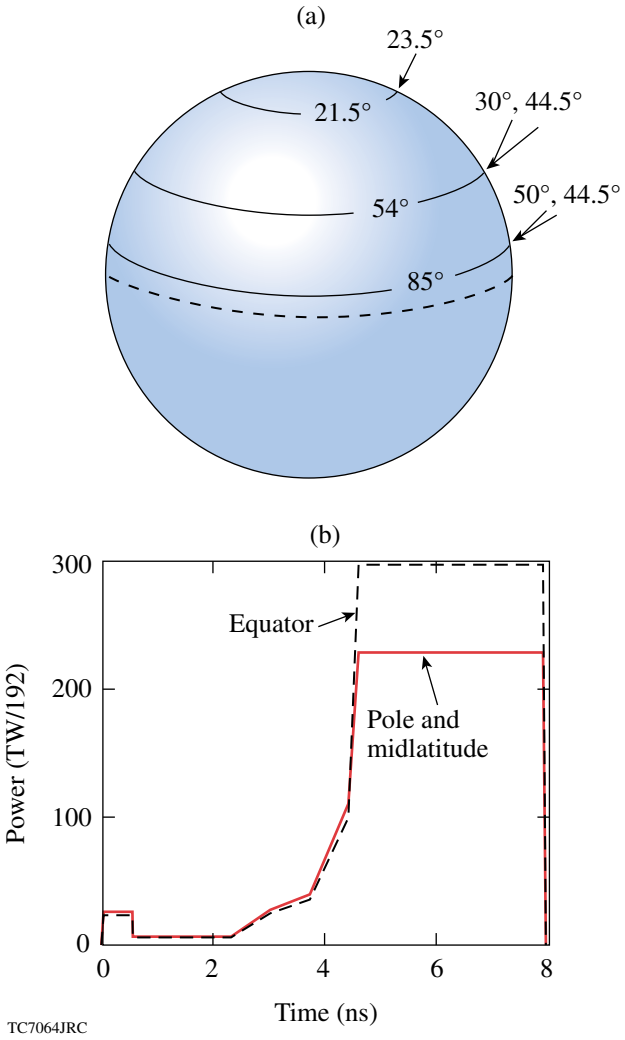

Figure 104.25
(a) Beam pointing strategy for polar direct dive. (b) Pulse shapes.

modification of this shape to allow for early-time shock timing and later-time target drive. The division occurred at 4.6 ns, at the start of the peak of the pulse. At that time, the peak power of the equatorial beams was increased by 30% to compensate for the reduced laser coupling for the oblique irradiation during

the target drive. At earlier times, the power was decreased by 10% to achieve good shock timing.

Target conditions near peak compression are shown in Fig. 104.26. Density contours and the ion-temperature contour lines of 10 and 15 keV are plotted. At this point in the simulation ignition has already occurred, and the thermonuclear burn wave is starting to propagate outward. This simulation results in a target gain of 35. This target gain is maintained over a range of laser conditions. Figure 104.27 shows how the gain varies as the pointing of the three rings changes. High performance is maintained over a spread of 40 μm in pointing, which is well within the capability of the NIF.

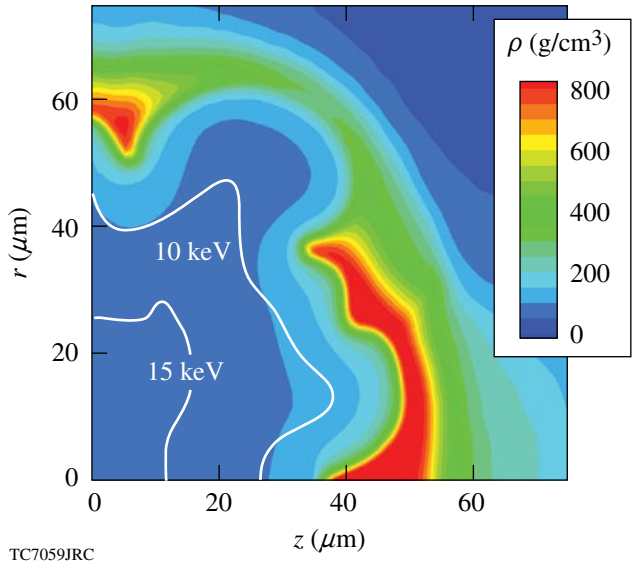

Figure 104.26
Density and temperature contours of the target near peak compression. At this point, the target has ignited and the burn has started to propagate.

Similarly, the sensitivity of target gain to variations in pulse shapes was examined. Three variations were considered: (1) variations in the length of the low-power foot of the pulse, (2) variations in the peak power, and (3) variations in the ratio of peak powers between the equatorial beams and the polar beams (and midlatitude beams). Over a reasonable range, the high gain is maintained.

Finally, the effect of inner surface roughness was considered (Fig. 104.28). Nonuniformity modes 2–10 were used in the simulations, with a spectrum similar to that obtained in current cryogenic experiments on the OMEGA laser. Most of the nonuniformity was concentrated in mode 2. The sensitiv-

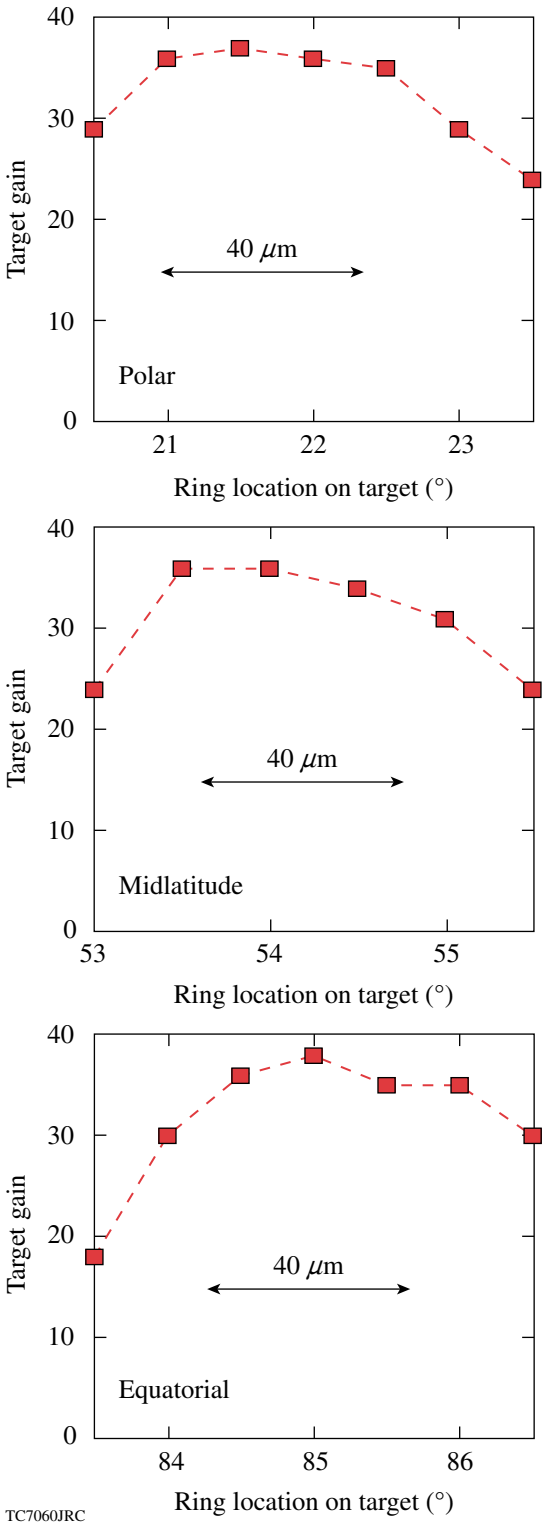

Figure 104.27
Sensitivity of target gain to beam pointing.

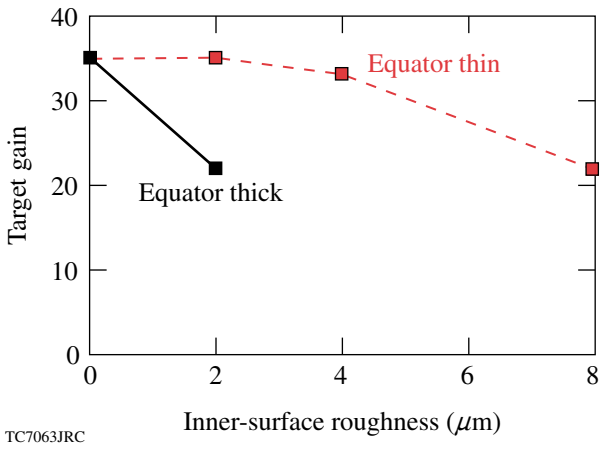

Figure 104.28
Sensitivity of target gain to inner-surface ice roughness.

ity of target gain to this form of nonuniformity depends on how the phases of the modes add up. When the phases result in a thinning of the equator (and a corresponding thickening of the pole) the target can survive a relatively large amount of nonuniformity. The target is much more sensitive to a thickening of the equator. This suggests that PDD might benefit from "shimming" the ice layer to make the equator intentionally thinner. For a shimmed target, a different beam-pointing strategy might be more optimal.

Further work is in progress to validate these results. This includes simulations with higher resolution, and examination of sensitivity to alternate numerical techniques.

ACKNOWLEDGMENTS

This work was supported by the U.S. Department of Energy Office of Inertial Confinement Fusion under Cooperative Agreement No. DE-FC52-92SF19460, the University of Rochester, and the New York State Energy Research and Development Authority. The support of DOE does not constitute an endorsement by DOE of the views expressed in this article.

REFERENCES

1. S. Skupsky, J. A. Marozas, R. S. Craxton, R. Betti, T. J. B. Collins, J. A. Delettrez, V. N. Goncharov, P. W. McKenty, P. B. Radha, T. R. Boehly, J. P. Knauer, F. J. Marshall, D. R. Harding, J. D. Kilkenny, D. D. Meyerhofer, T. C. Sangster, and R. L. McCrory, Phys. Plasmas **11**, 2763 (2004).

Hydrodynamic Simulations of Integrated Experiments Planned for the OMEGA/OMEGA EP Laser Systems

Introduction

The fast-ignitor concept[1,2] separates the fuel assembly and fuel heating by using a laser pulse to compress the fuel to a high density and an ultrafast, high-intensity laser to heat the fuel. The ultrafast laser produces relativistic electrons with high efficiency (up to 50% has been reported[3]) that heat the fuel, significantly easing the requirements on the compression driver.[2,4] Several options for the compression driver have been considered, including using a laser-heated or heavy-ion-beam-heated hohlraum or a direct-drive laser.

The Laboratory for Laser Energetics is building the OMEGA EP Laser System[5] that will consist of two short-pulse (1 to 10 ps), high-intensity (>10^{19} W/cm^2) laser beams, each capable of delivering 2.6 kJ of energy to the 60-beam OMEGA[6] target chamber. OMEGA EP is designed to act as a backlighter source for imploded high-areal-density cryogenic targets and as a tool to study high-intensity interaction physics and the transport of the relativistic electrons in imploded cryogenic targets. Integrated implosions on the combined OMEGA/OMEGA EP Laser Systems, starting in 2008, will validate the models used for the source and the transport of the relativistic electrons used in the simulation of hydrodynamic codes.

In this article, we present results of simulations of the interaction of relativistic electrons with cryogenic targets that are imploded with a pulse designed to achieve areal densities near 0.5 g/cm^2. The article is organized as follows: **Transport Model and Target Design** (p. 189) describes the models used in the source and transport of the relativistic electrons and the target and laser pulse designed to reach the required areal densities; **Simulation Results for Symmetric Implosions** (p. 191) presents the results of simulations carried out for uniform conditions; **Effect of Nonuniformity** (p. 193) describes the results for nonuniform implosions (power balance and ice roughness); and **Conclusions** (p. 194).

Transport Model and Target Design

The simulation of the effects of the relativistic electron beam produced by the OMEGA EP laser requires the modeling of the electron source and the transport of relativistic electrons in high-density materials. The characteristics of the electron source—the conversion efficiency, the spectrum (temperature) of the source, and the divergence of the electrons—are not well known because they are obtained from experiments and simulations that are carried out under conditions that are significantly different from those in an imploding target. Conditions at the end of a laser-produced channel or at the apex of a gold cone near the imploded core are that of a warm plasma (~200 eV) at near-solid density or slightly lower. Particle-in-cell (PIC) simulations are carried out for sharply rising pulses interacting with hot (several keV), low-Z targets.[7] In experiments, short-pulse lasers ≤1 ps are focused on solid, mid-Z targets (usually Al) and the electron source characteristics are measured indirectly, mostly from K_α x-ray emission.[8] For the simulations reported here, the source electrons are assumed to be Maxwellian with the semi-empirical temperature scaling given by[7]

$$T = 511 \times \left[\left(1 + I/1.37 \times 10^{18}\right)^{0.5} - 1\right](\text{keV}), \qquad (1)$$

where I is the laser intensity in W/cm^2. The electron source temperature, spectrum, and range are shown in Fig. 104.29 for a 2.5-kJ, 20-μm-radius laser pulse. A Gaussian laser pulse is assumed with 10-ps full width at half maximum (FWHM). The peak laser intensity and source temperature are 2×10^{19} W/cm^2 and 1.4 MeV, respectively.

The physics of the transport of the electrons is very complex. PIC code and hybrid PIC code results show complicated magnetic and electric field structures near the electron source and filamentary structures that depend on the background electron density.[9] A simple straight-line transport model has been chosen since such high-energy electrons are not scattered much in low-Z plasmas. In this model, the electrons lose energy because of collisions with thermal electrons and ions and to collective oscillations according to a formulation that takes into account multiple scattering.[10] The model does not include electric or magnetic fields and Joule heating by the return current. Figure 104.29(c) shows the penetration depth as a function of electron energy in 300-g/cm^3, 5-keV DT. A total areal density

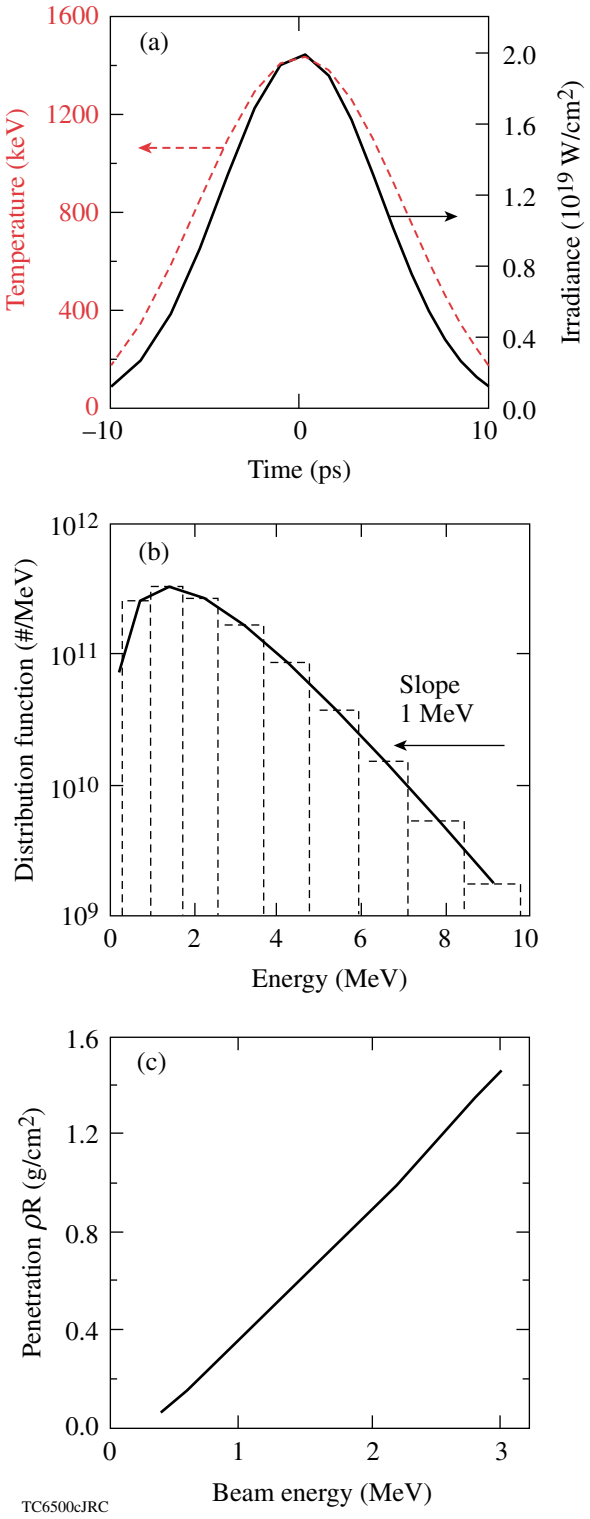

Figure 104.29
Details of the electron source: (a) temporal evolution of the laser intensity (dashed line) and source temperature (solid line) from Ref 7, (b) distribution function for a 1-MeV temperature and grouping, and (c) penetration depth of electrons in a 5-keV, 300-g/cm^3 DT plasma.

of about 1 g/cm^2 is required to stop the 2-MeV electrons in the 1-MeV distribution in Fig. 104.29(b).

A cryogenic target has been designed to achieve the required core areal densities near 0.5 g/cm^2 that will stop electrons up to 2 MeV (total areal density of 1.0 g/cm^2 for a traversing electron). The target, shown in Fig. 104.30(a), is nearly identical to capsules currently being imploded on the OMEGA laser. The pulse shape in Fig. 104.30(b) was designed to provide 25 kJ at 351 nm while keeping the minimum isentrope during the

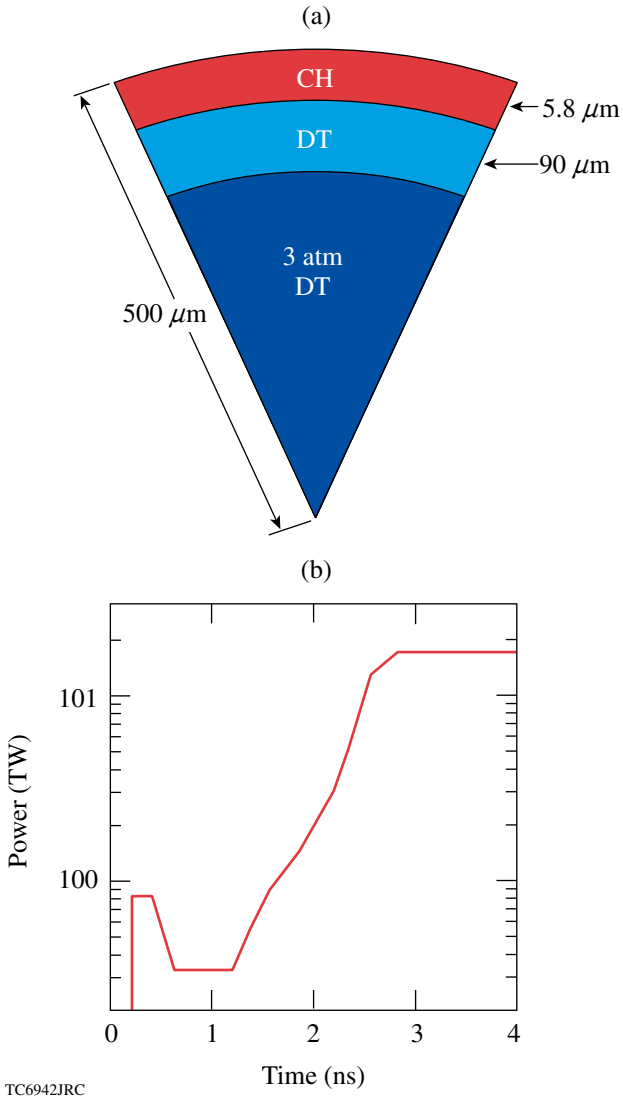

Figure 104.30
Target design for uniform implosion: (a) target details and (b) shaped pulse producing $\alpha = P_e/P_{\mathrm{TF}} < 2$. Nearly identical targets are being imploded on the OMEGA laser.

implosion to $\alpha = P_e / P_{TF} < 2$, where P_e is the electron pressure and P_{TF} is the Fermi pressure at $T_e = 0$. This isentrope is lower than that of present cryogenic implosions.[11] The maximum density and total areal density from a 1-D simulation with the hydrodynamic code *LILAC*[12] reach 500 g/cm^3 and 0.5 g/cm^2, respectively. At peak areal density (3.96 ns) the residual gas inside the target is heated to several kilovolts, whereas the high-density shell is kept below 200 eV.

Simulation Results for Symmetric Implosions

Simulations to study the hydrodynamic response of the target to the energy deposited by the electrons were carried out for a uniform implosion with the 2-D hydrodynamic code *DRACO*.[13] Uniform implosions can be simulated quickly and therefore permit the investigation of a larger parameter space than perturbed implosions. The electrons were produced at the pole as a cylindrical source directed parallel to the z-axis with radii varying from 5 to 30 μm. The source was injected where the background electron density is 2×10^{21} cm^3. The results are insensitive to the position of the source because the simulated electron beam has no divergence and the electrons are not effectively slowed until they reach much higher densities. The temporal Gaussian laser pulse produces 2.5 kJ of 1-μm light with the pulse duration varying from 1 to 30 ps FWHM. Two conversion efficiencies from the laser energy to the electron beam were assumed: 20% and 50%. The timing of the electron pulse with respect to the stagnation time was varied between –60 ps to 40 ps in intervals of 20 ps in order to study the sensitivity of the neutron yield to the timing.

The effect of the electron heating on the neutron production rate is illustrated in Fig. 104.31, where contours of neutron production rate per unit volume are shown at the time of peak neutron production. The mass density is shown in black contours. In Fig. 104.31(a), the neutron production in the case when the electron beam is not introduced is limited to the hot spot formed by the residual gas and a small layer inside the high-density shell. In Fig. 104.31(b), the neutron production extends over the path of the 20-μm-radius electron beam and has a greater spatial extent inside the shell than in Fig. 104.31(a). The peak neutron production occurs in a circular region in the hot core where a blast wave was created by the explosion of the shell from the heating by the relativistic electrons.

The temporal response of the stagnated core to the electron heating is shown in Fig. 104.32, where lineouts taken across the target 4 μm above the x axis in Fig. 104.31(b) of the neutron rate per volume, the ion temperature, and the mass density are plotted at four times with respect to the peak of the Gaussian high-intensity laser. The electron beam enters from the right. At the peak of the pulse [Fig. 104.32(a)], the shell has already been heated to about 2 keV as compared to the 200 eV shown in Fig. 104.30(c) without the heating beam. The shell starts to explode and decompresses and sends a blast wave into the core, which can be seen as a small jump in the ion temperature. Neutrons are produced in the high-density shell as well as in the core. The conditions in the shell are not uniform because more energy from the electron beam is deposited on the side nearer to the source (right-hand side) than on the far side. Since the

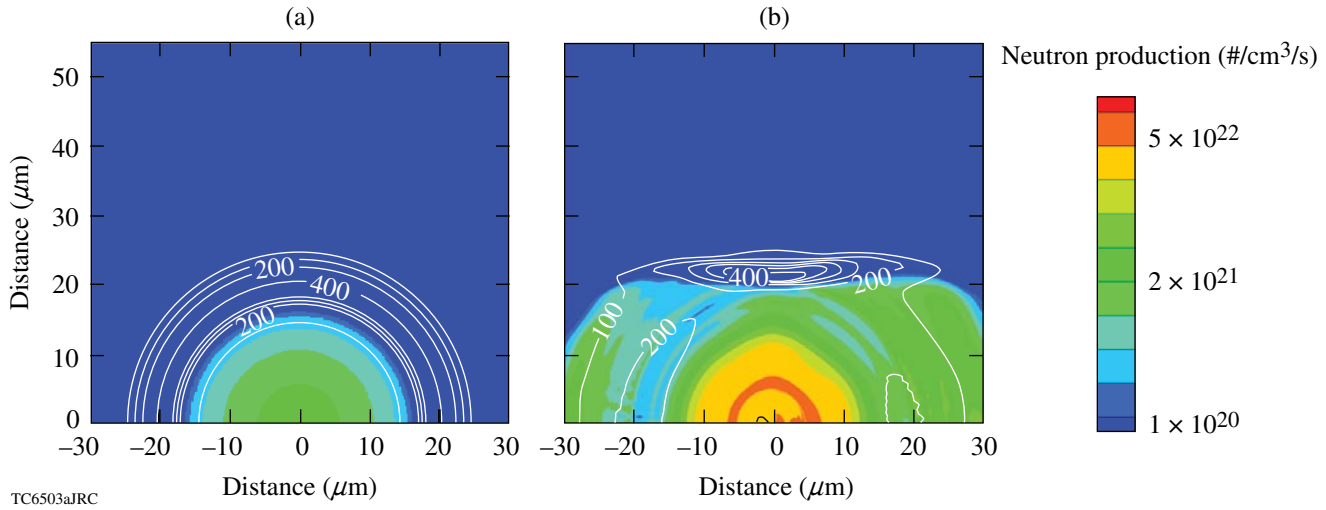

Figure 104.31
Contours of the neutron production rate per unit volume and mass density (black contours) at the time of peak neutron production in the case without an electron beam (3.95 ns) (a) and no electron beam. (b) 2.5-kJ, 50% conversion efficiency, 10-ps FWHM, and 20-μm-radius electron beam peaked at 3.94 ns.

electrons are produced over a range of energies, the less-energetic electrons deposit most of their energy in the shell nearer the source, while the more-energetic electrons deposit their energy uniformly in both sides of the shell. In Fig. 104.32(b), 4 ps after the peak, the blast wave can be seen as small steps in both the ion temperature and the mass density. The neutron production rate is enhanced behind the blast wave. At 8 ps after the peak of the electron pulse [Fig. 104.32(c)], the shell density has decreased to about half its peak uniform value and the blast wave has almost reached the center of the core, heating it to about 10 keV. Neutrons are still being produced in the high-density shell where the ion temperature reaches almost 4 keV. In Fig. 104.32(d), 12 ps after the peak of the electron pulse, the blast wave has reflected from the target center, creating ion temperatures reaching 13 keV and a large neutron production rate, although the actual number of neutrons produced in that region is small because of its small volume. Large neutron rates still occur in the shell, though it is beginning to cool.

The sensitivity of the neutron yield to the timing of the high-intensity pulse for several laser conditions is shown in Fig. 104.33. In all cases, the peak yield occurs when the peak of the pulse is timed about 20 ps before peak stagnation (3.96 ps);

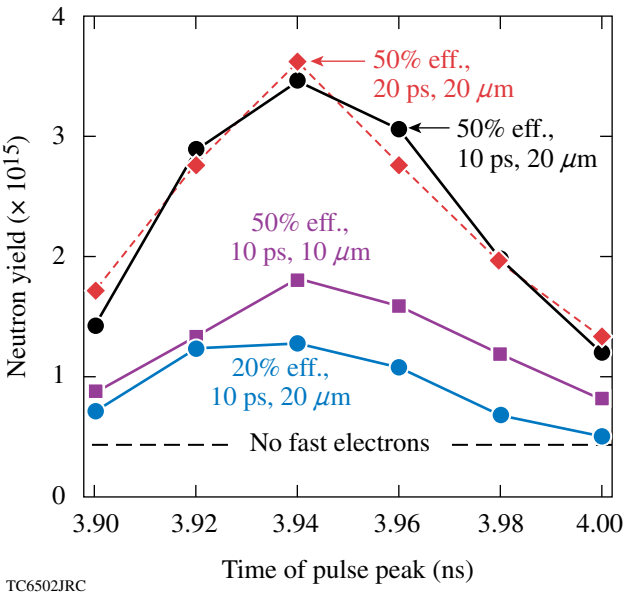

Figure 104.33
Sensitivity of the neutron yield to the laser pulse timing and characteristics. Peak areal density occurs at 3.96 ns.

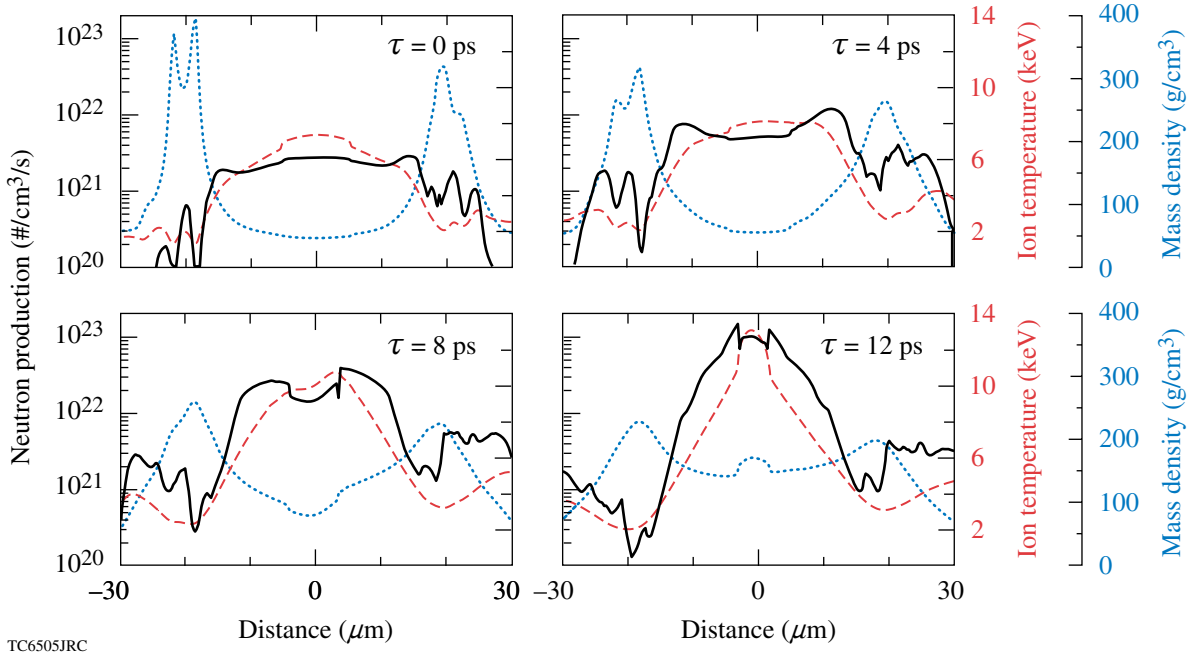

Figure 104.32
Lineouts 4 μm above the x-axis of the neutron production rate (solid curve), the ion temperature (dashed curve) and the mass density (dotted curve); times are with respect to the peak of the 10-ps Gaussian electron pulse timed at 3.94 ns. The electron beam enters from the right.

the highest yield is about a factor of 8 higher than the yield from the implosion without electrons. The yield remains within a factor of 2 of the peak yield within a 100-ps range for the pulse timing. The 20-ps requirement on the timing specification for the OMEGA EP beams is well within this range. For the 50% conversion efficiency, the yields were the same for the 20-ps and the 10-ps beam FWHM and a 20-μm-beam radius. The higher source temperature from the shorter pulse's higher intensity is compensated by the deposition of more electron energy early in time before the shell has decompressed. Reducing the beam radius reduces the yield by about a factor of 2 because of two effects: the higher intensity leads to a higher source-electron temperature that produces more electrons that escape the core, and the beam only partially covers the core radius, heating less of the high-density shell. Reducing the efficiency to 20% reduces the neutron yield by about a factor of 3.

Effect of Nonuniformity

A series of simulations was carried out with the power-balance nonuniformity caused by the OMEGA 60-beam geometry; they also included alpha-particle transport during neutron production. A modified target design reached a slightly lower areal density than the previous one, 0.45 g/cm^2, and a lower peak density, 360 g/cm^3, because the beam delivered 18 kJ instead of 25 kJ in the previous series of simulations. The high-intensity laser configuration and electron source are the same as in the previous series. Figure 104.34 shows the sensitivity of the neutron yield on the timing of the ignitor pulse for three beam radii (10, 20, and 30 μm) from a 2.5-kJ, 10-ps FWHM laser with 50% conversion efficiency to electrons. The implosions without the electron beam produce a yield of 1.25 $\times$ 10^{14}. Introducing the electron beam increased the yield by about a factor of 25. A radius of 10 μm results in a lower yield because the laser intensity and the resulting electron source temperature are too high. The implosions with the larger electron-beam radii yield about the same maximum number of neutrons but at different beam timings. This is because the 30-μm beam produces a lower temperature electron source than that of the 20-μm beam, which is more efficient in heating the core uniformly earlier in time when the areal density of the shell is lower. The higher-temperature electrons from the 20-μm beam are more efficient later, near peak areal density. The timing sensitivity for producing more than half the peak yield is about 80 ps. The yields increased by about 50% when the alpha transport was included, showing the early phase of bootstrap heating.

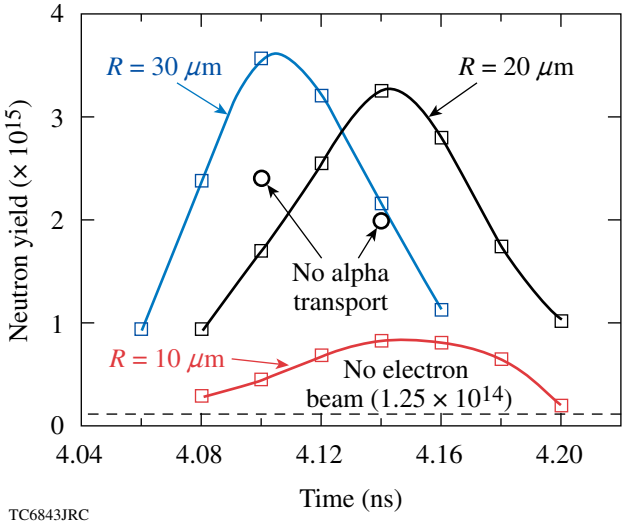

Figure 104.34
Sensitivity of the neutron yield to the laser pulse timing and characteristics for implosions that include the illumination nonuniformity due to OMEGA beam geometry. The pulse is 2.5 kJ, 10-ps FWHM with a 50% conversion efficiency. Open circles show the results of turning off the alpha transport.

Another series of simulations was carried out with the same target design and relativistic electron conditions as above but included two levels of inner-ice layer roughness, 2 and 4 μm σ_{rms}, which are larger than the expected values for these implosions.[14] Figure 104.35(a) shows the perturbation cosine spectrum applied to the inner-ice surface with a random phase of 0,π. The resultant core at the time of peak areal density (3.76 ns) in Fig. 104.35(b) shows nonuniform shell densities varying from 200 to 700 g/cm^3. A 2.5 kJ, 10-ps FWHM laser pulse with a 20-μm radius was timed 40 ps before shell stagnation. The yields for the simulations with and without the electron beam are shown in Fig. 104.36(a) as a function of the inner-ice roughness σ_{rms}. As expected, the yield decreases in the absence of the electron beam because of the core distortions caused by the ice roughness,[14] as shown in Fig. 104.35(b), down to about a factor of 6 from the uniform case at 4 μm of ice roughness. The neutron yield with the electron beam is almost a constant 10^{15} over the range of nonuniformity; in the case of 4 μm of ice roughness, the yield has improved by about a factor of 120 from that with no electron beams.

The neutron yield remains constant with increasing ice roughness when the electron beam is included because the radius of the high-density shell, whether distorted or not, is less than 20 μm [Fig. 104.35(b)], smaller than the 20-μm electron beam used in these simulations. Thus the electron beam heats the entire shell and raises the same amount of core material to the same temperatures in all cases of ice roughness, shown in Fig. 104.36(b). In the 4-μm-σ_{rms} case, the blast wave does not

converge uniformly as in the zero ice roughness case because of the nonuniform pressure in the distorted shell where it is generated. This leads to lower ion temperatures than in the uniform case, causing the small decrease in the yield observed in Fig. 104.36(a) for the electron beam case.

Conclusions

Two-dimensional hydrodynamic simulations were carried out to model the response of a cryogenic target imploded on the 60-beam OMEGA laser to the relativistic electron beam created by an OMEGA EP ultrafast laser beam. Targets were designed to produce areal densities near 0.5 g/cm^2 at stagnation. A study with uniform implosion showed that the shell, heated by the electron beam, explodes and sends a blast wave into the low-density core. The neutron yield reached a factor of 8 higher than that of the case without the electron beam because of production in the heated (~2 keV) dense shell and increased

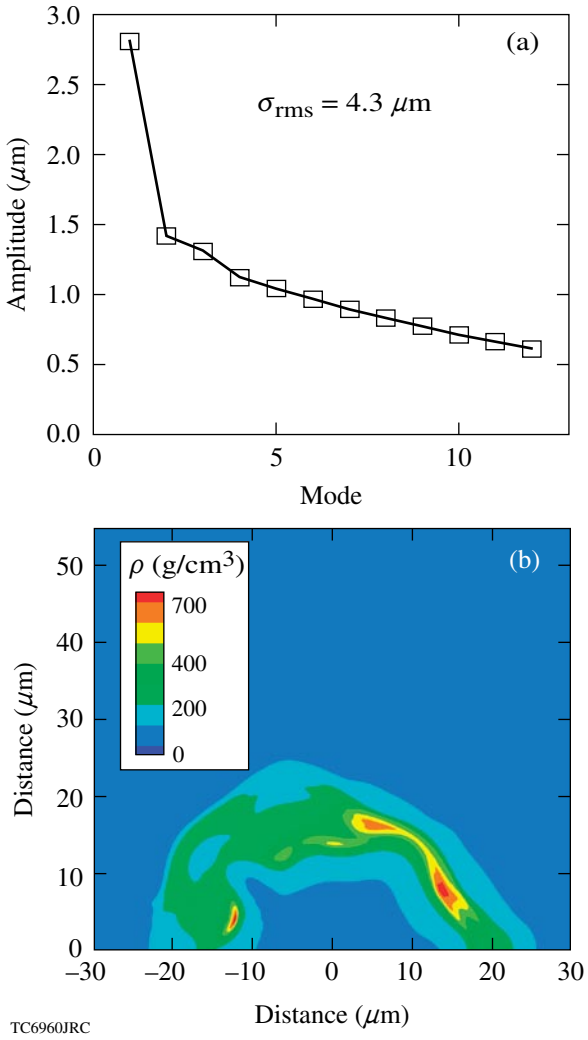

Figure 104.35
(a) Spectrum of the inner-ice roughness for 4-μm σ_{rms} and (b) core condition at stagnation.

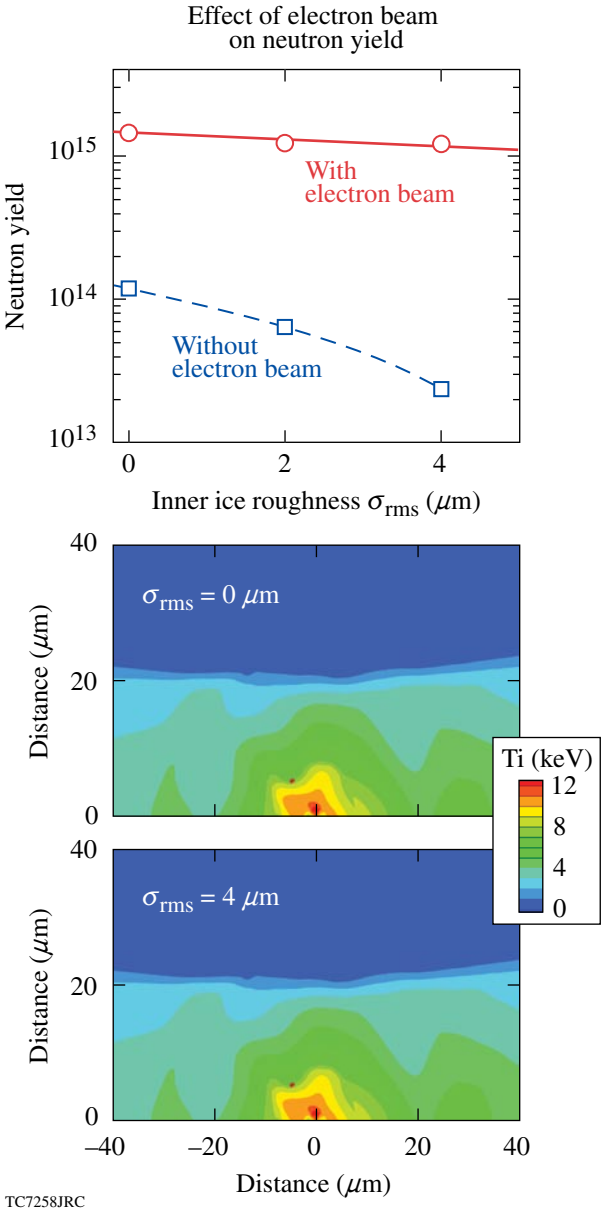

Figure 104.36
(a) Effect of the inner-ice roughness on the neutron yields—with the electron beam, the yield is constant for all levels of nonuniformity. (b) Ion temperature contours near time of peak neutron production for two ice roughness cases, σ_{rms} = 0 μm and 4 μm, showing that the same amount of shell material is heated by the 20-μm electron beam.

production in the low-density core heated by the blast wave. The highest yields—about 3.5×10^{15} and about a factor of 8 above the yield without the electron beam—were obtained for a 20-μm-radius beam with pulse durations of 10 and 20 ps timed 20 ps before stagnation. Yields within a factor of 2 of the peak yield were produced within a 100-ps timing window centered at stagnation. In a second study carried out with the illumination nonuniformity due to the OMEGA beam geometry, the highest yields (about 3.5×10^{15}) were produced at different beam timings for the 20- and 30-μm radii. These yields are about a factor of 25 larger than those without the electron beam. The inclusion of the alpha transport during neutron production increased the yield by about 50%. The final series of simulations were carried out with two levels of inner-ice nonuniformity, which produced a stagnating shell with nonuniform mass densities ranging from 200 to 700 g/cm^3. A 10-ps FWHM, 20-μm-radius laser beam timed 40 ps before peak areal density increased the neutron yields by a factor of 120 from that without the electron beam for the largest level of ice roughness. The OMEGA EP beam is expected to produce neutron yields in excess of 10^{15} for all levels of inner-ice nonuniformity and to show the effects of bootstrap heating.

ACKNOWLEDGMENT

This work was supported by the U.S. Department of Energy Office of Inertial Confinement Fusion under Cooperative Agreement No. DE-FC52-92SF19460, the University of Rochester, and the New York State Energy Research and Development Authority. The support of DOE does not constitute an endorsement by DOE of the views expressed in this article.

REFERENCES

1. N. G. Basov, S. Yu. Gus'kov, and L. P. Feokistov, J. Sov. Laser Res. **13**, 396 (1992).
2. M. Tabak *et al*., Phys. Plasmas **1**, 1626 (1994).
3. K. Yasuike *et al*., Rev. Sci. Instrum. **72**, 1236 (2001).
4. S. Atzeni, Phys. Plasmas **6**, 3316 (1999).
5. J. D. Zuegel, S. Borneis, C. Barty, B. LeGarrec, C. Danson, N. Miyanaga, P. K. Rambo, T. J. Kessler, A. W. Schmid, L. J. Waxer, B. E. Kruschwitz, R. Jungquist, N. Blanchot, E. Moses, J. Britten, C. LeBlanc, F. Amiranoff, J. L. Porter, J. Schwarz, M. Geissel, I. C. Smith, I. Jovanovic, and J. Dawson, "Laser Challenges for Fast Ignition," submitted to Fusion Science and Technology; L. J. Waxer, D. N. Maywar, J. H. Kelly, T. J. Kessler, B. E. Kruschwitz, S. J. Loucks, R. L. McCrory, D. D. Meyerhofer, S. F. B. Morse, C. Stoeckl, and J. D. Zuegel, Opt. Photonics News **16**, 30 (2005).
6. T. R. Boehly, D. L. Brown, R. S. Craxton, R. L. Keck, J. P. Knauer, J. H. Kelly, T. J. Kessler, S. A. Kumpan, S. J. Loucks, S. A. Letzring, F. J. Marshall, R. L. McCrory, S. F. B. Morse, W. Seka, J. M. Soures, and C. P. Verdon, Opt. Commun. **133**, 495 (1997).
7. S. C. Wilks *et al*., Phys. Rev. Lett. **69**, 1383 (1992).
8. K. B. Wharton *et al*., Phys. Rev. Lett. **81**, 822 (1998).
9. L. Gremillet, G. Bonnaud, and F. Amiranoff, Phys. Plasmas **9**, 941 (2002).
10. C. K. Li and R. D. Petrasso, Phys. Rev. E **70**, 067401 (2004).
11. T. C. Sangster, J. A. Delettrez, R. Epstein, V. Yu. Glebov, V. N. Goncharov, D. R. Harding, J. P. Knauer, R. L. Keck, J. D. Kilkenny, S. J. Loucks, L. D. Lund, R. L. McCrory, P. W. McKenty, F. J. Marshall, D. D. Meyerhofer, S. F. B. Morse, S. P. Regan, P. B. Radha, S. Roberts, W. Seka, S. Skupsky, V. A. Smalyuk, C. Sorce, J. M. Soures, C. Stoeckl, K. Thorp, J. A. Frenje, C. K. Li, R. D. Petrasso, F. H. Séguin, K. A. Fletcher, S. Padalino, C. Freeman, N. Izumi, J. A. Koch, R. A. Lerche, M. J. Moran, T. W. Phillips, and G. J. Schmid, Phys. Plasmas **10**, 1937 (2003).
12. J. Delettrez, R. Epstein, M. C. Richardson, P. A. Jaanimagi, and B. L. Henke, Phys. Rev. A **36**, 3926 (1987).
13. P. B. Radha, T. J. B. Collins, J. A. Delettrez, Y. Elbaz, R. Epstein, V. Yu. Glebov, V. N. Goncharov, R. L. Keck, J. P. Knauer, J. A. Marozas, F. J. Marshall, R. L. McCrory, P. W. McKenty, D. D. Meyerhofer, S. P. Regan, T. C. Sangster, W. Seka, D. Shvarts, S. Skupsky, Y. Srebro, and C. Stoeckl, Phys. Plasmas **12**, 056307 (2005).
14. P. W. McKenty, V. N. Goncharov, R. P. J. Town, S. Skupsky, R. Betti, and R. L. McCrory, Phys. Plasmas **8**, 2315 (2001).

Proton Core Imaging of the Nuclear Burn in Inertial Confinement Fusion Implosions

Introduction

Images of the nuclear burn region in inertial confinement fusion (ICF)[1,2] experiments can provide critical information about the complex dynamics of fuel capsule implosions, showing the spatial distributions of nuclear reactions that result from the cumulative effects of drive and compression including fuel–shell mix, implosion asymmetries, and radiation and heat transport. Such image data provide exacting tests for simulations. Burn images of deuterium–tritium-filled capsules have previously been envisioned[3] and made using 14.1-MeV neutrons,[4–7] 3-MeV protons,[8–10] or 3.5-MeV alpha particles[10] (see other papers cited in Ref. 11).

This article is the second in a series that discusses another burn imaging method based on the energetic 14.7-MeV protons from reactions in fuel with deuterium (D) and 3-helium (^{3}He) ions. This method, utilizing multiple proton-emission cameras, allows us to study the sizes and asymmetries of burn regions in a wide range of imploded thick plastic-shell capsules that are not amenable to imaging with lower-energy charged particles (which cannot penetrate the shell) and with more angular views than have been obtained so far with neutron imaging. The first article[11] described the general method, presented mathematical algorithms used, and evaluated the spatial resolution and signal-to-noise issues. Here we describe details of the imaging hardware, a sample analysis of a radial burn profile measurement, and experiments and calculations that have been performed to test the accuracy of the measurements. In future articles we will show more details about analysis algorithms,[12] systematic studies of the effects of capsule and drive conditions on burn region size for a large number of nominally symmetric implosions,[12,13] and the effects of drive asymmetry and capsule-shell asymmetry on implosion asymmetry.[14]

The proton-emission imaging cameras generate penumbral images of the burn region that are deconvolved using techniques described in Refs. 11 and 12. Two separate approaches are utilized; one generates a 2-D surface-brightness image of the burn, while the other generates a radial burn profile (reactions per unit volume) for nominally symmetric implosions. The work described here uses only the second approach.

The structure of this paper is as follows. **Hardware and Design Features** (p. 196) describes the camera hardware, which consists primarily of an imaging aperture and a detector pack utilizing CR-39 solid-state nuclear track detectors. **Sample Data From a Capsule With a Plastic Shell** (p. 199) shows sample raw experimental data obtained from an implosion along with the corresponding deconvolved radial profile of emissivity in the imploded capsule. **Demonstration That Possible Sources of Image Broadening are Unimportant** (p. 200) investigates four possible sources of image degradation, all of which are shown to be unimportant. **Fidelity of the Measured Burn Region Sizes** (p. 204) discusses several experimental demonstrations of the fidelity of the reconstructed images, and **Discussion** (p. 205) summarizes the main results.

Hardware and Design Features

Three identical proton core imaging system (PCIS) cameras have been fabricated and used simultaneously for imaging D^{3}He burn from three (nearly) orthogonal directions at the OMEGA Laser Facility.[15] Design criteria for individual cameras included flexibility in imaging geometry and detector filter assignments for imaging of various implosion types, modularized design for simplified installation and minimization of turn-around time between successive experiments, and a redundant "dual detection" scheme for verifying results and backup in case of defective detectors.

The integrated system has proven very effective and practical for obtaining burn images at OMEGA. Figure 104.37 shows a schematic of three proton-emission imaging cameras mounted on the OMEGA target chamber, where each camera is positioned by a special diagnostic shuttle system. The simultaneous use of three cameras makes possible studies of burn symmetry[11,14] and camera consistency [see **Fidelity of the Measured Burn Region Sizes** (p. 204)]. The structure of an individual camera is shown in Fig. 104.38.

After leaving an imploded capsule, protons pass through a round aperture before striking a detector pack. The aperture is typically a 2000-μm-diam hole machined into a 500-μm-thick tantalum (Ta) substrate, although diameters as small as 500 μm have occasionally been used. An accurate, clean, and burr-free edge for the aperture wall is obtained using electrodischarge machining. Each aperture is inspected and quantitatively characterized on both sides using a microscope with a calibrated *X*–*Y* stage and a high-resolution camera to determine that deviations from roundness are small; going around the circumference, the rms deviation from constant radius is not allowed to exceed 3 μm and is usually considerably smaller.

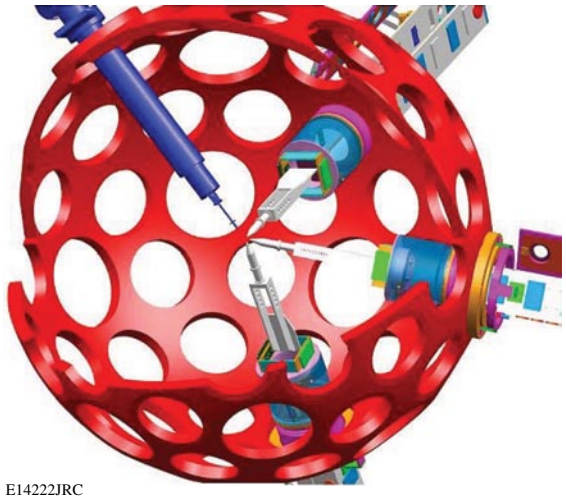
E14222JRC

Figure 104.37
Schematic of the OMEGA target chamber with three cameras for imaging a capsule implosion. The capsule is positioned at target chamber center by the positioning system located at 11 o'clock. The three structures at 1, 4, and 5 o'clock are the PCIS cameras, located approximately orthogonal to each other. This orthoganality is especially important for probing asymmetric burn.

The distance of the aperture from the imploded capsule, which is located at target chamber center (TCC), is usually as small as possible (~3 cm) to maximize counting statistics;[11] closer placement is not possible without interfering with laser beams. The region between the aperture and the detector is enclosed within a conductive housing [Fig. 104.38(a)]. This enclosure prevents stray charged particles from reaching the detectors and shields signal protons from possible electric and magnetic fields.

The detector pack consists of a layered assembly of metallic foils and CR-39 detectors[16] held in an aluminum (Al) support. The metallic foils act as ranging filters for reducing the energy of incoming protons to the energy range 0.5 to 8 MeV, where CR-39 proton detection efficiency is essentially 100%. After exposure, each detector is etched in NaOH and scanned on an automated microscope system that locates the track of each incident proton to submicron accuracy. The distribution of proton track density on the detector forms the penumbral image referred to above.

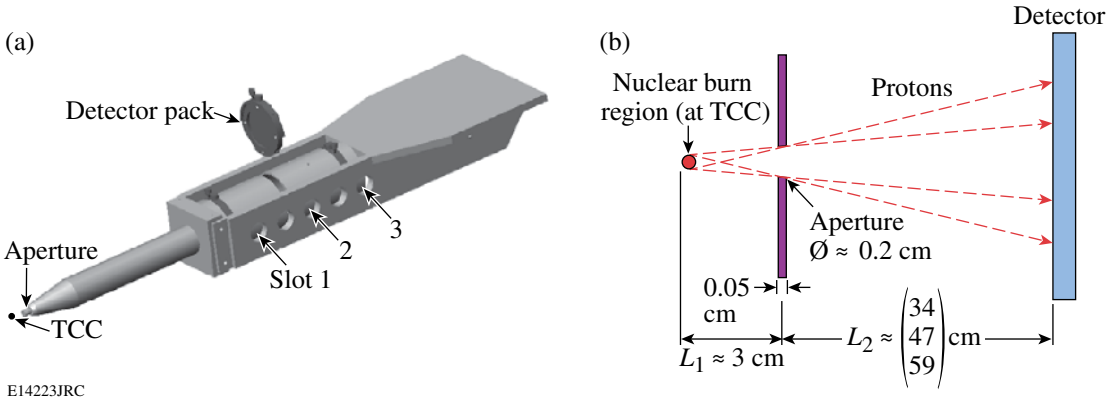

Figure 104.38
(a) Illustration of the proton-emission imaging hardware. The capsule implosion is located at target chamber center (TCC), which is about 3 cm from the imaging aperture. A detector pack may be positioned in one of three available slots (34, 47, and 59 cm from the aperture), providing geometric magnification of the capsule structure ($M \equiv L_2/L_1$) of 12.5, 16, or 20. The aperture consists of a 0.2-cm hole in a 500-μm-thick tantalum substrate. The total length of the instrument is 93 cm. (b) A line diagram illustrates the dimensions.

The choice of filters depends on the expected proton spectrum, which can be different for different types of capsule implosions. Figure 104.39 shows spectra for a 20-μm-thick plastic-shell capsule and a 2-μm-thick glass-shell capsule, which had mean proton energies of 13 MeV and 14.5 MeV, respectively. The plastic-shell implosion might be imaged using a single 800-μm-thick Al filter, while the glass-shell implosion might require a 1000-μm filter. Rather than a single filter, a series of filters and sheets of CR-39 are usually stacked to provide two redundant images from a single camera. As illustrated in Fig. 104.40(a), two images of the D^3He burn are obtained when a thick filter is placed in front of two back-to-back sheets of CR-39. The filter and first sheet of CR-39 range down the energetic D^3He protons for optimal detection on the back of the first sheet and again on the front of the second sheet. The redundant data are occasionally useful if one CR-39 detector has any defects (such as anomalous intrinsic noise[16]). Figure 104.40(b) illustrates another filter configuration that can be used for redundant data. This one places a thin filter between the two pieces of CR-39 so that the proton energy is slightly different at the two detector surfaces. This can be useful if there is a significant uncertainty in what the proton energy will be or if the proton spectrum is particularly wide; if the spectrum at the first sheet is not optimum for detection, the spectrum at the other sheet may be better.

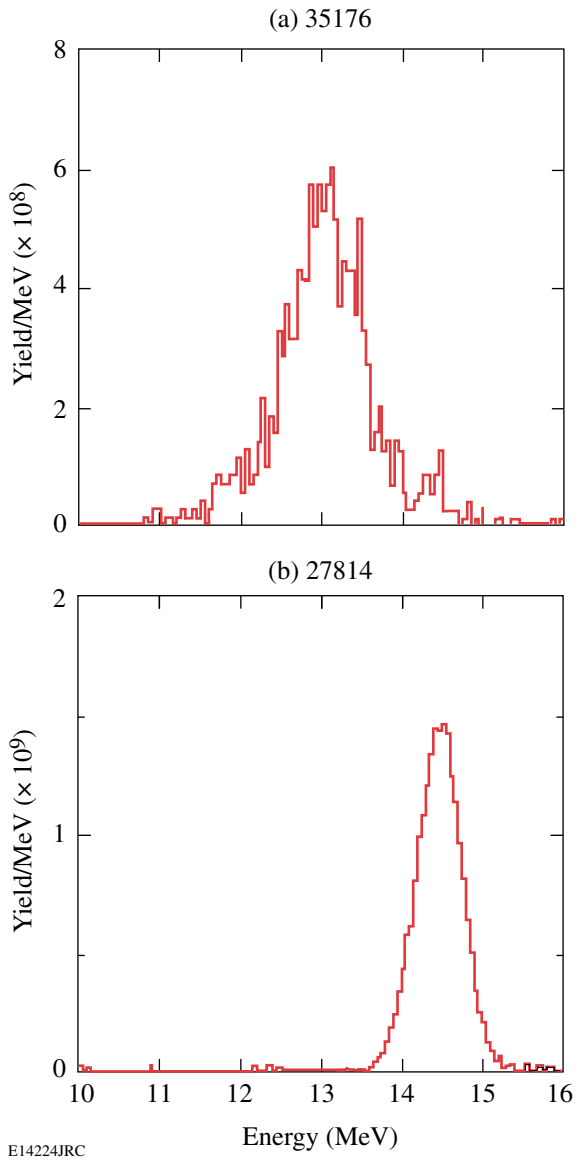

Figure 104.39
For proton-emission imaging, filters are used to reduce the incident proton energies to the range 0.5–8 MeV, where the CR-39 detectors are 100% efficient. Different implosion types result in somewhat different proton energies, as shown here, and filters must be chosen accordingly. (a) A 20-μm-thick CH capsule (shot 35176). (b) A 2.3-μm glass capsule (shot 27814).

The distance from the aperture to the detector pack can be varied by positioning the detector in any of three designated slots [shown in Fig. 104.38(a)]. The first slot provides a nominal 12.5× geometric magnification M (the ratio L_2/L_1), the second

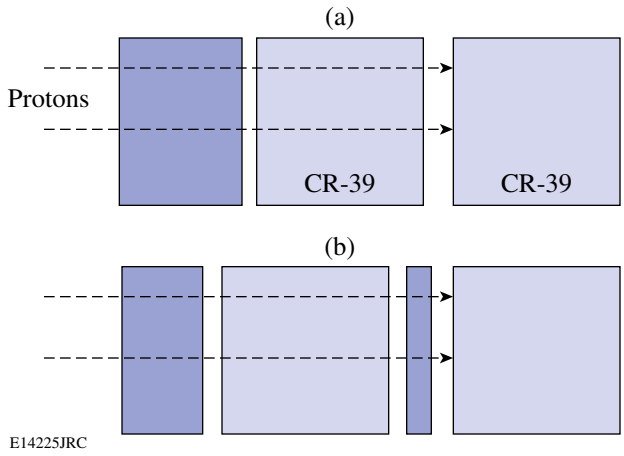

Figure 104.40
Two examples of how CR-39 detectors and filters can be stacked for redundant "front–back" particle detection. (a) Protons lose enough energy while passing through the filter and the first piece of CR-39 so that their energies are in the range of 100% detection efficiency and they leave tracks on both the back side of the first piece and the front side of the second piece. This provides protection against the possibility that either detector has a defect. (b) Protons lose enough energy while passing through the first filter and the first piece of CR-39 so that they leave tracks on the back side of the first piece. They lose slightly more energy while passing through another thin filter, leaving tracks on the front side of the second piece. This provides some protection against the possibility that the proton energy was too low at the second piece; the higher energy at the back of the first piece may then be optimal.

provides 16×, and the third provides 20×. The position is usually chosen to optimize the density of proton tracks on the detectors, which begin to saturate if the incident proton density exceeds ~10^6 protons/cm^2. The third slot makes possible the formation of images for D^{3}He yields up to ~5×10^{10}.

Each camera is secured to a ten-inch manipulator (TIM) on the OMEGA target chamber by way of the large, flat structure at the back end of the system (Fig. 104.38). The TIM's are diagnostic shuttle systems used to position diagnostics near the implosion. There are six TIM's on the OMEGA target chamber, allowing for the use of multiple PCIS cameras. The TIM's facilitate the installation, positioning, and removal of the cameras. Ease of access is essential since the aperture and detector pack of each camera must be replaced between every laser shot. Modularized aperture and detector packs have been implemented to ensure that the replacement time does not exceed the typical shot-to-shot time interval of the OMEGA laser.

Sample Data From a Capsule With a Plastic Shell

The proton-emission imaging cameras have been used to examine many implosions at the OMEGA Laser System; the majority of these involved direct illumination of warm plastic-shell capsules filled with a D^{3}He gas mixture. These capsules were usually driven by 60 beams of frequency-tripled (0.35-μm) UV light, with total laser energy of 23 kJ delivered in a 1-ns square pulse.[17] Individual beams underwent 1.0-THz 2-D smoothing by spectral dispersion and polarization smoothing applied through the use of birefringent wedges.[18]

Structural information about the source of protons in an experiment is obtained by deconvolving a penumbral-camera image using the method described in Ref. 11 and expanded in Ref. 12, which gives the time-integrated radial burn profile (reactions per μm^3) in the implosion. First the azimuthally averaged proton density $N(R)$ in the penumbral image is used to calculate the radial derivative dN/dR, as illustrated in Fig. 104.41. An example using real data is shown in Fig. 104.42(a) (from OMEGA implosion 36730, with 18-atm D^{3}He in a 17-μm-thick plastic shell). This derivative is then fit with a family of functions of varying shapes that are analytically or numerically related to functions describing the radial profile $S_{\text{burn}}(r)$ of proton emissivity per unit volume. The result is a determination of the shape and the characteristic size of the burn region itself. The size can be quantified in different ways, but the radius R_{burn} containing 1/2 of the total local emission seems quite independent of the emission profile shape (as discussed in Ref. 12) and will be used here. For local emission profile shapes we can use the family of super-Gaussians

$$S_{\text{burn}}(r) = S_0 \exp\left[-\left(r/r_0\right)^{2/p}\right], \tag{1}$$

where p is a "peakedness" shape parameter and $r_0 = r_0(R_{\text{burn}},p)$ is a radius. Numerically converting $S_{\text{burn}}(r)$ to functions for comparison with dN/dR, we find the best fit illustrated in Fig. 104.42(a); the corresponding radial profile of emissivity in the capsule is shown in Fig. 104.42(b) and has R_{burn} = 32 μm. To give an idea of statistical errors, Fig. 104.42(b) shows inferred local emission profiles corresponding to alternative fits to the raw data with total χ^2 value higher than the minimum by one. The uncertainty in the shape is significant, but the uncertainty in R_{burn} is only about 1.6 μm (see Ref. 12 for discussion). Note that the analysis produces absolutely normalized emissivity values.

The D^{3}He burn data from many nominally symmetric implosions have been characterized in this way. A range of R_{burn} values from 20 to 80 μm has been measured in other experiments, demonstrating the applicability of this imaging technique to widely different implosion types. The dependence of R_{burn} on implosion type is discussed in Ref. 12.

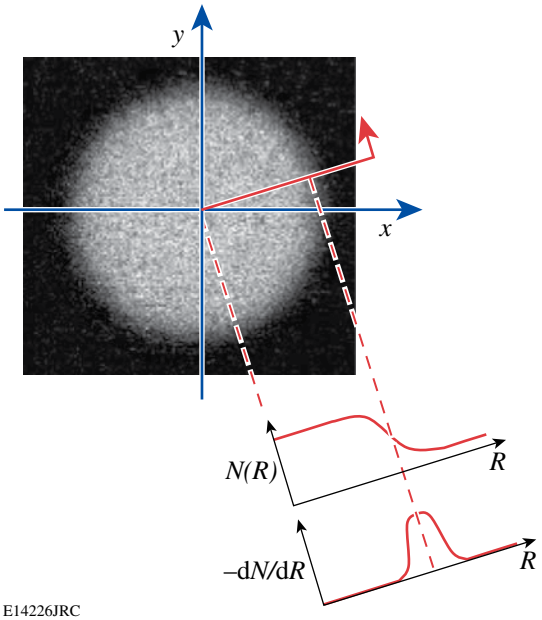

Figure 104.41
Illustration of the relationship between a raw penumbral image (brightness is proportional to the number of protons N per unit area on the detector) and its radial derivative. In the method implemented here, only the azimuthal average of this derivative is used. In the more general case, where asymmetric burn regions are studied, the angular variation of the radial derivative is used.[11]

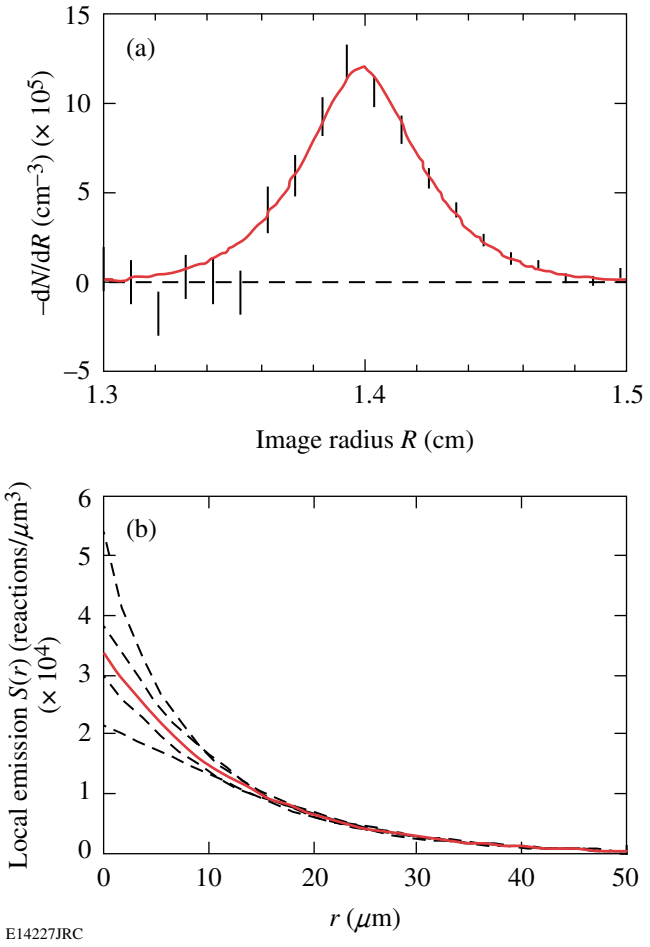

Figure 104.42
(a) The radial derivative of the azimuthally averaged detected proton density (dN/dR) as a function of detector radius for OMEGA implosion 36730. The data were obtained with one of three proton-emission imaging cameras, and the implosion involved a 17-μm plastic shell with an 18-atm D^3He-gas fill. The statistical error bars are larger (smaller) toward the left (right) of the peak where dN/dR represents a small difference between two large (small) numbers. The solid line, representing the best fit to the data, corresponds to the radial burn profile (D^3He reactions per unit volume) shown in (b) with R_{burn} = 32 μm. The error envelope shown by the dashed lines in (b) was generated by using alternate fits to the raw data with χ^2 values exceeding χ^2_{min} by 1. Although the uncertainty in the shape is significant, the uncertainty in R_{burn} is only ±1.6 μm.

Demonstration that Possible Sources of Image Broadening are Unimportant

As illustrated in **Sample Data From a Capsule With a Plastic Shell** (p. 199), statistical errors in the measurement of burn region size are typically a few microns. In this section we investigate other possible sources of error. The protons that generate a penumbral image may experience trajectory shifts while traversing electric and magnetic fields and while interacting with different materials such as the capsule shell, aperture substrate, and ranging filters. If these trajectory shifts are severe enough, the spatial structure in the penumbral image may be artificially broadened; the structure in deconvolved burn images or radial burn profiles will therefore also be broadened. The azimuthal average of the penumbra can also be broadened if the aperture is not round, and errors in analysis can occur from use of incorrect geometric parameters. If broadening with a characteristic length l occurs in the penumbral image, the deconvolved image of a point source (the point response function prf) will have a characteristic size l/M, where M is the geometric magnification of the camera (the value 12.5 is used in the following calculations). The effects of trajectory shifts are discussed in order of occurrence, beginning at the location of D^3He proton production and ending at the detector, and are followed by a consideration of errors in system geometry.

1. Scattering in the Compressed Capsule

The first significant materials encountered by the protons are the remnants of the shell that surround and compress the heated fuel region (see Fig. 104.43). Since the majority of implosions imaged with PCIS involved 20-μm-thick CH-plastic shells, this type of capsule will be examined. At the time of peak proton production, the shell material remaining after the ablation phase consists of a highly dense (~20 g/cc), low-temperature (~500-eV) plasma.[19,20] Spectral analysis

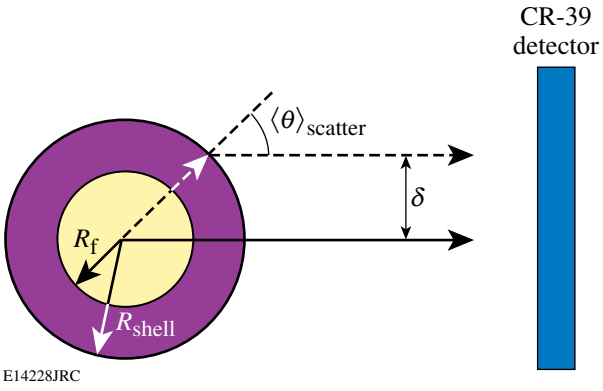

Figure 104.43
Illustration of the assumed geometry for estimating the degree of proton scattering in shell material. The radius of the fuel region R_f was taken to be 45 μm; the outer radius of the shell R_{shell} was 80 μm. Two proton paths originating from a point source are illustrated. The solid line represents the path taken by unscattered protons; the dashed line represents the worst-case path of scattered protons. The average scattering angle $\langle\theta\rangle_{scatter}$ was estimated both for cold CH and for a fully ionized CH plasma shell. The results were ~1° and 2°, respectively, producing corresponding source broadening δ of ~1 μm and 3 μm. Both are negligible compared to typical measured burn radii of ~30 μm.

of D^3He fusion protons has shown that the shell material, with a corresponding ρR of ~60 mg/cm^2, is responsible for a downshift of a couple mega-electron volts from the 14.7-MeV birth energy [Fig. 104.39(a)].[21,22] Although proton slowing down is associated with drag of the background electrons, a small amount of scattering will occur off background ions. To estimate the amount of this scattering and its effect on the broadening of the *prf* of the imaging system, two separate calculations were performed.

In the first calculation, the shell material was treated as a cold, dense solid. The Monte Carlo code TRIM[23] was used to simulate the slowing down and scatter of 14.7-MeV protons in the cold-shell material. The shell was treated as a 50/50 atomic mixture of carbon and hydrogen with a density of 20 g/cc and a thickness of 35 μm (a ρR of 70 mg/cm^2). The calculated average transmitted energy was 12.2 MeV, in reasonable agreement with experimental observations [Fig. 104.39(a)]. The average scattering angle was found to be 0.9°. Assuming the fuel–shell interface is at a radius of 45 μm and all scattering occurs on the outside edge of the shell, a worst-case amount of apparent source broadening was estimated to be ~1 μm (see Fig. 104.43).

In the second, more realistic calculation, the compressed shell material was treated as hot plasma at a temperature of 500 eV.[19,20] At this temperature and density, the shell atoms are fully ionized.[24] With minor modifications to Rutherford's scattering formula,[25] the mean squared angle of the scattered particles is given by

$$\langle \theta^2 \rangle \cong 2\pi N_i \left(2\, ze\, Ze / pv\right)^2 (\ln \Lambda) t, \qquad (2)$$

where N_i is the ion species density in the background plasma; t is the shell thickness; Ze is the charge of the scattering material; ze is the charge of the incident particle, with momentum p, and speed v; and ln Λ is the Coulomb logarithm. The mean scattering angle was calculated for 12-MeV protons passing through 35 μm of a 500-eV, 20-g/cc CH plasma with a Coulomb logarithm of approximately 13.[19,20] (An initial energy of 12 MeV and a ρR of 70 mg/cm^2 were selected to overestimate the effect.) The calculations gave an average scatter angle of ~2°, corresponding to a broadening of the *prf* by ~3 μm. (A similar calculation was performed for scattering in the fuel region, but the effect was much smaller.)

2. Trajectory Shifts Due to Electric Fields

During the laser pulse of a direct-drive implosion, hot electrons are blown off the capsule and may redeposit themselves on surrounding structures, temporarily establishing electric fields. The purpose of this section is to examine the effect a potential difference between the capsule and the aperture could have on proton trajectories and ultimately on the *prf* of the instrument. Although the effect is complicated by the structure of the OMEGA target chamber and the dynamics of the implosion, these calculations look at simplified geometries to produce an order of magnitude estimate of the effect.

A program was developed for tracking the trajectories of 14.7-MeV protons emitted from a point source as they pass through a negatively charged aperture substrate and on to the CR-39 detector plane. A diagram of the geometry is shown in Fig. 104.44(a). The aperture was positioned 3.3 cm from the

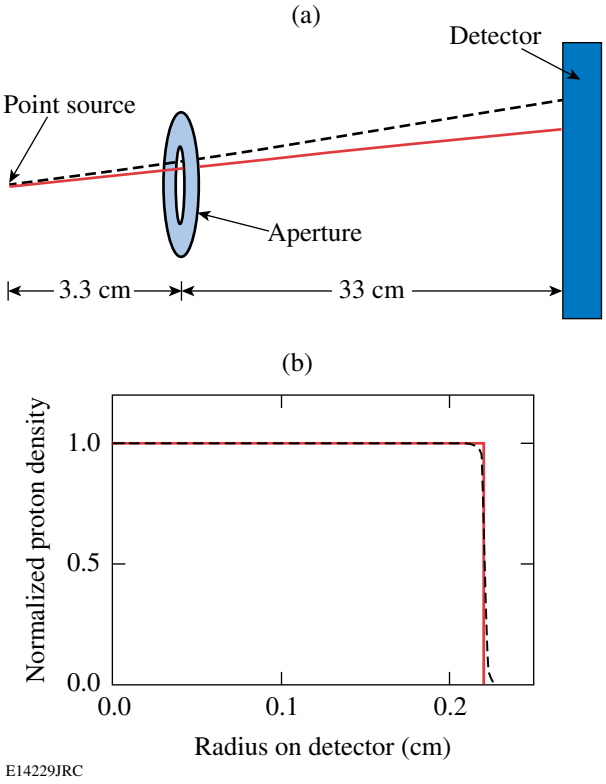

Figure 104.44
(a) Illustration of the effect of electric fields on proton trajectories. The dashed line schematically represents the proton path when a 200-μm-radius aperture carries a potential of 1 MV relative to the source (an overestimate of realistic conditions), while the solid line represents the proton path when no potential is present. Calculations were performed to estimate the image broadening of a point source. (b) The simulated proton density striking the detector for the case of no potential (solid line) and 1-MV potential (dashed line). The result was a slight outward shift of the image and a broadening of the point source by ~1 μm. This broadening is small compared to a typical burn radius of ~30 μm.

source, and the detector plane was positioned an additional 33 cm past the aperture. The figure illustrates one possible effect of a charged aperture where a proton path is indicated for two scenarios: for the case of a charged aperture (dashed line) and the case of an uncharged aperture (solid line).

The aperture substrate was modeled by a 1-cm-radius disk carrying a uniform negative charge corresponding to a potential between the source and this disk of 1 MV. The magnitude of the potential was chosen to overestimate the experimental values expected. Experiments indicate that the capsule itself may carry a charge of approximately 1 MV during the laser pulse, but that the potential quickly dissipates once the laser pulse is terminated.[26,27] For the PCIS experiments, the proton production occurs several hundred picoseconds after laser pulse is terminated, providing a significant period of time in which the potential is known to have substantially decayed.

Calculations were performed for a 200-μm-radius aperture located in the center of the 1-cm-radius disk. Protons were launched through the aperture in all allowable directions. The code calculated particle forces and trajectories on a time scale corresponding to a 5-μm step in the linear dimension using a standard integration for the velocity and a second-order Runge–Kutta integration for the radial position. Simulations were performed with the electric field symmetric on both sides of the aperture as well as with the field turned off between the aperture and the detector, modeling the limit of a perfectly conductive cavity enclosing the instrument. Particle trajectories were individually tracked and particle-particle interactions were not included, as the particle density in the experiments is small. The simulated proton density striking the detector is shown in Fig. 104.44(b) for the case of symmetric fields. The solid line represents the proton density when no net potential exists between the source and the aperture, and the dashed line represents the proton density for a 1-MV potential.

The purpose of this study was to estimate the effect of a potential difference between the aperture and the capsule on the *prf* of the camera. For both symmetric and asymmetric fields, the *prf* was found to be broadened by only ~1 μm. (Additional simulations were also performed for a 500-μm-radius aperture, as well as for a 0.1-MV potential. None of the studies produced a significant broadening of the image.)

3. Scattering in Aperture Walls

One advantage of proton-emission imaging is that a thin aperture substrate is sufficient to stop D^3He protons, providing a well-defined aperture edge. The apertures commonly used consist of a 2000-μm-diam cylindrical hole in a 500-μm-thick Ta substrate. The 14.7-MeV protons would be completely stopped by ~400 μm of Ta. Protons that travel through less Ta may be stopped in the ranging filters located in the detector pack. Ideally, no detected protons would have scattered in the Ta. Since no aperture is perfectly tapered to match the trajectories of incoming protons, however, some protons will strike the inner walls of the aperture and scatter through a thinner section of Ta, as illustrated in Fig. 104.45(a). If the

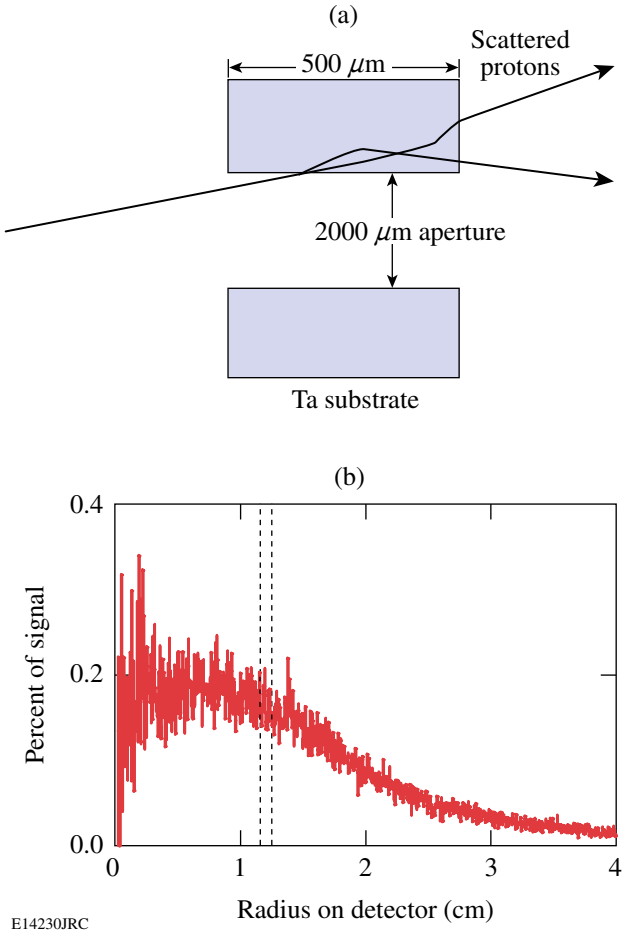

Figure 104.45
(a) Illustration of a cross sectional view of an aperture, defined as a 2000-μm-diam hole in a 500-μm-thick tantalum substrate. Not shown are the source and the detector, located 3 cm to the left and 33 cm to the right, respectively. As seen in the figure, the geometry dictates that protons may encounter less than 500 μm of Ta. If the amount of Ta encountered is sufficiently small, the protons will exit the tantalum and may broaden the image. (b) The simulated ratio of scattered proton density to unscattered signal proton density on the detector. The dotted lines represent the approximate location of an image penumbra from an ~30-μm source. The calculated broadening of the point source was <<1 μm.

section is thin enough, protons may exit the opposite side, travel to the detector pack, pass through the ranging filters, and be detected on the CR-39. The result would be a slight broadening of the penumbra.

Simulations were performed to estimate the degradation of the camera *prf* by proton scattering in the Ta substrate utilizing the Monte Carlo program TRIM[23] to evaluate the slowing down and scatter of charged particles in matter. The source was treated as a 12-MeV monoenergetic point source of protons, chosen to approximate the observed mean energy of D^3He protons after escaping an imploded 20-μm CH-shell capsule. TRIM was used to determine the amount of scatter produced by discrete thicknesses of Ta; since the aperture wall presents a continuous range of thicknesses to protons, some assumptions were made to transform the 1-D TRIM output into the 2-D geometry of the aperture. Instead of modeling the continuous range of thicknesses, a series of seven discrete thickness steps was used. Depending on where the proton entered the aperture wall, the encountered material was approximated by one of seven Ta sheets, ranging in thickness from 10 μm to 150 μm. (Any proton passing through more than 150 μm of Ta would be stopped by the ranging filters.) Several million protons were tracked through each discrete thickness. Upon exiting the Ta material, the energy and trajectory of each proton was recorded.

These trajectories, along with the system geometry, were used to predict whether scattered protons would strike the detector plane. The system geometry mimicked the actual experimental hardware; modeling of the three main components, the source, the aperture, and the detector was included. The geometry was similar to that seen in Fig. 104.38(b), where the distance from TCC to the aperture was taken to be 3 cm and the distance from the aperture to the detector was 33 cm. The aperture was modeled by a 2000-μm-diam hole centered in a 500-μm-thick Ta disk. Based on this geometry and the recorded trajectories from TRIM, the scattered protons that reached the detector pack were isolated from those that did not.

Each proton deflected toward the detector pack then encountered additional filtering before reaching the detector. The filtering, placed directly in front of the detector, was assumed to be 20 μm of Al followed by 1000 μm of Mylar and an additional 100 μm of Al. (Mylar has chemical composition and stopping properties similar to those of CR-39). The proton was assumed detected if the energy was great enough to allow passage through these additional filters.

Thus, a record of the detection locations of all the scattered protons with an appropriate trajectory and energy was created. The ratio of the scattered proton density to unscattered signal proton density as a function of the detector radius is shown in Fig. 104.45(b); the dotted lines indicate the approximate location of the image penumbra from an ~30-μm source. The simulations showed that the scattered protons represent less than 0.3% of the detected protons in the penumbral region and that the radial profile of scattered protons is fairly flat. Since the radial derivative of the proton density ultimately determines the size and shape of the source,[11] the small-amplitude slowly varying background would have little effect. Broadening of the *prf* was found to be $<<1$ μm.

4. Scattering in Filters

Upon reaching the detector pack, protons pass through several ranging filters that are designed to reduce the incident proton energy for optimal detection efficiency. Along with the desired loss of energy, the protons will experience some lateral straggling, another possible source of spatial broadening. To estimate the magnitude of this effect, the Monte Carlo code TRIM was used to track 12-MeV protons from a point source through 20 μm of Al, 1000 μm of Mylar, and a final 100 μm of Al. The lateral positions for protons exiting the filters were recorded and fit by a Gaussian distribution with an *e*-folding radius at the detector of ~30 μm. This translates to a broadening in the camera *prf* of ~30 μm/M ~ 3 μm.

5. Geometric Error

Accuracy in the inference of burn profiles from penumbral images requires accurate knowledge of imaging system dimensions. Of primary importance is the radius of the aperture projection on the detector, which may not be exactly as expected if either the capsule–aperture distance or the aperture–detector distance has any uncertainty. But the radius is actually determined from the data as an integral part of the analysis [see Refs. 11 and 12 and Fig. 104.42(a)], so this is not a source of error beyond the statistical fit error. If the aperture itself is not perfectly round and has deviations from its average radius with the rms value $\delta R_{\text{aperture}}$, the rms deviation from round at the detector will be $(M+1)\ \delta R_{\text{aperture}}$; this will cause a broadening of the system *prf* by $[(M+1)/M]\ \delta R_{\text{aperture}} \approx \delta R_{\text{aperture}}$. If the deviation from roundness is due to ellipticity, either from bad fabrication or from the aperture not being exactly perpendicular to the capsule–detector direction, this effect is identified in the data processing and corrected. Other types of deviation from roundness can sometimes be identi-

fied in the data, but in the worst case, uncorrected deviations should have $\delta R_{\text{aperture}} < 3\ \mu$m as discussed in **Hardware and Design Features** (p. 196).

Another source of error would come from an inaccurate value of the magnification M (see Fig. 104.38 and its caption), which could be different from the expected value if L_1 or L_2 were not measured accurately. Since M represents the ratio of structure size at the detector to structure size in the burn region, any error in M would not cause a broadening of the *prf* but would cause a multiplicative error in the inferred burn region size. But since the radius of the aperture itself, R_{aperture}, is measured in advance to better than 0.1%, and since the radius of its projection on the detector, $(M+1)R_{\text{aperture}}$, is determined as part of the data analysis, a self-consistent value of M is determined from the data and is not subject to measurement error.

6. Net Broadening

The net result of these broadening effects can be estimated for the data shown in Fig. 104.42 where the measured R_{burn} was found to be 32 μm with a statistical error of $\pm 1.6\ \mu$m. If we assume that the five sources of error discussed in the previous subsections are independent and that each generates a distortion in the system *prf* that is approximately Gaussian, then the net system *prf* would be a Gaussian whose radius r_{prf} is the sum (in quadrature) of the individual radii. In this case, taking the upper limit for geometric error,

$$r_{prf} \approx \sqrt{3^2 + 1^2 + 0^2 + 3^2 + 3^2}\ \mu\text{m} \approx 5\ \mu\text{m}.$$

The measured burn radius would then be the true burn radius added in quadrature with r_{prf}. The error would be

$$\delta R_{\text{burn}} = R_{\text{burn,measured}} - R_{\text{burn,true}}$$

$$\approx 32\ \mu\text{m} - \sqrt{32^2 - 5^2}\ \mu\text{m} \approx 0.4\ \mu\text{m}, \qquad (3)$$

which is small compared to the statistical uncertainty of $\pm 1.6\ \mu$m.

Fidelity of the Measured Burn Region Sizes

The following subsections describe experimental tests that demonstrate the repeatability and fidelity of the measured burn region sizes. In **Consistency of the Measured Burn Profiles** (p. 204), measurement consistency is experimentally demonstrated when six independent measurements of R_{burn} made during the same symmetrically driven implosion are compatible. **Lack of Dependence on Imaging Geometry** (p. 204) shows that the reconstructed burn profiles are independent of changes in the system magnification and the aperture size. **Lack of Distortion by Ambient Fields** (p. 205) presents data suggesting that ambient fields do not affect the system response.

1. Consistency of the Measured Burn Profiles

Figure 104.42(a) shows six separate measurements of R_{burn} made during the same symmetrically driven implosion (OMEGA shot 36730, a capsule with a 17-μm-thick plastic shell filled with a mixture of 6 atm of D_2 and 12 atm of ^{3}He gas). The implosion was imaged with three separate PCIS cameras, fielded in TIM's 2, 3, and 4. (TIM-3 is located 109° from TIM-2, and TIM-4 is 101° from TIM-2 and 79° from TIM-3.) Each camera produced two measurements of R_{burn} using the redundant detector method described in **Hardware and Design Features**. The error bars in the figure represent statistical uncertainties, as discussed in **Sample Data From a Capsule With a Plastic Shell** (p. 199), and the set of six measurements is self-consistent.

2. Lack of Dependence on Imaging Geometry

A measurement of R_{burn} should be independent of any changes in the geometric parameters of the camera, and this is demonstrated by data plotted in Fig. 104.46. Lack of dependence on aperture diameter is illustrated in Fig. 104.46(b), which shows results from five successive implosions of capsules with 19-μm-thick plastic shells filled with 10.5-atm D_2 and 6-atm ^{3}He. For each implosion, one TIM was equipped with a PCIS camera. The diameter of the aperture used for the first two and last two implosions was 2000 μm, while the diameter used for the third implosion was 600 μm. All results were statistically consistent with the mean value of 30 μm. Lack of dependence on the geometric magnification was demonstrated by simultaneous use of cameras with different M on each of two implosions. In Fig. 104.46(a), data were taken with M = 12.5 and M = 20, while in Fig. 104.46(c) M = 6 and M = 9 were used. In each case the two different values of M resulted in the same measured R_{burn}.

3. Lack of Distortion by Ambient Fields

Several plastic-shell implosions were used to look for possible systematic errors associated with stray fields. The two cameras used for shot 35004 were set up identically except that L_1 = 5.4 cm for TIM-3 and L_1 = 3.7 cm for TIM-4. If fields were significantly influencing protons in the region between the capsule and the aperture, we would expect to see a difference

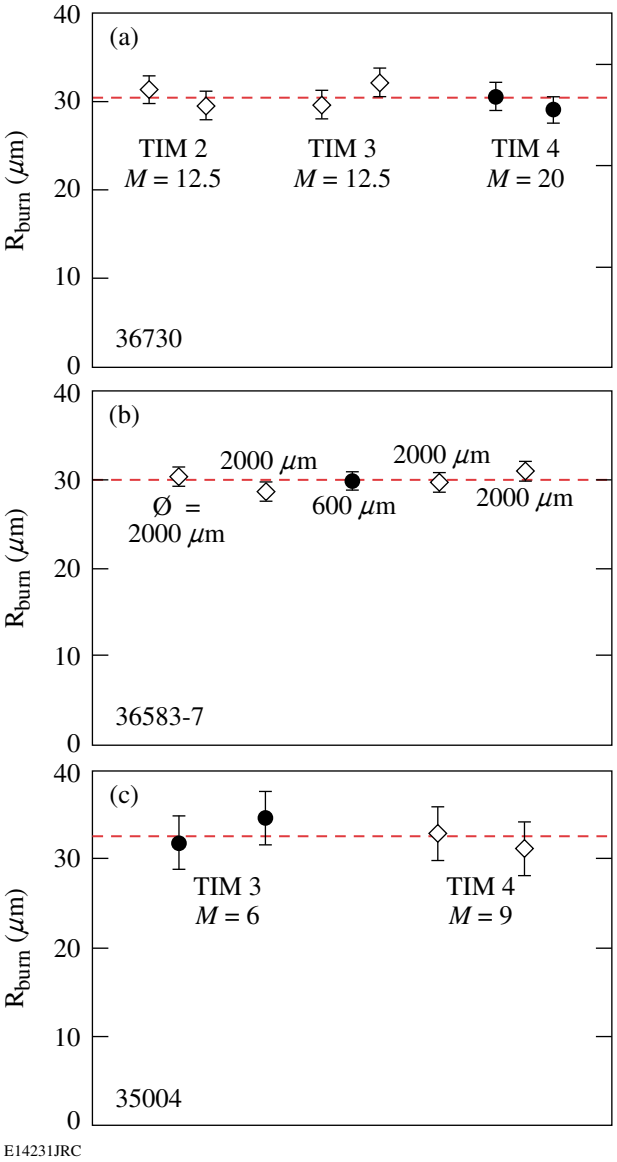

Figure 104.46
R_{burn} data are shown with the average measurement value (dashed line) for a series of implosions. (a) A 17-μm-thick plastic shell with 18-atm D^3He gas fill (OMEGA implosion 36730) was imaged by three nearly orthogonal imaging cameras with different aperture-to-detector distances, located in TIM's 2, 3, and 4. The redundant-detector method was used to generate two data sets for each camera. The geometric magnification (M) of each camera is listed. The data show that different cameras and different aperture-to-detector distances give the same result. (b) A single camera imaged a series of 19-μm-thick plastic shells filled with 10.5 atm D_2 and 6 atm ^3He. The aperture diameter (Ø) used for each camera is indicated; R_{burn} was unaffected by the change in aperture size. (c) A 20-μm-thick plastic shell with 18-atm D^3He gas fill was imaged by two cameras having different capsule-to-aperture distances, placed in TIM's 3 and 4. The separately inferred values of R_{burn} were statistically compatible. Note that the error bars in all plots are statistical errors.

in the measured R_{burn} from these two cameras. The results shown in Fig. 104.46(c) report essentially the same R_{burn} for both cameras, suggesting that there were no serious field effects in the region before the aperture.

The three cameras used for shot 36730 were set up identically except that L_2 = 36.6 cm for TIM-2 and TIM-3 while L_2 = 58.6 cm for TIM-4. If fields were affecting the protons between the aperture and the detector (a region surrounded by a conductor), we would expect to see differences in the measured values of R_{burn}. Figure 104.46(a) shows that all R_{burn} results were consistent, suggesting that there were no serious field effects in the region behind the aperture.

Another recent experiment[28] also provides evidence that fields do not dramatically alter the trajectory of D^3He protons in the region past the aperture. In this test, a steel mesh (50-μm-diam wires with 100 wires per inch) was placed directly in front of the imaging aperture. Examination of the proton-emission image revealed no distortions in the mesh-induced pattern, suggesting that fields are not significantly altering the trajectories of 14.7-MeV D^3He protons.

Discussion

Three proton core imaging cameras have been built and installed at OMEGA using the design discussed here, and they have now been used to study the spatial distributions of nuclear burn in a range of different implosion types using algorithms described elsewhere.[11,12] An example of the analysis of the radial burn profile of a symmetric implosion was shown in **Sample Data From a Capsule With a Plastic Shell** (p. 199) with a 32-μm burn radius. In another article,[12] other types of implosions are studied and are shown to have burn radii ranging from 20 to 80 μm; clear correlations are shown between the burn radius and implosion parameters (capsule shell material and thickness, fill gas pressure, and laser energy). In addition, 2-D reconstruction techniques have been used together with three nearly orthogonal imaging cameras to study asymmetric burn regions and to show clear relationships between laser drive asymmetry and burn asymmetry.[14] In Ref. 11 the issues of spatial resolution and statistical noise were studied theoretically. A range of calculations and measurements, described in **Demonstration that Possible Sources of Image Broadening are Unimportant** (p. 200) and **Fidelity of the Measured Burn Region Sizes** (p. 204), investigated other possible sources of error in measured burn region sizes. So far there is no evidence of any other errors that are as important as the statistical errors; more calculations and measurements as well as comparisons with x-ray and neutron images will be pursued in the future for

further verification. In the meantime, proton emission imaging is providing interesting and useful data bearing on the understanding of capsule implosion dynamics and performance. A particularly nice feature of this imaging mode, which will be utilized in future studies, is the fact that the same reaction product studied here (the D^3He proton) is also utilized by other diagnostics. Proton spectrometers[16] measure the proton energy at different angles around a capsule, determining the areal density of the compressed shell from the energy loss, while the proton temporal diagnostic[29,30] measures the time evolution of the burn. The spatial distribution of D^3He burn can therefore be combined with the angular distribution of areal density in the colder shell material and the time evolution of burn, as well as other types of diagnostic measurements, for a more complete picture of implosion dynamics.

ACKNOWLEDGEMENTS

The authors express their gratitude to the OMEGA engineers and operations crew who supported these experiments. In addition, we would like to personally thank Candice Culligan, and Jocelyn Schaeffer for their continuous help. This work has been supported in part by LLE (Subcontract No. P0410025G) and LLNL (Subcontract No. B313975), and by the U.S. Department of Energy Office of Inertial Confinement Fusion (Grant No. DE-FG03-99DP00300) and under Cooperative Agreement No. DE-FC03-92SF19460, the University of Rochester, and New York State Energy Research and Development Authority.

REFERENCES

1. J. Nuckolls *et al*., Nature **239**, 139 (1972).
2. S. E. Bodner, D. G. Colombant, J. H. Gardner, R. H. Lehmberg, S. P. Obenschain, L. Phillips, A. J. Schmitt, J. D. Sethian, R. L. McCrory, W. Seka, C. P. Verdon, J. P. Knauer, B. B. Afeyan, and H. T. Powell, Phys. Plasmas **5**, 1901 (1998).
3. K. A. Nugent and B. Luther-Davies, J. Appl. Phys. **58**, 2508 (1985).
4. D. Ress *et al*., Rev. Sci. Instrum. **59**, 1694 (1988).
5. R. A. Lerche *et al*., Laser Part. Beams **9**, 99 (1991).
6. C. R. Christensen, D. C. Wilson, C. W. Barnes, G. P. Grim, G. L. Morgan, M. D. Wilke, F. J. Marshall, V. Yu. Glebov, and C. Stoeckl, Phys. Plasmas **11**, 2771 (2004).
7. L. Disdier, R. A. Lerche, J. L. Bourgade, and V. Yu. Glebov, Rev. Sci. Instrum. **75**, 2134 (2004).
8. Y.-W. Chen *et al*., Opt. Commun. **73**, 337 (1989).
9. M. Nakai *et al*., Rev. Sci. Instrum. **61**, 3235 (1990).
10. A. P. Fews *et al*., Phys. Rev. Lett. **73**, 1801 (1994).
11. F. H. Séguin, J. L. DeCiantis, J. A. Frenje, S. Kurebayashi, C. K. Li, J. R. Rygg, C. Chen, V. Berube, B. E. Schwartz, R. D. Petrasso, V. A. Smalyuk, F. J. Marshall, J. P. Knauer, J. A. Delettrez, P. W. McKenty, D. D. Meyerhofer, S. Roberts, T. C. Sangster, K. Mikaelian, and H. S. Park, Rev. Sci. Instrum. **75**, 3520 (2004).
12. F. H. Séguin, J. L. DeCiantis, J. A. Frenje, C. K. Li, J. R. Rygg, C. D. Chen, R. D. Petrasso, J. A. Delettrez, S. P. Regan, V. A. Smalyuk, V. Yu. Glebov, J. P. Knauer, F. J. Marshall, D. D. Meyerhofer, S. Roberts, T. C. Sangster, C. Stoeckl, K. Mikaelian, H. S. Park, H. F. Robey, and R. E. Tipton, "Measured Dependence of Nuclear Burn Region Size on Implosion Parameters in Inertial Confinement Fusion Experiments," submitted to Physics of Plasmas.
13. J. L. DeCiantis, "Proton Emission Imaging of the Nuclear Burn in Inertial Confinement Fusion Experiments," M.S. thesis, Massachusetts Institute of Technology (2005).
14. F. H. Séguin, J. L. DeCiantis, J. A. Frenje, C. K. Li, J. R. Rygg, C. D. Chen, R. D. Petrasso, V. A. Smalyuk, F. J. Marshall, J. A. Delettrez, J. P. Knauer, P. W. McKenty, D. D. Meyerhofer, S. Roberts, T. C. Sangster, H. S. Mikaelian, and H. S. Park, Bull. Am. Phys. Soc. **49**, 63 (2004); F. H. Séguin, J. DeCiantis, C. K. Li, J. A. Frenje, J. R. Rygg, R. D. Petrasso, S. Regan, J. A. Delettrez, J. P. Knauer, F. J. Marshall, D. D. Meyerhofer, S. Roberts, T. C. Sangster, V. A. Smalyuk, H. S. Mikaelian, H. S. Park, H. Robey, and R. Tipton, Bull. Am. Phys. Soc. **50**, 114 (2005); *ibid*., "Measured Effects of Drive Asymmetry and Shell Asymmetry on Nuclear Burn Region Symmetry in Direct-Drive ICF Implosions," to be submitted to Physics of Plasmas.
15. T. R. Boehly, D. L. Brown, R. S. Craxton, R. L. Keck, J. P. Knauer, J. H. Kelly, T. J. Kessler, S. A. Kumpan, S. J. Loucks, S. A. Letzring, F. J. Marshall, R. L. McCrory, S. F. B. Morse, W. Seka, J. M. Soures, and C. P. Verdon, Opt. Commun. **133**, 495 (1997).
16. F. H. Séguin, J. A. Frenje, C. K. Li, D. G. Hicks, S. Kurebayashi, J. R. Rygg, B.-E. Schwartz, R. D. Petrasso, S. Roberts, J. M. Soures, D. D. Meyerhofer, T. C. Sangster, J. P. Knauer, C. Sorce, V. Yu. Glebov, C. Stoeckl, T. W. Phillips, R. J. Leeper, K. Fletcher, and S. Padalino, Rev. Sci. Instrum. **74**, 975 (2003).
17. A series of burn images have been obtained from thin glass implosions involving less than 23 kJ of laser energy,[12] several thick plastic-shell implosions involving 18 kJ and 30 kJ of laser energy,[12,14] and a few implosions involving different shaped laser pulses.[13]
18. T. R. Boehly, V. A. Smalyuk, D. D. Meyerhofer, J. P. Knauer, D. K. Bradley, R. S. Craxton, M. J. Guardalben, S. Skupsky, and T. J. Kessler, J. Appl. Phys. **85**, 3444 (1999).
19. C. Li and R. D. Petrasso, Phys. Plasmas **2**, 2460 (1995).
20. C. K. Li and R. D. Petrasso, Phys. Rev. Lett. **70**, 3059 (1993).
21. C. K. Li, D. G. Hicks, F. H. Séguin, J. A. Frenje, R. D. Petrasso, J. M. Soures, P. B. Radha, V. Yu. Glebov, C. Stoeckl, D. R. Harding, J. P. Knauer, R. L. Kremens, F. J. Marshall, D. D. Meyerhofer, S. Skupsky, S. Roberts, C. Sorce, T. C. Sangster, T. W. Phillips, M. D. Cable, and R. J. Leeper, Phys. Plasmas **7**, 2578 (2000).

22. F. H. Séguin, C. K. Li, J. A. Frenje, S. Kurebayashi, R. D. Petrasso, F. J. Marshall, D. D. Meyerhofer, J. M. Soures, T. C. Sangster, C. Stoeckl, J. A. Delettrez, P. B. Radha, V. A. Smalyuk, and S. Roberts, Phys. Plasmas **9**, 3558 (2002).

23. *SRIM*, a code for calculations of *The Stopping and Range of Ions in Matter*, J. F. Ziegler and J. P. Biersack, Version 2000.39 (2000).

24. D. E. Post *et al*., At. Data Nucl. Data Tables **20**, 397 (1977).

25. J. D. Jackson, *Classical Electrodynamics*, 3rd ed. (Wiley, New York, 1999).

26. D. G. Hicks, C. K. Li, F. H. Séguin, J. D. Schnittman, A. K. Ram, J. A. Frenje, R. D. Petrasso, J. M. Soures, D. D. Meyerhofer, S. Roberts, C. Sorce, C. Stoeckl, T. C. Sangster, and T. W. Phillips, Phys. Plasmas **8**, 606 (2001).

27. D. G. Hicks, C. K. Li, F. H. Séguin, A. K. Ram, J. A. Frenje, R. D. Petrasso, J. M. Soures, V. Yu. Glebov, D. D. Meyerhofer, S. Roberts, C. Sorce, C. Stöckl, T. C. Sangster, and T. W. Phillips, Phys. Plasmas **7**, 5106 (2000).

28. C. K. Li, F. H. Séguin, J. R. Rygg, J. A. Frenje, R. D. Petrasso, T. C. Sangster, V. A. Smalyuk, J. A. Delettrez, J. P. Knauer, S. P. Regan, J. Soures, F. J. Marshall, P. W. McKenty, D. D. Meyerhofer, C. Stoeckl, R. P. J. Town, P. Patel, A. J. MacKinnion, P. Amendt, N. Izumi, and O. Landen, Bull. Am. Phys. Soc. **50**, 266 (2005).

29. J. A. Frenje, C. K. Li, F. H. Séguin, J. Deciantis, S. Kurebayashi, J. R. Rygg, R. D. Petrasso, J. Delettrez, V. Yu. Glebov, C. Stoeckl, F. J. Marshall, D. D. Meyerhofer, T. C. Sangster, V. A. Smalyuk, and J. M. Soures, Phys. Plasmas **11**, 2798 (2003).

30. V. Yu. Glebov, C. Stoeckl, S. Roberts, T. C. Sangster, J. A. Frenje, R. D. Petrasso, R. A. Lerche, and R. L. Griffith, "Proton Temporal Diagnostics for ICF Experiments on OMEGA," submitted to Review of Scientific Instruments.

Hot Surface Ionic Line Emission and Cold K-Inner-Shell Emission From Petawatt-Laser-Irradiated Cu Foil Targets

Introduction

There is much interest in both experimental and theoretical studies of laser–solid target interactions with picosecond laser beams at relativistic intensities because of their relevance to fast ignition in laser fusion[1] and backlighter development.[2,3] High-intensity, ultrashort laser pulses impinging onto solid or gaseous targets produce large quantities of suprathermal electrons ranging from ~100 keV up to several MeV with conversion efficiencies of several tens of a percent from the incident laser energy into electron energy.[4–7] A precise physical understanding of the MeV electron production and transport in dense plasma is crucial for the success of the fast-ignition concept. This has triggered vigorous research efforts in both experimental[8–12] and theoretical studies.[13–16]

Strong self-generated magnetic and electric fields influence the transport of relativistic electrons in high-energy-density plasmas.[12,15,17] Inhibited heat flux in insulators due to strong longitudinal electrical fields has recently been predicted at subrelativistic intensities with a one-dimensional Monte Carlo collisional particle-in-cell (PIC) code.[18] Depending on the experimental conditions, the fields might collimate the electron beam or compromise the effectiveness of electron penetration because of flux inhibition.[17,19,20] The guiding of electrons with MeV energy in a plasma fiber over a distance of ~1 mm is attributed to strong laser-generated fields.[21] Many plasma processes influence the heating of solid matter by laser-generated relativistic electrons and their return currents. One example is an observed annular heating pattern that is attributed to a strong Weibel instability growth because of sharp transverse gradients in the input electron-beam current.[11]

Hard x-ray bremsstrahlung and characteristic inner-shell line emissions, predominantly from the K shell, are produced when energetic electrons propagate into the bulk of a solid target. The measurement of inner-shell emission lines is a valuable diagnostic to characterize the suprathermal electron distribution.[4,6,7,22–24] Measurements of electron temperatures and temperature gradients provide important guidance for simulations to study energy transport in relativistic laser–solid density plasmas. The standard method used to infer electron density and temperature in laser-produced plasmas is x-ray line spectroscopy;[25] this method has been applied to petawatt laser–plasma experiments, e.g., Koch *et al*., using aluminum K-shell spectra.[11] The dense and hot plasma environment shifts and broadens the spectral lines because of the interactions of the charged-particle plasma constituents. The comparison of measured line shapes and line ratios with calculations then allows the plasma parameters to be inferred.

In this work, measurements of the surface electron temperatures for petawatt-laser-produced copper plasmas are presented. Measurements of the scaling of the Cu K-shell emission with laser intensity and target thickness are shown and analyzed. The following three sections will present the **Experimental Setup** (p. 208), **Experimental Results** (p. 209), and **Analysis and Discussion** (p. 213). The third section contains two subsections: Resonance-Line Emission From Hot Plasmas (p. 213) and Inner-Shell Emission (p. 216), which compares the measured K_α laser-intensity scaling to a model calculation. **Summary and Conclusions** (p. 218) are presented in the last section.

Experimental Setup

A schematic of the experimental setup is shown in Fig. 104.47. Laser pulses from either the Rutherford Appleton Laboratory Petawatt (PW)[26] or the 100-TW[27] facilities were focused with *f*/3 off-axis parabolas to a spot size of the order of ~10 μm in diameter.[28] The fraction of the nominal laser energy transported onto the target through the compressor and subsequent optics of the PW and the 100-TW laser systems is 75% and 60% respectively. About half of this energy is contained in the main focal spot while the remainder is distributed over a larger area.[28,29] The laser energy was measured for each shot before the beam entered the compressor. The maximum achievable intensities on target were $4(\pm 2) \times 10^{20}$ W/cm^2 and $4(\pm 2) \times 10^{19}$ W/cm^2 with the PW and the 100-TW lasers, respectively. The relatively large uncertainty in intensity on target is mainly due to changes in the focal-spot pattern on a shot-to-shot basis.

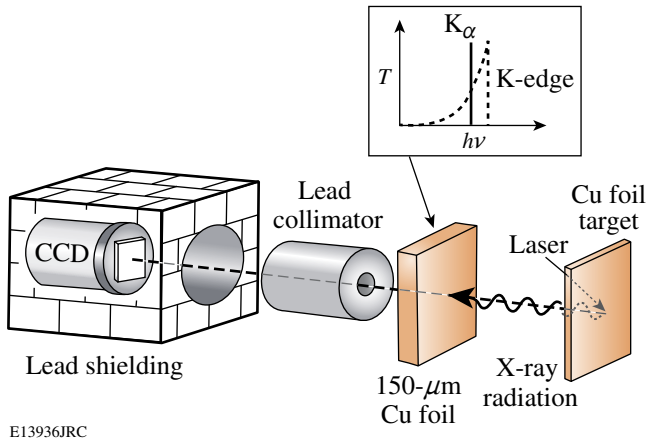

Figure 104.47
Experimental setup. The petawatt laser is focused onto a thin copper foil target. A single-hit CCD camera measures the x-ray emission from the target's front side. Lead collimators and lead shielding provide the necessary suppression of unwanted background radiation. A 150-μm copper foil provides bandpass filtering of the Cu K-shell emission while suppressing the background radiation. The inset shows qualitatively the foil transmission versus photon energy and the position of the K_α line.

Preplasma formation was measured side-on with a frequency-doubled, 1-ps probe beam and a Wollaston prism interferometer, which showed that the plasma surface with an electron density of 10^{19} cm^{-3} expands at most by 40 μm from the original target surface at 100 ps prior to the main pulse interaction. Higher electron densities are not accessible by this diagnostic because of probe-light refraction out of the *f* number of the collecting lens in the probe line. Prepulse measurements show an amplified spontaneous emission (ASE) pulse starting at 1.5 ns ahead of the main pulse with an intensity of 5×10^{-8} of the main pulse intensity. The overall intensity contrast is better than 10^5 in a time window between 10 ns and 50 ps before the main pulse.[28] The *p*-polarized light was focused at a 30° angle of incidence onto thin (<30 μm) copper foil targets with an area of <2000 × 2000 μm^2. The targets were mounted as flags on 6-μm-diam carbon fibers.

A single-photon–counting, x-ray back-illuminated, charge-coupled-device (CCD) camera (SI 800-145, Spectral Instruments-Photonics, Tucson AZ) measured the plasma emission from the laser irradiation side ("target front side") at a viewing angle of 16° with respect to the target normal. Radiation shielding of the CCD camera with a lead housing and lead collimators was crucial in obtaining good signal-to-noise spectra by suppressing the hard x-ray background generated by the petawatt laser.[30] In addition, a 150-μm-thick Cu foil filter in front of the CCD was used to adjust the signal level of the K-shell emission to the single-photon–counting regime and to improve the signal-to-noise ratio. The experimental setup with the 100-TW facility was similar to that described above. The CCD detector was located closer to the plasma source in that case, 1.4 m instead of 3.8 m, leading to an increased solid angle by a factor of ~7.

When an x-ray photon is absorbed in the material of the CCD, a certain number of free-charge carriers proportional to the x-ray photon energy are created. A significant number of x-ray events are split between adjacent pixels. Adding the value of the pixels surrounding the event centroid might be used to reconstruct the total charge collected from an event. This is useful at very low photon fluxes, especially in astronomical applications. The single pixel analysis, as used here, ignores the spread of the absorbed x-ray energy over several pixels and typically takes only ~20% of the absorbed 8 to 9 keV photons into account.[31] Single pixel analysis has a slightly higher spectral resolution than summed pixel analysis.[31,32] A CCD quantum efficiency of ~10% with single pixel analysis is reported in the 8 to 9 keV range for an x-ray imaging spectrometer used in the x-ray astronomical satellite Astro-E.[31] A quantum-efficiency measurement of a SI-800 camera at 8 keV revealed a value of ~5% with single-pixel analysis.[33] The same kind of chip (CCD42-40 chip, e2v technologies, Chelmsford UK) was used in the two SI cameras, one for calibration and one in this experiment. The quantum efficiency is a factor 2 lower compared to the Astro-E CCD, which is probably due to a smaller pixel size and a thinner depletion layer of the SI-800 chip.

Experimental Results

Figure 104.48 shows a copper K-shell spectrum from the target's front side for laser shot 0311271. Laser pulses with an energy of 447 J and a pulse duration ~0.7 ps were focused to an intensity of ~3 × 10^{20} W/cm^2 onto a 20-μm-thick Cu foil target. The continuum x-ray background is subtracted while the filter transmission of the 150-μm Cu foil has not yet been taken into account. The measured spectrum (dashed curve) consists of four overlapping lines. The other curves denote a fit of Gaussian line shapes to the measurement, indicating a full width at half maximum of ~220 eV for each line. The four peaks are identified as the lines of the Cu K_α (8.04 keV), He_α (8.35 keV), Ly_α (8.69 keV), and K_β (8.91 keV) transitions.[34,35] The He_α line dominates the spectrum. The observation of He_α and Ly_α is distinctly different from Cu K-shell spectra observed previously with ultrashort laser pulses at lower laser intensities.[24] The appearance and intensity of the He_α and Ly_α lines depend strongly on the laser intensity, as shown in Fig. 104.49. The K-shell emission was measured with 0.7 ps pulses for

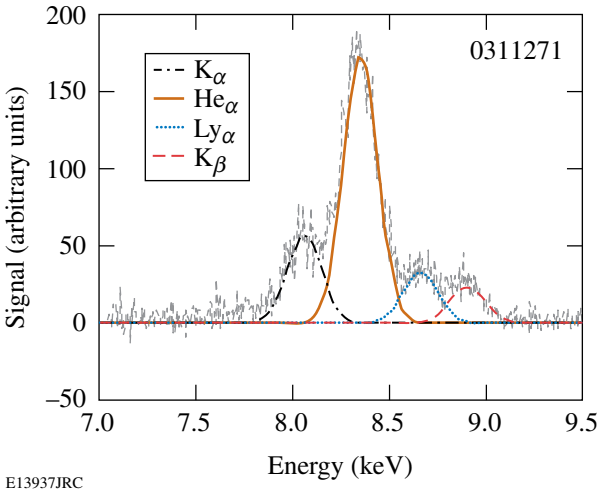

Figure 104.48
Copper K-shell spectrum from the target's front side for a laser intensity of 3×10^{20} W/cm^2 and a pulse duration of 0.7 ps and E_L = 447 J. The gray curve denotes the measurement while the other curves are Gaussian fits to the various emission lines. The He$_\alpha$ resonance line of helium-like copper ion dominates the spectrum.

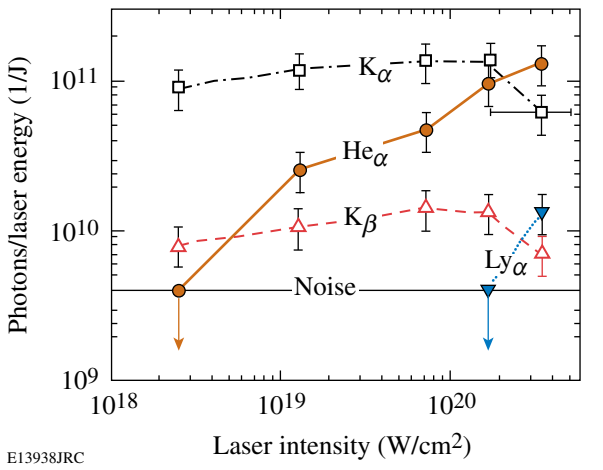

Figure 104.49
Integral x-ray photon number normalized to the laser energy contained in the central laser spot as a function of the laser intensity for Cu K$_\alpha$ (open squares), He$_\alpha$ (solid dots), K$_\beta$ (open triangles), and Ly$_\alpha$ (solid inverted triangles). Square Cu foils with thicknesses of 20 μm and 30 μm and areas ranging from 500×500 μm^2 through 2000×2000 μm^2 were used. The intensity was varied by the focal spot (10 to 100 μm) and the beam energy (~200 to ~500 J) while keeping the pulse duration constant at 0.7 ps. The apparent threshold of Ly$_\alpha$ is 3×10^{20} W/cm^2, while only K$_\alpha$ and K$_\beta$ are observed at 2.5×10^{18} W/cm^2. A representative error bar of the laser intensity is shown for one K$_\alpha$ data point.

various laser intensities between ~2×10^{18} W/cm^2 and ~3×10^{20} W/cm^2 by varying the spot size within 10 to 100 μm and the beam energy in the range from ~200 J to ~500 J. The Ly$_\alpha$ line of hydrogen-like copper disappears below 3×10^{20} W/cm^2, while He$_\alpha$ is observed down to 1×10^{19} W/cm^2, and only K$_\alpha$ and K$_\beta$ are measured at 2.5×10^{18} W/cm^2. No measurements with 0.7-ps pulses are available between 2.5×10^{18} W/cm^2 and 1×10^{19} W/cm^2. Additional measurements in this intensity range with longer pulses (5 to 14 ps) show the He$_\alpha$ signal down to ~6×10^{17} W/cm^2. For 0.7-ps pulses, the noise level prevents the detection of He$_\alpha$ below 3×10^{18} W/cm^2, while for higher intensities it is always measured and steadily increases with laser intensity. In contrast, K$_\alpha$ and K$_\beta$ stay about constant between 2×10^{18} W/cm^2 and 1×10^{20} W/cm^2 and slightly decrease for intensities above 10^{20} W/cm^2.

The absolute number of x-ray photons in each line normalized to the laser energy contained in the central laser spot was calculated by integrating the number of hits and by taking the solid angle, filter transmission, and quantum efficiency of the CCD in single-pixel analysis mode into account. An isotropic emission into a 4π steradians solid angle is assumed. Reabsorption of the radiation inside the foil target has not been taken into account. The relative error bars are estimated to be ~30% based on the standard deviation of several measurements at the same intensity. The absolute error is estimated to be a factor of 2 based on an estimated uncertainty in the CCD quantum efficiency for single-pixel analysis.

The Cu K-shell spectrum was studied as a function of the foil thickness with the 100-TW laser facility for low-mass, small-area targets. Figure 104.50 shows the measured K$_\alpha$, He$_\alpha$, and K$_\beta$ lines for Cu foils of various thicknesses. Laser pulses with 14 ps (a) and 10 ps [(b)–(d)] durations and beam energies of ~100 J were focused to an ~10-μm spot size, providing an intensity of ~3×10^{18} W/cm^2. The thickness is indicated in each figure. The foil area was 500×500 μm^2 in (a) while it was 100×100 μm^2 in (b), (c), and (d). The ratio of K$_\alpha$ to He$_\alpha$ emission changes with thickness, and the relative helium-like emission becomes larger with thinner foils for the smaller areas. Only a limited number of spectra were sampled, however, and shot-to-shot fluctuations especially influence the He$_\alpha$ signal. The resulting x-ray photon number per laser energy is plotted semilogarithmically as a function of the foil thickness in Fig. 104.51. The cold inner-shell emission that is created mainly by suprathermal electrons traversing the foil behaves differently than the ionic line emission. The K$_\alpha$ signal is relatively independent of foil thickness. A significant decrease is observed only below 3 μm, which might be due to

several effects: (1) an increased volumetric heating might lead to a depletion of cold material and (2) an increased transfer of hot-electron energy into channels other than K_α emission for very low volume targets, notably ion acceleration,[36,37] might quench the inner-shell signal. The K_β intensity drops by a factor of ~4 from 30 μm to 20 μm, and then stays about constant with smaller thicknesses and decreases again below 3 μm. The strong decrease from 30 μm to 20 μm is probably due to the larger foil area, which is further discussed in **Resonance-Line Emission From Hot Plasmas** (p. 213). While the inner-shell x-ray photon number decreases with thinner foils, the ionic line emission seems to show an opposite trend for large thicknesses. The He_α signal first increases with diminishing thickness, peaks at 5 μm, and then decreases to its initial value at 1 μm. The relatively large scattering of the values is probably due to shot-to-shot fluctuations in the laser conditions and the focus position on the small target.

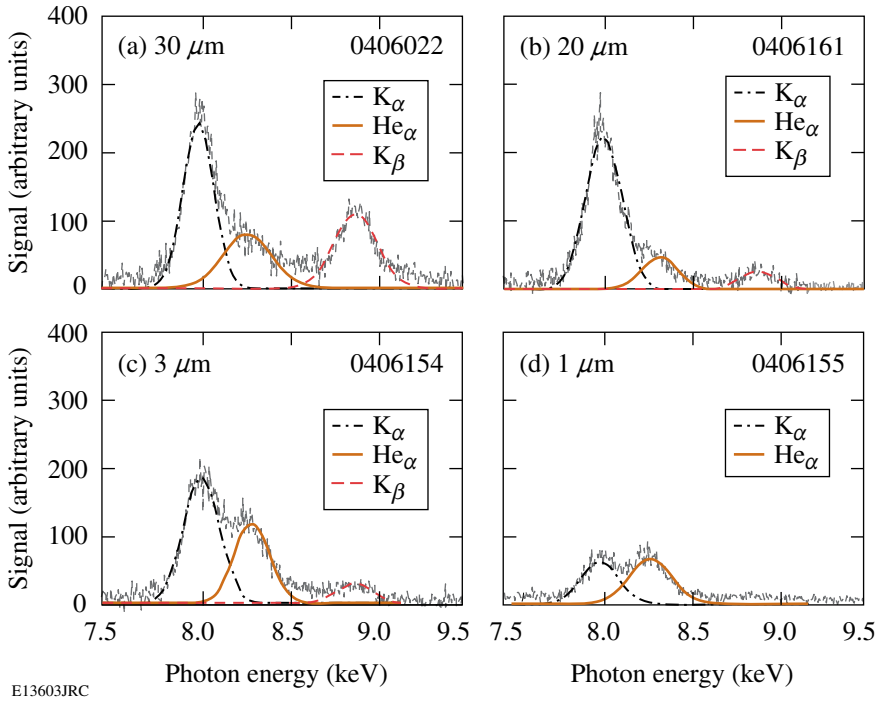

Figure 104.50
K-shell spectra showing the K_α, He_α, and K_β lines for various Cu foil thicknesses as is indicated in each figure. The foil areas were 500×500 μm^2 (a) and 100×100 μm^2 for the measurements in (b)–(d). The laser energies in (a)–(d) were 102 J, 118 J, 116 J, and 97 J, respectively. Laser pulses with 14-ps (a) and 10-ps (b)–(d) durations were focused to an ~10 μm spot, providing intensities of $\sim 3 \times 10^{18}$ W/cm^2.

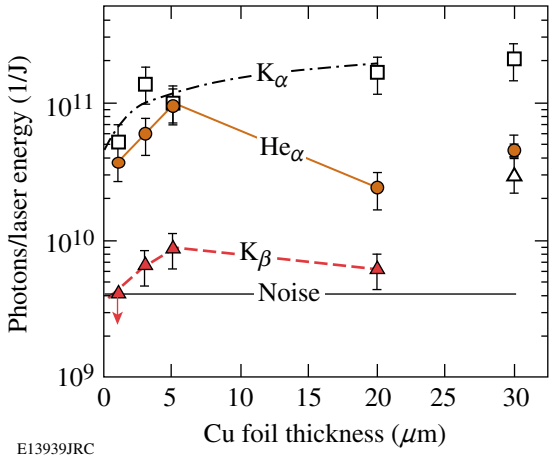

Figure 104.51
X-ray photon number per laser energy in the central laser spot versus foil thickness determined from the measured cold K_α, K_β, and the hot He_α emission. The experimental conditions are the same as in Fig. 104.50. The dash–dotted curve is a guide for the eye. The foil volume diminished from 30 μm to 20 μm by a factor of ~40 because of the smaller area. An increased volume heating probably depletes the copper M-shell population, yielding a decreased K_β signal while the K_α is not significantly affected.[55]

Evidence that the ionic emission originates from front-surface plasmas was obtained from measurements of Cu-foil targets covered with a thin layer of a different material. Figures 104.52(a)–104.52(c) show spectra at an intensity of 1.5×10^{20} W/cm^2 on copper-foil targets without a cover layer (a), with a 1-μm-thick aluminum layer (b), and with a 0.5-μm-thick tantalum layer (c). The comparison of (a) and (b) shows that the He$_\alpha$ emission is significantly reduced by a factor of ~5, while K$_\alpha$ and K$_\beta$ are diminished by a factor of ~2. The data suggest that, with the Al coating, the hot plasma is created mainly in the aluminum with relatively little heating of the copper. The reduction in K$_\alpha$ and K$_\beta$ may indicate stopping of hot electrons in the Al layer. The Ly$_\alpha$ is not observed at this laser intensity. An additional experiment, Fig. 104.52(c), at the same intensity with a 0.5-μm Ta overcoat on 20-μm Cu foil gives further evidence that the Cu He$_\alpha$ line emission originates from a thin layer on the target's front side. Beside the Cu K$_\alpha$ and a strong L-shell emission from tantalum peaking at 8.75 keV, no Cu He$_\alpha$ line at 8.35 keV is measured. The mass densities of solid tantalum and aluminum are 16.7 g/cm^3 and 2.7 g/cm^3, respectively. The factor of 6 higher mass density explains why Ta is more efficient in blocking energy transport through the surface despite half of the film thickness, leading to plasma temperature at the Ta–Cu boundary that is not sufficient to generate He-like Cu ions.

It is interesting to compare the result from copper (Z = 29) to the K-shell emission of a target material with a much higher atomic number. Figure 104.53 shows the result of an experiment with a 50-μm-thick silver foil target (Z = 47) at ~2×10^{20} W/cm^2. Only the inner-shell emission (but no He$_\alpha$ and Ly$_\alpha$ lines) is observed for the higher-Z target. This indicates that the temperature is not high enough to create He- and H-like silver ions, which require estimated electron temperatures above ~50 keV.[38]

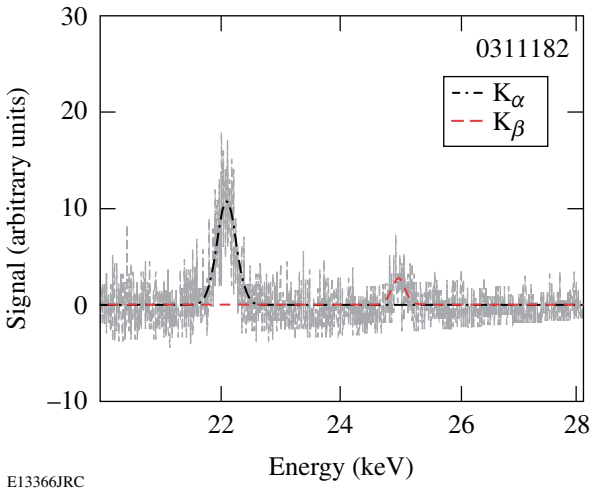

Figure 104.53
Measurement of the silver K-shell emission from a 50-μm-thick Ag-foil target. The laser energy, pulse duration, and intensity were 275 J, 0.7 ps, and ~2×10^{20} W/cm^2, respectively. Only K$_\alpha$ and K$_\beta$ inner-shell emission lines are measured, but not the ionic line emission.

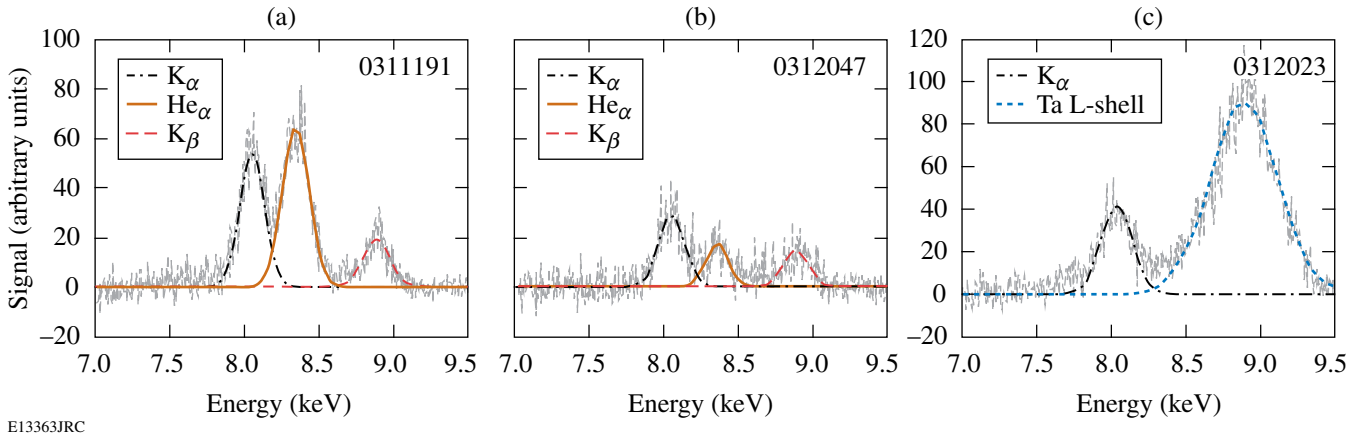

Figure 104.52
Copper K-shell spectra with the target's front side covered with a thin layer of different materials that leads to a suppression of the ionic line emission. (a) is without a cover layer, while (b) and (c) denote the results with a 1-μm-thick aluminum and with a 0.5-μm-thick tantalum layer, respectively. The He$_\alpha$ line emission is strongly reduced (b) and even absent (c) compared to the no cover layer (a), indicating that the hot plasma is generated in a thin layer on the target's front side. The laser energies, pulse duration, and intensity were 254 J (a), 227 J (b), 227 J (c), 0.7 ps, and ~1.5×10^{20} W/cm^2.

Analysis and Discussion

Two emission processes occur in these experiments: inner-shell emission and resonance-line emission. The K_α and K_β lines are emitted by inner-shell transitions when an L- or M-shell electron fills a vacancy in the K-shell, and the corresponding excess energy is radiated away by a photon in competition with Auger decay. X rays and energetic electrons may both produce inner-shell vacancies, assuming that the radiation has sufficient energy to excite above the K-edge (for Cu $h\nu > 9$ keV). Indirect inner-shell emission due to absorption of continuous x-ray radiation that is produced while suprathermal electrons decelerate in the target is, however, relatively negligible for elements with an atomic number <30.[39] Energetic electrons are the main contribution to K_α and K_β production in a high-intensity, ultrashort, laser–solid interactions with low- and mid-Z materials.[22,24] In contrast, the He_α and Ly_α lines are electronic transitions from the first excited to the ground level in the helium-like and hydrogen-like ions. Sufficient thermal plasma temperatures are required to generate these highly stripped ions. While the inner-shell radiation originates from the cold bulk material, the ionic lines are produced in hot plasmas, which is depicted in a schematic in Fig. 104.54. Resonance-line emission originates from a hot plasma on the laser target side while fast electrons generated by the laser–plasma interaction propagate into the cold bulk and produce the inner-shell emission.

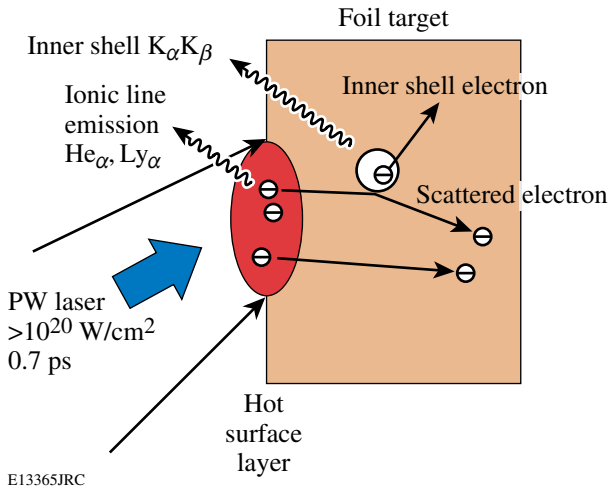

Figure 104.54
Schematic representation of the resonance and inner-shell emission generation process. The ionic lines stem from a hot surface layer while fast electrons produce the inner-shell emission.

1. Resonance-Line Emission From Hot Plasmas

Calculations with the commercially available *PrismSPECT* program[40] were performed to estimate the plasma conditions that lead to the ionic resonance-line emission from the hot plasma. *PrismSPECT* is a collisional-radiative code that takes all the necessary details of the excitation and de-excitation paths, opacity, and atomic physics into account. The plasmas are assumed to be in steady state, in nonlocal thermodynamic equilibrium conditions in slab geometry with a specified thickness, and have a homogeneous density and electron temperature. Time-dependent collisional-radiative calculations of the ionization dynamics of solid-density aluminum plasmas at $T_e = 1$ keV show that steady-state conditions are established within ~0.5 ps.[41] Similar time-dependant calculations performed for $T_e = 1$ keV and $n_e = 10^{23}$ cm^{-3} show the Cu plasma reaching steady state within ~1 ps.[42] Steady state is therefore a reasonable assumption for near-solid-density plasmas in our experiment. Suprathermal electrons were not included in the calculation. This assumption is supported by calculations of the charge-state distribution of a 1-keV, 10^{23} cm^{-3} Cu plasma including the ionization effect of a hot-electron component. The charge-state distribution is essentially given by the thermal plasma, and up to a fraction of 10% of hot electrons with an average energy of 3 MeV has no significant influence.[42] The overcoat measurements (Fig. 104.52) show that the hot plasma is formed from a layer that has initially $t \approx 1$-μm thickness at solid density. Figure 104.55(a) shows a comparison for the experimentally measured ionic K-shell emission for shot 0311271 (solid square symbols) to calculations for an electron density of $n_e = 2.3 \times 10^{24}$ cm^{-3}, $t = 1$ μm, and various electron temperatures between 1 keV and 3 keV. The electron density corresponds to a solid density of $n_{ion} = 8.5 \times 10^{22}$ cm^{-3} and an average degree of ionization of 27. The K_α and K_β lines are suppressed to allow a better comparison of the resonance-line emission to the calculations. The filter transmission of the 150-μm Cu foil was taken into account, and the calculated spectra were convolved with an instrumental resolution of 200 eV. The *PrismSPECT* calculation reveals that the measured He_α peak is a complicated array of lines including the He_α line, the intercombination line, dipole forbidden lines, and lithium-like ion satellite lines that merge together. The effective line width of this feature is ~90 eV at solid density and explains the slightly larger measured spectral width of ~220 eV for He_α. The ratio of the He_α and Ly_α lines is sensitive to the temperature and a good agreement is obtained for an electron temperature of 1.8 keV.

The ASE laser pulse pedestal causes some ablation of the front layer before the main laser pulse impinges on the target.

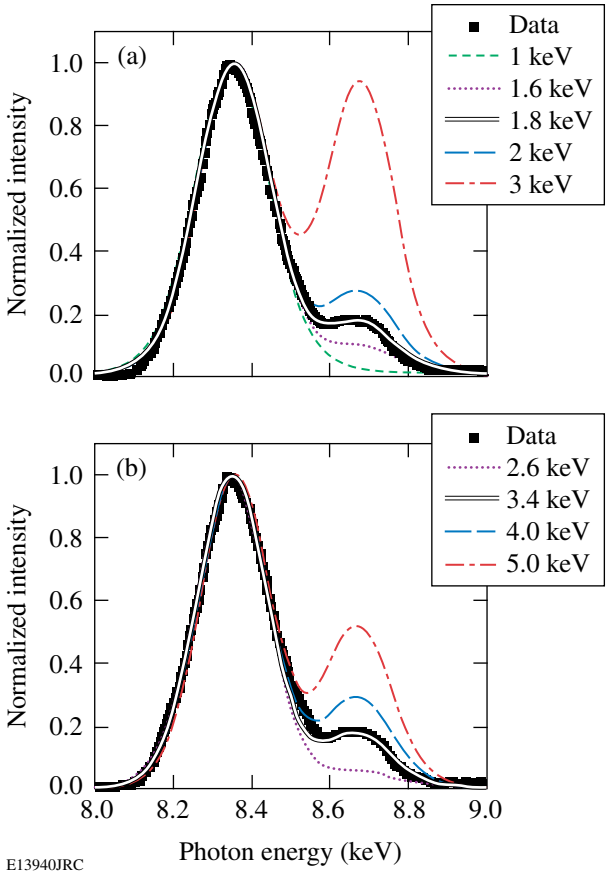

Figure 104.55
Comparison of the experimentally measured ionic K-shell emission (solid square symbols) to calculations with the computer program *PrismSPECT*[40] for (a) solid-density ($n_e \approx 2.3 \times 10^{24}$ cm^{-3}) 1-μm-thick plasma slab, and various electron temperatures between 1 keV and 3 keV. Figure (b) shows a comparison for an electron density of 2.3×10^{23} cm^{-3}, plasma slab thickness of 1 μm, and various electron temperatures between 2.6 keV and 5 keV.

The main pulse then interacts with less than solid density plasma and an increased density scale length. The density profile depends on the laser contrast, pulse profile, and hydrodynamic expansion of the preplasma. To model the density profile generated by the ASE pulse, a two-dimensional hydrodynamic simulation of the expansion and structure of the preplasma was performed using the Eulerian code POLLUX.[43] A 2.5×10^{13} W/cm^2 Gaussian temporal pulse shape was assumed with a 1.5-ns pulse duration. In the radial direction, a Gaussian-shaped intensity profile with a FWHM of 7 μm was used for the simulation. Figure 104.56 shows a lineout of the calculated electron-density profile along the target normal at the peak of the interaction pulse. The critical density expanded ~2 μm from the original surface. The interaction of the main pulse with relativistic intensities and the corresponding electron mass increase leads to a higher critical density than in the nonrelativistic case. A distance of ~1 μm is then calculated for the relativistic corrected critical density. The distance from the original target surface to the 10^{19} cm^{-3} contour is ~45 μm, which agrees well with the shadowgraph measurements. Preplasma formation on the Vulcan 100-TW laser has been previously experimentally and theoretically investigated.[37,44] Density scale lengths of ~3 μm and ~10 μm were determined at the critical density and at one-tenth of the critical density, respectively.

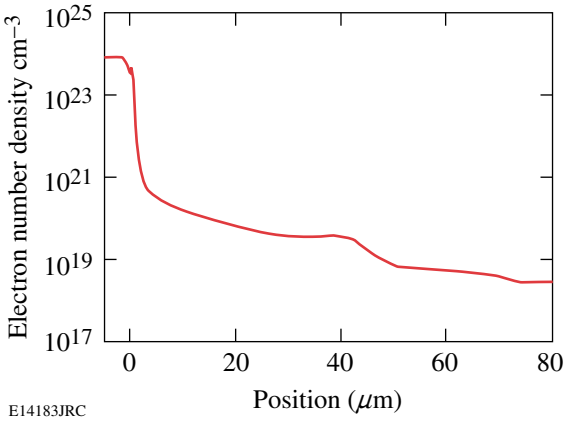

Figure 104.56
Calculated electron density profile along the target normal that is generated by an ASE prepulse; see text for details. The 2-D Eulerian code POLLUX[43] was used for the simulation.

The density profile shows that the ablated mass below critical density is a factor of ~10 smaller compared to the 1-μm layer from critical density up to solid density. Accordingly, the number of ionic line emitters in the ablation plume is negligible compared to the emitter number above critical density where most of the absorbed laser energy is deposited. Thermal energy transport into the target is estimated to be several microns deep with close to solid density based on the overcoating experiments. Figure 104.55(b) shows a comparison of measured and calculated spectra for $n_e = 2.3 \times 10^{23}$ cm^{-3}, $t = 1$ μm, and various temperatures with the best agreement at $T_e = 3.4$ keV. Not shown is the comparison for $n_e = 2.3 \times 10^{23}$ cm^{-3} and $t = 10$ μm, yielding $T_e = 2.6$ keV, which has roughly the same emitter number as the solid density, $t = 1$ μm calculation. Opacity effects in the blowoff plasma are negligible because of the low concentration of He- and H-like ions. The electron temperature is thus estimated to be in the range of 2 to 3 keV for a close-to-solid-density plasma and slab thickness between 1 and 10 μm. The number is in agreement with highly resolved Cu K-shell spectral measurements performed at similar experimental conditions yielding a front side electron temperature of ~2 keV.[45]

Two-dimensional opacity effects and heating of the underdense plasma by the short interaction pulse were not considered. Optical-field-ionized He- and H-like ion generation in the underdense plasma along the laser channel is negligible. Using a simple over-the-barrier suppression calculation for electric field ionization,[46] estimated saturation intensities of 2×10^{20} W/cm^2 and 7×10^{22} W/cm^2 are required to produce helium- and hydrogen-like copper ions with an ionization probability close to unity. The creation of He-like Cu ions by field ionization is therefore possible only at the highest accessible laser intensity. Ponderomotively accelerated electrons and ions in a radial direction[37] that might modify the charge-state distribution of the plasma as well as velocity gradients because of the tight-focusing condition and the resulting spherical expansion geometry that might affect the opacity[47] were not included in the analysis.

A precise comparison between the measured absolute He_α and Ly_α photon numbers and the predicted numbers by *PrismSPECT* are not straightforward and out of the scope of this article. A detailed knowledge of the angular emission characteristic, source area, and temporal emission characteristic is required. Laser plasmas are highly transient with strong spatial gradients in density and temperature, and a comparison to the measurement requires detailed multidimensional hydrodynamic simulations coupled to a multidimensional, time-dependent radiation transport model. An estimate of the source area may be obtained from measurements of Cu K_α images, typically yielding an area of 50 to 100 μm FWHM in diameter,[12,24] and from Ni Ly_α imaging measurements with ~30 μm spots that were obtained under similar experimental conditions.[48] Town *et al*., recently reported on simulations to calculate K_α images under similar experimental conditions and obtained agreement with measured K_α spot sizes.[49] Assuming an isotropic He_α and Ly_α emission and neglecting multidimensional and time-dependent opacity effects, the comparison of measured photon numbers and steady-state calculations for a solid-density, $t = 1$ μm surface layer plasma suggests average emission times of several picoseconds.

The increase in He_α emission with a laser intensity above 10^{18} W/cm^2 shown in Fig. 104.49 shows an energy transport growing with intensity into the solid-density plasma where electron–ion collisions create the ions in the hot-plasma environment. An enhanced energy transport into the solid results in higher temperatures and a larger fraction of He-and H-like Cu ions in the hot surface plasma. The absorption of the laser energy takes place in the density range close to the critical density and is dominated by collisionless absorption mechanisms that produce electrons with quasi-Maxwellian energy spectra and temperatures from hundreds of keV to several MeV for all intensities discussed here.[50] The angular distribution is generally into the target. The electron source parameters vary with the local intensity and therefore also have a spatial pattern related to the laser focal-spot intensity pattern. Energy transport by these electrons is highly complicated and, up to now, not fully understood. Their binary collision range is generally much greater than the thin layer, which is strongly heated. Several processes may contribute to localizing energy deposition in a surface layer. Simple ohmic potential due to the cold electron return current can limit electron penetration, as discussed by Bell *et al*.[19] Electrons can be trapped at the surface by their small Larmor radius in the surface region azimuthal thermoelectric B field generated by the axial increase of density and radial decrease of temperature (dB/dt scaling as $\nabla N \times \nabla T$), with the axial ambipolar electric field in the blowoff plasma causing a rapid radial drift (scaling as $E \times B$). This effect, well known from nanosecond experiments, particularly with CO_2 lasers, has been discussed in connection with petawatt-class, short-pulse experiments by Stephens *et al*.[12] and modeled recently by Mason *et al*.[51] Three-dimensional PIC simulations by Sentoku *et al*.,[16] have shown that there can be very strong collisionless energy deposition in a thin surface layer attributable to the "ohmic" heating effect of the return current due to anomalous resistivity induced by the scattering of the return current electrons on microscopic clumps of the B field generated by collisionless Weibel and two-stream instability. There is also evidence in PIC modeling by Adam *et al*.[52] and Ruhl[53] that the strongest filamentation occurs in a thin surface layer. These processes may all contribute to the observed thin, high-temperature layer, but further work is needed to establish their relative importance.

The energy required to create a significant amount of He-like and H-like Cu ions is estimated by assuming the mass of the hot layer to be equivalent to an ~1-μm-thick layer at solid density, as determined from the overcoat experiments. For example, an energy of ~3.5 J is needed to heat a mass of solid copper contained in a disk with a 50-μm diam and 1-μm thickness to ~3 keV and the resulting average charge state of 27. This is small compared to laser energies of the order of 100 J.

It should be noted that the spectral measurements indicate that K_α and He_α are two distinctive lines with no significant continuum merged between them. This is supported by highly resolved measurements with a crystal spectrograph under similar experimental conditions.[54] The upshift of K_α emission from partially ionized Cu ions has been discussed by Gregori

et al.[54] There is a small spectral shift as M-shell electrons are removed because of the heating of the bulk of the target by binary collisions of hot electrons and ohmic heating by the return current. It is indistinguishable in our low-resolution K_α spectra. Removal of L-shell electrons at higher temperatures gives larger shifts as the hot layer is heated and emission occurs at each stage of ionization. The He-like ion is, however, present over a wide temperature range and, in particular, during the emission occurring after the initial heating, leading to a dominant He_α spectral feature in our spectra. This heating partially ionizes the bulk, resulting in a K_α emission shifted to higher energies.

Measurements of the K-shell emission as a function of foil thickness between 30 μm and 1 μm for a constant laser intensity of ~3×10^{18} W/cm^2 show that the K_α emission remains about constant with diminishing foil thicknesses down to 3 μm. This is expected if no other hot-electron energy-loss mechanisms become significant; the electron temperature of the foil is so low that ionization does not significantly affect the L-shell, and the majority of the electrons are refluxing from an electrostatic sheath field. The decreasing yield for targets thinner than 3 μm might imply that a significant amount of cold material is depleted. Another possible explanation is that, for very small volume targets, additional energy dissipation channels draining hot-electron energy might become important and influence the K_α signal. A possible channel is energy transfer into accelerated ions, which is enhanced in very thin targets.[36] The K_β yield is expected to be more sensitive to a temperature increase of the bulk of the target since K_β is eliminated when the M-shell is ionized, which might explain the decrease by factor of ~4 from 30 μm to 20 μm while no change is measured for K_α. The target volume changed by a factor of ~40 because a 500×500 μm^2 foil area was used at 30-μm thickness while 100×100 μm^2 was applied for the thinner targets. R. Snavely *et al.*, recently reported on similar observations and extensively discussed how the laser heating of very small target volumes affects the inner-shell emission.[55] The resonance-line emission from the 1-μm top layer is not expected to be significantly affected by the foil thickness. Nevertheless, varying He_α emission is observed with a peak at 5-μm thickness. This variability may be due to slight changes in the laser conditions from shot to shot. As shown in the measurement in Fig. 104.49, the He_α signal is more sensitive to the applied laser intensity than is the inner-shell emission.

2. Inner-Shell Emission

Implicit-hybrid PIC simulations with the code *LSP*[56] were performed to study inner-shell production with various foil areas in the range from 500×500 μm^2 to 100×100 μm^2 and thicknesses of 20 μm to 5 μm, similar to the simulations recently reported by R. Town.[49] No significant change of K_α yield with the target area and thickness is calculated, which is attributed to the refluxing of most of the hot electrons at the target boundaries.[36] These calculations have solved the Maxwell equations coupled with the equations of motion for multiple particle species in a two-dimensional cylindrical geometry. The initially cold ions and bulk electrons of the target were modeled with fluid equations, and the hot laser-produced electrons were treated kinetically. The propagation and interaction of the high-intensity laser was not included, rather, the hot electrons were introduced into the calculation in an *ad hoc* manner by converting or "promoting" bulk electrons within a skin depth on the front of the target into the kinetic species. The kinetic electrons were given an isotropic Gaussian distribution in momentum space with a temperature that was determined by the ponderomotive potential of the local laser intensity.[13] The local conversion rate was determined by assuming a 10% coupling efficiency from the local incident laser power into hot electrons. The laser spot shape was taken to be the same as in the experiment, both spatially and temporally. Although the heating of the target was modeled, the ionization of the target material was ignored.

The measured K_α photon numbers, per unit laser energy, are in general agreement with other experiments.[20,24] In Ref. 20, 2×10^{11}/J K_α photons were reported for 8-μm-thick Cu foil targets irradiated with 528-nm laser pulses at intensities of ~10^{19} W/cm^2. Similar numbers were reported in Ref. 24; however, these experiments used thick targets where the reabsorption of the K_α photons was strong, and the controlling mechanism was the interplay between electron-penetration depth relative to the K_α photon-attenuation length. With the targets considered here, reabsorption gives a modest correction; e.g., for solid copper, the transmission fraction f_{trans} is estimated to be 0.91, 0.69, and 0.58 for foil thicknesses of d = 5, 20, and 30 μm respectively.

The expected number of photons generated N_k can be computed by integrating along the path of electrons whose initial energies are described by an energy distribution $f(E_0)$ so long

as the electron stays within the material, its energy loss is accurately described with a continuous slowing down formula (dE/ds), and that cold cross sections σ_k for K-shell ionization are appropriate (note that for copper, only direct K-shell ionization is significant[39]). The yield N_k is then given by

$$N_k = N_e \int_0^\infty dE_0 f(E_0) \int_{E_0}^0 dE \omega_k n_{Cu} \sigma_k \left(\frac{dE}{ds}\right)^{-1}, \quad (1) \text{ and } (2)$$

$$= N_e \int_0^\infty dE_0 f(E_0) \int_0^{s(E_0)} ds \omega_k n_{Cu} \sigma_k,$$

where N_e is the total number of hot electrons, $\omega_k = 0.425$ is the fluorescence yield, and n_{Cu} is the number density of copper atoms in the target. From this model the electron-to-K_α photon-generation efficiency $\eta_{e\to k}$ is determined. This efficiency is defined according to $E_k = \eta_{e\to k} E_e$, where the energy in the electrons is given by $E_e = N_e \int Ef(E)dE$ and in K_α photons by $E_k = \varepsilon_k N_k$ with ε_k being the fluorescence energy (8.05 keV for copper K_α). This simple model accounts only for the collisional energy loss and neglects ohmic effects and energy transfer to fast ions.

A direct comparison between the experimental production efficiency (yield/laser energy) and the calculated generation efficiency is not straightforward. The experimentally observable quantity is $N_{k,\mathrm{obs}}$ from which the efficiency may be computed as

$$\eta_{e\to k} = \frac{\varepsilon_k \left(N_{k,\mathrm{obs}} / f_{\mathrm{trans}}\right)}{E_L} \frac{1}{\eta_{L\to e}} \quad (3)$$

only if the transmission fraction and the hot-electron production efficiency $\eta_{L\to e} = E_e/E_L$ are known. Here, E_L is the energy in the laser pulse. The transmission fraction can be easily computed, but the electron-production efficiency is uncertain. Assuming that the hot-electron density within the foil is uniform, the K_α photon transmission fraction is estimated by $f_{\mathrm{trans}} = \left(L_a/d\right)\left[1 - \exp\left(-d/L_a\right)\right]$ with the attenuation length L_a = 25 μm. The predicted efficiency, obtained using Eq. (1), further requires specification of the hot-electron spectrum $f(E)$.

The predicted total K_α energy of the model divided by the laser energy, together with experimental data, are shown in Fig. 104.57 for different $\eta_{L\to e}$ assuming exponentially distributed electron energies, $f(E)dE = \left(1/T\right)/\exp\left(-E/T\right)dE$, and using slowing down and cross section data from the ITS code.[57] The total K-shell ionization cross section is from Ref. 58 and, unlike the cross section in Ref. 39, it is valid for relativistic electron energies. For highly relativistic electrons, the cross section increases with particle energy. In Ref. 59, an increased K_α yield was measured with laser intensities above 10^{19} W/cm^2 and attributed to an enhanced K-shell ionization cross section for relativistic electrons. In contrast to this work, an increase in the K_α yield with the laser intensity is not observed. Calculations have also been performed with a 3-D relativistic distribution function, leading to slightly higher predicted efficiencies, but with no change to our overall conclusions. Although different intensity temperature scaling appears in the literature,[29,60] in Fig. 104.57 we have chosen the ponderomotive scaling of Wilks,[13,61]

$$T_{\mathrm{MeV}} = 0.511\left[\left(1 + I_{18}\lambda_{\mu\mathrm{m}}^2 / 1.37\right)^{1/2} - 1\right],$$

to connect the laser intensity to the hot-electron temperature. No spatial-laser intensity distribution was taken into account in this calculation.

In Fig. 104.57, the experimental data is almost independent of laser intensity, except at the highest laser intensity, $I = \sim 3 \times 10^{20}$ W/cm^2. This independence of efficiency on hot-electron temperature, over the experimental range of intensities, is a consequence of Eq. (1), displayed by the solid model curves. The efficiency is determined by the relative importance of energy loss due to nonionizing collisions and the cross section for K-shell ionization. The latter is quite flat for energies above 100 keV,[62] while the collisional cross section drops with increasing energy. The electron range is not restricted by the target thickness for the solid curve in order to mimic the effect of electron refluxing. The net result is that the number of photons produced per unit electron energy is only a weakly increasing function. The solid curves can be made to agree quantitatively with the experimental data if we select an ~8% hot-electron coupling efficiency. This is lower than the $\eta_{L\to e}$ ~ (20% to 40%) usually quoted in the literature for these intensities, e.g., in Ref. 4 (upper solid curve). Given the relative large uncertainty in the experimental points because of the CCD calibration uncertainty, the current measurement is in rough agreement with the previous measurements. In addition, the calculated 8% hot-electron coupling efficiency should be regarded as a lower bound because fast-electron energy loss into other channels, such as energy transfer into fast ions and ohmic effects, were not included in the model. Accounting for additional losses would shift the theoretical curves downward, leading to a higher $\eta_{L\to e}$ for the measurement.

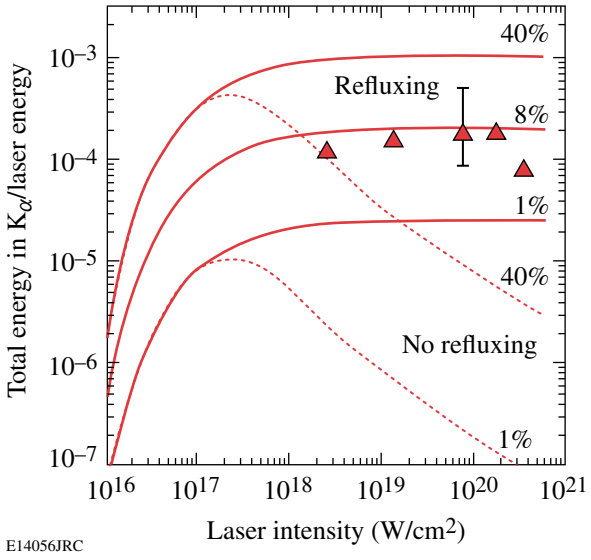

Figure 104.57
Total energy in K_α photons normalized to laser energy in the central laser spot as a function of laser intensity. The solid triangles are the experimental data points. The solid curves correspond to the model described in **Inner-Shell Emission** (p. 216) with perfect confinement of the hot electrons (refluxing) and with a hot-electron conversion efficiency of 40%, 8%, and 1%. The dotted curves correspond to the case (40% and 1%) with no refluxing, as described in the text. An 8% hot-electron coupling efficiency is calculated, which should be regarded as a lower bound because fast-electron energy loss into other channels, such as energy transfer into fast ions and ohmic effects, were not included in the model. A representative error bar shows the measured efficiency uncertainty.

The dotted curves illustrate the effect of truncating the electron path length s in the integral, Eq. (2), whenever it exceeds the target thickness $s(E_0) \rightarrow \min[s(E_0), d]$. Electrons in Cu have ranges from ~1 μm to ~700 μm for energies from 10 keV to 1 MeV.[57] Only a small fraction of the fastest electrons can escape out the foil, resulting in quickly charging up the target and confining the rest of the electrons that are reflected back from surface sheath fields. Refluxing has previously been discussed in the context of proton generation, showing the importance of the recirculation of the MeV electrons on the electrostatic fields that accelerate protons to multi-MeV energies.[36] As expected, ignoring refluxing in the model shows disagreement with the experimental data by an order of magnitude or more. Physically, the solid curves correspond to the case where hot electrons are confined within the target due to reflection or "refluxing" from surface sheath fields until it is stopped, whereas the dashed curves correspond to the case where the electron and its energy are lost as soon as its path length equals the target thickness. Refluxing has been observed in PIC calculations, leading to a yield that is independent of target volume.

The fact that the experimental efficiencies are lower than might be expected based on the simple refluxing model presented here might have several causes: refluxing might not be perfect. With a significant loss fraction, the range of the electrons might be overestimated (which leads to higher efficiencies) due to "anomalous" stopping mechanisms related to large, self-generated magnetic and electric field fluctuations, presumably becoming more important at higher intensities.[16] Target heating might invalidate the use of the cold cross sections.

Summary and Conclusions

For the first time, He_α and Ly_α lines in the K-shell emission of solid Cu targets irradiated with a 0.7-ps petawatt laser beam were observed at intensities >10^{20} W/cm^2. This is attributed to the formation of a ~2 to 3 keV near-solid-density hot plasma on the laser irradiation target side. A suppression of the ionic line emission is observed when the Cu targets are coated with either a 1-μm thin layer of aluminum or with a 0.5-μm tantalum layer, indicating that the strongest heating is confined to a thin layer.

Measurements of the K-shell emission as a function of foil thickness between 30 μm and 1 μm for a constant laser intensity of ~3×10^{18} W/cm^2 and ~10-ps pulses show that the He_α emission varies by a factor of ~4 with a peak at 5-μm thickness, while the K_α yield stays about constant. A decreased K_α yield measured for targets thinner than 3 μm might be explained by a stronger heating of the small target volume and an increased hot-electron energy transfer into ions. Changing laser conditions especially affecting the surface layer could cause the variation of the He_α emission. The current data set is limited by its small sample size, and more shots are necessary to investigate this observation.

The K-shell emission of solid Cu foil targets was studied as a function of laser intensity between 2×10^{18} W/cm^2 up to 3×10^{20} W/cm^2 in low-area (~0.5×0.5 to 2×2 mm^2) thin foils (~20 to 30 μm) and 0.7-ps pulses. The yield of the ionic lines strongly increases with laser intensity such that, at the maximum intensity, the spectrum is dominated by the He_α emission. An approximately constant yield of ~1×10^{11} photons/J and ~1×10^{10} photons/J were measured for the K_α and K_β inner-shell emission, respectively, between intensities of 2×10^{18} W/cm^2 and 1×10^{20} W/cm^2. Above 1×10^{20} W/cm^2, the inner-shell emission yield drops. A comparison of the measured intensity scaling of the K_α yield with a model shows that refluxing of suprathermal electrons and their confinement in the target volume is crucial to explain these results. Calculations that ignore refluxing show a strongly decreasing K_α yield with

laser intensity and disagree with the experimental data by more than an order of magnitude.

ACKNOWLEDGMENT

This work was supported by the U.S. Department of Energy Office of Inertial Confinement Fusion under Cooperative Agreement No. DE-FC52-92SF19460, the University of Rochester, the New York State Energy Research and Development Authority, and the University of California Lawrence Livermore National Laboratory under contract No. W-7405-Eng-48 UCRL_PRES213395. The support of DOE does not constitute an endorsement by DOE of the views expressed in this article.

REFERENCES

1. M. Tabak *et al*., Phys. Plasmas **1**, 1626 (1994).
2. O. L. Landen *et al*., Rev. Sci. Instrum. **72**, 627 (2001).
3. H.-S. Park *et al*., Rev. Sci. Instrum. **75**, 4048 (2004).
4. K. B. Wharton *et al*., Phys. Rev. Lett. **81**, 822 (1998).
5. S. P. Hatchett *et al*., Phys. Plasmas **7**, 2076 (2000).
6. K. Yasuike *et al*., Rev. Sci. Instrum. **72**, 1236 (2001).
7. R. Kodama *et al*., Phys. Plasmas **8**, 2268 (2001).
8. M. H. Key, M. D. Cable, T. E. Cowan, K. G. Estabrook, B. A. Hammel, S. P. Hatchett, E. A. Henry, D. E. Hinkel, J. D. Kilkenny, J. A. Koch, W. L. Kruer, A. B. Langdon, B. F. Lasinski, R. W. Lee, B. J. MacGowan, A. MacKinnon, J. D. Moody, M. J. Moran, A. A. Offenberger, D. M. Pennington, M. D. Perry, T. J. Phillips, T. C. Sangster, M. S. Singh, M. A. Stoyer, M. Tabak, G. L. Tietbohl, M. Tsukamoto, K. Wharton, and S. C. Wilks, Phys. Plasmas **5**, 1966 (1998).
9. P. A. Norreys *et al*., Phys. Plasmas **6**, 2150 (1999).
10. K. A. Tanaka *et al*., Phys. Plasmas **7**, 2014 (2000).
11. J. A. Koch *et al*., Phys. Rev. E **65**, 016410 (2001).
12. R. B. Stephens *et al*., Phys. Rev. E **69**, 066414 (2004).
13. S. C. Wilks *et al*., Phys. Rev. Lett. **69**, 1383 (1992).
14. B. F. Lasinski *et al*., Phys. Plasmas **6**, 2041 (1999).
15. L. Gremillet, G. Bonnaud, and F. Amiranoff, Phys. Plasmas **9**, 941 (2002).
16. Y. Sentoku *et al*., Phys. Rev. Lett. **90**, 155001 (2003).
17. A. R. Bell and R. J. Kingham, Phys. Rev. Lett. **91**, 035003 (2003).
18. A. J. Kemp *et al*., Phys. Plasmas **11**, L69 (2004).
19. A. R. Bell *et al*., Plasma Phys. Control. Fusion **39**, 653 (1997).
20. T. Feurer *et al*., Phys. Rev. E **56**, 4608 (1997).
21. R. Kodama *et al*., Nature **432**, 1005 (2004).
22. H. Chen, B. Soom, B. Yaakobi, S. Uchida, and D. D. Meyerhofer, Phys. Rev. Lett. **70**, 3431 (1993).
23. A. Rousse *et al*., Phys. Rev. E **50**, 2200 (1994).
24. D. C. Eder *et al*., Appl. Phys. B **70**, 211 (2000).
25. H. R. Griem, *Spectral Line Broadening by Plasmas* (Academic Press, New York, 1974).
26. J. L. Collier *et al*., *Central Laser Facility Annual Report 2002/2003*, 168, Rutherford Appleton Laboratory, Chilton, Didcot, Oxon, England, RAL Report No. RAP-TR-2003-018 (2003).
27. C. N. Danson *et al*., J. Mod. Opt. **45**, 1653 (1998).
28. P. K. Patel, M. H. Key, A. J. Mackinnon, H.-S. Park, R. Shepherd, H. Chen, R. A. Snavely, N. Izumi, J. Kuba, J. Koch, S. C. Wilks, M. May, R. Van Maren, J. A. King, B. Zhang, K. Akli, R. Freeman, S. Kar, L. Romagnani, M. Borghesi, C. Stoeckl, W. Theobald, R. Eagleton, M. Mead, R. J. Clarke, R. Heathcote, P. A. Brummitt, D. R. Neville, D. Neely, and R. Stephens, *Central Laser Facility Annual Report 2003/2004*, 34, Rutherford Appleton Laboratory, Chilton, Didcot, Oxon, England, RAL Report No. RAL-TR-2004-025 (2004).
29. F. N. Beg *et al*., Phys. Plasmas **4**, 447 (1997).
30. C. Stoeckl, W. Theobald, T. C. Sangster, M. H. Key, P. Patel, B. B. Zhang, R. Clarke, S. Karsch, and P. Norreys, Rev. Sci. Instrum. **75**, 3705 (2004).
31. M. Nishiuchi *et al*., in *EUV, X-Ray, and Gamma-Ray Instrumentation for Astronomy IX*, edited by O. H. Siegmund and M. A. Gummin (SPIE, Bellingham, WA, 1998), Vol. 3445, pp. 268–277.
32. D. H. Lumb and A. D. Holland, Nucl. Instrum. Methods Phys. Res. A **273**, 696 (1988).
33. H.-S. Park, Lawrence Livermore National Laboratory, private communication (2005).
34. J. A. Bearden, Rev. Mod. Phys. **39**, 78 (1967).
35. R. L. Kelly, J. Phys. Chem. Ref. Data **16**, 651 (1987).
36. A. J. Mackinnion *et al*., Phys. Rev. Lett. **88**, 215006 (2002).
37. H. Habara *et al*., Phys. Rev. E **70**, 046414 (2004).
38. D. E. Post *et al*., At. Data Nucl. Data Tables **20**, 397 (1977).
39. M. Green, Solid-State Electron. **3**, 314 (1961); M. Green and V. E. Cosslett, J. Phys. D **1**, 425 (1968).
40. Prism Computational Sciences, Inc., Madison, WI, 53711.
41. J. J. MacFarlane *et al*., in *Inertial Fusion Sciences and Applications 2003*, edited by B. A. Hammel *et al*. (American Nuclear Society, La Grange Park, IL, 2004), pp. 457–460.
42. H. K. Chung, Lawrence Livermore National Laboratory, private communication (2005).
43. G. J. Pert, J. Comput. Phys. **43**, 111 (1981).

44. M. I. K. Santala *et al*., Phys. Rev. Lett. **84**, 1459 (2000).

45. M. Key *et al*., presented at the 8th International Workshop on Fast Ignition of Fusion Targets, Tarragona, Spain, 29 June–1 July 2005.

46. S. Augst, D. Strickland, D. D. Meyerhofer, S. L. Chin, and J. H. Eberly, Phys. Rev. Lett. **63**, 2212 (1989).

47. L. Labate *et al*., Phys. Plasmas **12**, 083101 (2005).

48. M. Key, Lawrence Livermore National Laboratory, private communication (2005).

49. R. P. J. Town, presented at the International Workshop on Fast Ignition and High Field Physics, Kyoto, Japan, 25–29 April 2004 (Paper P2633); R. P. J. Town, presented at the 8th International Workshop on Fast Ignition of Fusion Targets, Tarragona, Spain, 29 June–1 July 2005.

50. P. Gibbon and E. Förster, Plasma Phys. Control. Fusion **38**, 769 (1996).

51. R. J. Mason, E. S. Dodd, and B. J. Albright, Phys. Rev. E **72**, 015401(R) (2005).

52. J.-C. Adam, A. Héron, and G. Laval, presented at the International Workshop on Fast Ignition and High Field Physics (FIHFP 2004), Kyoto, Japan, 25–29 April 2004 (Paper P2630).

53. H. Ruhl *et al*., presented at the International Workshop on Fast Ignition and High Field Physics (FIHFP 2004), Kyoto, Japan, 25–29 April 2004 (Paper P2631).

54. G. Gregori *et al*., Contrib. Plasma Phys. **45**, 284 (2005).

55. R. Snavely *et al*., presented at the 8th International Workshop on Fast Ignition of Fusion Targets, Tarragona, Spain, 29 June–1 July 2005.

56. D. R. Welch *et al*., Nucl. Instrum. Methods Phys. Res. A **464**, 134 (2001).

57. M. J. Berger, in *Methods in Computational Physics: Advances in Research and Applications*, edited by B. Alder, S. Fernbach, and M. Rotenberg, Volume 1: Statistical Physics (Academic Press, New York, 1963), pp. 135–215.

58. H. Kolbenstvedt, J. Appl. Phys. **38**, 4785 (1967).

59. F. Ewald, H. Schwoerer, and R. Sauerbrey, Europhys. Lett. **60**, 710 (2002).

60. D. W. Forslund, J. M. Kindel, and K. Lee, Phys. Rev. Lett. **39**, 284 (1977).

61. G. Malka and J. L. Miquel, Phys. Rev. Lett. **77**, 75 (1996).

62. C. Hombourger, J. Phys. B **31**, 3693 (1998).

LLE's Summer High School Research Program

During the summer of 2005, 15 students from Rochester-area high schools participated in the Laboratory for Laser Energetics' Summer High School Research Program. The goal of this program is to excite a group of high school students about careers in the areas of science and technology by exposing them to research in a state-of-the-art environment. Too often, students are exposed to "research" only through classroom laboratories, which have prescribed procedures and predictable results. In LLE's summer program, the students experience many of the trials, tribulations, and rewards of scientific research. By participating in research in a real environment, the students often become more excited about careers in science and technology. In addition, LLE gains from the contributions of the many highly talented students who are attracted to the program.

The students spent most of their time working on their individual research projects with members of LLE's technical staff. The projects were related to current research activities at LLE and covered a broad range of areas of interest including computational hydrodynamics modeling, cryogenic target fabrication and characterization, liquid crystal chemistry, materials science, the development and control of laser fusion diagnostics, and OMEGA EP Laser System design and engineering (see Table 104.II).

The students attended weekly seminars on technical topics associated with LLE's research. Topics this year included laser physics, fusion, holographic optics, fiber optics, and femtosecond lasers and their applications. The students also received safety training, learned how to give scientific presentations, and were introduced to LLE's resources, especially the computational facilities.

The program culminated on 24 August with the "High School Student Summer Research Symposium," at which the students presented the results of their research to an audience including parents, teachers, and LLE staff. The students' written reports will be bound into a permanent record of their work that can be cited in scientific publications. These reports are available by contacting LLE.

One hundred ninety-one high school students have now participated in the program since it began in 1989. This year's students were selected from approximately 50 applicants.

At the symposium, LLE presented its ninth William D. Ryan Inspirational Teacher Award to Mr. Stephen Locke, a chemistry teacher at Byron-Bergen High School. This award is presented to a teacher who motivated one of the participants in LLE's Summer High School Research Program to study science, mathematics, or technology and includes a $1000 cash prize. Teachers are nominated by alumni of the summer program. Mr. Locke had the rare distinction of receiving his nomination from a whole family—Christine Balonek (2002) and her brothers Gregory, Robert, and Daniel (2004). "In the classroom, Mr. Locke's wealth of knowledge and fervor for chemistry in combination with his sense of humor, patience, and dedication to his students create an ideal teacher," Christine Balonek writes in her nomination letter. "He is never too busy to help a student during a study hall or after school with any science work. His endless devotion to students and the community is one worthy of recognition." According to her brother, Robert, "Mr. Locke not only taught the material given by the state, he also brought in real-life applications. His teaching methods brought home for me the power of science and technology." David Pescrillo, principal of Byron-Bergen High School, added, "Stephen is an excellent teacher who expects the best from his students. He is very kids-oriented. He comes in during the summer, during the weekends, and after school hours on his own time to tutor the kids who need help. He is a phenomenal guy!"

Table 104.II: High School Students and Projects—Summer 2005.

Name	High School	Supervisor	Project Title
Mary Brummond	Honeoye Falls-Lima	M. Guardalben	OMEGA EP Pulse Compressor Modeling: Misalignment and Power Errors
Philip Chang	Pittsford Sutherland	K. Marshall	Computational Modeling and Analysis of Nickel Dithiolene Structures
Brandon Corbett	Allendale Columbia	T. Collins/ R. Bahukutumbi	Optimization of High-Gain ICF Targets for the National Ignition Facility
Adam DeJager	Greece Odyssey	S. Morse/ R. Kidder	Optical Time-Domain Reflectometry on the OMEGA EP Laser
Frank Fan	Webster Schroeder	S. Craxton	A Model for Cryogenic Target Layering
Alex Grammar	Brighton	R. Boni/ P. Jaanimagi	Relative Quantum Efficiency Measurements of Streak Camera Photocathodes
Stewart Laird	Harley School	J. Knauer	Characterization of a Compound Refractive Lens
Brian MacPherson	Penfield	R. Epstein	Dynamic Energy Grouping in Multigroup Radiation Transport Calculations
Karyn Muir	Honeoye Falls-Lima	J. Lambropoulos	Micromechanics and Microstructure in WC Hard Metals
Brian Pan	Penfield	W. Seka	Improving the Illumination Uniformity of Cryogenic Targets Inside a Layering Sphere
Nicholas Ramos	Palmyra-Macedon	S. Mott/ D. Lonobile	Automated X-Ray Framing Camera Characterization
Valerie Rapson	Greece Olympia	K. Marshall	Contaminant-Resistant Sol-Gel Coatings
Martin Wegman	McQuaid	W. Donaldson	Superconducting Electronics for the ICF Environment
Lauren Weiss	Brighton	L. Elasky	Categorization and Analysis of Defects in Cryogenic Targets
Rosie Wu	Brighton	D. Edgell/ S. Craxton	Analysis of Inner Ice Surface Perturbations Using Bright Ring Characterization

FY05 Laser Facility Report

The OMEGA Facility continued to operate extended shifts during select weeks in FY05, accommodating user demand by conducting 1461 target shots (see Table 104.III). Highlights of other FY05 achievements include the following:

- The SSD, main, and "backlighter" OMEGA laser sources were converted to integrated front-end sources (IFES). The IFES replaces the existing OMEGA master oscillators (OMO's) and two pulse-shaping amplitude modulators. The IFES architecture consists of a single-frequency, continuous-wave (cw) fiber laser, a dual-amplitude modulator for pulse shaping, and a cw-pumped fiber amplifier that boosts the energy injected into OMEGA's diode-pumped regenerative amplifier. The IFES system requires significantly less maintenance, is easier to operate, requires no optical alignment, has improved pulse-shaping stability, and is much more reliable than the OMO system. The "fiducial" laser source will be converted to the IFES architecture early in FY06.

- TIM-based target positioning systems (TTPS) were utilized on a number of experimental campaigns. These instruments were developed to improve the speed and accuracy of alignment for complex targets. Previously, high-magnification x-ray imaging pinhole arrays had been mounted on the same stalk as the primary target. This configuration put the burden of alignment on target fabrication and often required several metrology iterations to establish the angle of the pinhole substrate with respect to the primary target within allowable specifications. By using separate targets, overall time spent in target fabrication, metrology, and alignment has been reduced dramatically and target positioning precision has improved.

- The planar Moving Cryostat Transfer Cart (Cart 4), was modified to accommodate cryogenic hohlraum experiments. Cart 4 is used routinely to provide cryogenic solid/liquid D_2 targets for experiments on D_2 equation of state (EOS), multiple shock timing and convergence, and Rayleigh–Taylor instability growth. These experiments directly support the National Ignition Campaign. Cryogenic gas-filled (He and H) hohlraums are part of the indirect-drive ignition point design. Cart 4 was modified to field hohlraums at temperatures appropriate for the ignition point design. The first experimental series provided valuable temperature/density data. The target design is currently being modified for experiments in FY06 to minimize the target debris associated with the thermal mass in contact with the hohlraum.

- High-yield cryogenic DT experiments are expected in early FY06 following a successful tritium readiness review in June 2005. In anticipation of these experiments, a number of new high-yield diagnostic systems have been (or are being) implemented on OMEGA. These include the 12-m nTOF (neutron time-of-flight diagnostic 12 m from target chamber center), a chemical vapor deposition (CVD) diamond detector for bang time, a light-pipe–based neutron temporal diagnostic for reaction history and γ-ray bang time, a permanent neutron imaging capability, and a magnetic recoil spectrometer for neutron spectroscopy and areal density. The full implementation of this new instrumentation suite should be completed in FY06 and will give the facility diagnostic capabilities for high-yield DT implosions comparable to those for the lower yield standard D_2 implosions.

- A continuously pumped centralized vacuum system for OMEGA's harmonic energy detector (HED) vacuum tubes was designed and installed. This system significantly increases the flexibility to refurbish and perform maintenance on the vacuum tubes, ensuring operational readiness. Approximately one-sixth of OMEGA is outfitted with the modified tube design, with the remainder to be installed in FY06.

- The east wall of the OMEGA Target Bay was modified to support transport of the OMEGA EP beams to the OMEGA target chamber. OMEGA Facility modifications planned for FY06 include the installation of OMEGA EP beam transport into OMEGA target chamber port H9 and the installation of the off-axis parabola inserter on port H7. This installation will remove the GMXI diagnostic from port H9 and TIM-2 from port H7.

Table 104:III: The OMEGA target shot summary for FY05.

Laboratory	Planned Number of Target Shots	Actual Number of Target Shots
LLE	715	701
LLNL	375	400
LANL	140	138
SNL	30	34
NLUF	120	130
CEA	30	34
NRL	20	24
Total	1430	1461
LLE ISE		303
LLE SSP		172
LLE RTI		95
LLE ASTRO		38
LLE DD		30
LLE CRYO		23
LLE DDI		16
LLE LPI		16
LLE PB		8
LLE Total		701

National Laser Users' Facility and External Users' Programs

During FY05, 760 target shots were taken on OMEGA for external users' experiments. The external users' shots accounted for 52% of the total OMEGA shots produced in FY05. External users in FY05 included seven collaborative teams under the National Laser Users' Facility (NLUF) program as well as collaborations led by scientists from the Lawrence Livermore National Laboratory (LLNL), Los Alamos National Laboratory (LANL), Sandia National Laboratory (SNL), the Naval Research Laboratory (NRL), and the Commissariat à l'Énergie Atomique (CEA) of France.

NLUF Program

FY05 was the first of a two-year period of performance for the eight NLUF projects approved for FY05 funding. Seven of these NLUF campaigns were allotted OMEGA shot time and received 130 shots on OMEGA in FY05. Table 104.IV lists the accepted proposals.

Isentropic Compression Experiments (ICE) for Measuring EOS on OMEGA

Principal Investigator: J. R. Asay (Washington State University)

This research is developing three new areas of high-pressure research. First, techniques to generate high-accuracy, quasi-isentrope equation of state data into the Mbar regime will be developed. This effort will enable, for the first time using lasers, "cold" equation of state curves for standard materials in the Mbar regime. Second, wave profile data on candidate materials (Bi and Fe) upon compression through both solid–solid and solid–liquid phase transitions will be measured and compared with similar data measured with different loading times on other platforms (*Z* data, gun data, diamond anvil data). These data will then be used to benchmark models for the time dependence of phase transitions being developed at WSU. Finally, to ensure the phase transitions observed in these dynamic experiments correspond to the same phases as observed in

Table 104.IV: FY05–FY06 Proposals.

Principal Investigator	Affiliation	Proposed Title
J. Asay	Washington State University	Isentropic Compression Experiments for Measuring EOS on OMEGA
H. Baldis	University of California, Davis	Laser–Plasma Interactions in High-Energy-Density Plasmas
R. P. Drake	University of Michigan	Experimental Astrophysics on the OMEGA Laser
R. Falcone	University of California, Berkeley	NLUF Proposal: Plasmon Density of States in Dense Matter (no target shots allocated in FY05)
P. Hartigan	Rice University	Astrophysical Jets and HED Laboratory Astrophysics
R. Jeanloz	University of California, Berkeley	Recreating Planetary Core Conditions on OMEGA
R. Mancini	University of Nevada, Reno	Three-Dimensional Study of the Spatial Structure of Direct-Drive Implosion Cores on OMEGA
R. D. Petrasso and C. K. Li	Massachusetts Institute of Technology	Implosion Dynamics and Symmetry from Proton Imaging, Spectrometry, and Temporal Measurements

static experiments, dynamic x-ray diffraction will be used to determine lattice structure. This past year the most difficult of these goals were achieved; we developed the platform to produce high-accuracy and high-pressure isentrope data on aluminum. In addition, it was observed that the elastic–plastic transition is much larger than expected from previous work at *Z*. This issue is being investigated.

Twelve shots were performed on isentropic compression targets in the past year (Feb. 22th: shots 38961–38966, June 14th: shots 40121–40127). The purpose of these initial campaigns was to (1) develop a shockless compression platform with a pressure drive of ~1% planarity over a several hundred micron region and (2) use this planar drive to extract a single-shot series of equation of state (EOS) data for Al to peak pressures in excess of 1 Mbar. The ICE-EOS package, as shown in Fig. 104.58, consists of a Au halfraum, a plastic reservoir followed by a vacuum gap, and a double-stepped Al target. Fifteen beams from the OMEGA laser at 0.35-μm wavelength, containing a combined energy of 5–6 kJ in a 2-ns temporally flat pulse, are focused symmetrically onto the inner walls of the Au hohlraum laser entrance hole (LEH): 1.7-mm; diameter: 2.2 mm; length: 1.7 mm). This confined high-*Z* geometry results in a near blackbody distribution of thermal x rays (T_h ~ 120 eV) with uniform temperature gradients over a spatial region close to the diameter of the hohlraum. The hohlraum is attached to a 180-μm-thick, 12% Br-doped polystyrene foil [$C_8H_6Br_2$]. The x-ray field within the hohlraum launches an ablatively driven shock through the foil. The initial region of planarity is expected to approach that of the diameter of the halfraum and can extend over millimeters. The Bromine dopant absorbs the high-energy Au M-band x rays generated within the hohlraum, which otherwise could preheat the Al step sample. After breakout from the rear surface, shock heating and momentum cause the Br-CH to dissociate and unload across a 400-μm vacuum gap. Transit across the vacuum gap causes mass-density gradients along the target axis to relax as a function of distance from the original Br-CH/vacuum-gap interface. The unloading Br-CH monotonically loads up against the Al sample and the imparted momentum launches a ramp stress wave through the material. The temporal profile of the compression wave may be shaped by varying the size of the vacuum gap, the density of the reservoir, or the temperature within the hohlraum. In our FY05 experiments, the main targets consisted of 10-20-30-μm Al steps coated onto a well impedence-matched LiF window.

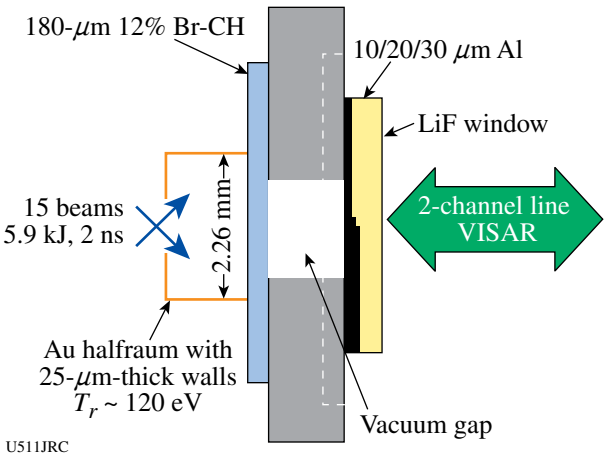

Figure 104.58
Standard ICE target design.

Probing through the LiF window, the time history of the Al/LiF interface acceleration is recorded with a line imaging velocity interferometer (velocity interferometry system for any reflector or VISAR) with two channels set at different sensitivities. The time-resolved fringe movement recorded by a streak camera is linearly proportional to the velocity of the reflecting surface, which in this case is the Al-LiF interface. This allows for accurate measurement of the particle velocity (after taking into account the refractive index of the LiF window) as a function of time. Shown in Fig. 104.59(a) is the streak camera output of the VISAR for the target conditions described in Fig. 104.58.

The image provides spatial resolution at the target plane over ~500 μm and temporal resolution of the interferometer fringe displacement over a 30-ns time window. We observe excellent planarity across the field of view with smooth ramp unloading from the 10-, 20-, and 30-μm Al samples at progressively later times. The velocity sensitivity (set by the resolving element within the VISAR) is 0.86 km/s/fringe shift. Using Fourier analysis, and after deconvolving the data for temporal and spatial distortions within the streak camera, the time-resolved particle velocity profile for each Al thickness [Fig. 104.59(b)] can be extracted.

The iterative analysis technique described by Rothman *et al.*[1] was used along with the particle velocity profiles in Fig. 104.59(b) to generate a path through stress-density space (Fig. 104.60). Also shown for comparison is the isentrope from the Mie–Grüneisen equation of state. The error bars on the experimentally determined σ–ρ curve are ±5% (stress space) and ±2.5% (density space) up to a peak stress of ~83 GPa.

The errors are dominated by uncertainties in measuring of the (~0.1 km/s), time (~50 ps), step height (~1%), and initial density (0.6%) and are due to random noise within the system (poor fringe visibility). The error bars can be reduced linearly with increasing step height. This is the first such measurement on a laser platform and opens up the possibility of extracting EOS data well into the multi-Mbar regime. Note that the extracted stress-density path is stiffer than the predicted Al isentrope, which may be due to strength effects or potential systematic errors in the experiment.

Shockless compression was demonstrated over a range of peak pressures and rise times (Fig. 104.61). The highest achieved pressure was 210 GPa, which corresponds to a particle velocity of ~6 km/s. An enhanced elastic wave precursor was observed, several times in excess of the reported Hugoniot elastic limit (HEL), for ramp compressions which occur over shorter time scales. This is not presently understood and is being investigated. If true, this is a significant discovery and it is expected that it will highlight the uniqueness of laser-driven ramp loading for measuring the yield strength of materials at high shockless strain rates. In the second year of the proposal,

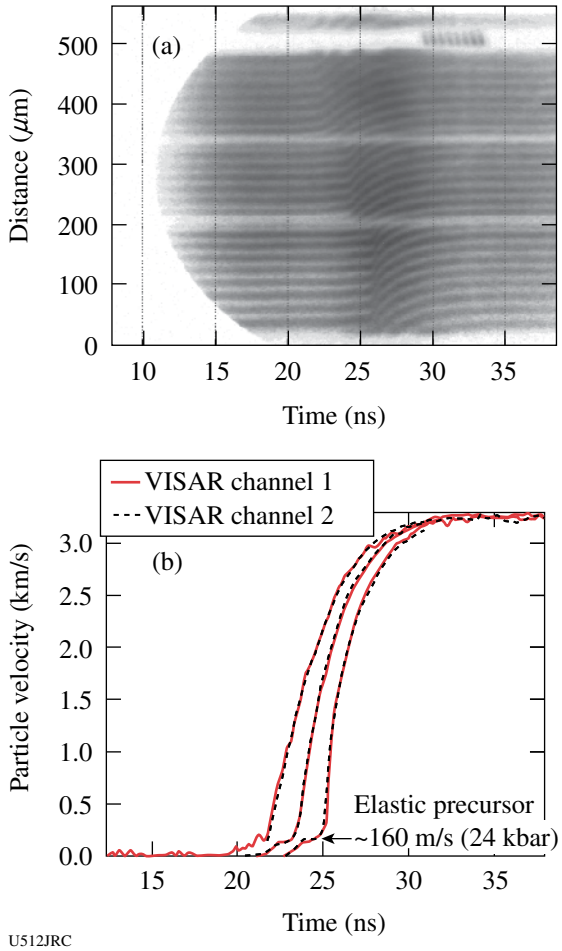

Figure 104.59
(a) Streak camera output of VISAR for shot 40127. (b) Extracted particle velocity profiles for shot 40127.

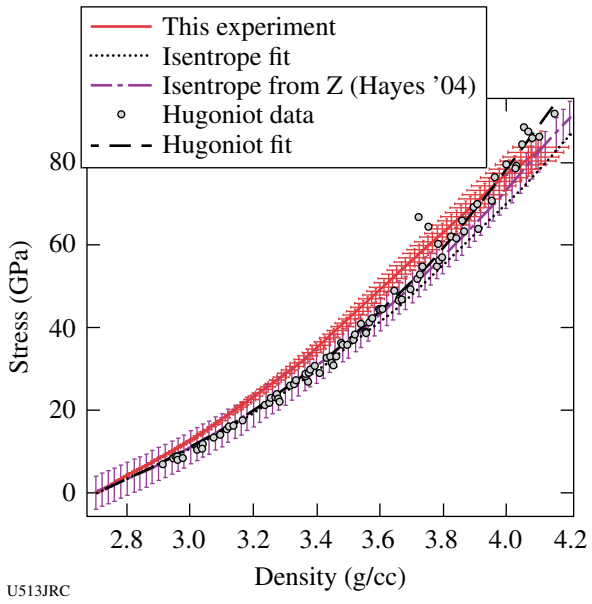

Figure 104.60
Stress-density path calculated from a double-stepped Al target.

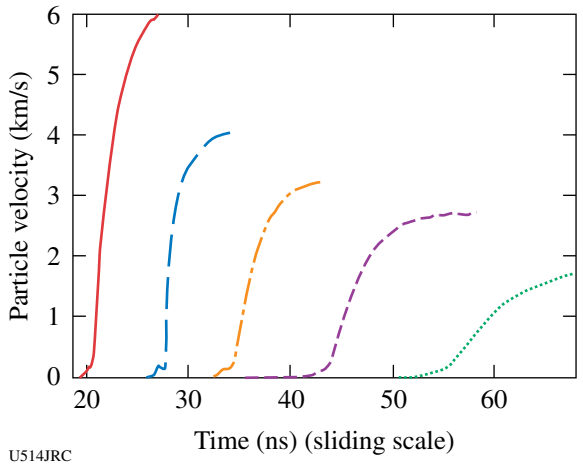

Figure 104.61
The compression of Al samples for different compression times shows a difference in the elastic-plastic structure with loading rate.

it is intended to extract EOS and strength information for free-surface Ta in excess of 1 Mbar and to determine the rate dependence of phase transformations for materials with multiple solid phases. A sophisticated analysis technique is also being developed to analyze free-surface stepped data so that a window material is not needed as a reference. Some effort will also be dedicated to develop techniques to shape the pressure profile of the compression wave.

Laser–Plasma Interactions in High-Energy-Density Plasmas
Principal Investigator: H. Baldis (University of California, Davis)

Laser–plasma interactions in high-energy-density plasmas display a broad palette of features that prove useful in furthering the understanding and characterization of these unexplored plasma regimes. To access these regimes, reduced-size (below 1 mm in diameter and length), Au cylindrical enclosures are irradiated by intense laser beams at around 10-TW power in 1 ns. These hot holhlraums act as converters of laser energy into x-radiation, and because of the high power pumped into such a small target, the radiation temperature reaches high values, above 300 eV. The plasmas created into and around the laser channels are characterized by elevated electron temperatures (~10 keV), with densities varying up to the critical density (for 351 nm $n_{cr} = 9.1 \times 10^{20}$ cm^{-3}).

The intrinsic dependence of the stimulated Raman scattering (SRS) on plasma temperature and density gives the possibility of using the process as a plasma diagnostic tool. From the resonance condition coupled to the dispersion relation, one can infer the electron temperature in hot plasmas (above 5 keV) as the Bohm–Gross shift becomes significant and SRS wavelengths extend beyond 702 nm (= $2\lambda_0$, where λ_0 is the laser wavelength). The hot hohlraum is irradiated by 19 OMEGA laser beams. Each beam carries ~500 J energy onto the target, in 1 ns pulses, at 351-nm wavelength. The beams are bundled in cones at ~23° (cone 1), ~48° (cone 2), and 59° to 62° (cone 3) as shown in Fig. 104.62.

Figure 104.63 illustrates a SRS spectrum measured by a full-aperture backscattering station (FABS) at OMEGA. The SRS wavelength rises quickly in the first half of the laser pulse, as the laser channel fills with plasma. The electron density

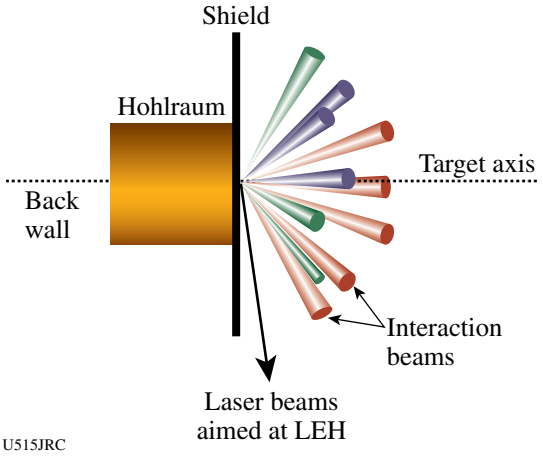

Figure 104.62
Hohlraums irradiated by the OMEGA beams are used for new studies of laser–plasma interaction in high-energy density plasmas.

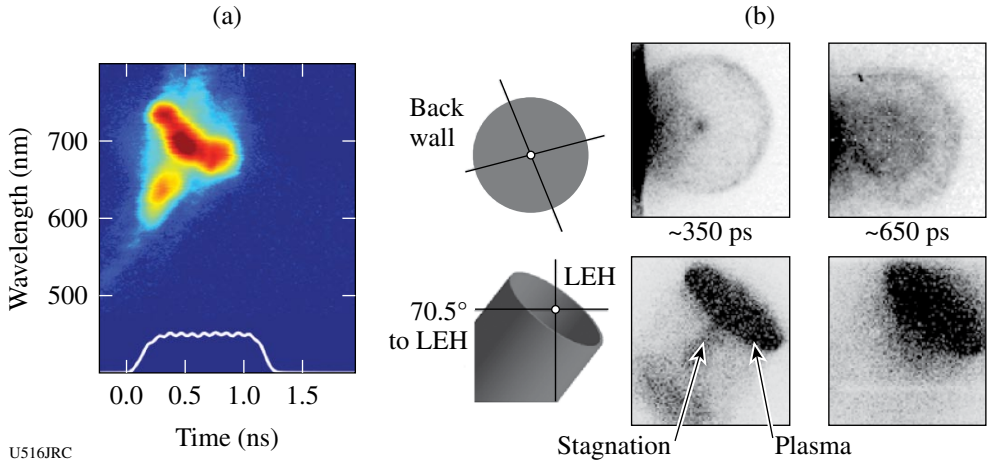

Figure 104.63
(a) A time-resolved Raman spectrum measured in hot hohlraums is characterized by a wavelength above 702 nm. This is an indication of high electron temperatures. (b) Two different views (end-on and near side-on) of the Au plasma-emitting x-rays with photon energies above 7 keV. The stagnation on axis is visible at 350 ps, with the bright emission at the LEH.

increases above 0.1 n_{cr}, and the plasma fill moves the laser energy deposition region to the laser entrance hole (LEH). Indications of plasma filling are given by the Raman spectra at the time when the SRS wavelength reaches its maximum and then stays constant or decreases. It is likely that SRS, occurring along a density gradient outside the target, is pushed to a lower density (shorter wavelength) as the laser beam filaments.

X-ray framing-camera images [Fig. 104.63(b)] confirm the filling time inferred from SRS spectra. The images were taken for x-ray photon energies above 7 keV, through the thin Au back wall of the hohlraum and also at 70.5° to the LEH. The Au plasma stagnation may be important for the scattering as it produces high electron temperatures (T_e ~ 10 keV). The stagnated plasma eventually moves to the LEH where it is further heated by the laser. This is reflected in the spectral shift that brings the SRS wavelength above 730 nm, which corresponds to T_e ~ 8 keV (as deduced from SRS dispersion relation). Time-integrated spectroscopic measurements of a Au L-band measured an average charge state of around 58 to 59, consistent with an average T_e ~ 7 to 8 keV.

Experimental Astrophysics on the OMEGA Laser
Principal Investigator: R. P. Drake (University of Michigan)

The OMEGA laser can address important issues in astrophysics because, through laser ablation, it can produce pressures of >>10 Mbars over areas of square millimeters. Two such issues, the contribution of hydrodynamic instabilities to the structure in supernovae and the dynamics of radiative shock waves, are the topics of this project. In experiments performed in this project, it was found that, under conditions well scaled to supernova explosions, spikes of dense material can penetrate much farther than previously anticipated. To explore this phenomenon, it was necessary to develop new radiographic diagnostics capable of improved imaging in two orthogonal directions. This goal was achieved (Fig. 104.64) and work is now proceeding to study the contributions of various initial modes to the enhanced spike penetration.

In the experiments, ten beams of the OMEGA laser irradiate a polyimide disk with UV light at an irradiance of ~10^{15} W/cm^2 for 1 ns. This launches a 50-Mbar shock into the material, which later evolves to form a blast wave not unlike that produced during a supernova explosion. The blast wave crosses a structured interface to lower-density material, which is a surrogate for the structured interfaces that are present in a presupernova star. The subsequent, unstable evolution is monitored by radiographically detecting the structure of Bromine-doped

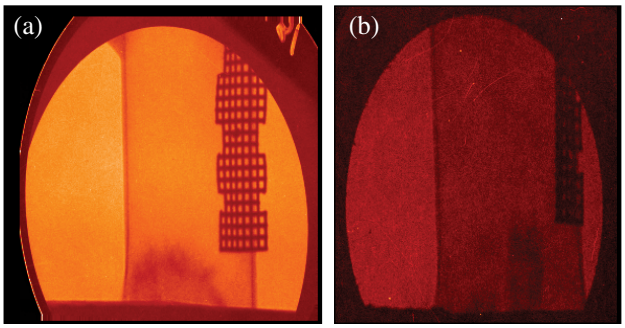

U517JRC

Figure 104.64
Data from the first experiments to obtain physics data using simultaneous, orthogonal, point-projection backlighting [viewing direction of image in (b) is orthogonal to that of (a)]. The data are obtained by using a brief (1 ns) x-ray source to project a signal onto an exposed piece of x-ray film. One can see on these images the structures that have evolved from an initial condition defined by $a_0\sin(kx)\sin(ky)$, where $a_0 = 2.5\ \mu$m, $k_x = k_y = 2\pi/(71\ \mu\text{m})$. During the next year, the impact of a selected range of initial conditions will be studied.

material that was initially a strip within the high-density disk. The experiments can study some issues at a level of detail not possible in present-day simulations.

Astrophysical Jets and HED Laboratory Astrophysics
Principal Investigator: P. Hartigan (Rice University)

The series of experiments for the NLUF program on astrophysical jets and high-energy-density (HED) laboratory astrophysics was designed to explore what can be learned about astrophysical jets by simulating them in the laboratory while at the same time testing how well the advanced numerical codes *RAGE* and *PETRA* follow the evolution of shocked flows. In FY05, this program was granted one shot day on 25 May and another on 31 August. For the May shots, a series of baseline experiments were carried out to test the reproducibility of the jet creation. Results from these shots are shown in Fig. 104.65. The overall structure of the jet closely resembles that of the numerical simulations, and images taken at the same time from different shots are nearly identical in most cases. Hence, there is confidence that variations in the target construction are not dominating the experimental results. For the 31 August shots, a more advanced target design will be implemented in which a dense ball is embedded within the foam. This design shows many interesting shock waves in the numerical simulations and begins to address the astrophysical case of a jet deflecting from a dense molecular cloud or a jet entraining dense fragments within bow shocks. Such flows are of interest to astrophysicists as they are observed to occur in a variety of star formation

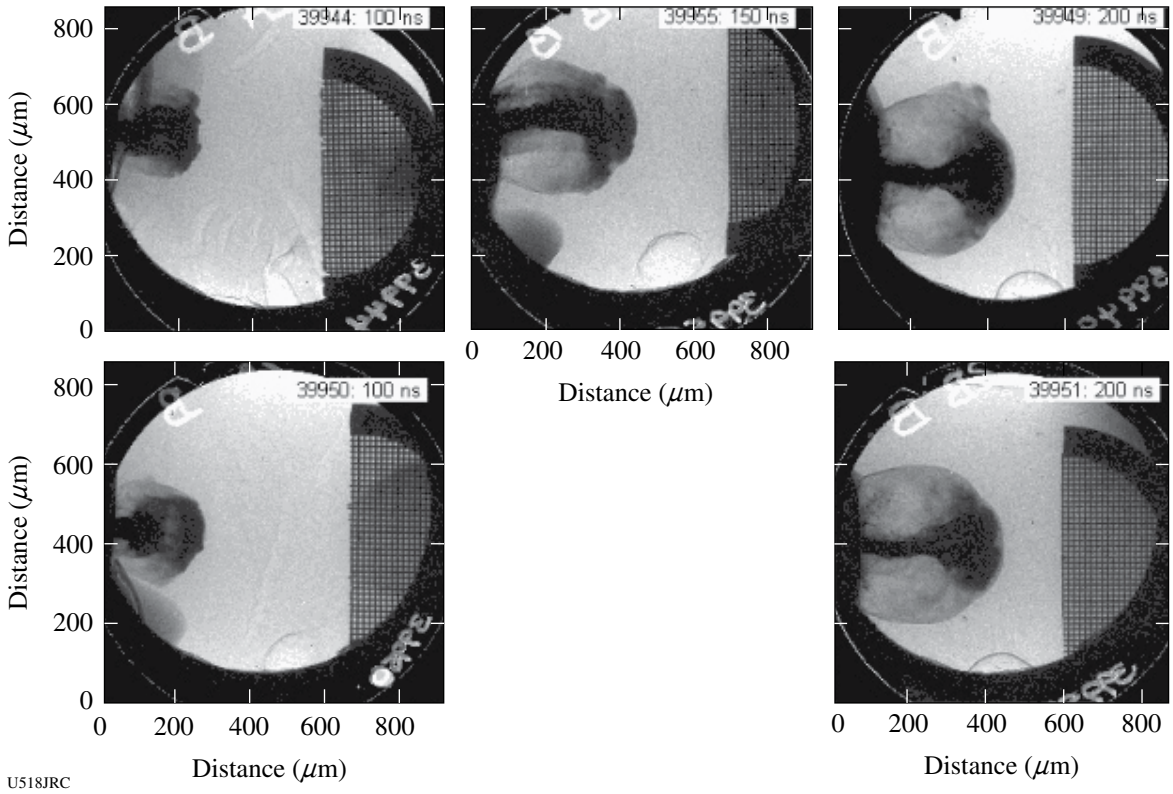

Figure 104.65
Time-framed x-ray backlit images showing the time evolution of jets on two OMEGA shots [39944 (top) and 39950 (bottom)].

settings and may help address issues such as the generation of turbulence in molecular clouds. The parameter space associated with dense clumps and shock waves is very rich, and it should be possible to explore a variety of phenomenon such as clump lifetimes, fragmentation, turbulence, and jet deflection for various sized clumps and impact parameters in future shots, provided these new targets perform as anticipated.

Creating the Core Conditions of Giant Planets in the Laboratory

Principal Investigator: R. Jeanloz (University of California, Berkeley)

During the past year, 13 OMEGA shots were conducted on diamond anvil cells filled with H_2, D_2, He, and He/H_2 mixtures. The primary focus of the work over the past year has been on dense He. Gas samples were precompressed (see Fig. 104.66) from 0.2 to 1.5 GPa and shocked to pressures as high as 200 GPa (2 Mbar). The experiments are designed to access the extreme densities of the interior regions of the giant planets Jupiter and Saturn. The technique combines a diamond anvil cell target with a laser-driven shock. With this technique, the initial sample pressure is much higher than ambient (1 to 5 GPa), and the initial density may be from 1.5× to 4× higher than ambient (depending on the sample)—a large increase compared to nonpressurized preparation methods. Furthermore, in the important case of the He/H_2 mixtures that compose giant planets, precompression is the only way to produce a uniform single-phase target sample for high-pressure/density experiments. The higher initial density results in a significantly larger final density and correspondingly lower temperature in the shock-compressed state.

Using the active shock breakout (ASBO)/shock optical pyrometers (SOP) diagnostic, it was possible to determine pressure and density in the shocked sample as well as its optical reflectance. The temperature is simultaneously measured with the pyrometer capability of the diagnostic. Such equation-of-state measurements provide crucial constraints on models that describe planetary structure (current internal state) and internal

evolution, which is a key requirement for understanding the origins of planets. Electrical conductivity inferred from optical reflectance measurements are used as input data for models of planetary magnetic-field generation.

A quartz reference technique was employed for all of the samples tested to produce quantitative measurements of the Hugoniot parameters (P, V, and E), temperature (T), and shock-front reflectivity (R) that can be related to electrical conductivity (σ). The recent experiments provide measurements of the properties of dense He to the highest pressures yet achieved under shock compression. Detailed data are now available on the insulator-conductor transition in He at conditions near 1 g/cm^3 and ~2 to 5 eV; from these data it is estimated that the transition to metallic-like conducting states is near 360 GPa and 1 eV. This pressure is significantly lower than the estimated metallic transition along the cold compression curve (~1200 GPa). A significant data set on H_2 has also been collected at three different initial densities. These new data will provide an interesting comparison to the current extensive data set on cryogenic liquid deuterium. Finally, for the first time, two data points were produced on a 50% He/H_2 mixture. The preliminary Hugoniot results indicate that the compressibility of the mixture is consistent with an idealized mixing model based on the equations of state of pure He and H_2; it is planned to increase this data set with the future OMEGA experiments that are currently being planned.

Figure 104.67(a) shows a compact representation of the He Hugoniot data plotted as a function of the particle speed. It turns out that all available theoretical models predict that the family of Hugoniot curves corresponding to an ensemble of precompressed states are parallel to each other and offset from

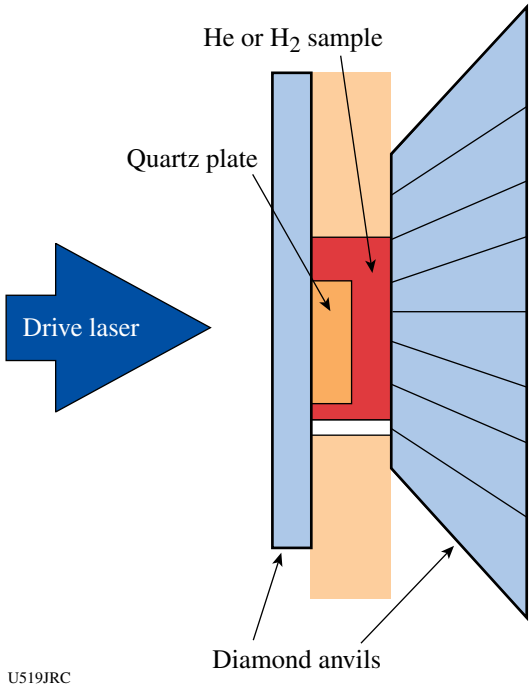

Figure 104.66
Schematic of the precompressed target arrangement.

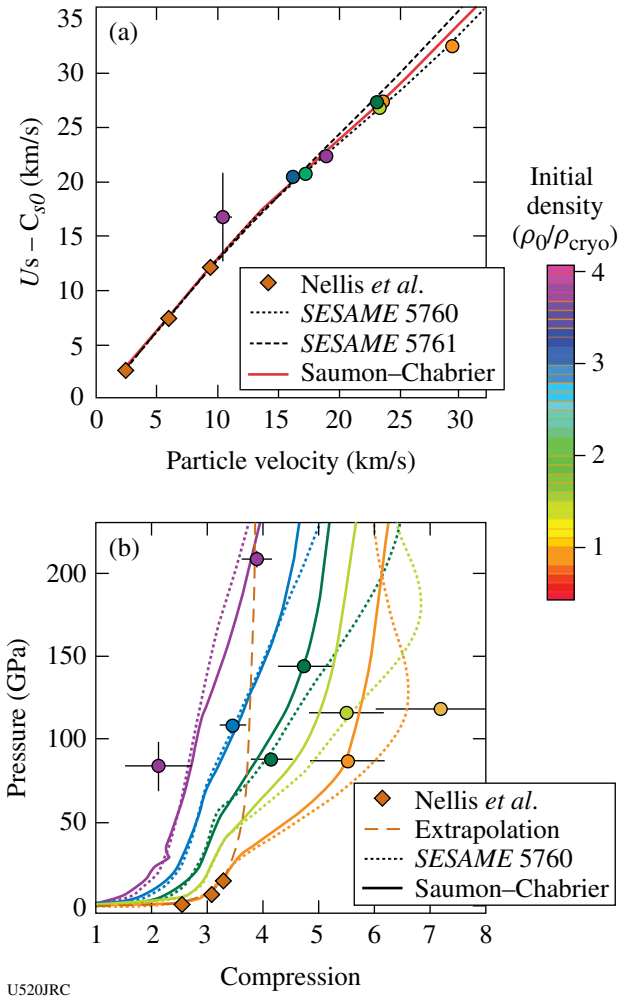

Figure 104.67
(a) He Hugoniot measurements plotted in a reduced form. Shock velocity minus the sound velocity of the initial state is plotted as a function of particle velocity. The shades of the points indicate initial density relative to the cryogenic liquid density (0.122 g/cm^3), as indicated by the scale. (b) Pressure as a function of compression for shock-compressed He at three different initial densities. Points show our data, the solid curves are predictions from the SCVH EOS, and the dotted curves are from the *SESAME* 5760 table. The dashed curve is an extrapolation of a linear fit to the low-pressure EOS data.

the origin by the initial-state sound velocity. Different models predict different slopes for the Hugoniots, but all models are similar in that the Hugoniot for a range of precompressed states can be represented by a single average curve after the sound velocity offset is subtracted. Accordingly, the ordinate in Fig. 104.67(a) is given by the measured shock velocity minus the sound velocity of the initial state. As is evident in the figure, all of the data converge to a common reduced Hugoniot. Note that the slope of the high-pressure portion of the Hugoniot (particle velocity >10 km/s) is distinctly different from the slope of the low-pressure segment measured by Nellis *et al.*[2] The reduced slope observed for the high-pressure states indicates that the He Hugoniot undergoes a marked softening relative to its lower-pressure behavior. In this range, all the samples have become conducting, and thus the softening is probably associated with ionization.

Figure 104.67(b) shows the same data represented in terms of compression as a function of pressure. The near-vertical dashed line shows the behavior of the low-pressure Hugoniot if it is extrapolated to higher pressures—little can be said about compressions beyond about 3.5 because temperature dominates the pressure at this point (our precompression experiments avoid this problem). The solid curves show the behavior predicted by a commonly used astrophysical model calculated by Saumon, Chabrier, and van Horn (SCVH), and the solid curves show the same for the *SESAME* 5760 table. The softening at high pressures is predicted by both the SCVH and *SESAME* models. In addition to the Hugoniot EOS data, we extracted temperature and shock-front reflectance for cases where the latter was observable. These data are summarized in Fig. 104.68 for all of our He data set. The temperature data also show broad agreement with the SCVH EOS for He. The reflectivity data are strongly correlated with temperature, indicating that the driving mechanism for the conductivity is a thermal activation process.

The reflectivity data have been fit to a simple semiconductor model of the ionizing fluid. From the fit it is estimated that metallic-like conditions in dense He will be achieved near 2.7 g/cm^3 and 1-eV temperature, corresponding to ~360 GPa on the Jupiter isentrope. These data and the fit are also in good agreement with the data of Ternovoi *et al.*,[3] who measured the conductivity of dense He with a reverberating shock technique, and with the plasma–chemical model of Forster *et al.*[4] Figure 104.69(a) shows details of the fit to the semiconductor model; Fig. 104.69(b) shows the estimated metallization boundary on the pressure-temperature (P-T) phase plane.

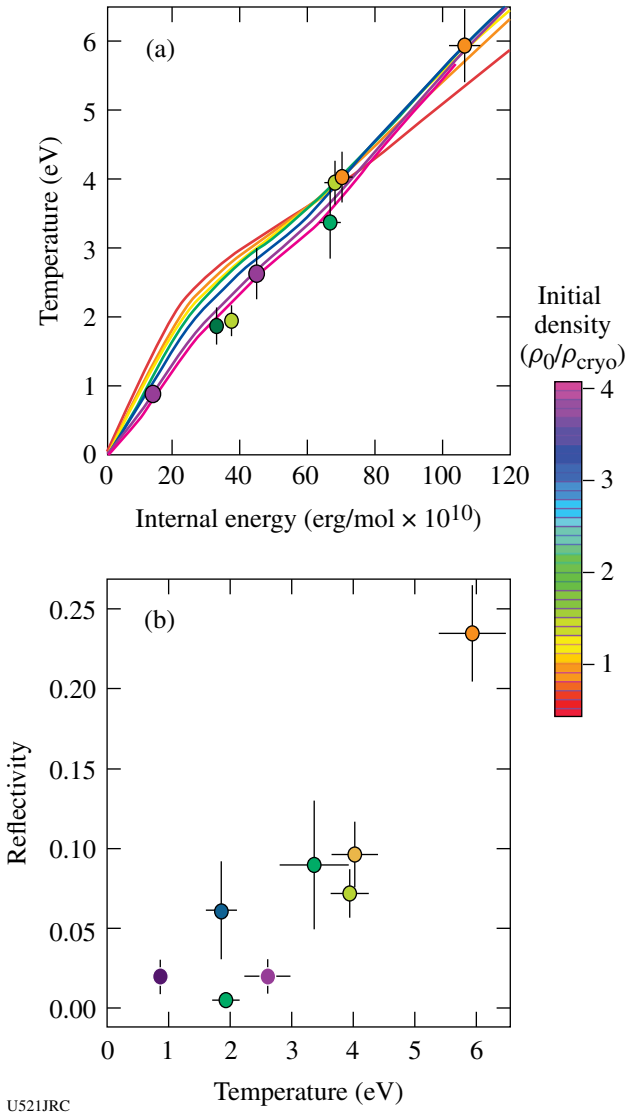

Figure 104.68
(a) Temperature as a function of internal energy for He (points) in comparison with the SCVH model (solid curves); the tone scheme is the same as described in Fig. 104.67. (b) Reflectivity as a function of temperature for shock-compressed He.

In addition to the He results, high-pressure data on H_2 continued to be collected, and Hugoniot data have been obtained, centered at three different initial densities (not shown here). Analysis of these data is ongoing, as the completion of an accurate model for the release response of the quartz standard is in progress. This will be the first high-pressure data set available to compare the high-pressure response of H_2 with the current extensive set of data for shock-compressed D_2.

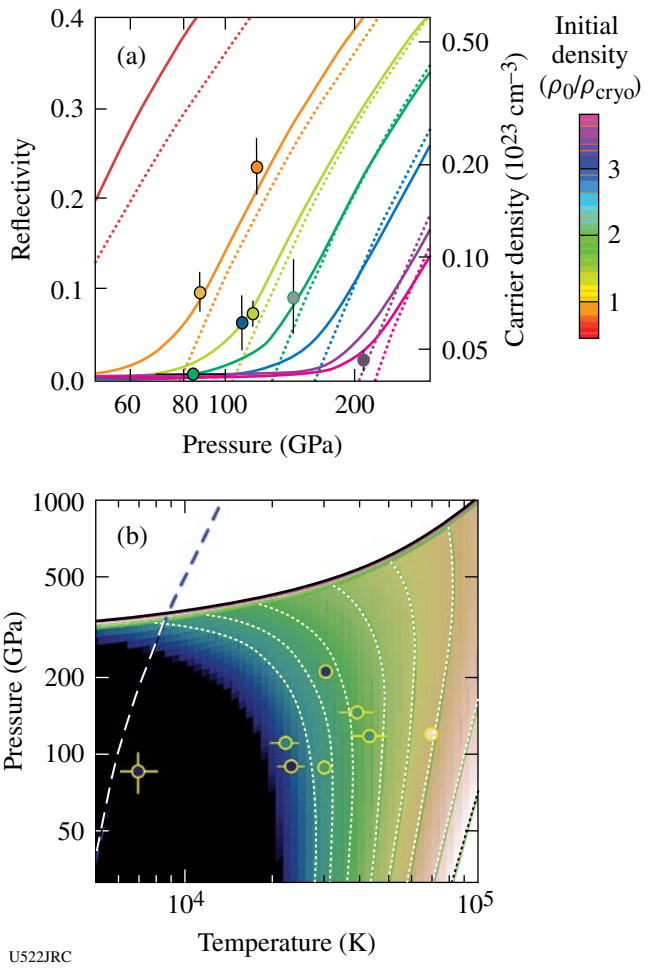

Figure 104.69
(a) Reflectivity of He as a function of shock pressure in comparison with a semiconductor model fit (solid curves). Dashed curves show the corresponding carrier density (right scale). (b) Points show the locations on the P-T plane of the data points in (a). The dotted curves and the tonal scale show contours of constant ionization from the model, the thick solid curve is the 2.7 g/cm^3 isochore (indicating the metallization boundary), and the dashed curve is the Jupiter isentrope.

Finally, the first two experiments on He/H_2 mixtures have been completed. The Hugoniot results, shown in Fig. 104.70, indicate that the compression curve of the mixture is well modeled by an equation of state constructed by linear mixing of the SCVH He and Ross H_2 models. This is work in progress; considerably more analysis must be performed and more data collected before strong conclusions can be made.

Currently, a wide range of states in He and H_2 have been explored, and the first two experiments on He/H_2 mixtures have been performed. For the coming year, this investigation will focus on He/H_2 mixtures. Because they are immiscible fluids, at ambient pressure and low temperature, these mixtures have never been studied at high pressures. The studies will begin to address the issues of He/H_2 miscibility, the transition to conducting states in the mixture, and the effect of the mixture on the equation of state. The conductivity (inferred from reflectance) in He/H_2 mixtures allows the determination of ionization properties. These data will provide insight on the electrical conductivity and the miscibility of He/H_2 mixtures in the giant planets.

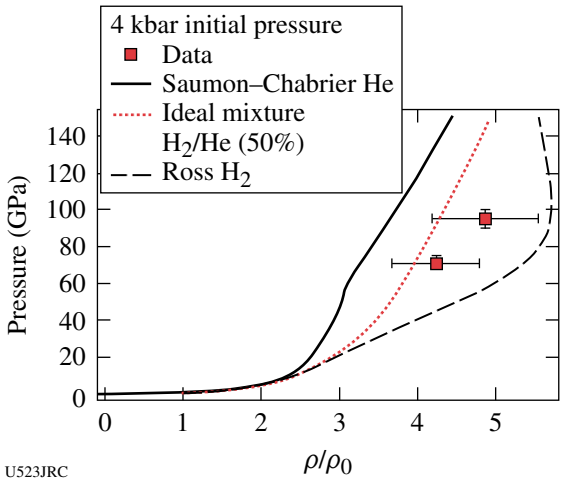

Figure 104.70
(a) Initial Hugoniot data on a 50% mixture of He/H_2, shown in comparison with a theoretical Hugoniot calculated based on ideal mixing of the SCVH-He model and the Ross H_2 model.

Three-Dimensional Study of the Spatial Structure of Direct-Drive Implosion Cores at OMEGA

Principal Investigator: R. Mancini (University of Nevada, Reno)

The goal of this project is to determine the three-dimensional spatial structure of temperature and density distributions in high-energy-density core plasmas arising from OMEGA direct-drive implosions. Targets are plastic shells with a gas fill made out of deuterium and a tracer amount of argon for spectroscopic diagnostics. The data for the analysis consists of space-integrated, time-resolved x-ray argon line spectra recorded with streaked crystal spectrometers and gated x-ray narrow-band images based on argon line spectral features obtained along three quasi-orthogonal directions.

Data modeling and analysis is performed using a spectral model that considers collisional-radiative level population kinetics, detailed Stark-broadened line shapes for both resonance- and satellite-line transitions, and radiation transport. Two analysis methods have been developed to extract temperature and density gradients from the data. On the one hand, using emissivity maps obtained from image data inversion temperatures are determined from narrow-band emissivity ratios and then densities are computed by solving a set of emissivity equations. On the other hand, a search and reconstruction algorithm driven by a Pareto genetic algorithm searches parameter space for the temperature and density gradients that yield the best simultaneous fits to the space-integrated line spectrum and a set of narrow-band emissivity maps and image intensity distributions, i.e., multi-objective data analysis.

Three multimonochromatic x-ray imagers (MMI) were designed, built, and fielded in OMEGA direct-drive implosion experiments during FY05. These (identical) instruments recorded gated narrow-band x-ray images of the core along three quasi-orthogonal directions at the collapse of the implosion based on the Ly_α, He_β, and Ly_β (and associated Li- and He-like satellites) line transitions of argon. In addition, a pre-existing x-ray imager at OMEGA was modified for better performance and fielded in the same experiments to obtain another Ly_β image along a direction diametrically opposite to one of the MMI's line of eight. This extra image permits an experimental check on the opacity of the Ly_β line emission in the core. Work is in progress in the analysis of the data.

Implosion Dynamics and Symmetry from Proton Imaging, Spectroscopy, and Temporal Measurements

Principal Investigator: R. D. Petrasso (Massachusetts Institute of Technology)

NLUF Proton Radiography Experiments

Initial experiments were conducted on OMEGA as part of this NLUF program to explore the use of proton radiography to study transient electric and magnetic fields generated by the interaction of OMEGA laser beams with plastic foils. In each experiment, a plastic foil was illuminated by a single OMEGA laser beam, and a projection radiograph was made of the foil using a source of nearly monoenergetic 14.7-MeV protons and a CR-39 area detector for image recording. The protons passed through a wire mesh (see Fig. 104.71) before impinging on the foil, and the distortion in the mesh pattern at the detector shows how the proton trajectories were deflected through interaction with the fields generated by laser–plasma interaction at the foil.

The proton source for these experiments was formed by imploding a D^3He-filled, glass-shell capsule with 20 OMEGA laser beams in a 10-kJ, 1-ns pulse. The capsule diameter of the proton source target was unusually small, at about 440 μm, in order to provide a smaller-than-usual burn radius for optimal spatial resolution in the radiograph; the full width at half maximum (FWHM) of the proton source was about 50 μm, measured with proton emission imaging. The mesh was mounted on the foil assembly about 1 cm away, and the center-to-center spacing of the mesh wires was either 150 μm or 200 μm. The CR-39 detector was about 36 cm away. The burn duration of the D^3He implosion was short (~100 ps) relative to the 1-ns duration of the foil illumination; adjusting the timing of the implosion relative to the foil illumination allows images to be recorded at different times. Sample images are shown in Fig. 104.72. Magnetic fields of the order of ~0.5 MG in the vicinity of the laser-irradiated foil are estimated on the basis of the proton deflection observed on these images (see Fig. 104.73).

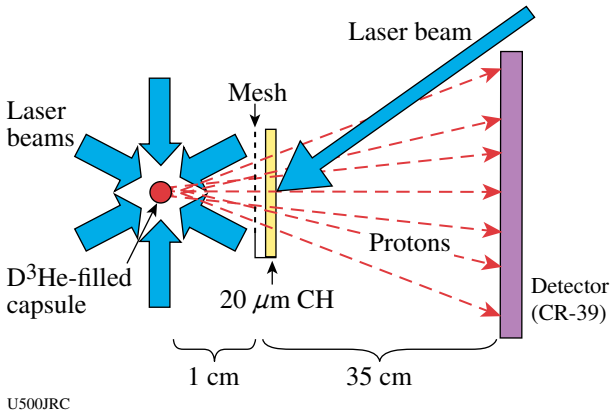

Figure 104.71
Physical arrangement of the proton backlighter (imploded D^3He-filled capsule), mesh, CH foil, CR-39 imaging detector, and OMEGA laser beams, as used for radiography.

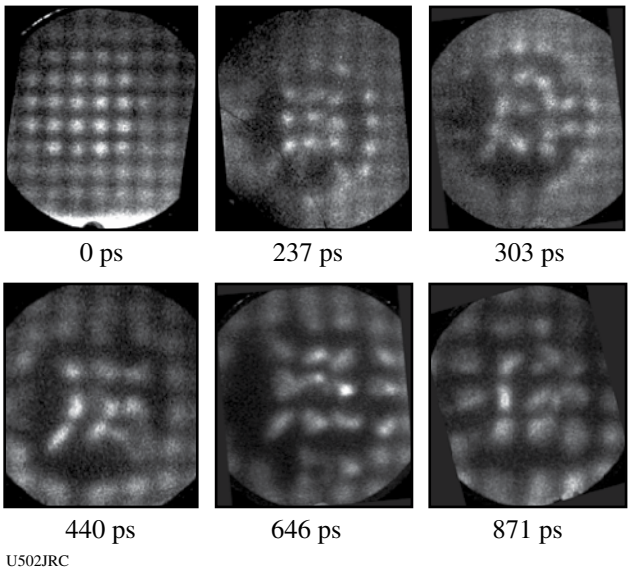

Figure 104.72
Images recorded on the CR-39 detectors during different OMEGA shots. Each image is labeled by the difference between the time at which the protons passed the foil and the time when the foil was struck by a laser beam. The first three images were made using a mesh with 150-μm (center-to-center) spacing, while the last three were made with a 200-μm mesh.

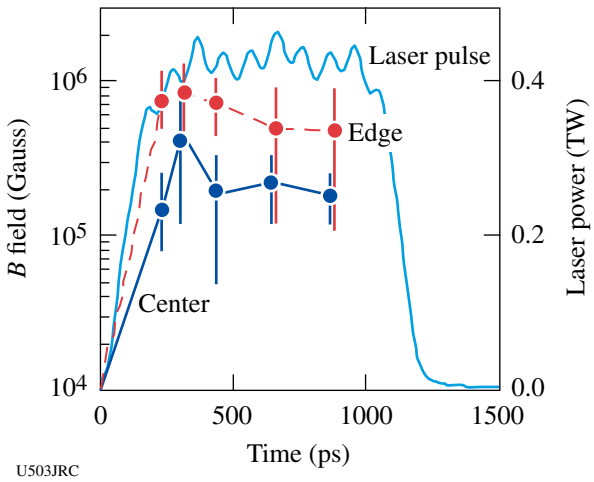

Figure 104.73
Time evolution of magnetic-field amplitude at two locations on the laser-irradiated foil (center and edge of the laser beam)—referenced to the plasma-generating laser pulse (thick solid line).

LLNL Experiments on OMEGA in FY05

During FY05, LLNL was scheduled for 372 shots on OMEGA. These were distributed into 191 planned shots for the Inertial Confinement Fusion (ICF) program, and 181 planned shots for the High-Energy-Density Sciences (HEDS) program. The actual OMEGA performance averaged 7.5% more shots than scheduled (400 shots). A brief summary of the various campaigns follows, starting with HEDS experiments.

Hot Hohlraum Experiments: Hot hohlraum experiments were carried out; their objectives were to explore the laser–plasma interaction limits of very small half-hohlraums ("halfraums") and to maximize the effective radiation temperature. Figure 104.74 shows x-ray images recorded at various times and photon energies, which show the hohlraum filling to overcritical densities.

Hohlraum Development: In hohlraum development experiments, high-Z foam (approximately 5% of solid density) was substituted for solid gold for the hohlraum wall and measured a predicted increase in x-ray conversion efficiency.

Double-Shell Capsules: Pusher single-shell experiments used a glass capsule (coated with a plastic ablator) to explore physics issues associated with double-shell capsules.

Isentropic Compression Experiments (ICE): Isentropic compression experiments used a carefully shaped laser pulse to create a smoothly increasing, shockless compression of various target materials for equation of state measurements. These included diffraction experiments where x-ray diffraction from crystalline materials was used to diagnose change of state. Low-temperature Rayleigh–Taylor experiments also used the isentropic drive to investigate the hydrodynamic stability of solid materials under strong acceleration.

X-Ray Backlighting Development: Backlighter capability experiments were conducted with the aim of improving the x-ray backlighting capabilities. These experiments included backlit pinholes for point-projection measurements as well as various mid-Z (e.g., Ti) doped foams for increased x-ray conversion efficiency into multi-keV photons.

Radiation Flow: Radiation flow experiments continued from the previous year. These experiments used foam-filled hohlraums to measure x-ray propagation through various low-density materials.

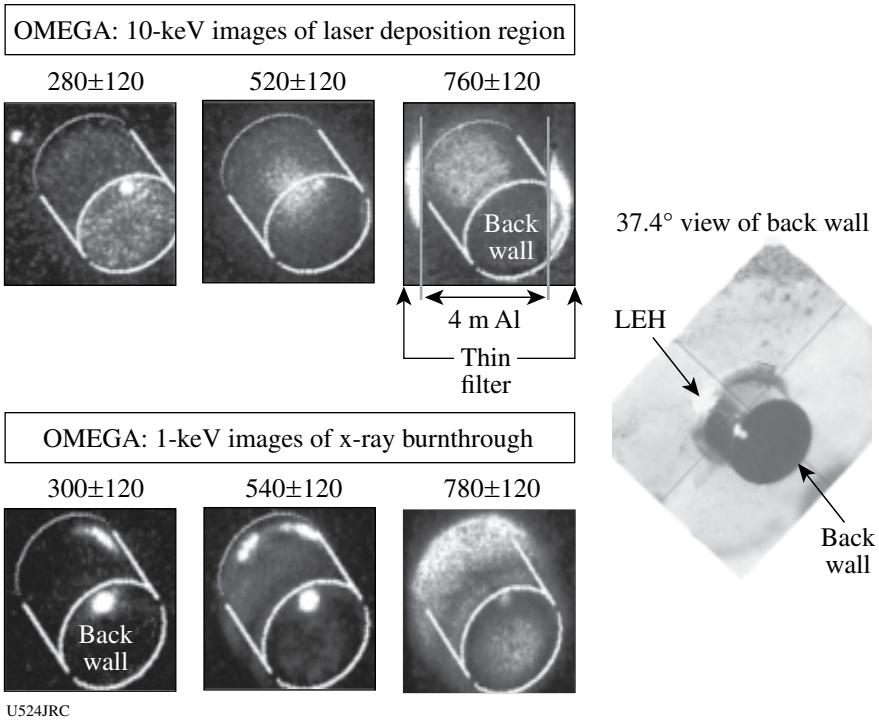

Figure 104.74
X-ray images of "halfraum" plasma fillings (view is 37.4° to the back wall). The time is given in picoseconds. The 10-keV images show that the laser deposition region moves from the back wall toward the LEH. The 1-keV images show that burnthrough occurs first near the LEH.

NWET: NWET (effects test) experiments concentrated on fielding multiple diagnostics to measure electromagnetic pulse and x rays from laser-driven hohlraums filled with low-density, mid-*Z* foams. These experiments were a collaboration between LLNL, LLE, and NRL and required the extensive installation of specialized diagnostics. Figure 104.75 shows the x-ray spectra recorded from 5-mg/cc aerogel (silicon dioxide) foam, doped with 20 atom-% Ge. Such targets produced an overall conversion efficiency of ~0.3% into x rays in the 9.4 to 13.8 keV range.

Opacity: An extensive opacity campaign was conducted on OMEGA. Early experiments were dedicated to developing appropriate x-ray backlighting sources, leading to future measurements of the opacity of warm materials.

Planar Double Shell: Planar double-shell experiments using a geometry that allowed diagnostic access were carried out to investigate the effects of x-ray preheat on the inner shell of a double-shell capsule.

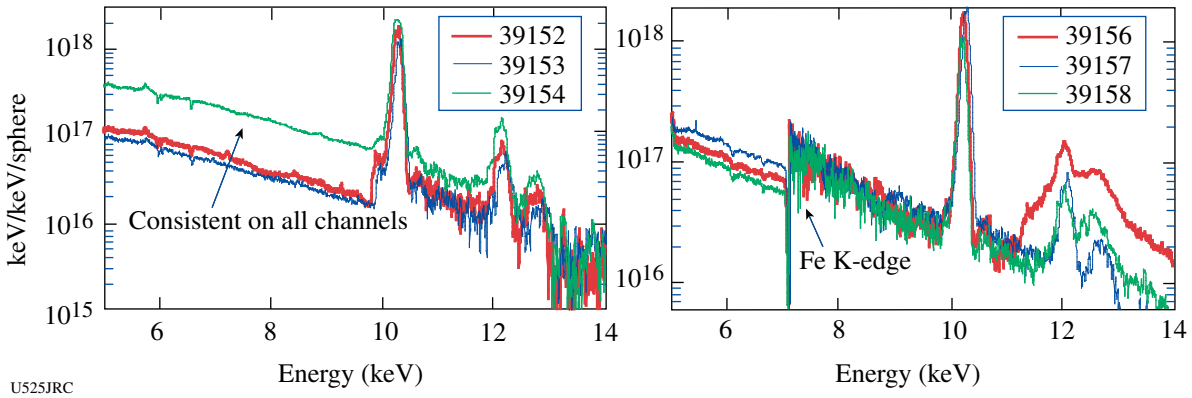

Figure 104.75
Sample x-ray spectra obtained using the HENWAY spectrometer from targets containing SiO_2 foam (aerogel) at a density of ~4.8 mg/cc doped with 20 atom-% Ge. These data indicate x-ray yields ranging from 50 to 100 J for Ge K-shell radiation. On shots 39152 to 39154, the continuum is from 12-μm Al and 1-mil Be strips and T_e ~ 2.5 to 2.8 keV. On shots 39156 to 39158, the continuum features are due to a 12.6-μm Fe foil, T_e ~ 2.0 to 2.4 keV.

DPP: A series of experiments dubbed DPP investigated jets of material driven into foams with varying cell sizes. X-ray backlighting was used to measure the propagation of the jets into the foams.

Low- and Mid-Z Liners: The first ICF experiments of FY05 were designed to investigate laser–plasma issues and x-ray drive measurements of hohlraums with low- and mid-*Z* liners and foam fills. These liners and foams are designed to inhibit inward motion of the hohlraum walls and are an alternative to gas-filled designs.

Fill Tubes: A campaign was initiated to investigate the effects of fill tubes on capsules. These indirectly driven capsules used a single perturbation on the surface of the capsule to simulate, in a calculable way, the effect of an actual fill tube on the hydrodynamic stability of the shell. Figure 104.76 shows high-magnification x-ray images of such targets. The perturbation grows and produces a jet of mid-*Z* material (originally implanted in the inner wall of the capsule). This material becomes visible in x-ray wavelengths as it is heated by the hot core.

Gas Hydro: "Gas-hydro" experiments were carried out using large, plastic, gas-filled hohlraums with a foam ball at the center. The objective of this campaign was to reduce the x-ray drive so that the direct, hydrodynamic effects of the laser-heated fill gas on a capsule could be observed and compared with simulations. Figure 104.77 shows the results of the first of such attempts. The shock front in the foam surrogate target, observed with x-ray backlighting, shows the effects of the laser-heated gas pressure for low initial fill pressures. Contrary to simulations, however, no effect was observed at higher initial fill pressures. A new experiment, designed to have reduced sensitivity to target alignment, will explore these issues.

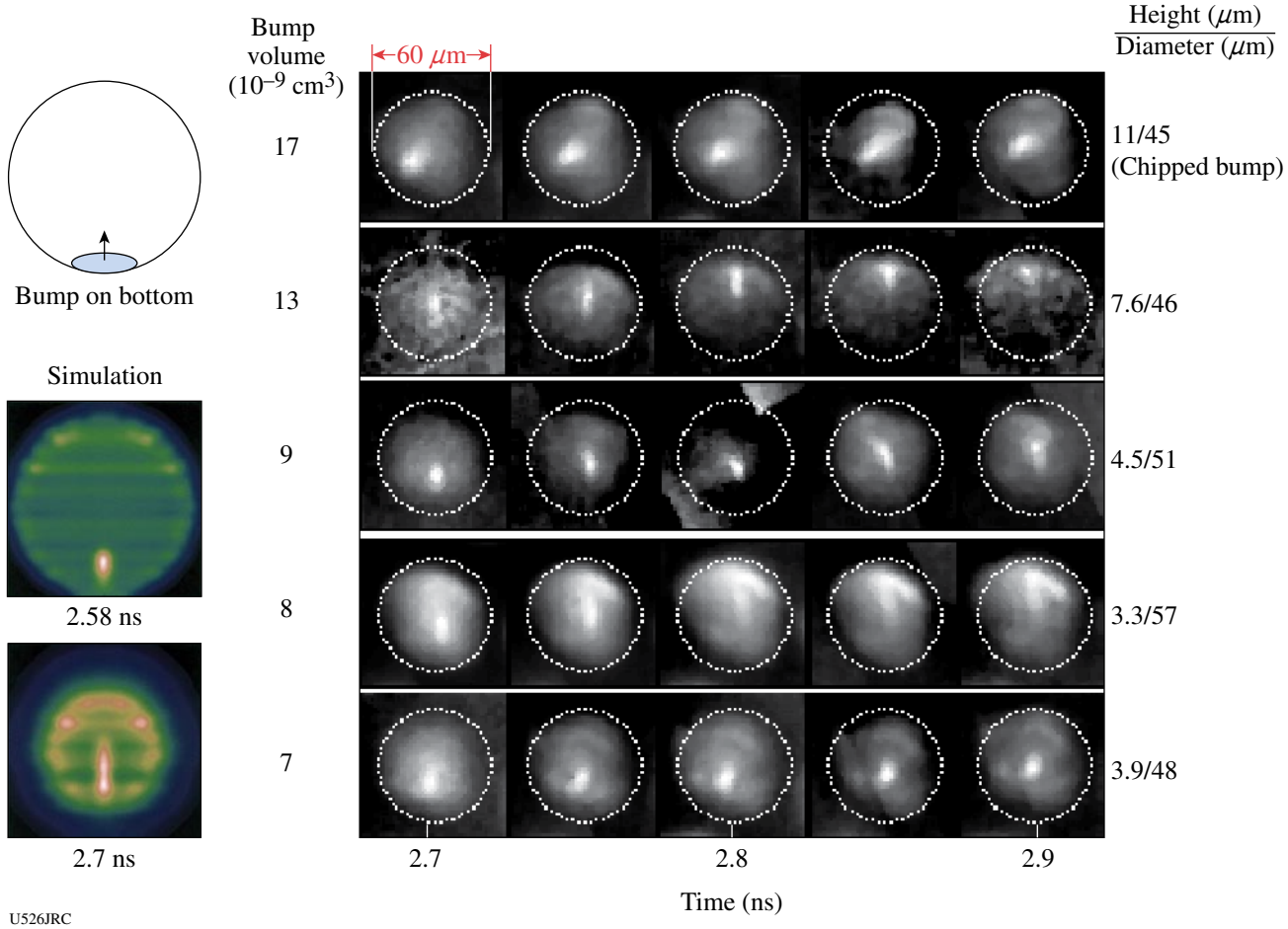

Figure 104.76
Simulations (left) and x-ray framing camera images of capsules with imposed bumps that are used to simulate a fill tube.

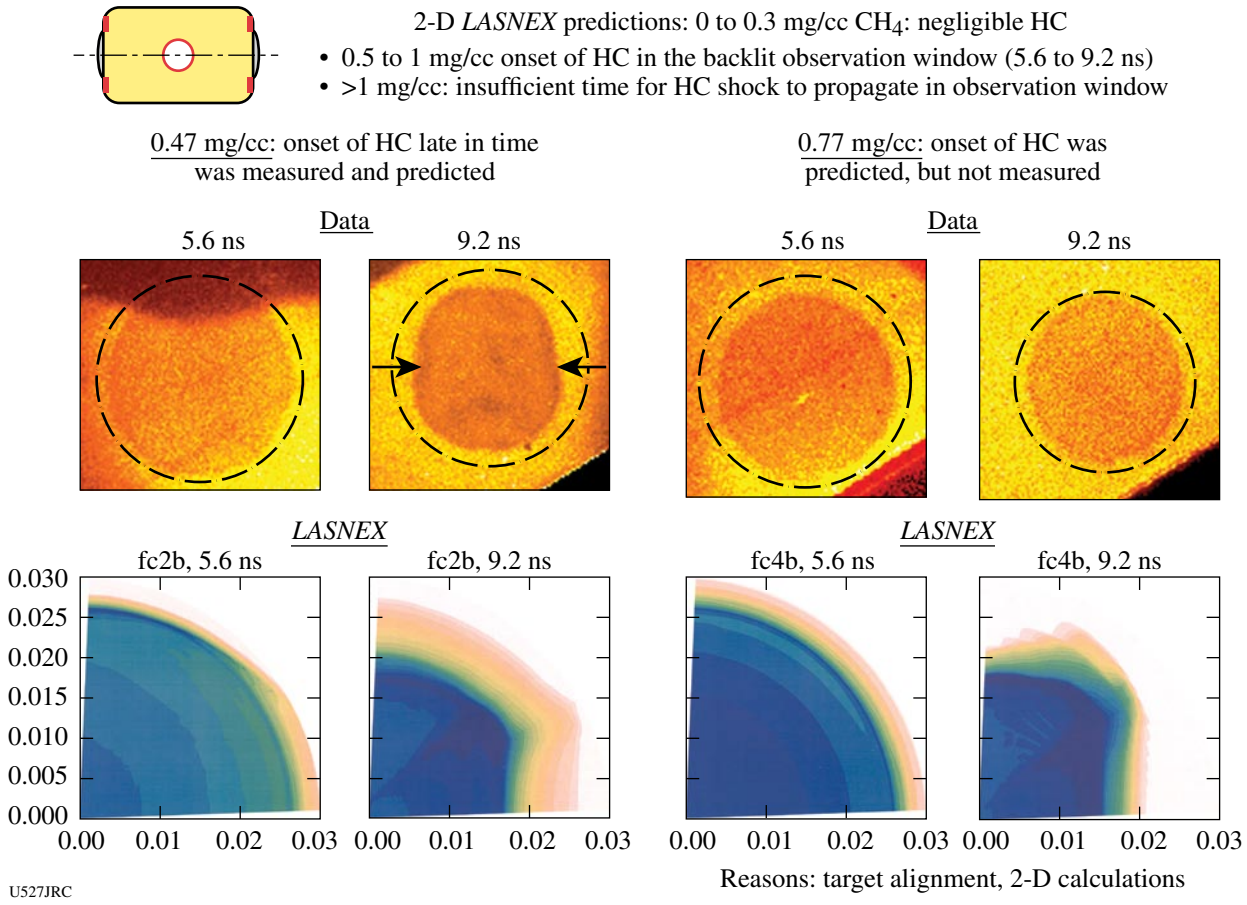

Figure 104.77
X-ray images from "gas-hydro" experiments. Top: X-ray backlit images of foam targets in 0.47 mg/cc and 0.77 mg/cc CH_4-filled hohlraums. Bottom: *LASNEX* simulations showing effects of gas hydrodynamics coupling to the implosion. The onset of hydrodynamic coupling was measured and predicted at low fill density but not observed at high density.

RTI in Be-Doped CH: Experiments were conducted to develop a Rayleigh–Taylor instability platform for accurately measuring the Rayleigh–Taylor growth rate of Be and Be doped with Cu ablators in direct comparison with more traditional CH ablators.

HEP-4: The HEP-4 series of implosions are integrated experiments that use standardized hohlraums and laser pulse shapes while varying the surface finish of the capsules by deliberately roughening them. The resulting neutron yields are compared to simulations with capsule-fuel mix models; the initial measured capsule perturbation spectrum is included in the simulation for each capsule to enable direct comparison with the experimental results. These experiments have been carried out on OMEGA for some time and were completed this year. Results are shown in Fig. 104.78.

Cocktail Experiments: "Cocktail" experiments were measurements of the effective x-ray drive power in hohlraums made of a mixture of high-*Z* materials (typically Au, Dy, U), in contrast to a single material. In FY05, considerable research and development from target fabrication at LLNL and GA was applied to reduce the impurity level of oxides in these targets, leading to measured unambiguous expected increases in x-ray flux (Fig. 104.79).

2ω LPI Experiments: A week of experiments was done with beam 25 converted to 2ω (530 nm). Measurements of laser–plasma interaction physics with "green" light were done in both hohlraum and open (using gas-bag targets) geometries. Figure 104.80 shows measurements from a 2ω beam that was propagated axially along a laser-heated hohlraum. Measurements of the 2ω beam transmission and stimulated backscatter

are shown. In addition, experiments were done with half-hohlraums to measure the overall x-ray conversion efficiency of 2ω light in direct, simultaneous comparison to the efficiency when using the 3ω light typical of OMEGA.

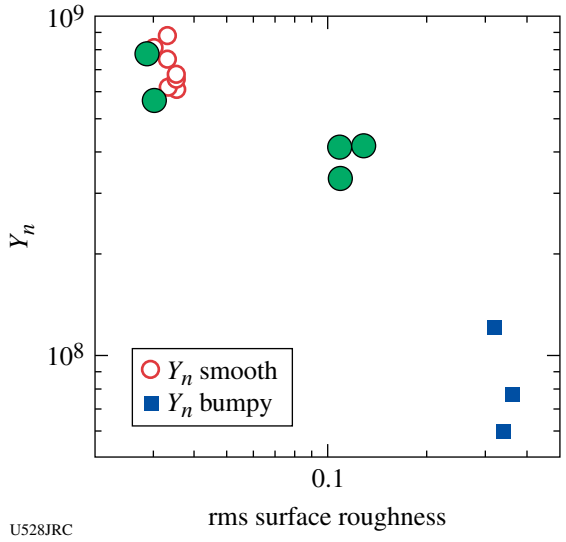

Figure 104.78
Neutron yield as a function of capsule roughness for HEP-4 experiments. Large filled data points were obtained in April 2005. Small open dots are smooth capsule data and square data were obtained in the prior campaigns.

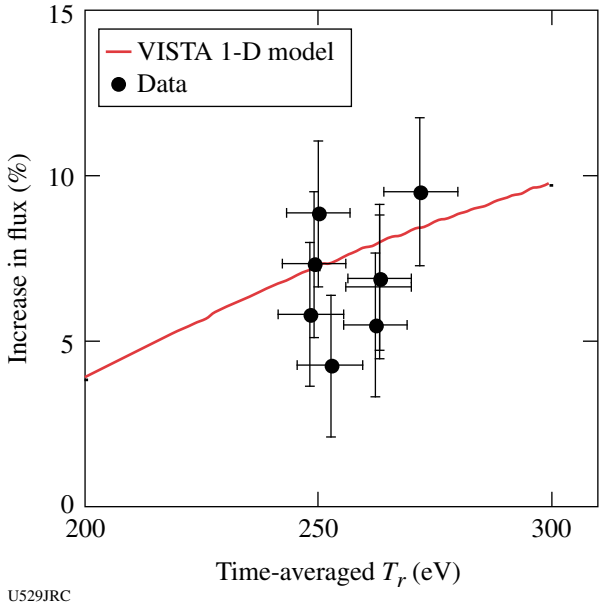

Figure 104.79
A plot of the measured (black dots) and VISTA 1-D model predicted an increase in x-ray flux of a cocktail hohlraum with a composition of $Au_{0.2}U_{0.6}Dy_{0.2}$ versus conventional Au hohlraums as a function of time-averaged radiation temperature (T_r).

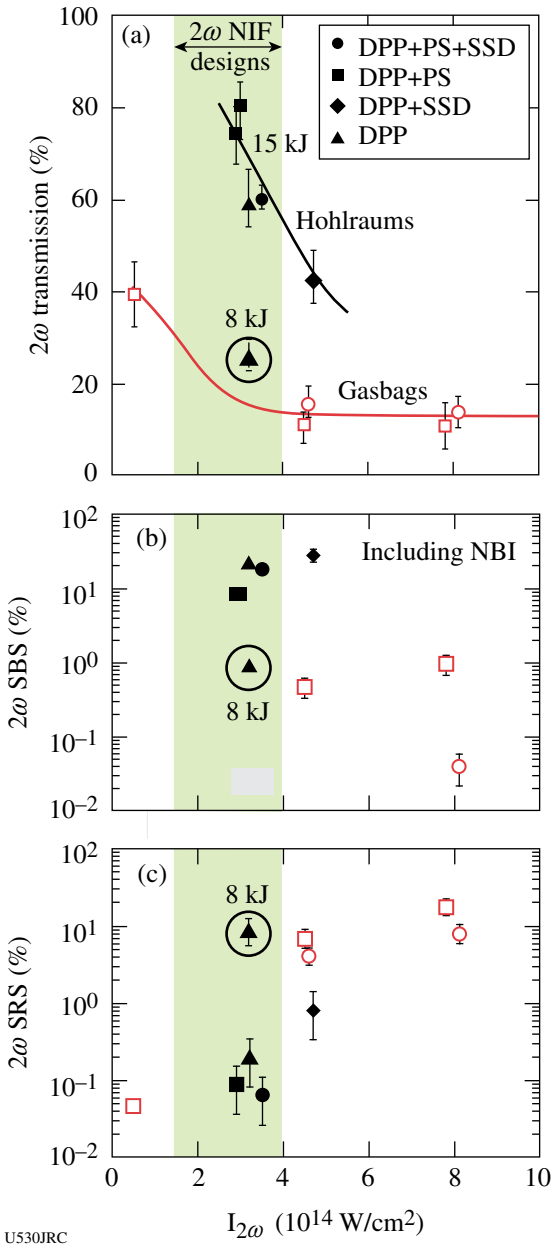

Figure 104.80
(a) Plots of 2ω beam transmission through a hohlraum (solid data points) and through gas bags (open points). Similar comparison for SBS (b) and SRS (c).

Plan "B": After encouraging laser–plasma interaction physics were obtained from SiO_2 foam-filled hohlraums, a series of foam-filled hohlraums with implosion capsules inside them were shot ("Plan B"). These yielded results similar to traditional vacuum hohlraums, indicating little or no deleterious effects on the x-ray drive for ICF-relevant foam fills.

X-Ray Thomson Scattering: X-ray scattering experiments were carried out, showing expected spectral features after scattering a strong line source from the hot plasma. The data were used to infer an electron temperature in the plasma.

4ω Thomson Scattering: A week of experiments was done with beam 25 converted to 4ω (260 nm). The principal focus was using the 4ω light for Thomson scattering measurements. Numerous improvements were made to the diagnostics from previous experiments, and the resulting data was of high quality, enabling the measurement of the electron temperature immediately external to a hohlraum laser entrance hole and from within a hohlraum. Figure 104.81 shows the Thomson-scattering-derived electron temperature from within a gas-filled hohlraum for three different laser energies. Careful characterization of these hohlraums is preliminary to their future use for LPI studies.

FY05 LANL OMEGA Experimental Programs

Los Alamos National Laboratory (LANL) successfully fielded a range of experiments on OMEGA during FY05 to study the physics relevant to inertial confinement fusion (ICF) and high-energy-density (HED) science in support of the National ignition effort. Many of these experiments were focused on developing underlying physics, diagnostics, and platforms for future experiments on the National Ignition Facility (NIF). LANL conducted a total of 138 target shots on OMEGA. Collaborations with LLNL, LLE, and AWE remain an important component of LANL's program on OMEGA. With the consolidation of ignition research in the United States into the National Ignition Campaign (NIC), healthy partnerships are required to achieve success in our National scientific objectives.

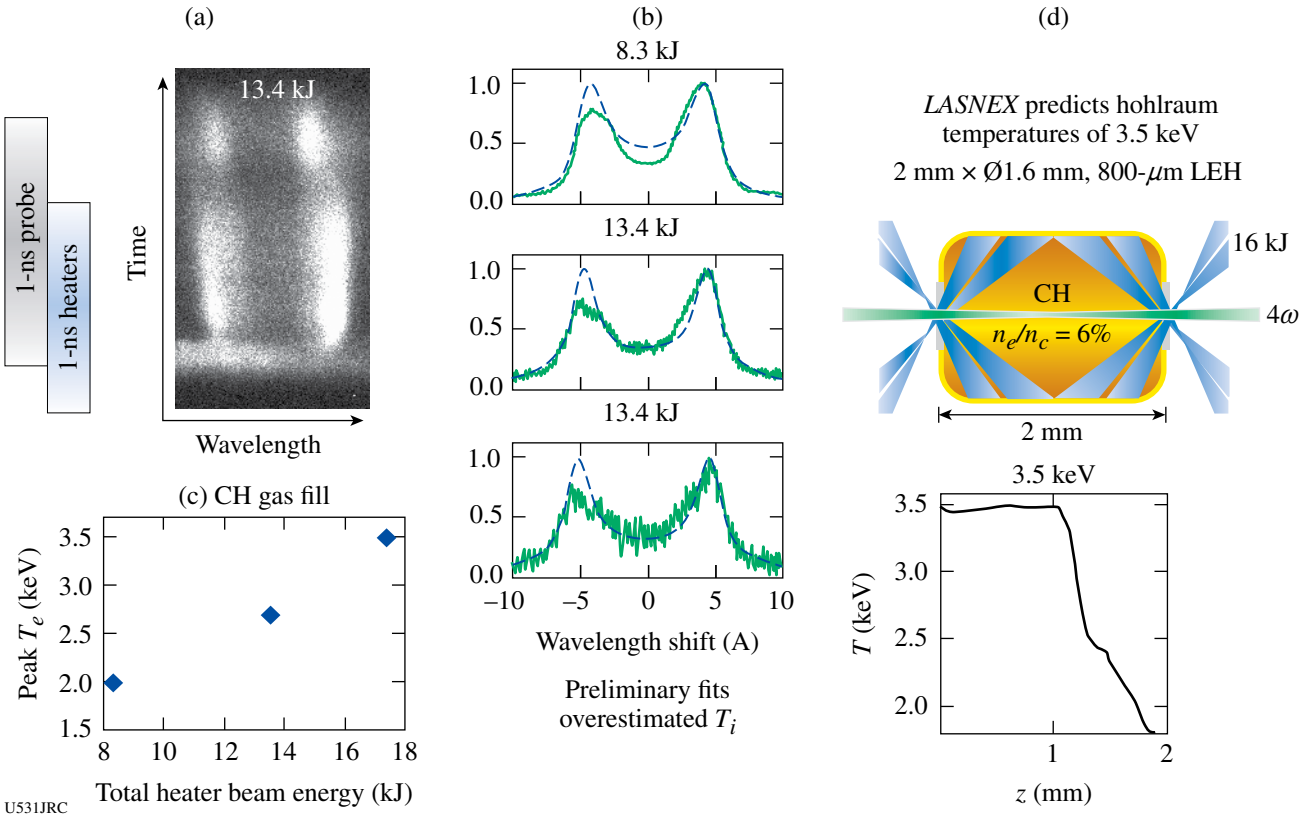

Figure 104.81
Data from 4ω Thomson scattering experiments: (a) streak camera record of spectrally resolved Thomson scattering spectrum, (b) scattering light spectra at various heater beam energies, (c) inferred electron temperature from these spectra, and (d) *LASNEX* predictions.

Beryllium Ablator Microstructure Stability (BAMS): The end goal of this project remains the delivery of a specification for the microstructure of ignition-capsule ablators to the National ICF program with the current focus on beryllium-copper ablators with 0.9% Cu by atom.

Two days of experiments using gas-filled hohlraums demonstrated the fabrication of small-amplitude Be sinusoids and measured growth of the sine wave perturbations in Be in a radiation-drive environment for the first time. The composite laser pulse consists of a combination of two separate OMEGA pulse shapes with a duration approaching 6 ns. Through VISAR measurements, a ~1-Mbar first shock in the Be (Cu) samples was observed. The methane gas fill held the Au walls of the hohlraum back for >10 ns to enable late-time, face-on x-ray radiography, thus demonstrating the growth of the sinusoid and evolution toward a spike-and-bubble behavior. Figure 104.82 shows a face-on, 1.7-keV radiograph of a sinusoid taken at 9.3 ns after the drive began. A lineout showing spike-and-bubble formation is illustrated in Fig. 104.83. The loss of laser energy to laser–plasma instabilities is modest (<10%), concentrated late in time, and clamps the radiation temperature near 145 eV.

In x-ray sidelighting experiments, differences between powder-pressed Be samples and sputtered samples as they are ejected from the hohlraum were observed. This difference may be related to excessive voids in the sputtered samples. The LANL theoretical group is modeling the shock breakout and preheat of the BeCu samples to reproduce the as-measured radiation drive and to duplicate the "rollover" in growth rates of the instability growth with large-amplitude (2.5-μm) sinusoids.

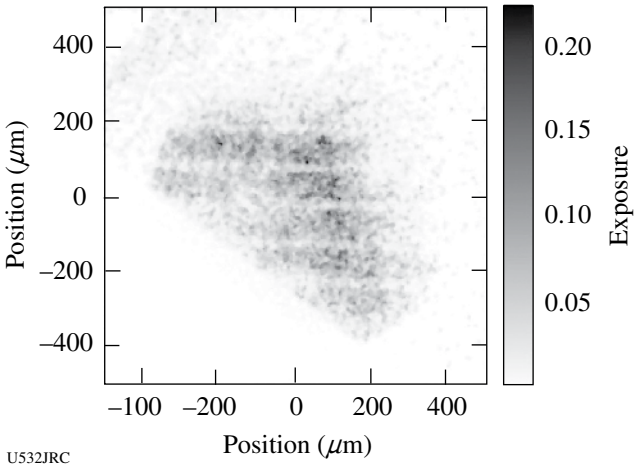

Figure 104.82
A face-on radiograph of a BeCu sinusoid (shot 39660) at 9.3 ns after the start of hohlraum drive.

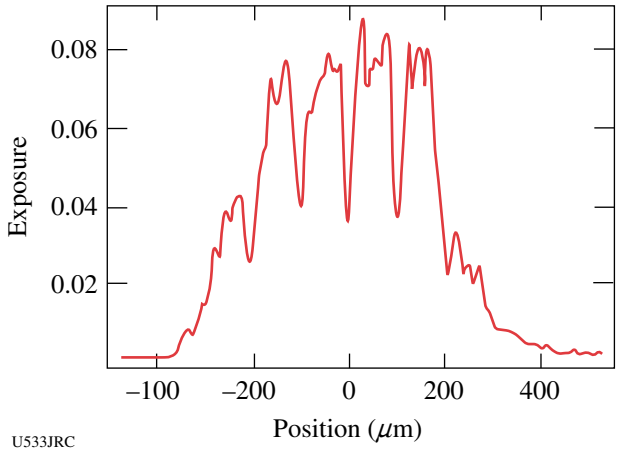

Figure 104.83
A lineout from the 9.3-ns data showing the growth of the sinusoidal perturbations and bubble–spike formation.

Off-Hugoniot Stability: The off-Hugoniot (OH) campaign studies material dynamics under heated and shocked conditions. In ignition capsules, defects arising from the manufacturing process undergo significant evolution because of heating from Au M-band radiation prior to the passage of the main shock. It has not been demonstrated that the hydrocodes being used to model these experiments accurately capture the physics of this interaction. The OH platform provides the means to study the complex interactions between shocks and heated material.

The OH platform utilizes a Be housing that is coated with a thin layer of tin. Inside the housing are layers of foam and epoxy. Thirty-three beams strike the tin, produce L-shell radiation that permeates throughout the package, heating the epoxy and foam (Fig. 104.84). A short time later, seven beams launch a strong shock into the foam. As the heated epoxy expands in the foam, the shock interaction with this system is imaged radiographically.

This year, the last phase of test bed development was completed in which shock planarity and speed were characterized and the interaction with an unheated defect was observed (Fig. 104.85). The next phase of campaign will advance to the fully integrated experiments of shock interaction with preheated material interfaces.

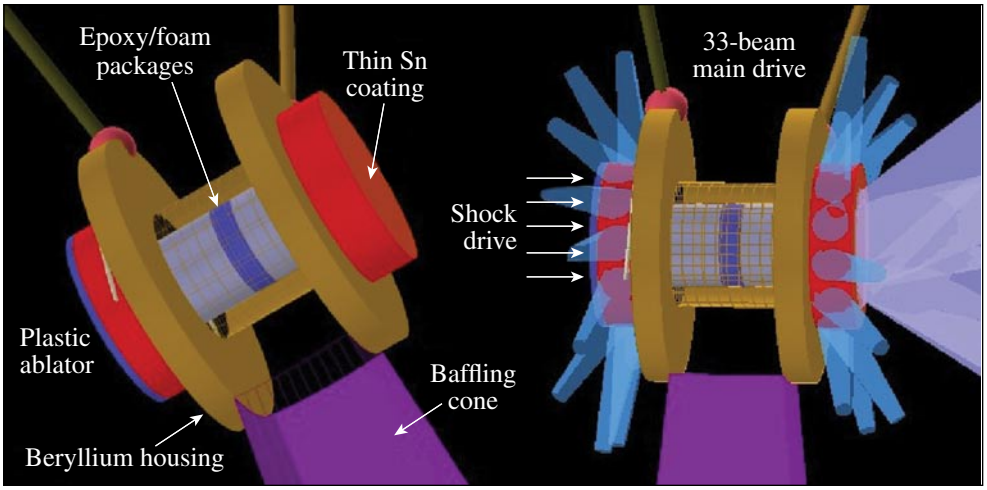

U534JRC

Figure 104.84
The target configuration for the off-Hugoniot experiment. A beryllium housing stuffed with layers of epoxy and foam are heated by exciting tin L-shell radiation. The evolution of the epoxy expanding into the foam is imaged via radiography.

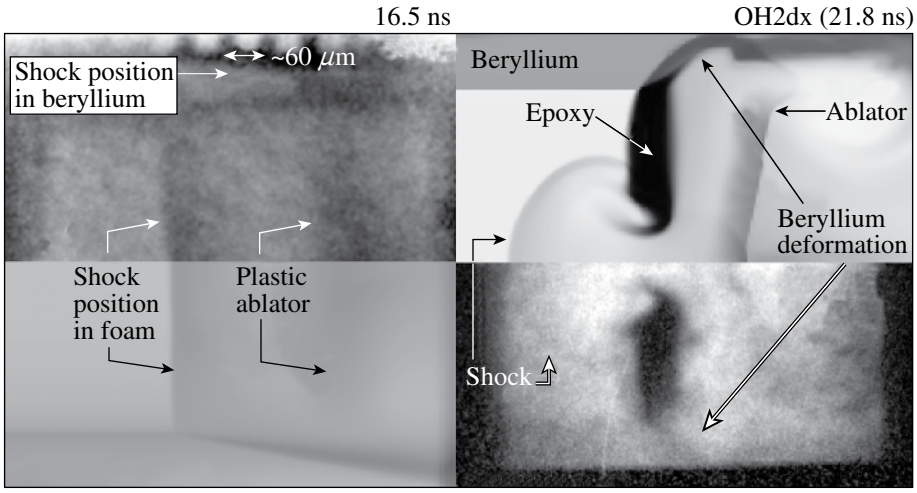

U535JRC

Figure 104.85
(a) Comparisons between measurement and simulation (*RAGE*) of the shock position and planarity and (b) the unheated defect having experienced a strong shock.

Double-Shell Implosions: Double-shell implosions may provide a noncryogenic path ICF. Because of their complex implosion dynamics, however, double-shell capsules are much more sensitive to symmetry than their single-shell counterparts. Moreover, engineering defects, such as gaps formed during manufacturing, can play a large role in affecting their fusion yield.

To better understand these issues, two experimental campaigns were conducted on OMEGA. The first characterized the zero-order implosion dynamics of a double-shell capsule implosion. The second measured how a gap purposefully machined in the outer shell evolved throughout the implosion. Selected results are presented.

Figure 104.86 shows the measurements of the inner and outer shell positions as compared with the simulated radiographs from *LASNEX*. Figure 104.87 displays a pre-shot radiograph and obtained shot data from a double-shell implosion with a deliberate engineering defect applied to the interior side of the outer surface. This data is used to quantify the defect's impact on the implosion symmetry.

Inhomogeneous Radiation Flow: Radiation transport calculations become greatly complicated in regions where two or more materials are inhomogeneously mixed. Laboratory experiments were performed to test the modeling of radiation transport through inhomogeneous plasmas.

A laser-driven hohlraum creates a radiation front, which propagates through a foam/gold particle mixture (Fig. 104.88). The position of the radiation front is measured as a function of time with a soft x-ray imager (Fig. 104.89). Three different foam–gold mixtures were examined experimentally (Fig. 104.90). One mixture was purely foam, another mixture was loaded with 2-μm-diam gold particles, and the last mixture was loaded with 0.5-μm-diam gold particles. Each of the doped foams contained the same amount of gold volumetrically. Preliminary results from these experiments show the radiation front propagation slows in the presence of smaller gold particles. The next set of planned experiments have the objective of making a single temperature measurement of the radiation front.

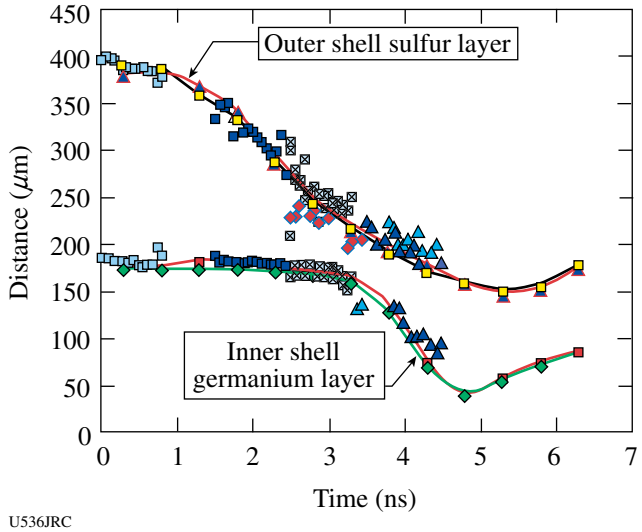

Figure 104.86
Measurements (symbols) of the outer and inner shell marker layers, showing collision near 3.6 ns. The solid lines are the *LASNEX* predictions as extracted from the simulated radiographs.

Beryllium Fill-Tube Defect Studies: Current ignition target designs for the NIF use a copper-doped beryllium (BeCu) ablator. Since DT cannot diffuse through the Be ablator, another filling method is required. The leading option is to use a fill tube, however, the tube provides a perturbation on the capsule that may affect the ignition capsule implosion. Initial experiments were performed that developed a planar platform to investigate the effect of a fill tube on ICF capsule performance.

The experimental configuration (Fig. 104.91) consists of a driven hohlraum, which heats and shocks the attached Be (0.9% Cu). Beryllium material then jets through the hole and into the surrounding vacuum. Two backlighters are used to image different aspects of the experiment. An iron backlighter resolves the shock position in the Be disk. A Teflon (C2F4) backlighter captures the jet with its C and F He-α lines (310 eV and 740 eV, respectively) using the soft x-ray imager. We also obtained images with the Teflon continuum. A definite jet was observed (Fig. 104.92) with a 30-μm-diam hole. The jet has a length and width of the order of 100 μm. This series of experiments validate the planar platform, which will be used by NIC in future experiments.

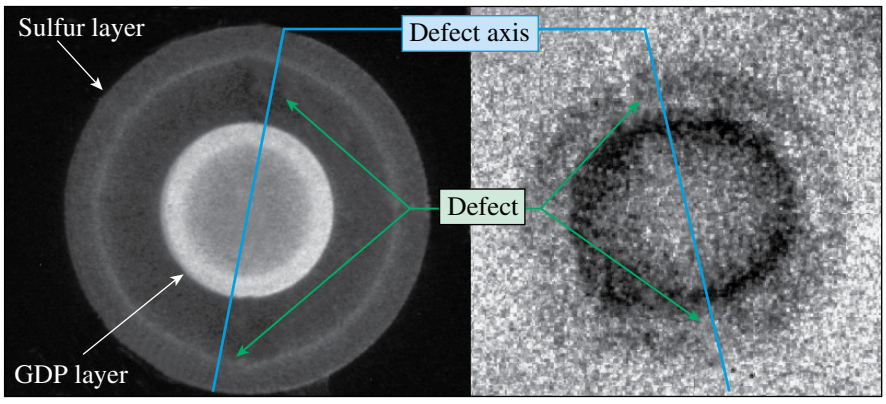

Figure 104.87
(a) A preshot radiograph of a defect capsule. (b) An image of the implosion near 3.8 ns showing the interaction between the defect and inner shell.

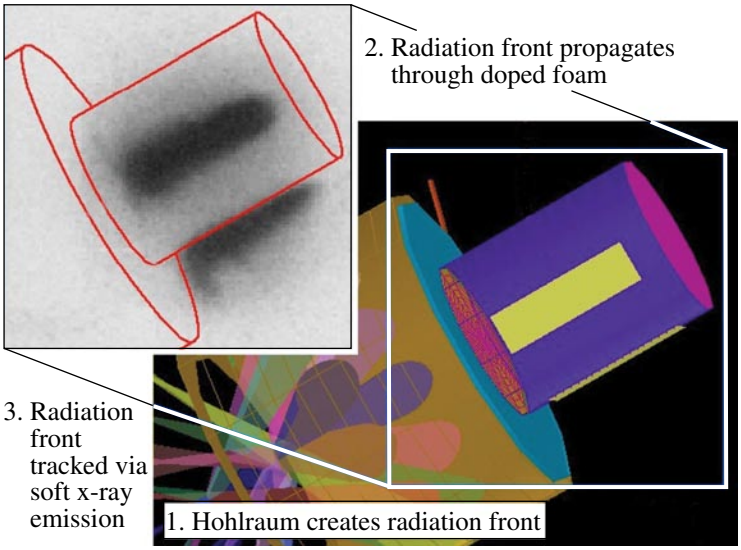

Figure 104.88
Sixteen beams heat a gold hohlraum, which produce a radiation front that propagates through the foam. Diagnostics slits allow measurement of the front's progression.

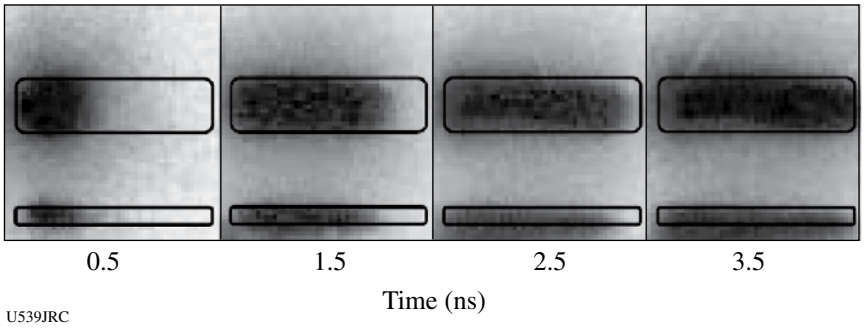

Figure 104.89
The temporal evolution of the radiation front as tracked by the soft x-ray emission.

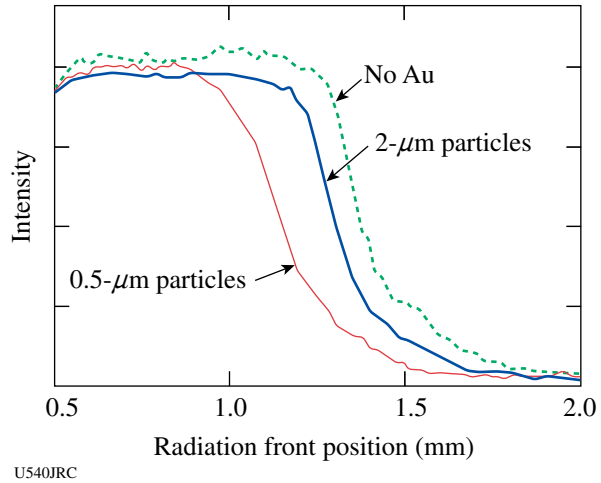

Figure 104.90
The radiation front position at 3.5 ns as it propagates through three foam types: no gold, 2-μm particles, and 0.5-μm particles. Data clearly show that propagation is slowed as gold particulates become smaller.

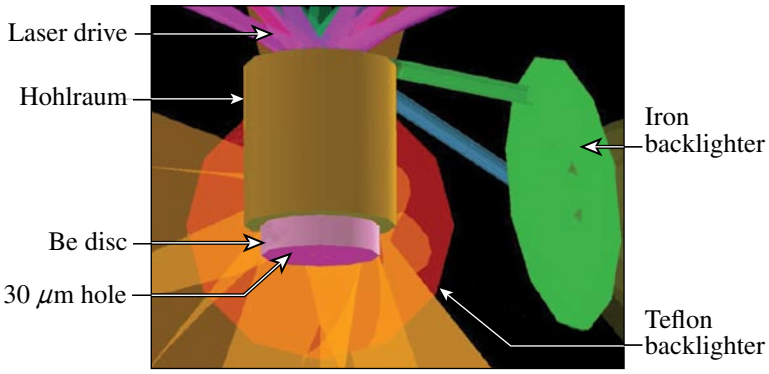

Figure 104.91
A heated gold hohlraum drives a shock into the beryllium disc creating a jet as the Be is forced out the small hole at the bottom. The Be jet and disc are imaged from two orthogonal directions.

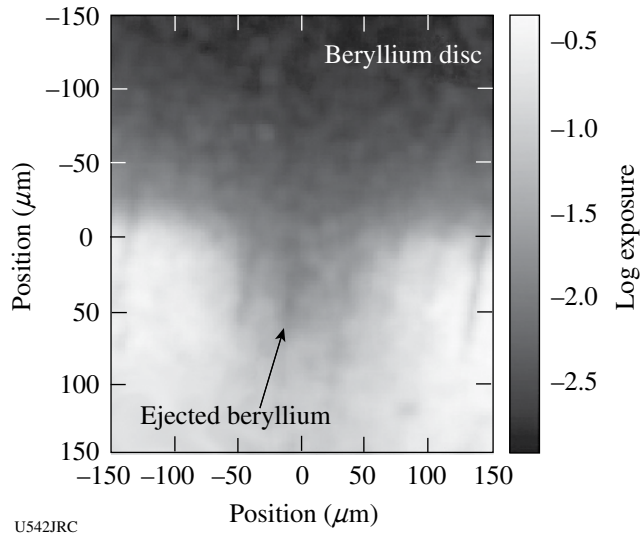

Figure 104.92
Radiograph from shot 40407 showing the jetting of copper-doped (0.9%) beryllium at 4 ns. The central photon energy was 310 eV (C He-α). The jet has expanded about 100 μm into the vacuum.

ACE-D: The ACE-D experiment on OMEGA investigated several areas of radiation hydrodynamics in preparation for experiments using two bundles of the NIF. One research avenue was to decrease the size of the hohlraums to create higher radiation temperatures. Using 3/4-scale hohlraums, radiation temperatures of higher than 220 eV were reached. A second test was to line the hohlraum with a low-density (9 mg/cm^3) aerogel foam to decrease the influx of Au wall material into the radiographic line of sight. The liner noticeably prevented the wall from occluding the line of sight, but the radiation temperature was also reduced substantially. There was, however, no increase in backscattered energy due to either stimulated Raman scattering (SRS) or stimulated brillouin scattering (SBS) as measured by the full-aperture backscatter (FABS) calorimeter.

Pinhole-Apertured, Point-Projection Backlighter (PAPBL) Studies: Imaging experiments at the NIF require the use of pinhole-apertured, point-projection backlighting (PAPBL) with gated instruments. Although this technique provides a much more efficient use of backlighter photons, the absence of a pinhole array between the target and imaging system greatly enhances the susceptibility to extraneous noise sources. With this in mind, backlighter development experiments were performed at OMEGA to developed techniques to mitigate these undesired sources that degrade image quality.

The main objective of these experiments was to successfully image a driven hohlraum using zinc and germanium K-shell lines. The target consisted of a hohlraum with two gold grids mounted on the rear. Two orthogonal backlighters were used and a conical shield served to mitigate the noise source arising for the driven hohlraum (Fig. 104.93).

Images were obtained of the hohlraum's rear, including the grids for both undriven and driven hohlraums using a zinc backlighter. Moreover, we also obtained an undriven image of the hohlraum using a Ge (10.3 keV) backlighter (Fig. 104.94). This experiement's results provide confidence that orthogonal PAPBL imaging can be used successfully in the future.

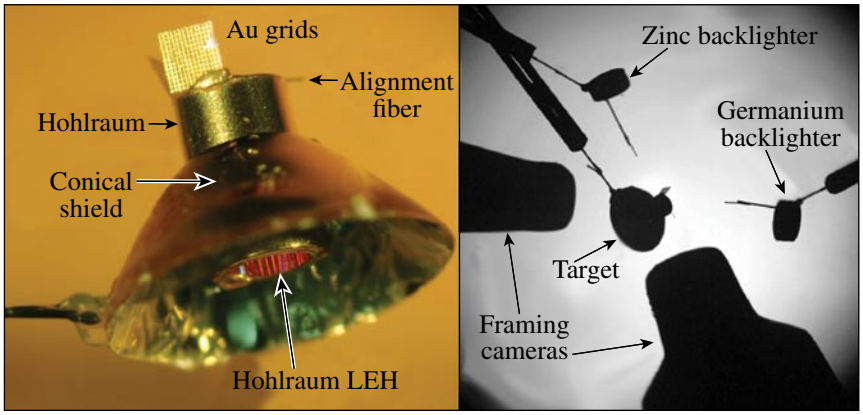

U543JRC

Figure 104.93
(a) An optical picture of the target showing the hohlraum, gold grids, and large gold conical shield. (b) The pre-shot target viewing system image of the experimental configuration showing the locations of the hohlraum, Zn and Ge backlighters, and two nose tips for the diagnostics.

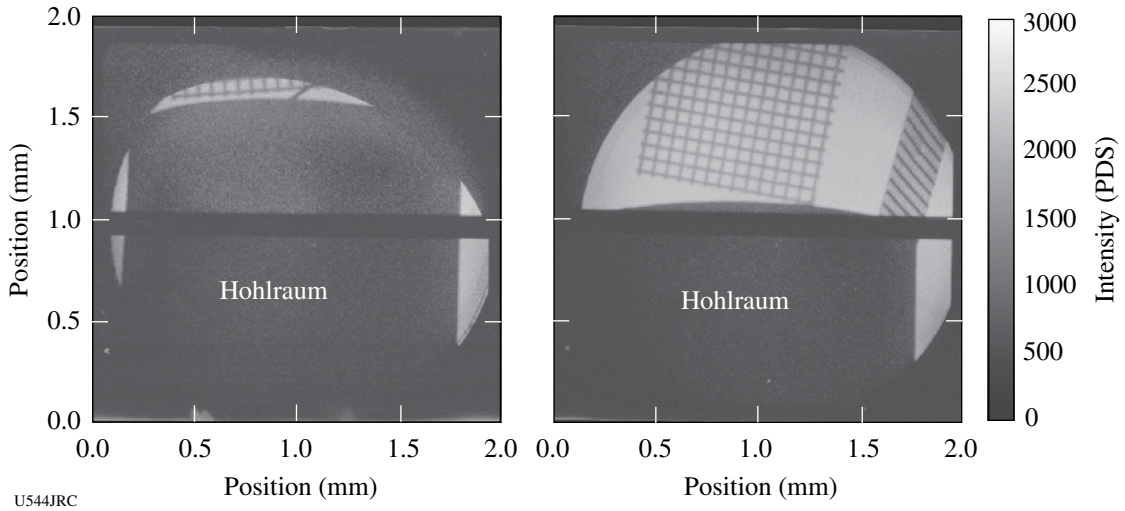

U544JRC

Figure 104.94
(a) An image of a driven hohlraum with a Zn (~9 keV) backlighter. Some background noise from the driven hohlraum is still present, but the grid is still quite resolved. (b) An undriven hohlraum using a Ge backlighter (10.3 keV). As expected, the grids show very nice resolution.

High-Z Shell Implosions: Initial proof-of-principle experiments studying the effect of high-*Z* dopants on capsule burn were completed. These early experiments utilized deuterium-filled ignition capsules in which differing levels of krypton gas were introduced as a dopant. Previous experiments show that our hydrocodes calculate the effect of the high-*Z* dopant in ignition capsules poorly. Measurements of the neutron yield, ion temperature, and x-ray emission from the hot gas were obtained. Initial results indicate that the yield was lower than predicted, the ion temperature was higher than predicted, and the x-ray emission was lower than expected. More detailed analysis is being done to understand these results and to design FY06 experiments.

Time-Dependent Mix: The time-dependent mix campaign seeks to explore the mixing of shell material into the fuel of an inertial confinement fusion implosion. A thin layer of lightly doped titanium plastic is embedded into the inside surface of the plastic capsule. As the shell mixes into the fuel, the titanium heats up and radiates characteristic atomic lines that give information about the electron density and temperature in the vicinity of the titanium ions. The titanium was carefully chosen such that the ratio of more highly ionized to less ionized titanium could be used to infer the temperature at the point of emission, and thus tell us how far into the hot core the mix has reached at any particular time. The layer of titanium can be placed at the inside surface of the capsule or embedded

beneath the surface at a predefined depth. A series of capsules with progressively greater depths can tell us how much of the capsule material participates in mix. When the embedding depth is greater than the thickness of the layer that mixes, the hydrogenic titanium emission will disappear.

X-ray images of the capsule's implosion are shown in Fig. 104.95. The data clearly show the onset of K-shell emission arising from the titanium that has mixed into the core. We have determined that the amount of shell mix is between 0.5 and 1.0 μm and have also observed more mix than simulations would predict, thus constraining the parameters used in these models. This is apparent both from the nuclear yield and the amount of x-ray emission.

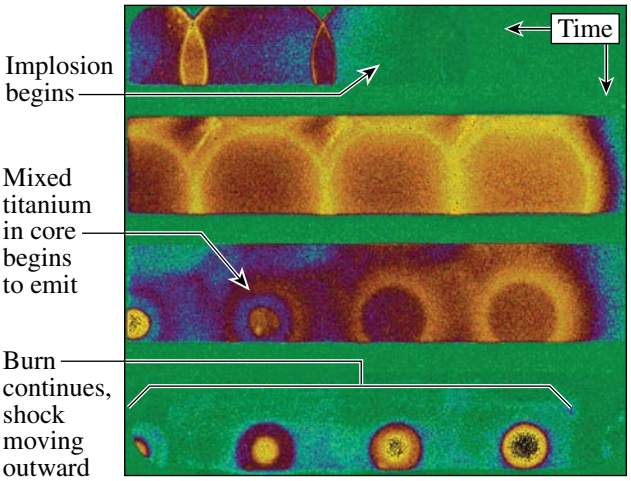

Figure 104.95
X-ray images of the capsule implosion showing the onset of titanium K-shell emission arising from the titanium that has mixed into the core.

FY05 Sandia National Laboratories Experiments on OMEGA

SNL performed 31 target shots on OMEGA in FY05.

Modification of a Laser Hohlraum Spectrum via a Mid-Z Wall Liner: A typical laser hohlraum has a radiation spectrum that includes a significant component of non-Planckian, high-energy photons (such as Au M-band x rays) that originate in and near the hot, low-density coronal plasma in which the laser light is absorbed and converted into x-rays. These hard x-rays can have undesirable effects for an inertial confinement fusion (ICF) application, such as causing preheat ahead of the shock front in the ablator of an indirect-drive capsule.[5] In FY04 a new concept was implemented for tailoring the spectrum in a hohlraum that uses a thin, mid-*Z* liner to supply plasma for the x-ray conversion with an underlying high-*Z* wall for x-ray containment.[6] In a series of FY05 experiments performed at the OMEGA Laser Facility, this concept was demonstrated to be effective for a wide range of laser intensities and hohlraum temperatures. The DANTE unfolded radiation temperature shown in Fig. 104.96 illustrate the dramatic reduction in M-band flux as the associated hohlraum temperatures increase over the range of 120 to 200 eV.

X-Ray Preheat in Indirect-Drive ICF Ablator Materials: In previous work[5] measurements of ablator shock velocities, shock temperatures, and preheat temperatures were made using a 280-nm streaked optical pyrometer (SOP).[7] More recent ablator experiments on OMEGA have extended this work by using an absolutely calibrated 600 to 800 nm SOP[8] with a line-imaging velocity interferometer.[9] Important new information has been obtained relating to ablator surface movement prior to shock breakout, ablator preheat temperature, and preheat effects on the anvil and window components of the shock-timing diagnostic system. Results from an experiment involving a 32-μm-thick beryllium ablator are shown in Fig. 104.97. In this experiment, 15 OMEGA beams delivered 2.8 kJ (in a 3.7-ns square pulse) into the interior of the hohlraum. The DANTE measurement of the hohlraum radiation temperature is shown in Fig. 104.97(a); the SOP measurement of the temperature of the exterior-facing side of the Be sample in Fig 104.97(b); and the VISAR measurement of the surface velocity of the Be sample in Fig 104.97(c). For all plots, time is relative to laser turn on at t = 0. Shock breakout occurs at ~1.5 ns with peak of the shock flash intensity occuring approximately 200 ps later. As indicated in Fig. 104.97(a), the hohlraum radiation temperature prior to t = 1.5 ns is in the range of 75 to 115 eV. Figure 104.97(b) indicates a pre-shock heating of the external Be surface to ~2 eV prior to shock breakout. Figure 104.97(d) indicates that the Be surface begins moving soon after the laser turn on and reaches a pre-shock velocity exceeding 6 μm/ns. As can be seen in Fig. 104.97(c), this velocity cannot measured for times >1.1 ns because of the loss of surface reflectivity. Per Fig. 104.97(b), the surface temperature at the time of reflectivity loss is approximately 1 eV.

Indirect-Drive ICF Shock Timing Diagnostic Development Experiments: Accurate measurements of shock timing and ablator x-ray burnthrough will be essential for the successful ignition of an indirect-drive ICF capsule. In FY05, we performed the initial tests of an experimental platform similar to the diagnostic proposed for accurate National Ignition Facility

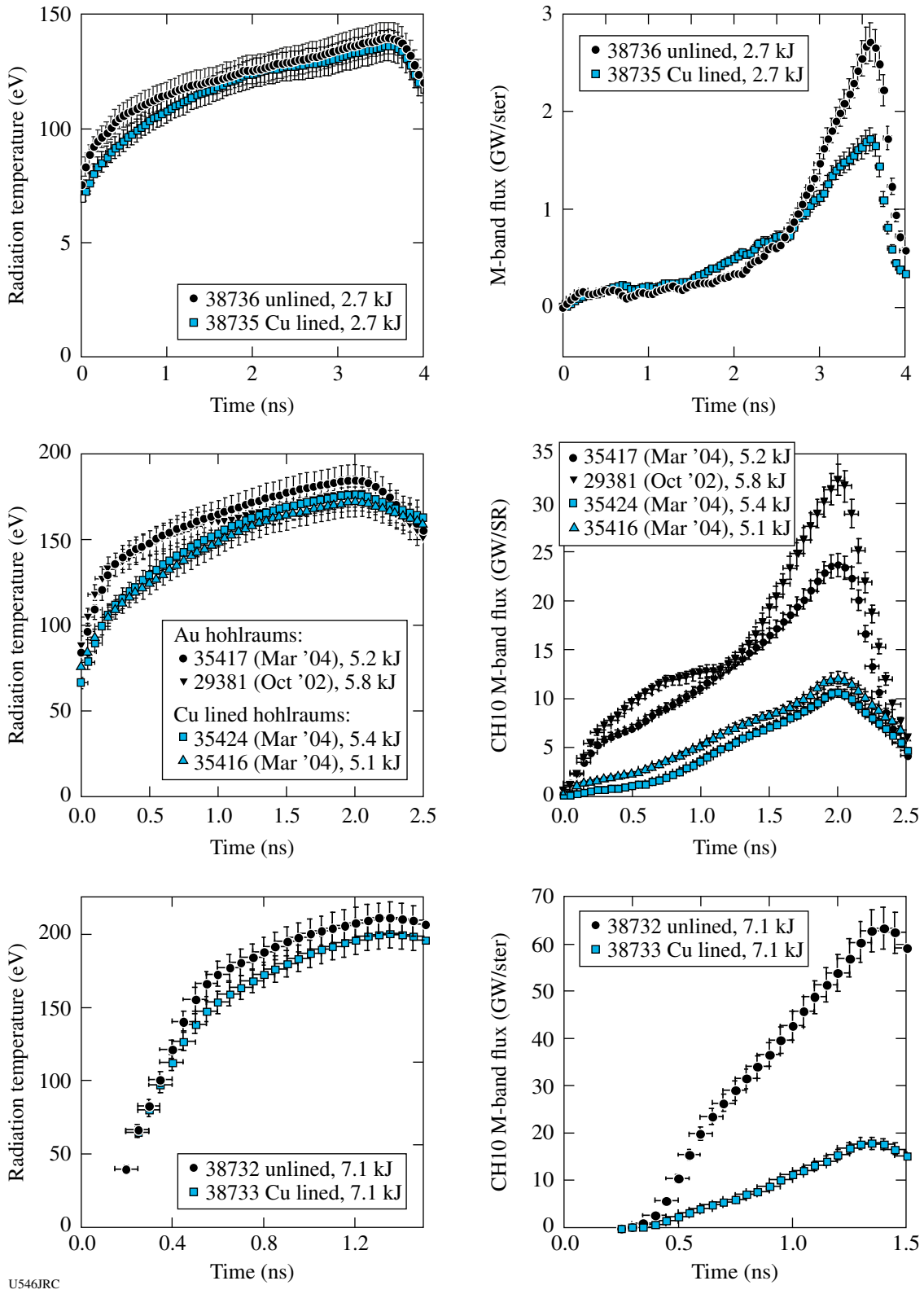

Figure 104.96
DANTE-unfolded radiation temperature as a function of time for several hohlraum configurations (three plots on the left). M-band intensity versus time for the same shots (three plots on the right).

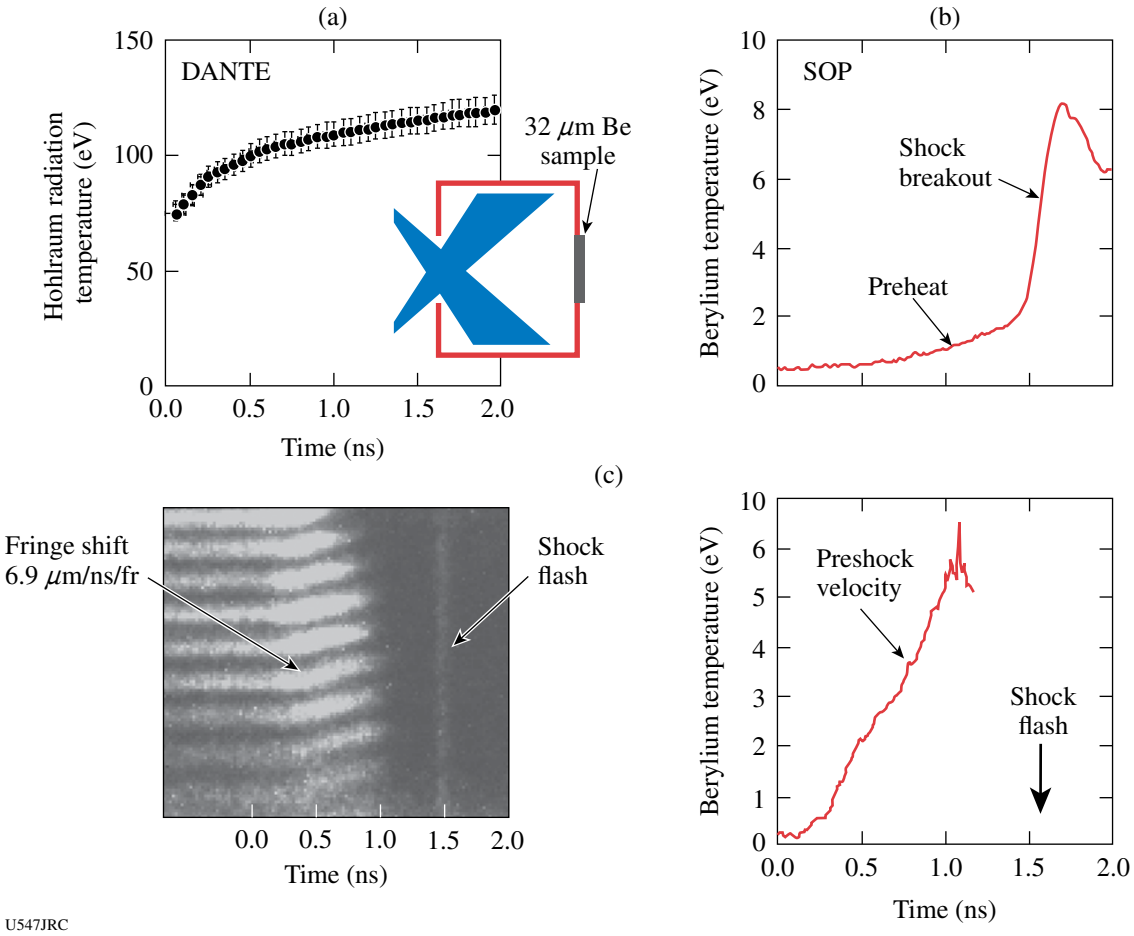

Figure 104.97
Indirect-drive experiment with a 32-mm-thick Be ablator. (a) DANTE measurement of hohlraum radiation temperature versus time, (b) SOP measurement of Be surface temperature versus time, (c) VISAR data showing fringe shift and shock flash, and (d) VISAR measurement of Be surface velocity.

(NIF) ignition shock-timing measurements.[10] Full-scale ignition capsules and pre-ignition shock-timing experiments at the NIF will utilize Cu-doped Be ablators with a thickness of ~150 μm. Our first attempts at testing the proposed shock-timing techniques utilized the geometry illustrated in Fig. 104.98. The 150-μm-thick ablator sample consisted of a pair of 75-μm-thick Be foils with a 0.5-μm-thick Cu foil sandwiched between the Be foils. In terms of overall ablator thickness and opacity, this approximates the proposed NIF ignition capsule ablator. A window was placed at a distance of ~1 mm from the ablator surface. In a few experiments, a liquid deuterium-filled cryostat was attached to the hohlraum, with the window at the same location (Fig. 104.99). Results from a experiment with a relatively low temperature hohlraum drive are shown in Fig. 104.98. In this experiment, the 15 OMEGA beams delivered 1.5 kJ (in a 3.7-ns square pulse) into the interior of the hohlraum. The DANTE measurement of hohlraum radiation temperature is shown in Fig. 104.98(a), and the SOP measurement of the temperature of the exterior-facing side of the Be sample is shown in Fig. 104.98(b). As can be seen in the figure, the surface preheat begins soon after laser turn on and the surface temperature levels off at ~3.7 ns, when the laser turns off. Shock breakout occurs at ~7.2 ns. In relation to the experiment of Fig. 104.97, the reduced preheat level in Fig. 104.98 is consistent with the lower hohlraum temperature, the Cu component, and the thicker ablator. As explained in Ref. 5, the lower shock temperature is consistent with the reduced level of ablator preheat. An important finding in these experiments is that as hohlraum temperatures (and laser-spot intensities) are increased, the window is (apparently) also preheated and becomes opaque. A quartz window remained transparent throughout the laser pulse for hohlraumm temperatures of up to 136 eV [Fig. 104.99(a)]. For hohlraum temperatures exceeding 140 eV (corresponding to laser intensities at the hohlraum

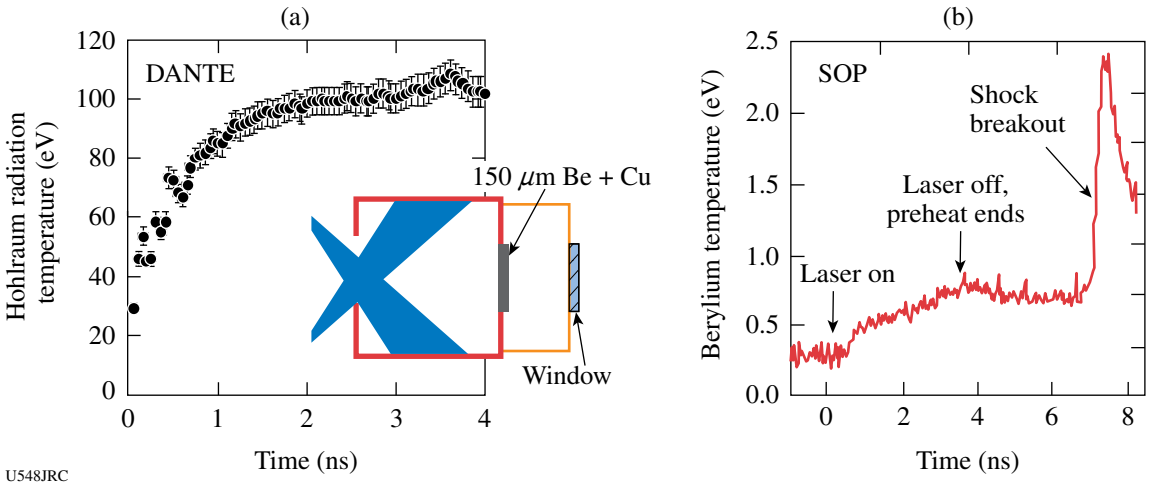

Figure 104.98
Shock breakout measurements: (a) DANTE-derived radiation temperature and (b) SOP-measured temperature of the exterior of the Be foil.

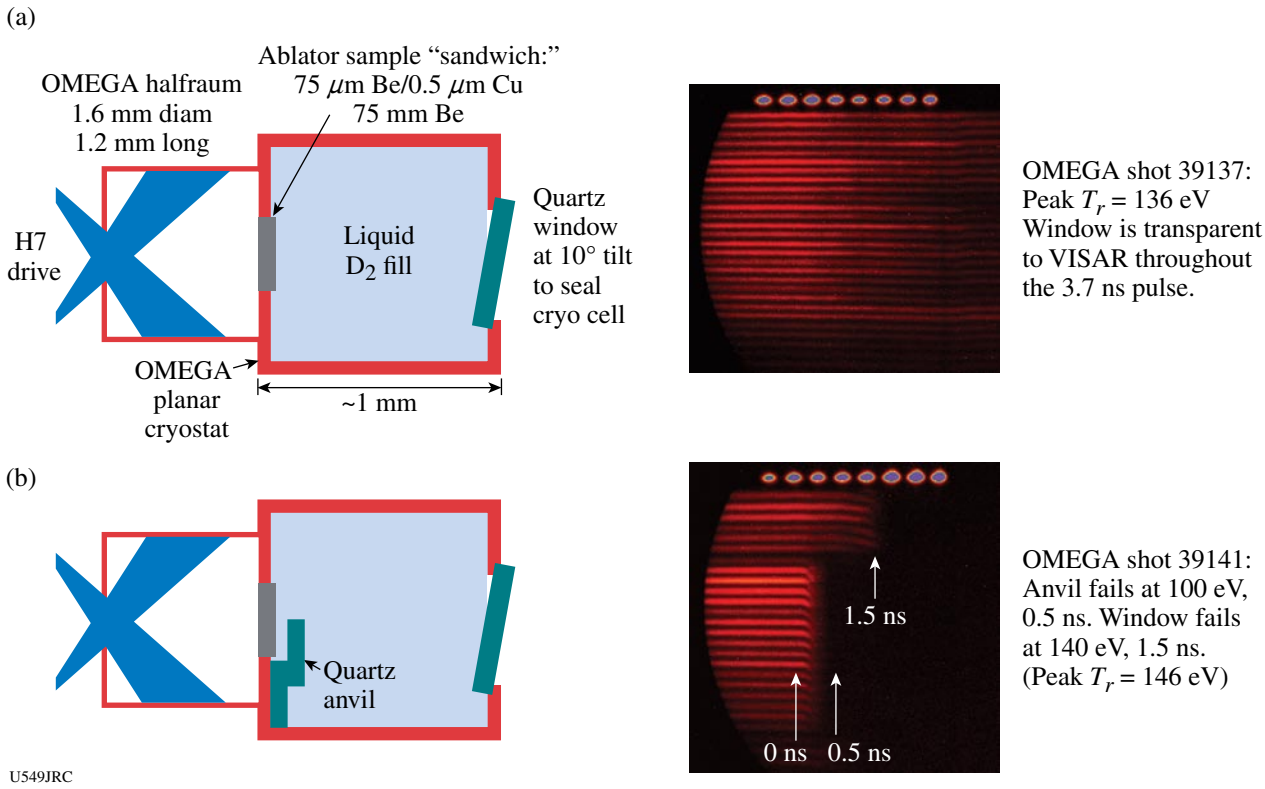

Figure 104.99
Window transparency: (a) quartz window maintains transparency up to $T_r \sim 136$ eV, (b) quartz anvil becomes opaque at $T_r > 100$ eV and window fails at 140 eV.

wall ~1×10^{14} W/cm^2), however, windows and anvils became opaque soon after laser turn on [Fig. 104.99(b)]. In the near future, new window materials, laser smoothing, and geometric effects will be tested in an attempt to reduce window and anvil preheat effects to a level consistent with the requirements of the proposed NIF shock-timing diagnostic.

Cocktail Burnthrough and Re-emission: SNL conducted 11 shots in June 2005 to study the relative difference in burnthrough time and x-ray re-emission between thin cocktail and Au foils. Figure 104.100 shows the sample geometry and example data for the experiments. These were the first tests of the layered 75% U, 25% Au cocktail material made by General Atomics that is currently specified as the hohlraum wall material in the NIF point design. The experiments studied the difference in performance between cocktails and Au in hohlraums with peak radiation temperatures of 175 eV, 235 eV, and 270 eV. Preliminary results show that the difference in burnthrough between Au and cocktails at 550-eV photon energy is ~0 ps at T_r = 170 eV, and ~50 ps at T_r = 230 eV (the foils in the 270-eV hohlraums burnthrough at a time when the radiation temperature is ~230 eV). Time-gated x-ray pinhole camera measurements were configured with four different filter-mirror combinations to sample the wall re-emission across spectral ranges of ~200 to 250 eV, ~400 to 500 eV, ~600 to 800 eV, and ~800 to 1000 eV. Preliminary results show a 20±15% increase in the re-emission from cocktails in the energy band from ~400 to 500 eV at hohlraum radiation temperatures >220 eV and no statistically significant increase or decrease in any other energy band. Future work will include detailed comparisons between the experimental data and integrated *LASNEX* calculations with the best known opacities of Au and U.

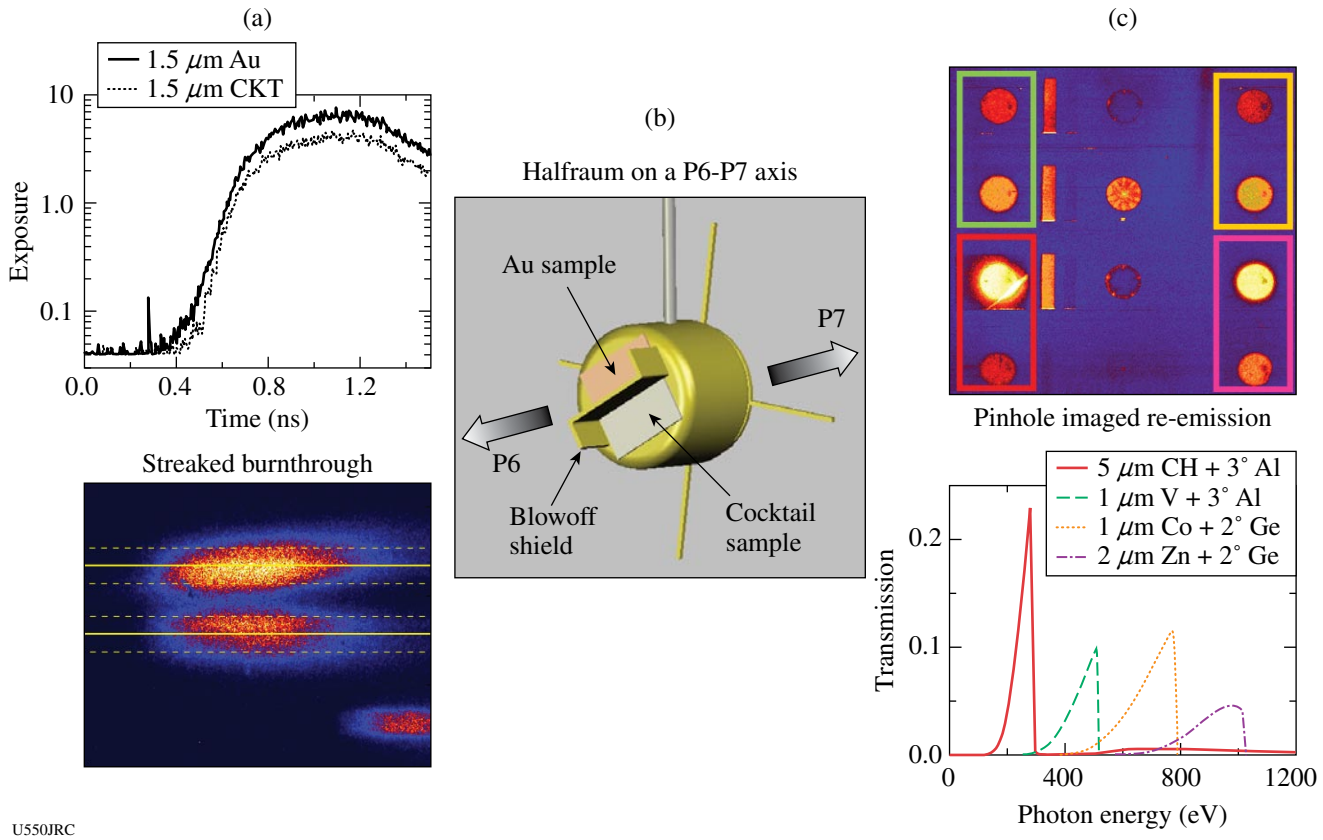

Figure 104.100
Example data, (a) and (c), and geometry (b) from cocktail burnthrough and re-emission experiments conducted by SNL in June 2005. On the left is burnthrough data (b) taken with an x-ray streak camera at P6, and on the right (c) is x-ray framing camera data at P7 with four different mirrored channels.

2005 CEA Experiments on OMEGA

Scientists from CEA led several OMEGA experimental campaigns in FY05 including the development of neutron imaging and hohlraum symmetry experiments. A total of 34 OMEGA target shots were taken for CEA experiments in FY05.

Penumbral and Annular Imaging for Inertial Confinement Fusion Neutron Images

1. Introduction

In inertial confinement fusion experiments, laser energy is used to compress a millimeter-sized (diameter) target filled with deuterium and tritium. The compression results in the creation of a hot spot where the fusion reactions begin. On the NIF (U.S.A.) or LMJ (France), 14-MeV neutron images will be used to determine the dimensions and the shape of the hot spot. Since the dimensions of the hot spot will be ~50 μm, a spatial resolution below 10 μm will be required in a neutron image to distinguish between the different failure mechanisms of the implosion (symmetry, laser pulse shaping, etc.).

CEA developed a neutron imaging system (NIS) using a penumbral[11,12] and, most recently, an annular[13] imaging technique with a high-resolution neutron camera that was tested on OMEGA during high-neutron-yield shots. The images obtained with these tests attained a 20-μm spatial resolution with a high signal-to-noise ratio (SNR). With these results we can now consider a preliminary design for a NIS with a resolution of 10 μm on OMEGA and 6 to 7 μm on the NIF or LMJ.

2. Experimental Setup

Neutrons emitted by the target go through a coded aperture that is placed 26 cm from target chamber center (TCC). Two coded apertures can be used: a penumbral or an annular. Both are made of a biconical hole built in a 10-cm-long DENAL (Tungsten alloy) cylinder. The diameter at the intersection of the cones is ~2 mm. The ring is obtained by placing a plug inside the hole so that the aperture is equivalent to a continuous assembly of 8-μm-diam pinholes distributed along a circle (Fig. 104.101).

An enlarged image of the coded aperture is projected on a neutron camera placed at a distance of ~8 m from TCC. The camera is composed of a coherent array of one-million glass capillaries, 85 μm in diameter, filled with a high-refractive-index organic liquid scintillator. Neutrons mainly interact by elastic scattering on hydrogen nuclei. As they lose kinetic energy, the recoil protons produce light, a part of which is guided through the stepped-index fiber optics made by glass (n = 1.49) and scintillator (n = 1.56). The image is then transported, intensified, and reduced to be registered on a one-million pixel CCD (20×20 mm^2).

The spatial resolution Δs of the overall system is given by

$$\Delta s = \sqrt{\left[\frac{\ln(2) \times FOV}{2 \times L_0 \times \mu}\right]^2 + \Delta s_{\text{det}}^2 \times \left(\frac{L_0}{L_1}\right)^2}, \qquad (1)$$

where FOV is the field of view, L_0 and L_1 the target to aperture and target to detector distances, respectively, Δs_{det} is the resolution of the camera, and μ is the attenuation of neutrons in the DENAL cylinder. During the past few years, improvements in the detector design have led to the achievement of a camera resolution of ~650-μm FWHM. Since the camera resolution is limited primarily by the recoil length of protons, this value can be reduced to 400 μm by replacing hydrogen atoms with deuterium in the scintillator.[14]

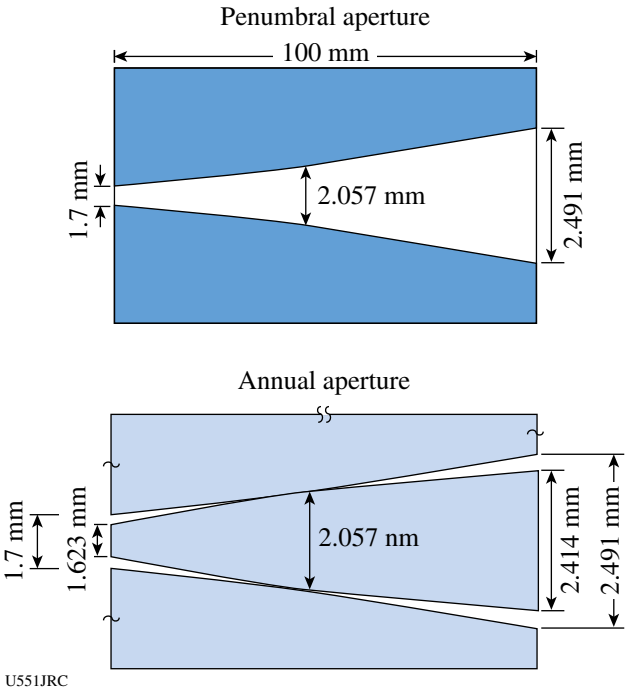

Figure 104.101
Sections of the penumbral- and annular-coded apertures. Both have the same dimensions. A plug is placed inside the second aperture to define a ring equivalent aperture.

3. 2005 High-Yield Shots

In 2004, neutron images were acquired with the penumbral technique. A spatial resolution of 20 μm and a SNR of ~20 to 25 were demonstrated with this system. In 2005, the detector was unchanged except for replacement of the fiber optic reducer (taper) between the capillary array and the microchannel plate (MCP). The quality of this taper improved the uniformity and the transmission of the image on the whole field of view. The annular imaging technique was tested and compared with results obtained with the penumbral aperture for the same type of targets to prove the reliability of the technique. Figure 104.102 presents raw images, penumbral and annular, for plastic-shell targets and compares annular images for a plastic and a glass target. Glass targets produce a larger core than plastic ones. This is confirmed by observing the raw images as the thickness of the ring is directly related to the source diameter in one dimension. Figure 104.103 shows unfolded images for both techniques on DT(15)CH[15], DT(15)CH[20], and DT(15)SiO_2[2.5] targets. The images have a 20-μm spatial resolution. The corresponding neutron yields Y_n and SNR are written on each image. Plastic targets have a high convergence ratio for relatively high yields, which leads to very good SNR around 30 to 40. Though glass targets result in higher neutron yields, the larger cores produce images with a lower SNR of ~15. Comparison of the penumbral and annular images shows that the dimensions and shape of the hot-spot dimensions are the same for similar targets. The ring technique was chosen because it will result in a high SNR in high-resolution images. This was confirmed by applying a 20-μm and then a 10-μm FWHM low-pass filter on the image for both techniques. The SNR of both penumbral and annular images was near 40 for a 20-μm filter, though it decreased to 14 in the penumbral image and still remained 28 in the ring image for a 10-μm filter.[15]

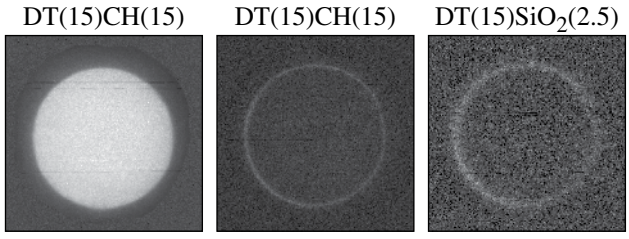

Figure 104.102
Raw images obtained with a penumbral (left) and an annular (center and right) apertures.

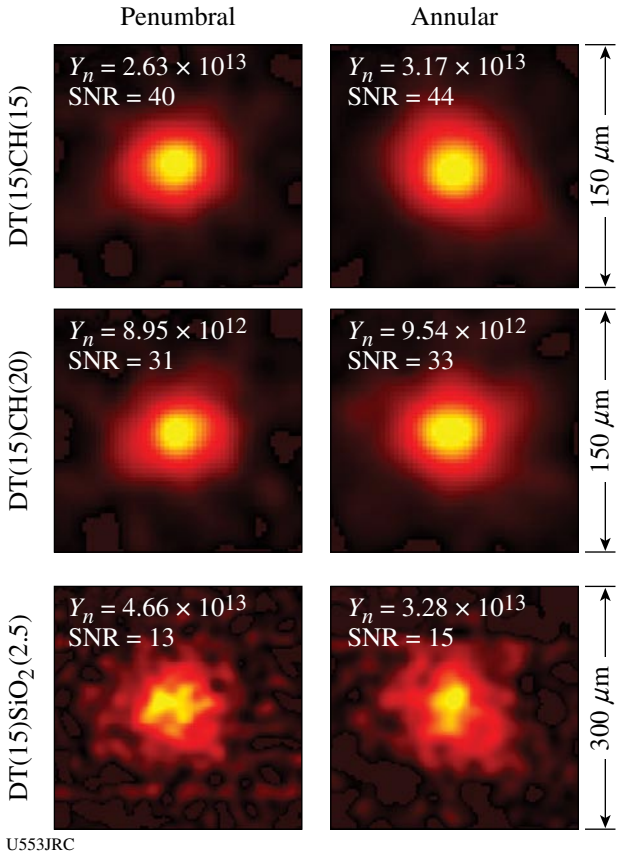

Figure 104.103
Unfolded images obtained during 2005 high-yield shots. Comparison between penumbral and annular techniques for three types of targets.

4. 2005 DD Shots

With 2.45-MeV DD neutrons, the recoil ion length in the scintillator is much shorter. As a consequence, the resolution of the detector is much better, ~230 μm compared to ~650 μm for DT neutrons. The improved sensitivity of the camera is sufficient to acquire a DD image with a neutron yield of about 10^{11}. Neutron images were thus registered on DD shots, including cryogenic targets. Figure 104.104 shows examples of neutron images obtained with a cryogenic target (left) and with a gas-filled plastic shell target (right). The resolution is set to 50 μm and 35 μm, respectively, because of the low yield relatively close to the threshold of sensitivity of the camera, which implies a compromise between resolution and SNR.

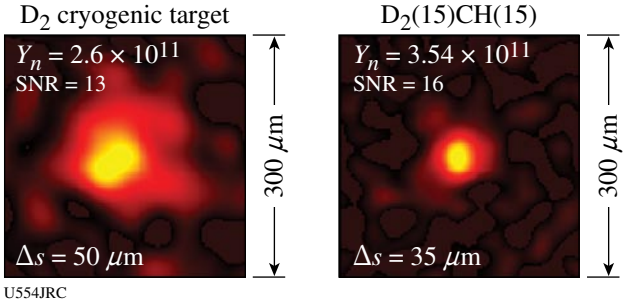

Figure 104.104
Neutron images of DD targets.

5. Conclusions

During the 2005 high-yield shots on OMEGA, DT neutron images were acquired with a 20-μm spatial resolution and very high SNR. The annular imaging technique was tested and demonstrated higher signal-to-noise ratio images compared to the penumbral imaging technique. With an enhanced detector and a ring-coded aperture, a 10-μm spatial resolution on OMEGA and 10-μm spatial resolution on the NIF or LMJ is now projected.

The neutron camera was sensitive enough to acquire DD images, but the low yield resulted in a reduction to the resolution to improve the quality of the image. A new detector design is now being considered to acquire DD neutron images. This camera will have an enhanced detection quantum efficiency with smaller dimensions to work with a lower magnification ratio.

CEA Symmetry Experiments

In previous years, CEA carried out an experimental campaign to study the irradiation symmetry of radiation-driven capsules in cylindrical hohlraums heated by a multicone arrangement of beams. In FY05, CEA experiments were carried out to characterize the symmetry by imaging the core x-ray emission[16] of 500-μm, 50-atm, D_2-filled capsules doped with 0.1-atm argon. These capsules were produced by CEA/Valduc. Shell thickness variation was used to probe symmetry at different times during the implosion.

Figure 104.105(a) gives an example of a core image obtained with a 37-μm CH, 2% at., Ge-doped capsule. This image is obtained at an instant (3.1 ns) close to peak compression. The convergence ratio Cr ~ 7 can be determined on a similar capsule by backlighting the shell implosion. From Cr and core ellipticity, we can infer an irradiation P2 component of ~1% (Ref. 17), which is consistent with the expected symmetry from previous foam-ball experimental data, time-integrated evolution of flux P2 component in simulations, and also with data reported in Ref. 18.

Backlighting tests of imploding capsules were carried out. Figure 104.105(b) shows an example of a shot where a simultaneous image of core emission and backlighting of the dense shell is recorded. This provides valuable data to benchmark hydrodynamic simulations. We can infer from these data an implosion velocity of ~100 μm/ns and a convergence ratio from the minimum radius of the dense part of the shell of ~7.

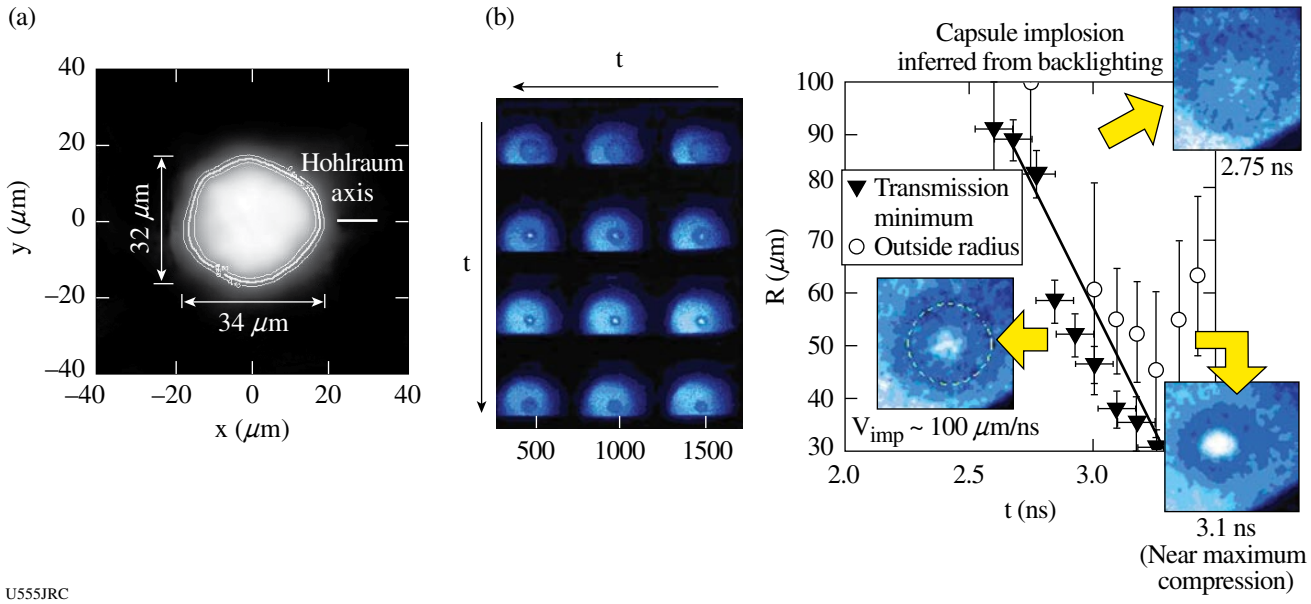

Figure 104.105
(a) Example of an imploded core image. (b) Backlit image of imploding capsule showing, on the same data, an image of core emission and absorption through the dense part of the shell.

REFERENCES

1. S. D. Rothman *et al.*, J. Phys. D **38**, 733 (2005).
2. W. J. Nellis *et al.*, Phys. Rev. Lett. **53**, 1248 (1998).
3. V. Ya. Ternovoi *et al.*, in *Shock Compression of Condensed Matter, AIP Conference Proceedings 620*, edited by M. D. Furnish, N. N. Thadhani, and Y. Horie (American Institute of Physics, New York, 2002), pp. 107–110.
4. A. Forster, T. Kahlbaum, and W. Ebeling, Laser Part. Beams **10**, 253 (1992).
5. R. E. Olson *et al.*, Phys. Rev. Lett. **91**, 235002 (2003).
6. R. E. Olson *et al.*, Bull. Am. Phys. Soc. **49**, 24 (2004).
7. J. A. Oertel *et al.*, Rev. Sci. Instrum. **70**, 803 (1999).
8. J. Miller, T. R. Boehly, E. Vianello, W. J. Armstrong, C. Sorce, W. Theobald, D. D. Meyerhofer, J. Eggert, and D. G. Hicks, Bull. Am. Phys. Soc. **49**, 64 (2004).
9. P. M. Celliers, D. K. Bradley, G. W. Collins, D. G. Hicks, T. R. Boehly, and W. J. Armstrong, Rev. Sci. Instrum. **75**, 4916 (2004).
10. D. H. Munro *et al.*, Phys. Plasmas **8**, 2245 (2001).
11. A. Rouyer, Rev. Sci. Instrum. **74**, 1234 (2003).
12. R. A. Lerche *et al.*, Laser Part. Beams **9**, 99 (1991).
13. R. G. Simpson *et al.*, Opt. Eng. **14**, 490 (1975).
14. L. Disdier, R. A. Lerche, J. L. Bourgade, and V. Yu. Glebov, Rev. Sci. Instrum. **75**, 2134 (2004).
15. L. Disdier, A. Rouyer, I. Lantuejoul, O. Landuas, J. L. Bourgade, T. C. Sangster, V. Yu. Glebov, and R. A. Lerche, "Inertial Confinement Fusion Neutron Images," to be published in Physics of Plasma.
16. A. Hauer *et al.*, Rev. Sci. Instrum. **66**, 672 (1995).
17. J. D. Lindl *et al.*, Phys. Plasmas **11**, 339 (2004).
18. P. Amendt, R. E. Turner, and O. L. Landen, Phys. Rev. Lett. **89**, 165001 (2002).

Publications and Conference Presentations

Publications

V. Bagnoud, I. A. Begishev, M. J. Guardalben, J. Puth, and J. D. Zuegel, "5 Hz, >250 mJ Optical Parametric Chirped-Pulse Amplifier at 1053 nm," Opt. Lett. **30**, 1843 (2005).

V. Bagnoud, J. Puth, I. Begishev, M. Guardalben, J. D. Zuegel, N. Forget, and C. Le Blanc, "A Multiterawatt Laser Using a High-Contrast, Optical Parametric Chirped-Pulse Preamplifier," in *Conference on Lasers and Electro-Optics/Quantum Electronics and Laser Science and Photonic Applications, Systems and Technologies 2005* (Optical Society of America, Washington, DC, 2005), Paper JFA1.

S. Costea, S. Pisana, N. P. Kherani, F. Gaspari, T. Kosteski, W. T. Shmayda, and S. Zukotynski, "Use of Tritium in the Study of Defects in Amorphous Silicon," Fusion Sci. Technol. **48**, 712 (2005).

J. E. DeGroote, A. E. Marino, K. E. Spencer, and S. D. Jacobs, "Power Spectral Density Plots Inside MRF Spots Made with a Polishing Abrasive-Free MR Fluid," in *Optifab 2005* (SPIE, Bellingham, WA, 2005), Vol. TD03, pp. 134–138.

W. R. Donaldson, M. Millecchia, and R. Keck, "A Multichannel, High-Resolution, UV Spectrometer for Laser-Fusion Applications," Rev. Sci. Instrum. **76**, 073106 (2005).

R. A. Forties and F. J. Marshall, "*In Situ* Characterization of High-Intensity Laser Beams on OMEGA," Rev. Sci. Instrum. **76**, 073505 (2005).

H. L. Helfer, "The Local Dark Matter," in *Progress in Dark Matter Research*, edited by J. Val Blain (Nova Science, New York, 2005), Chap. 4, pp. 121–147.

D. G. Hicks, T. R. Boehly, P. M. Celliers, J. H. Eggert, E. Vianello, D. D. Meyerhofer, and G. W. Collins, "Shock Compression of Quartz in the High-Pressure Fluid Regime," Phys. Plasmas **12**, 082702 (2005).

Z. Jiang and J. R. Marciante, "Mode-Area Scaling of Helical-Core Dual-Clad Fiber Lasers and Amplifiers," in *Conference on Lasers and Electro-Optics/Quantum Electronics and Laser Science and Photonic Applications, Systems and Technologies 2005* (Optical Society of America, Washington, DC, 2005), Paper CThR3.

T. Z. Kosc, K. L. Marshall, S. D. Jacobs, and J. C. Lambropoulos, "Polymer Cholesteric Liquid-Crystal Flake Reorientation in an Alternating-Current Electric Field," J. Appl. Phys. **98**, 013509 (2005).

T. Kosteski, N. P. Kherani, W. T. Shmayda, S. Costea, and S. Zukotynski, "Nuclear Batteries Using Tritium and Thin Film Hydrogenated Amorphous Silicon," Fusion Sci. Technol. **48**, 700 (2005).

I. A. Kozhinova, H. J. Romanofsky, A. Maltsev, S. D. Jacobs, W. I. Kordonski, and S. R. Gorodkin, "Minimizing Artifact Formation in Magnetorheological Finishing of Chemical Vapor Deposition ZnS Flats," Appl. Opt. **44**, 4671 (2005).

S. G. Lukishova, A. W. Schmid, R. Knox, P. Freivald, R. W. Boyd, C. R. Stroud, Jr., and K. L. Marshall, "Deterministically Polarized Fluorescence from Single Dye Molecules Aligned in Liquid Crystal Host," in *Conference on Lasers and Electro-Optics/Quantum Electronics and Laser Science and Photonic Applications, Systems and Technologies 2005* (Optical Society of America, Washington, DC, 2005), Paper QTuE6.

J. R. Marciante and J. D. Zuegel, "High-Gain, Polarization-Preserving, Yb-Doped Fiber Amplifier for Low-Duty-Cycle Pulse Amplification," in *Conference on Lasers and Electro-Optics/Quantum Electronics and Laser Science and Photonic Applications, Systems and Technologies 2005* (Optical Society of America, Washington, DC, 2005), Paper JWB60.

M. Mikulics, R. Adam, M. Marso, A. Förster, P. Kordoš, H. Lüth, S. Wu, X. Zheng, and R. Sobolewski, "Ultrafast Low-Temperature-Grown Epitaxial GaAs Photodetectors Transferred on Flexible Plastic Substrates," IEEE Photonics Technol. Lett. **17**, 1725 (2005).

M. Mikulics, M. Marso, I. C. Mayorga, R. Güsten, S. Stancek, P. Kovác, S. Wu, X. Li, M. Khafizov, R. Sobolewski, E. A. Michael, R. Schieder, M. Wolter, D. Buca, A. Förster, P. Kordoš, and H. Lüth, "Photomixers Fabricated on Nitrogen-Ion-Implanted GaAs," Appl. Phys. Lett. **87**, 041106 (2005).

L. Parlato, R. Latempa, G. Peluso, G. P. Pepe, R. Cristiano, and R. Sobolewski, "The Characteristic Electron–Phonon Coupling Time of Unconventional Superconductors and Implications for Optical Detectors," Supercond. Sci. Technol. **18**, 1244 (2005).

N. G. Usechak and G. P. Agrawal, "An Analytic Technique for Investigating Mode-Locked Lasers," in *Conference on Lasers and Electro-Optics/Quantum Electronics and Laser Science and Photonic Applications, Systems and Technologies 2005* (Optical Society of America, Washington, DC, 2005), Paper CTuCC1.

N. G. Usechak and G. P. Agrawal, "Pulse Switching and Stability in FM Mode-Locked Fiber Lasers," in *Conference on Lasers and Electro-Optics/Quantum Electronics and Laser Science and Photonic Applications, Systems and Technologies 2005* (Optical Society of America, Washington, DC, 2005), Paper JWB46.

D. Wang, A. Verevkin, R. Sobolewski, R. Adam, A. van der Hart, and R. Franchy, "Magneto-optical Kerr Effect Measurements of Spin Dynamics in Cobalt Nanodots," IEEE Trans. Nanotech. **4**, 460 (2005).

L. J. Waxer, D. N. Maywar, J. H. Kelly, T. J. Kessler, B. E. Kruschwitz, S. J. Loucks, R. L. McCrory, D. D. Meyerhofer, S. F. B. Morse, C. Stoeckl, and J. D. Zuegel, "High-Energy Petawatt Capability for the OMEGA Laser," Opt. Photonics News **16**, 30 (2005).

B. Yaakobi, T. R. Boehly, D. D. Meyerhofer, T. J. B. Collins, B. A. Remington, P. G. Allen, S. M. Pollaine, H. E. Lorenzana, and J. H. Eggert, "EXAFS Measurements of Iron bcc-to-hcp Phase Transformation in Nanosecond-Laser Shocks," Phys. Rev. Lett. **95**, 075501 (2005).

B. Yaakobi, T. R. Boehly, D. D. Meyerhofer, T. J. B. Collins, B. A. Remington, P. G. Allen, S. M. Pollaine, H. E. Lorenzana, and J. H. Eggert, "Extended X-Ray Absorption Fine Structure Measurement of Phase Transformation in Iron Shocked by Nanosecond Laser," Phys. Plasmas **12**, 092703 (2005).

Forthcoming Publications

Y. V. Artemova, G. S. Bisnovatyi-Kogan, I. V. Igumenshchev, and I. D. Novikov, "Black Hole Advective Accretion with Optical Depth Transition," to be published in the Astrophysical Journal.

R. Betti and C. Zhou, "High-Density and High-ρR Fuel Assembly for Fast-Ignition Inertial Confinement Fusion," to be published in Physics of Plasmas.

A. C.-A. Chen, J. U. Wallace, L. Zeng, A. K.-H. Wei, and S. H. Chen, "Novel Light-Emitting Organic Materials with Variable Electron and Hole Conductivities," to be published in the Proceedings of SPIE.

D. Clay, D. Poslunsy, M. Flinders, S. D. Jacobs, and R. Cutler, "Effect of $LiAl_5O_8$ Additions on the Sintering and Optical Transparency of LiAlON," to be published in the Journal of European Ceramic Society.

J. E. DeGroote, A. E. Marino, J. P. Wilson, K. E. Spencer, and S. D. Jacobs, "Effects of Nanodiamond Abrasive Friability in Experimental MR Fluids with Phosphate Laser Glass LHG-8 and Other Optical Glasses," in to be published in the Proceedings of SPIE.

J. A. Delettrez, J. Myatt, P. B. Radha, C. Stoeckl, S. Skupsky, and D. D. Meyerhofer, "Hydrodynamic Simulations of

Integrated Experiments Planned for the OMEGA/OMEGA EP Laser Systems," to be published in Plasma Physics and Controlled Fusion.

D. H. Edgell, W. Seka, R. S. Craxton, L. M. Elasky, D. R. Harding, R. L. Keck, and M. D. Wittman, "Analysis of Cryogenic Target Shadowgraphs at LLE," to be published in Fusion Science and Technology.

D. R. Harding, T. C. Sangster, D. D. Meyerhofer, P. W. McKenty, L. D. Lund, and T. H. Hinterman, "Producing Cryogenic Deuterium Targets for Experiments on OMEGA," to be published in Fusion Science and Technology.

A. Jukna, I. Barboy, G. Jung, S. S. Banerjee, Y. Myasoedov, V. Plausinaitiene, A. Abrutis, X. Li, D. Wang, and R. Sobolewski, "Laser Processed Channels of Easy Vortex Motion in $YBa_2Cu_3O_{7-\delta}$ films," to be published in Applied Physics Letters.

A. K. Knight and D. R. Harding, "Modeling the Sensitivity of a Polymer Vapor Deposition Process to Different Operating Conditions and Parameters," to be published in Fusion Science and Technology.

K. L. Marshall, K. Adelsberger, B. Kolodzie, G. Mhyre, and D. W. Griffin, "A Second-Generation Liquid Crystal Phase-Shifting Point-Diffraction Interferometer Employing Structured Substrates," to be published in the Proceedings of SPIE.

R. L. McCrory, S. P. Regan, S. J. Loucks, D. D. Meyerhofer, S. Skupsky, R. Betti, T. R. Boehly, R. S. Craxton, T. J. B. Collins, J. A. Delettrez, D. H. Edgell, R. Epstein, V. Yu. Glebov, V. N. Goncharov, D. R. Harding, R. L. Keck, J. P. Knauer, J. Marciante, J. A. Marozas, F. J. Marshall, A. V. Maximov, P. W. McKenty, J. Myatt, P. B. Radha, T. C. Sangster, W. Seka, V. A. Smalyuk, J. M. Soures, C. Stoeckl, B. Yaakobi, J. D. Zuegel, C. K. Li, R. D. Petrasso, F. H. Séguin, J. A. Frenje, S. Padalino, C. Freeman, and K. Fletcher, "Direct-Drive Inertial Confinement Fusion Research at the Laboratory for Laser Energetics: Charting the Path to Thermonuclear Ignition," to be published in Nuclear Fusion.

A. G. Noto and K. L. Marshall, "Application of Computational Chemistry Methods to the Prediction of Chirality and Helical Twisting Power in Liquid Crystal Systems," to be published in the Proceedings of SPIE.

W. T. Shmayda, R. Janezic, T. W. Duffy, D. R. Harding, and L. D. Lund, "Tritium Operations at the Laboratory for Laser Energetics," to be published in Fusion Science and Technology.

V. A. Smalyuk, O. Sadot, J. A. Delettrez, D. D. Meyerhofer, S. P. Regan, and T. C. Sangster, "Fourier-Space, Nonlinear Rayleigh–Taylor Growth Measurements of 3-D Laser-Imprinted Modulations in Planar Targets," to be published in Physical Review Letters.

C. Stoeckl, T. R. Boehly, R. B. Stephens, J. A. Delettrez, S. P. Hatchett, J. A. Frenje, V. Yu. Glebov, C. K. Li, J. Miller, R. D. Petrasso, F. H. Séguin, V. A. Smalyuk, W. Theobald, B. Yaakobi, and T. C. Sangster, "Fuel-Assembly Experiments with Gas-Filled, Cone-in-Shell, Fast-Ignitor Targets on OMEGA," to be published in Plasma Physics and Controlled Fusion.

C. Stoeckl, J. A. Delettrez, J. H. Kelly, T. J. Kessler, B. E. Kruschwitz, S. J. Loucks, R. L. McCrory, D. D. Meyerhofer, D. N. Maywar, S. F. B. Morse, J. Myatt, A. L. Rigatti, L. J. Waxer, J. D. Zuegel, and R. B. Stephens, "High-Energy Petawatt Project at the University of Rochester's Laboratory for Laser Energetics," to be published in Fusion Science and Technology.

S. Wu, J. Karpinski, J.-R. Park, and R. Sobolewski, "Long-Lived Coherent Acoustic Oscillators in GaN Single Crystals," to be published in Applied Physics Letters.

L. Zheng, J. C. Lambropoulos, and A. W. Schmid, "Molecular Dynamics Study of UV-Laser-Induced Densification of Fused Silica. II. Effects of Laser Pulse Duration, Pressure, and Temperature, and Comparison with Pressure-Induced Densification," to be published in the Journal of Non-Crystalline Solids.

J. D. Zuegel, S. Borneis, C. Barty, B. LeGarrec, C. Danson, N. Miyanaga, P. K. Rambo, T. J. Kessler, A. W. Schmid, L. J. Waxer, B. E. Kruschwitz, R. Jungquist, N. Blanchot, E. Moses, J. Britten, C. LeBlanc, F. Amiranoff, J. L. Porter, J. Schwarz, M. Geissel, I. C. Smith, I. Jovanovic, and J. Dawson, "Laser Challenges for Fast Ignition," to be published in Fusion Science and Technology.

Conference Presentations

S. G. Lukishova, A. W. Schmid, R. Knox, P. Freivald, R. W. Boyd, C. R. Stroud, Jr., and K. L. Marshall, "Deterministically Polarized Fluorescence from Single-Dye Molecules Aligned in Liquid Crystal Host," IQEC/CLEO 2005, Tokyo, Japan, 11–15 July 2005.

The following presentations were made at the SPIE 50th Annual Meeting, San Diego, CA, 31 July–4 August 2005:

A. C.-A. Chen, J. U. Wallace, L. Zeng, A. K.-H. Wei, and S. H. Chen, "Novel Light-Emitting Organic Materials with Variable Electron and Hole Conductivities."

J. E. DeGroote, A. E. Marino, J. P. Wilson, K. E. Spencer, and S. D. Jacobs, "Effects of Nanodiamond Abrasive Friability in Experimental MR Fluids with Phosphate Laser Glass LHG-8 and Other Optical Glasses."

E. Fess, J. Schoen, M. Bechtold, and D. Mohring, "Ultraform Finishing Process for Optical Materials."

M. Haurylau, S. P. Anderson, K. L. Marshall, and P. M. Fauchet, "Electrical Tuning of Silicon-Based 2-D Photonic Bandgap Structures."

K. L. Marshall, K. Adelsberger, B. Kolodzie, G. Mhyre, and D. W. Griffin, "A Second-Generation Liquid Crystal Phase-Shifting Point-Diffraction Interferometer Employing Structured Substrates."

A. G. Noto and K. L. Marshall, "Application of Computational Chemistry Methods to the Prediction of Chirality and Helical Twisting Power in Liquid Crystal Systems."

The following presentations were made at the 14th APS Topical Conference on Shock Compression of Condensed Matter, Baltimore, MD, 31 July–5 August 2005:

T. R. Boehly, D. G. Hicks, J. H. Eggert, E. Vianello, J. E. Miller, J. F. Hansen, P. M. Celliers, G. W. Collins, and D. D. Meyerhofer, "Direct-Density Measurements of Multi-Mbar Shock Waves for Absolute Equation-of-State Studies."

D. D. Meyerhofer, "Creating Extreme Material Properties with High-Energy Laser Systems."

J. E. Miller, T. R. Boehly, E. Vianello, W. J. Armstrong, C. Sorce, W. Theobald, D. D. Meyerhofer, D. G. Hicks, J. H. Eggert, and P. M. Celliers, "Streaked Optical Pyrometer for Shock Wave and EOS Studies."

E. Vianello, T. R. Boehly, J. E. Miller, R. S. Craxton, V. N. Goncharov, I. V. Igumenshchev, D. D. Meyerhofer, D. G. Hicks, and P. M. Celliers, "Laser-Driven Shock-Timing Experiments in Planar CH and Cryogenic Deuterium Targets."

The following presentations were made at IFSA 2005, Biarritz, France, 4–9 September 2005:

R. Betti and C. Zhou, "Low-Adiabat Implosions for Fast-Ignition Inertial Confinement Fusion."

J. Bromage, J. D. Zuegel, S.-W. Bahk, D. S. Vickery, L. J. Waxer, D. Irwin, V. Bagnoud, R. Boni, M. D. Moore, R. Jungquist, and C. Stoeckl, "High-Intensity Laser Diagnostics for OMEGA EP."

D. H. Edgell, W. Seka, R. S. Craxton, L. M. Elasky, D. R. Harding, R. L. Keck, L. D. Lund, and M. D. Wittman, "Characterization of Cryogenic Direct-Drive ICF Targets During Layering Studies and Just Prior to Shot Time."

V. N. Goncharov, O. V. Gotchev, R. L. McCrory, P. W. McKenty, D. D. Meyerhofer, T. C. Sangster, S. Skupsky, and C. Cherfils-Clérouin, "Ablative Richtmyer–Meshkov Instability: Theory and Experimental Results."

J. H. Kelly, L. J. Waxer, V. Bagnoud, I. A. Begishev, J. Bromage, B. E. Kruschwitz, T. J. Kessler, S. J. Loucks, D. N. Maywar, R. L. McCrory, D. D. Meyerhofer, S. F. B. Morse, J. B. Oliver, A. L. Rigatti, A. W. Schmid, C. Stoeckl, S. Dalton, L. Folnsbee, M. J. Guardalben, R. Jungquist, J. Puth, M. J. Shoup III, D. Weiner, and J. D. Zuegel, "OMEGA EP: High-Energy Petawatt Capability for the OMEGA Laser Facility."

B. E. Kruschwitz, R. Jungquist, J. Qiao, S. Abbey, S. E. Dean, D. N. Maywar, M. D. Moore, L. J. Waxer, and M. E. Wilson, "Large-Aperture Deformable Mirror Correction of Tiled-Grating Wavefront Error."

F. J. Marshall, R. S. Craxton, M. J. Bonino, R. Epstein, V. Yu. Glebov, D. Jacobs-Perkins, J. P. Knauer, J. A. Marozas, P. W. McKenty, S. G. Noyes, P. B. Radha, W. Seka, S. Skupsky, V. A. Smalyuk, J. A. Frenje, C. K. Li, R. D. Petrasso, and F. H. Séguin, "Polar-Direct-Drive Experiments on OMEGA."

R. L. McCrory, D. D. Meyerhofer, S. J. Loucks, S. Skupsky, R. Betti, T. R. Boehly, T. J. B. Collins, R. S. Craxton, J. A. Delettrez, D. H. Edgell, R. Epstein, K. A. Fletcher, C. Freeman, J. A. Frenje, V. Yu. Glebov, V. N. Goncharov, D. R. Harding, I. V. Igumenshchev, R. L. Keck, J. D. Kilkenny, J. P. Knauer, C. K. Li, J. R. Marciante, J. A. Marozas, F. J. Marshall, A. V. Maximov, P. W. McKenty, S. F. B. Morse, J. Myatt, S. Padalino, R. D. Petrasso, P. B. Radha, S. P. Regan, T. C. Sangster, F. H. Séguin, W. Seka, V. A. Smalyuk, J. M. Soures, C. Stoeckl, B. Yaakobi, and J. D. Zuegel, "Progress in Direct-Drive Inertial Confinement Fusion Research at the Laboratory for Laser Energetics."

S. Skupsky, R. S. Craxton, F. J. Marshall, R. Betti, T. J. B. Collins, R. Epstein, V. N. Goncharov, I. V. Igumenshchev, J. A. Marozas, P. W. McKenty, P. B. Radha, J. D. Kilkenny, D. D. Meyerhofer, T. C. Sangster, and R. L. McCrory, "Polar Direct Drive—Ignition at 1-MJ."

J. D. Zuegel, V. Bagnoud, J. Bromage, I. A. Begishev, J. Puth, "High-Performance OPCPA Laser System."

S. D. Allen, S. I. Kudryashov, S. Papernov, and A. W. Schmid, "Nano-Spallation on Silica Film Surfaces by Acoustic Wave Emitted by Laser-Heated Artificial Absorbing Inclusions," 8th International Conference on Laser Ablation, Banff, Canada, 11–16 September 2005.

The following presentations were made at the Boulder Damage Symposium XXXVII, Boulder, CO, 19–21 September 2005:

J. Keck, J. B. Oliver, T. J. Kessler, H. Huang, J. Barone, J. Hettrick, A. L. Rigatti, T. Hoover, K. L. Marshall, A. W. Schmid, A. Kozlov, and T. Z. Kosc, "Manufacture and Development of Multilayer Diffraction Gratings."

J. B. Oliver, T. J. Kessler, H. Huang, J. Keck, A. L. Rigatti, A. W. Schmid, A. Kozlov, and T. Z. Kosc, "Thin-Film Design for Multilayer Diffraction Gratings."

J. B. Oliver, A. L. Rigatti, J. D. Howe, J. Keck, J. Szczepanski, A. W. Schmid, S. Papernov, A. Kozlov, and T. Z. Kosc, "Thin-Film Polarizers for the OMEGA EP Laser System."

S. Papernov, A. W. Schmid, A. L. Rigatti, J. B. Oliver, and J. D. Howe, "Damage Behavior of HfO_2 Monolayer Film Containing Gold Nanoparticles as Artificial Absorbing Defects."

K. L. Marshall, A. Trajkovska-Petkoska, T. Z. Kosc, and S. D. Jacobs, "Polymer Cholesteric Liquid Crystal (PCLC) Flake/Fluid Host Suspensions: A Novel Electro-Optical Medium for Reflective Color Display Applications," Eurodisplay 2005, Edinburgh, Scotland, 19–22 September 2005.

The following presentations were made at the 5th International Laser Operations Workshop, Livermore, CA, 20–22 September 2005:

M. J. Bonino, "Fielding Targets to Support OMEGA Experiments."

B. Kruschwitz, "High-Energy Capability for the OMEGA Laser Facility."

S. J. Loucks, "Laboratory for Laser Energetics Overview."

S. F. B. Morse, "Activation Operations Plan: OMEGA EP."

G. Pien, "Shot Specification Input Flow, Operational Use, and Lead Time Requirements."

K. A. Thorp, "OMEGA Availability and Experimental Effectiveness Data Collection and Analysis to Improve System Performance."

M. Bobeica, R. Q. Gram, and D. R. Harding, "An Experimental Method for Measuring the Response of a Target to the Thermal Environment of the Fusion Reaction Chamber," IEEE/NPSS Symposium on Fusion Engineering, Knoxville, TN, 26–29 September 2005.